CLINICAL IMPACT OF TECHNOLOGICAL INNOVATIONS IN NUCLEAR MEDICINE

EDITED BY: Désirée Deandreis, Ronan Abgral and Martin Huellner

PUBLISHED IN: Frontiers in Medicine

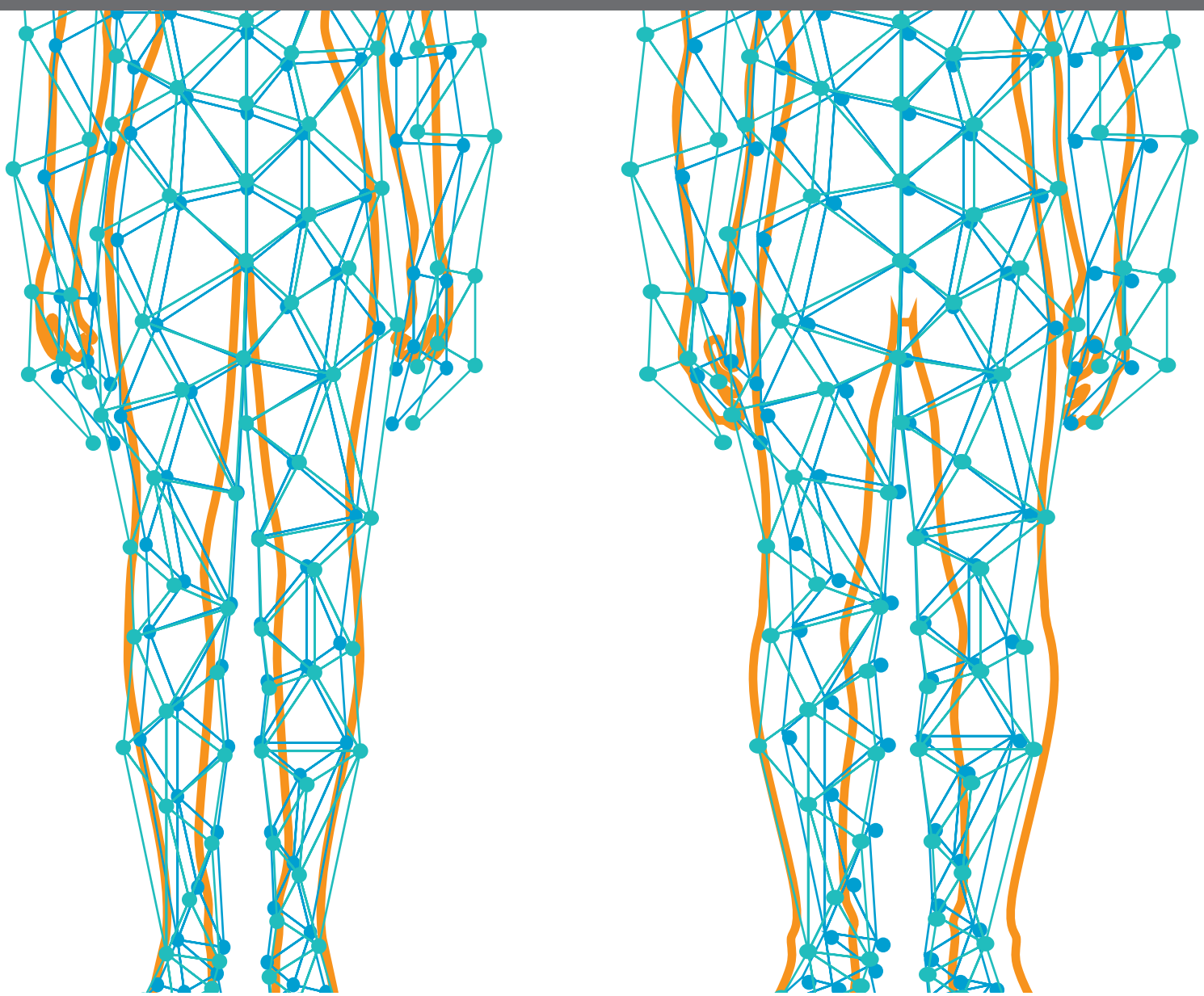

frontiers Research Topics

ISSN 1664-8714
ISBN 978-2-88976-267-5
DOI 10.3389/978-2-88976-267-5

About Frontiers

Frontiers is more than just an open-access publisher of scholarly articles: it is a pioneering approach to the world of academia, radically improving the way scholarly research is managed. The grand vision of Frontiers is a world where all people have an equal opportunity to seek, share and generate knowledge. Frontiers provides immediate and permanent online open access to all its publications, but this alone is not enough to realize our grand goals.

Frontiers Journal Series

The Frontiers Journal Series is a multi-tier and interdisciplinary set of open-access, online journals, promising a paradigm shift from the current review, selection and dissemination processes in academic publishing. All Frontiers journals are driven by researchers for researchers; therefore, they constitute a service to the scholarly community. At the same time, the Frontiers Journal Series operates on a revolutionary invention, the tiered publishing system, initially addressing specific communities of scholars, and gradually climbing up to broader public understanding, thus serving the interests of the lay society, too.

Dedication to Quality

Each Frontiers article is a landmark of the highest quality, thanks to genuinely collaborative interactions between authors and review editors, who include some of the world's best academicians. Research must be certified by peers before entering a stream of knowledge that may eventually reach the public - and shape society; therefore, Frontiers only applies the most rigorous and unbiased reviews.
Frontiers revolutionizes research publishing by freely delivering the most outstanding research, evaluated with no bias from both the academic and social point of view. By applying the most advanced information technologies, Frontiers is catapulting scholarly publishing into a new generation.

What are Frontiers Research Topics?

Frontiers Research Topics are very popular trademarks of the Frontiers Journals Series: they are collections of at least ten articles, all centered on a particular subject. With their unique mix of varied contributions from Original Research to Review Articles, Frontiers Research Topics unify the most influential researchers, the latest key findings and historical advances in a hot research area! Find out more on how to host your own Frontiers Research Topic or contribute to one as an author by contacting the Frontiers Editorial Office: frontiersin.org/about/contact

CLINICAL IMPACT OF TECHNOLOGICAL INNOVATIONS IN NUCLEAR MEDICINE

Topic Editors:
Désirée Deandreis, University of Turin, Italy
Ronan Abgral, Centre Hospitalier Regional Universitaire (CHU) de Brest, France
Martin Huellner, University Hospital Zürich, Switzerland

Citation: Deandreis, D., Abgral, R., Huellner, M., eds. (2022). Clinical Impact of Technological Innovations in Nuclear Medicine. Lausanne: Frontiers Media SA. doi: 10.3389/978-2-88976-267-5

Table of Contents

frontiers in Medicine

ORIGINAL RESEARCH
published: 22 April 2021
doi: 10.3389/fmed.2021.664529

Application of Artificial Neural Network to Preoperative ^{18}F-FDG PET/CT for Predicting Pathological Nodal Involvement in Non-small-cell Lung Cancer Patients

Silvia Taralli[1], Valentina Scolozzi[1], Luca Boldrini[2], Jacopo Lenkowicz[2], Armando Pelliccioni[3], Margherita Lorusso[1], Ola Attieh[4], Sara Ricciardi[5], Francesco Carleo[6], Giuseppe Cardillo[6] and Maria Lucia Calcagni[1,7]*

[1] Unità Operativa Complessa (UOC) di Medicina Nucleare, Dipartimento di Diagnostica per Immagini, Radioterapia Oncologica ed Ematologia, Fondazione Policlinico Universitario A. Gemelli IRCCS, Rome, Italy, [2] Unità Operativa Complessa (UOC) di Radioterapia Oncologica, Dipartimento di Diagnostica per Immagini, Radioterapia Oncologica ed Ematologia, Fondazione Policlinico Universitario A. Gemelli IRCCS, Rome, Italy, [3] Department of Occupational and Environmental Medicine, Istituto Nazionale Assicurazione Infortuni sul Lavoro (INAIL), Rome, Italy, [4] Nuclear Medicine Department, Jordanian Royal Medical Services, Amman, Jordan, [5] Department of Cardiothoracic Surgery, S. Orsola-Malpighi University Hospital, Bologna, Italy, [6] Unit of Thoracic Surgery, San Camillo Forlanini Hospital, Rome, Italy, [7] Dipartimento Universitario di Scienze Radiologiche ed Ematologiche, Università Cattolica del Sacro Cuore, Rome, Italy

OPEN ACCESS

Edited by:
Désirée Deandreis, University of Turin, Italy

Reviewed by:
Riccardo Laudicella, Università degli Studi di Messina, Italy
Pierpaolo Alongi, Institute Foundation G. Giglio, Italy

***Correspondence:**
Silvia Taralli
silvia.taralli@hotmail.it
orcid.org/0000-0002-1715-9953

Specialty section:
This article was submitted to Nuclear Medicine, a section of the journal Frontiers in Medicine

Received: *05 February 2021*
Accepted: *25 March 2021*
Published: *22 April 2021*

Citation:
Taralli S, Scolozzi V, Boldrini L, Lenkowicz J, Pelliccioni A, Lorusso M, Attieh O, Ricciardi S, Carleo F, Cardillo G and Calcagni ML (2021) Application of Artificial Neural Network to Preoperative ^{18}F-FDG PET/CT for Predicting Pathological Nodal Involvement in Non-small-cell Lung Cancer Patients. Front. Med. 8:664529. doi: 10.3389/fmed.2021.664529

Purpose: To evaluate the performance of artificial neural networks (aNN) applied to preoperative ^{18}F-FDG PET/CT for predicting nodal involvement in non-small-cell lung cancer (NSCLC) patients.

Methods: We retrospectively analyzed data from 540 clinically resectable NSCLC patients (333 M; 67.4 ± 9 years) undergone preoperative ^{18}F-FDG PET/CT and pulmonary resection with hilo-mediastinal lymphadenectomy. A 3-layers NN model was applied (dataset randomly splitted into 2/3 training and 1/3 testing). Using histopathological reference standard, NN performance for nodal involvement (N0/N+ patient) was calculated by ROC analysis in terms of: area under the curve (AUC), accuracy (ACC), sensitivity (SE), specificity (SP), positive and negative predictive values (PPV, NPV). Diagnostic performance of PET visual analysis (N+ patient: at least one node with uptake ≥ mediastinal blood-pool) and of logistic regression (LR) was evaluated.

Results: Histology proved 108/540 (20%) nodal-metastatic patients. Among all collected data, relevant features selected as input parameters were: patients' age, tumor parameters (size, PET visual and semiquantitative features, histotype, grading), PET visual nodal result (patient-based, as N0/N+ and N0/N1/N2). Training and testing NN performance (AUC = 0.849, 0.769): ACC = 80 and 77%; SE = 72 and 58%; SP = 81 and 81%; PPV = 50 and 44%; NPV = 92 and 89%, respectively. Visual PET performance: ACC = 82%, SE = 32%, SP = 94%; PPV = 57%, NPV = 85%. Training and testing LR performance (AUC = 0.795, 0.763): ACC = 75 and 77%; SE = 68 and 55%; SP = 77 and 82%; PPV = 43 and 43%; NPV = 90 and 88%, respectively.

Conclusions: aNN application to preoperative ^{18}F-FDG PET/CT provides overall good performance for predicting nodal involvement in NSCLC patients candidate to surgery, especially for ruling out nodal metastases, being NPV the best diagnostic result; a high NPV was also reached by PET qualitative assessment. Moreover, in such population with low *a priori* nodal involvement probability, aNN better identify the relatively few and unexpected nodal-metastatic patients than PET analysis, so supporting the additional aNN use in case of PET-negative images.

Keywords: PET/CT, 18F-FDG, non-small-cell lung cancer, artificial neural network, nodal staging

INTRODUCTION

The evaluation of lymph nodal status is of paramount importance for selecting the optimal therapeutic approach in patients with non-small-cell lung cancer (NSCLC), with N0 and N1 patients addressed to surgery (when clinically feasible), and N3 ones to non-surgical approaches, while N2 patients still have more controversial therapeutic options (1, 2). 18-Fluorine-Fluorodeoxyglucose Positron Emission Tomography/Computed Tomography (^{18}F-FDG PET/CT) is widely used for nodal staging in NSCLC patients, being recommended by the National Comprehensive Cancer Network (NCCN) guidelines (1). ^{18}F-FDG PET/CT shows an overall good accuracy for nodal evaluation with sensitivity and specificity values ranging from 72 to 90% and from 81 to 95%, respectively (1–6). More recently, machine learning methods have been applied to ^{18}F-FDG PET/CT as an advanced and innovative analysis tool in NSCLC patients for staging, treatment evaluation and prognostic stratification (7–10).

Neural Networks (NN) represent an application of machine learning based on an artificial reinterpretation of the human brain structure, that relies on the use of numerous layers of "neurons." Each neuron is characterized by a specific weight and importance in the context of the whole network. Similarly, each layer receives data, calculates scores and passes the output of the analysis to the next layer in a self-learning process. This architecture has been recently widely used in the context of biomedical imaging research and radiation oncology, aiming to predict clinical outcomes and enrich diagnostic information, describing the interactions and complex simultaneous relationships of variables belonging to different domains (11–13). Growing, although still limited, literature evidence has explored the application of NN to ^{18}F-FDG PET/CT for predicting nodal involvement in NSCLC patients, but burdened by differences in clinical and procedural aspects (14–17).

Aim of our study was to evaluate the performance of artificial neural network (aNN) applied to preoperative ^{18}F-FDG PET/CT for predicting pathological nodal involvement in clinically resectable NSCLC patients.

MATERIALS AND METHODS

Study Population

We retrospectively reviewed medical records of all consecutive patients referred to the PET/CT center of "Fondazione Policlinico Universitario Agostino Gemelli IRCCS" in Rome by a local Thoracic Surgery Unit between January 2007 and December 2017 for pulmonary lesions' evaluation. We included only patients with: (1) malignant pulmonary lesions histologically proven as NSCLC; (2) judged resectable at pre-operative Multidisciplinary Tumor Board evaluation (including those with single N2 station at pre-operative invasive mediastinal staging); (3) undergone lung resection and hilo-mediastinal lymphadenectomy; (4) not addressed to induction chemotherapy and/or radiotherapy. Exclusion criteria were: all patients not fitting the inclusion criteria; with proven N2 multistation or N3 at invasive mediastinal staging procedures. A set of clinical, anatomic, metabolic and histopathological data were retrospectively collected. Pathological TNM staging was defined according to the 8th staging system edition (18, 19). This retrospective study was approved by the local institution's ethics committee (Comitato Etico Lazio 1). For each patient, PET/CT imaging was performed in the clinical routine with written informed consent.

^{18}F-FDG PET/CT Image Acquisition and Interpretation

All PET/CT were acquired according to standard protocol (6 h fasting-state, blood glucose levels <150 mg/dl; acquisition time of 60 ± 10 min post-injection of 185–370 MBq of ^{18}F-FDG, according to BMI), using an integrated 3D PET/CT device (Gemini GXL by Philips Medical System, Cleveland, Ohio or Biograph mCT by Siemens Healthineers, Chicago, Illinois) with a low-dose unenhanced CT scan (120 kV, 50–80 mA) for anatomical localization and attenuation correction. All PET images (reconstructed with iterative algorithms) were evaluated by two independent nuclear medicine physicians (ST, VS), blinded to the final pathological TNM staging, using a dedicated fusion and display software (Syngo.via MM Oncology software; Siemens Medical Solutions). For primary lung tumor evaluation, a qualitative analysis was performed: PET was scored as positive if ^{18}F-FDG uptake was equal or higher than the mediastinal blood-pool, as negative if lower. A semiquantitative

TABLE 1 | Main clinical, anatomic, metabolic, and histopathological characteristics of the study population ($n = 540$).

Characteristics	*N*
Gender	
Male	333 (61.7%)
Female	207 (38.3%)
Age (years)	
Mean ± SD	67.4 ± 9
Tumor size (mm)	
Mean ± SD	25.3 ± 14.3
Tumor location	
Right lung	293 (54.2%)
Upper lobes[a]	348 (64.4%)
Central[b]	146 (27%)
Tumor visual PET result	
Positive	452 (83.7%)
Negative	88 (16.3%)
Tumor SUVmax	
Mean ± SD	6.6 ± 5.6
Tumor SUVmean	
Mean ± SD	4.2 ± 3.4
MTV (cm^3)	
Mean ± SD	7.6 ± 16.7
TLG	
Mean ± SD	52.6 ± 182.1
Nodal visual PET result	
Nodal status	479 N0 (88.7%), 61 N+ (11.3%)
Nodal staging	479 N0 (88.7%), 27 N1 (5%), 34 N2 (6.3%)
Histology	
Adenocarcinoma	385 (71.3%)
Squamous cell carcinoma	89 (16.5%)
Others	66 (12.2%)
Grading	
G1	73 (13.5%)
G1–G2, G2	26 (4.8%), 201 (37.2%)
G2–G3, G3	68 (12.6%), 167 (31%)
G4	5 (0.9%)
Pathological N result (pN)	
N0	432 (80%)
N1	45 (8.3%)
N2	63 (11.7%)

SD, standard deviation; MTV, metabolic tumor volume; TLG, total lesion glycolysis.
[a]The right middle lobe and lingula were included in the upper lobes location.
[b]The lung lesion was defined as central if located in the inner one-third of the lung parenchyma, and as peripheral if located in the outer two-thirds of lung parenchyma.

TABLE 2 | Comparison in collected features between training and testing groups.

Feature	*p*-value
Age[a]	0.17
Gender (*male/female*)	0.31
Location T (*right/left lung*)	0.22
Location T (*upper/lower lobe*)	0.57
Site T (*central/peripheral*)	1.00
Histology T0 (*neuroendocrine tumor*)[b]	0.95
Histology T1 (*adenocarcinoma*)[b]	0.94
Histology T2 (*squamous cell carcinoma*)[b]	0.97
Histology T3 (*adeno-squamous carcinoma*)[b]	1.00
Histology T4 (*pleomorphic carcinoma*)[b]	0.84
Histology T5 (*poorly differentiated carcinoma*)[b]	0.35
Grading T0 (*G1–G2*)[b]	0.65
Grading T1 (*G1*)[b]	0.27
Grading T2 (*G2*)[b]	0.61
Grading T3 (*G3*)[b]	0.25
Size T (*mm*)[a]	0.52
PET result T (*negative/positive*)	0.25
T SUVmax[a]	0.35
T SUVmean[a]	0.25
T TLG[a]	0.45
T MTV[a]	0.83
PET result N (*negative/positive*)	0.51
PET staging N0 (*N0/not N0*)[b]	0.51
PET staging N1 (*N1/not N1*)[b]	1.00

T, tumor; N, nodal.
[a]Numerical features were Z-standardized.
[b]Categorical features were binarized.

analysis was also performed: for lesions segmentation, a fixed relative threshold method was adopted and a 3D volumetric region of interest (VOI) was drawn semi-automatically over the primary tumor on fused PET/CT images, with a fixed threshold of 40% of the maximum standardized uptake value. Then, the following tumor semiquantitative parameters were extracted, applying the EQ·PET quantification technology (20): maximum and mean standardized uptake values (SUVmax, SUVmean), metabolic tumor volume (MTV, expressed in cm^3) and total lesion glycolysis (TLG, defined as the product of SUVmean and MTV). The anatomical consistency of tumor delineation was visually checked and volumetric region of interest was adjusted manually, if needed. For nodal evaluation, a visual patient-based PET nodal status was defined: any lymph node with ^{18}F-FDG uptake $\geq$ mediastinal blood-pool was classified as PET positive; each patient with at least one positive lymph node was scored as PET positive (PET N+), otherwise as negative (PET N0). Moreover, for each patient a PET nodal staging (PET N0, N1, N2, or N3) was defined, according to sites of PET positive nodes and the 8th edition of TNM staging. Any disagreement was resolved by consensus. Histological nodal status was used as reference standard to verify PET results.

Neural Network Development

The collected clinical, anatomic, metabolic, and histopathological features were used as input parameters of the model: patients' age and gender, tumor size and location (as right/left lung, upper/lower lobes, and central/peripheral), PET tumor visual result and semiquantitative parameters, PET nodal status, PET nodal staging, tumor histotype and grading. Categorical features were binarized and numerical features were *Z*-standardized. The dataset was randomly split into 2/3 training and 1/3 testing, being

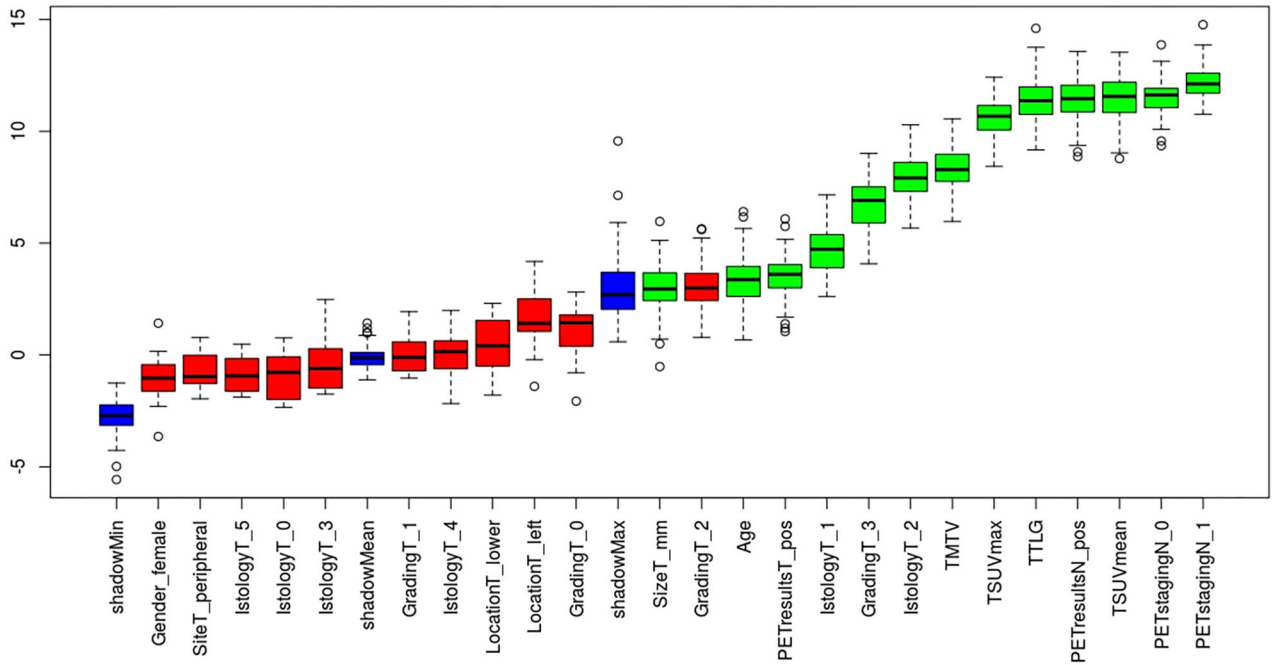

FIGURE 1 | Relevant features (*highlighted in green*) to the outcome of interest (pathological nodal involvement) selected with Boruta algorithm.

the sample size numerous enough to perform hold-out validation instead of cross-validation. Relevant features to outcome of interest (i.e., surgically-proven nodal status) were selected with Boruta algorithm on the training set (21). A NN based model was then realized with the selected features. Considering the sample size, the events distribution and the number of selected features, a 3-layers neural network (12, 6, and 2 activation neurons, respectively) was trained on the training set with the Boruta-selected features as input. Network training specifications were as follows: the first two layers had activation function ReLu, while the third layer (classification layer) had Softmax. Categorical cross-entropy was the loss function and Adam was the optimizer. The model was trained for 500 epochs with 150 batch size and 0.1 validation split. Classification performance of the trained network in predicting nodal involvement was evaluated on the testing set applying the Receiver Operating Characteristic (ROC) analysis, using histological nodal status as reference standard. Logistic regression (LR) model was also trained on the training set after Akaike information criterion (AIC)-based stepwise selection on the Boruta-selected features.

Statistical Analysis

Continuous variables were expressed as mean (with standard deviation) or median (with range) and categorical data as a percentage. Comparison between training and testing groups in collected features were performed using Mann–Whitney/Chi-square test for continuous and categorical data, respectively. On ROC analysis, the NN diagnostic performance for nodal involvement (on both training and testing sets) was calculated in terms of Area Under the Curve (AUC) and classification matrix at the Youden-index classification threshold were computed: accuracy (ACC), sensitivity (SE), specificity (SP), positive and negative predictive values (PPV and NPV). Diagnostic performances for nodal involvement (N0/N+) of the visual PET analysis and LR model (on both training and testing sets) were also assessed. PPV and NPV were calculated assuming that the individual pre-test probability of nodal metastatic disease was equal to the prevalence of pathological nodal involvement (pN+) found in our population. Results were reported with 95% Confidence Intervals (CIs). Statistical significance was set at $p < 0.05$. Statistical analyses were performed in R version 3.4 and Python version 3.7.

RESULTS

Study Population

Finally, 540 consecutive clinically resectable NSCLC patients (333 males; mean age: 67.4 ± 9 years), who underwent pre-operative ^{18}F-FDG PET/CT (44 ± 28 days before surgery) were selected. **Table 1** reports the main characteristics of the study population. Among the 540 patients, 528 underwent lobectomy, nine bi-lobectomy and three atypical pulmonary resection. A total of 1,620 nodal stations (from station 2 to 11) were histologically evaluated (3 ± 1 stations per patient), with a total of 4,158 examined nodes (8 ± 5 nodes per patient); peribronchial nodes found in the resected lobe were also pathologically assessed in 439 patients. Histopathological nodal involvement was found in 108/540 (20%) patients: 45/108 staged as pN1 and 63/108 as pN2. Overall, in the total 540 patients, 80% resulted as pN0, 8.3% as pN1 and 11.7% as pN2. According to pathologic staging, 383

TABLE 3 | Diagnostic performance of neural network, logistic regression, and visual ^{18}F-FDG PET/CT analysis for pathological nodal involvement.

	Training set (n = 356)		Test set (n = 184)		All dataset (n = 540)
	NN	LR	NN	LR	PET visual analysis
AUC (95%CI)	0.849 (0.751–0.838)	0.795 (0.700–0.800)	0.769 (0.699–0.827)	0.763 (0.669–0.820)	n.a.
ACC (95%CI)	0.80 (0.75–0.84)	0.75 (0.70–0.80)	0.77 (0.70–0.83)	0.77 (0.70–0.83)	0.82 (0.78–0.85)
SE (95%CI)	0.72 (0.60–0.82)	0.68 (0.56–0.73)	0.58 (0.41–0.74)	0.55 (0.38–0.72)	0.32 (0.24–0.42)
SP (95%CI)	0.81 (0.76–0.86)	0.77 (0.72–0.82)	0.81 (0.74–0.87)	0.82 (0.75–0.88)	0.94 (0.91–0.96)
PPV (95%CI)	0.50 (0.40–0.60)	0.43 (0.34–0.53)	0.44 (0.30–0.59)	0.43 (0.29–0.59)	0.57 (0.45–0.69)
NPV (95%CI)	0.92 (0.88–0.95)	0.90 (0.86–0.94)	0.89 (0.82–0.93)	0.88 (0.81–0.93)	0.85 (0.81–0.88)

NN, neural network; LR, logistic regression; AUC, area under the curve; CI, confidence interval; ACC, accuracy; SE, sensitivity; SP, specificity; PPV, positive predictive value; NPV, negative predictive value.

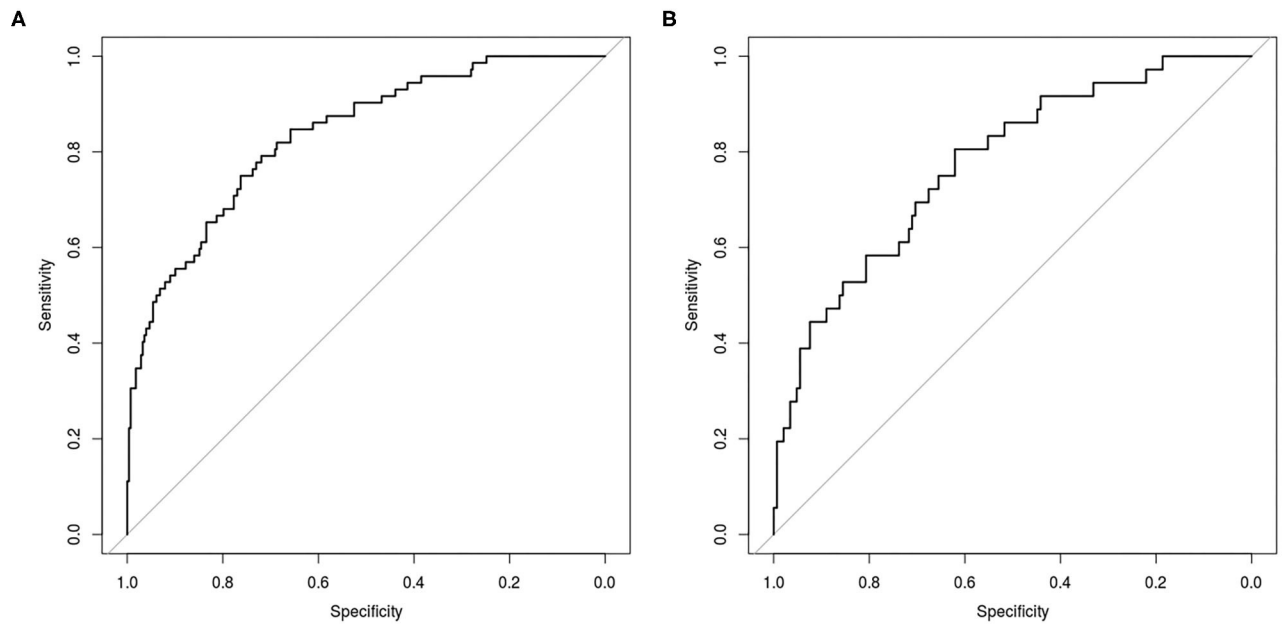

FIGURE 2 | Receiver Operating Characteristic (ROC) curve for prediction of nodal involvement according to NN analysis in the training set **(A)** and in the testing set **(B)**.

patients were classified as stage I (28 IA1; 152 IA2; 78 IA3; 125 IB), 74 stage II (13 IIA; 61 IIB), 80 stage III (70 IIIA; 10 IIIB), and 3 stage IVA (for pleural localizations).

Neural Network Analysis

No features differences ($p > 0.05$) were observed between training and testing sets (**Table 2**), that also showed the same proportion of pN0 and pN+ patients. From the set of collected features, Boruta algorithm selected 13 relevant as input parameters (**Figure 1**): patients' age, tumor size, PET tumor parameters (visual result, SUVmax, SUVmean, TLG, MTV), patient-based PET nodal status (as N0/N+) and PET nodal staging (as N0/N1/N2), tumor histotype (adenocarcinoma, squamous cell carcinoma) and grading (G3). The NN was then trained with all Boruta-selected features as input variables. From ROC analysis, NN diagnostic performance for nodal involvement (N+/N0) for the training and testing sets were: AUC = 0.849 (95%CI: 0.751–0.838), ACC = 0.80 (95%CI: 0.75–0.84), SE = 0.72 (95%CI: 0.60–0.82), SP = 0.81 (95%CI: 0.76–0.86), PPV = 0.50 (95%CI: 0.40–0.60), NPV = 0.92 (95%CI: 0.88–0.95), and AUC = 0.769 (95%CI: 0.699–0.827), ACC = 0.77 (95%CI: 0.70–0.83), SE = 0.58 (95%CI: 0.41–0.74), SP = 0.81 (95%CI: 0.74–0.87); PPV = 0.44 (95%CI: 0.30–0.59), NPV = 0.89 (95%CI: 0.82–0.93), respectively (**Table 3** and **Figure 2**).

^{18}F-FDG PET/CT

On PET visual analysis, 479/540 patients were classified as N0: 406/479 with no pathological nodal involvement (pN0, PET true-negatives), 73/479 with at least one metastatic node (pN+, PET false-negatives). The remaining 61/540 patients were classified as PET positive for nodal involvement: 35/61 histologically confirmed (pN+, PET true-positives), 26/61 with no pathological nodes (pN0, PET false-positives). Diagnostic performance of PET visual analysis for nodal involvement (N0/N+) was: ACC =

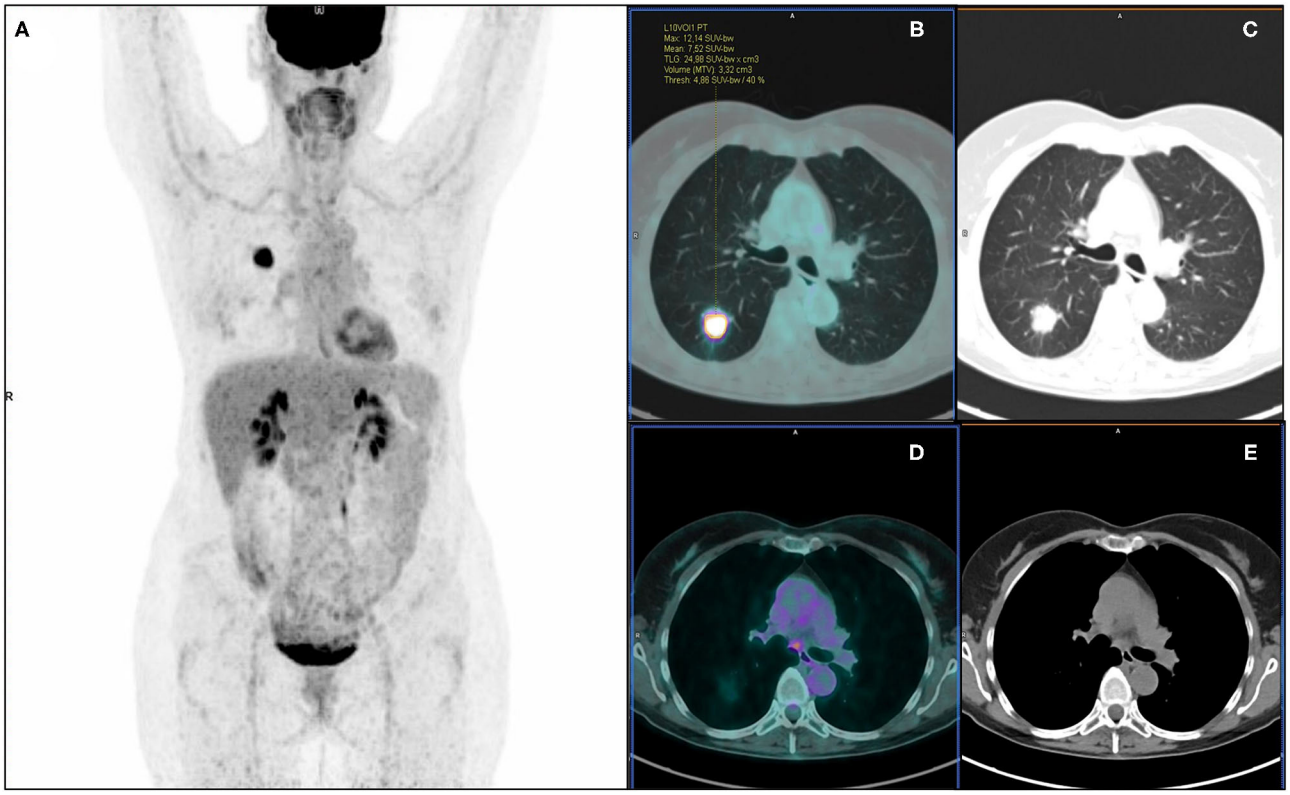

FIGURE 3 | ^{18}F-FDG PET/CT maximum intensity projection **(A)**, transaxial fused **(B)**, and coregistered CT images **(C)** of a 57-year-old female with lung adenocarcinoma of the right lower lobe (maximum axial diameter: 30 mm), showing increased metabolic activity in the primary tumor lesion (SUVmax: 12.14; SUVmean: 7.52; MTV: 3.32 cm^3; TLG: 24.98) and a focus of increased tracer uptake in a subcarinal mediastinal lymph node **(D,E)**. According to visual analysis, the patient was classified as PET positive for nodal involvement (PET N+). Further histopathological examination revealed no pathological nodal involvement (pN0, PET false-positive). Artificial NN correctly classified the patient as N0.

0.82 (95%CI: 0.78–0.85), SE = 0.32 (95%CI: 0.24–0.42), SP = 0.94 (95%CI: 0.91–0.96), PPV = 0.57 (95%CI: 0.45–0.69), NPV = 0.85 (95%CI: 0.81–0.88) (**Table 3**). When considering PET nodal staging, among the 479 PET negative patients, 406/479 (84.8%) were correctly staged resulting pN0, 73/479 (15.2%) were upstaged resulting pN1 (30/73) or pN2 (43/73). Regarding the 61 PET positive patients, 27 were classified as PET N1 and 34 as PET N2. Among PET N1 patients, 11/27 were correctly staged resulting pN1, 8/27 were downstaged resulting pN0 and 8/27 were upstaged resulting pN2. Among PET N2 patients, 12/34 were correctly staged resulting pN2, 22/34 were downstaged resulting pN1 (4/22) or pN0 (18/22). PET/CT images of illustrative cases are reported in **Figures 3**, **4**.

The LR model with stepwise selection based on AIC criteria gave the model in **Table 4**. Logistic regression diagnostic performance for nodal involvement at training and testing group were: AUC = 0.795 (95%CI: 0.700–0.800), ACC = 0.75 (95%CI: 0.70–0.80), SE = 0.68 (95%CI: 0.56–0.73), SP = 0.77 (95%CI: 0.72–0.82), PPV = 0.43 (95%CI: 0.34–0.53), NPV = 0.90 (95%CI: 0.86–0.94), and AUC = 0.763 (95%CI: 0.669–0.820), ACC = 0.77 (95%CI: 0.70–0.83), SE = 0.55 (95%CI: 0.39–0.72), SP = 0.82 (95%CI: 0.75–0.88), PPV = 0.43 (95%CI: 0.29–0.59), NPV = 0.88 (95%CI: 0.81–0.93), respectively (**Table 3**).

DISCUSSION

Aim of our study was to evaluate the diagnostic performance of aNN to preoperative ^{18}F-FDG PET/CT for predicting pathological nodal involvement in clinically resectable NSCLC patients. The main strength points of this study are: the largest lung cancer population on which NN were applied for the same aim; the use of the widest combination of clinical, anatomic, metabolic, and histopathological features as input parameters; the surgical lymphadenectomy as golden reference in all patients.

From our results, aNN provided overall good performance for predicting pathological nodal involvement with a diagnostic accuracy >75% at both training and testing sets; similar diagnostic performance on both datasets suggests that overfitting was successfully reduced, supporting the reliability of the results. NN showed higher specificity and NPV than sensitivity and PPV, providing the best diagnostic performance for ruling out nodal metastases. In this context, it has to be considered that the pre-test probability of nodal involvement (and in turn the positive and negative predictive values) mainly depends on the NSCLC clinical settings. Indeed, our population has low *a priori* probability of nodal involvement since deemed clinically resectable, as confirmed by the low prevalence of

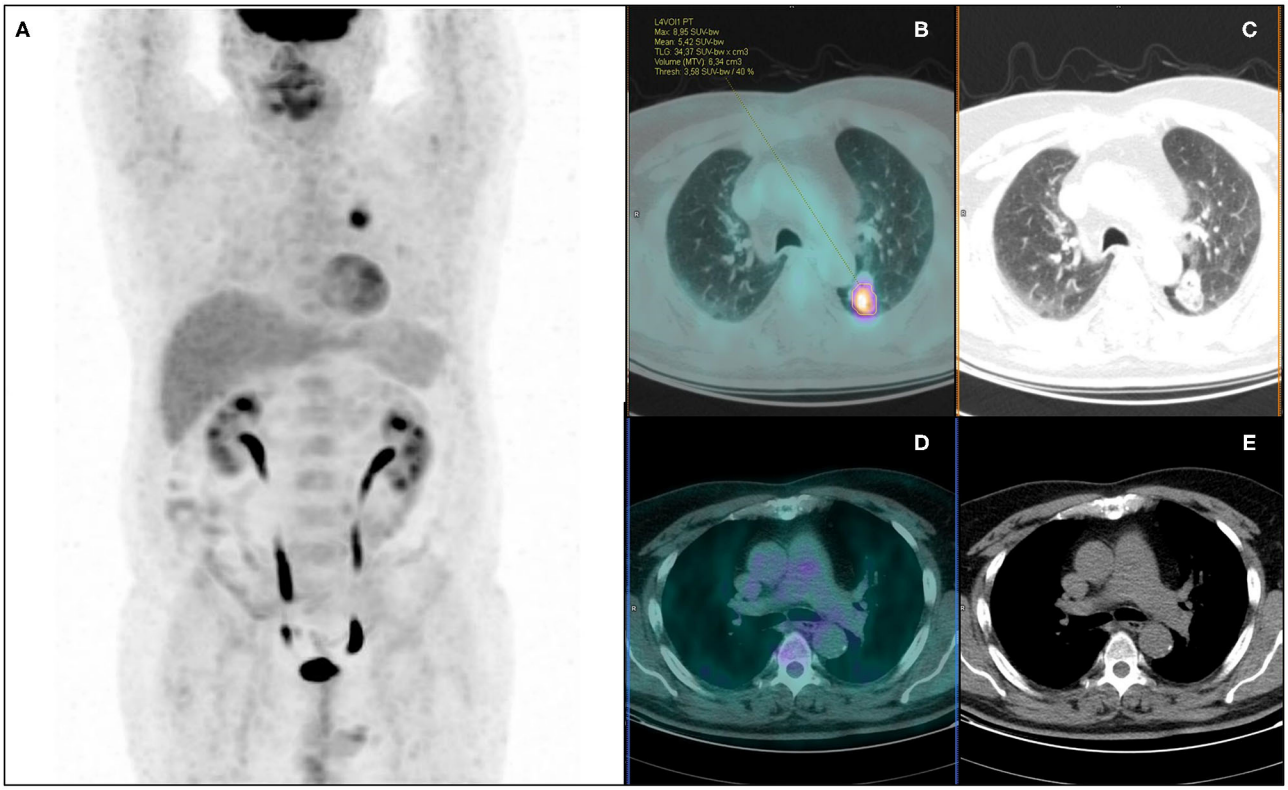

FIGURE 4 | ^{18}F-FDG PET/CT maximum intensity projection **(A)**, transaxial fused **(B)**, and coregistered CT images **(C)** of a 64-year-old male with lung adenocarcinoma of the left lower lobe (maximum axial diameter: 32 mm), showing increased metabolic activity in the primary tumor lesion **(A)** (SUVmax: 8.95; SUVmean: 5.42; MTV: 6.34 cm^3; TLG: 34.37), with no abnormal focus of increased tracer uptake in hilo-mediastinal lymph nodes **(D,E)**. According to visual analysis, the patient was classified as PET negative for nodal involvement (PET N0). Further histopathological examination revealed metastatic homolateral hilar nodes (pN+, PET false-negative). Artificial NN correctly classified the patient as N+.

nodal-metastatic patients and the high NPV. On the other hand, preoperatively identifying the relatively few and unexpected nodal-metastatic patients assumes great relevance, since other treatment strategies rather than the planned up-front surgery can be considered. However, PET visual analysis provided a poor sensitivity, with occult lymph nodal metastases mainly due to small size of metastatic lymph nodes, nodal micro-metastases (22) or metastatic hilar nodes masked by the intense activity of close primary tumor (14, 23). Although suboptimal, the sensitivity provided by aNN resulted relevantly higher than visual analysis (72 vs. 32%, respectively), suggesting that aNN may reduce the chance of ^{18}F-FDG PET/CT false negative results. From a practical point of view, this finding may support the additional use of aNN to the PET/CT reporting activity in case of visually negative images. This diagnostic advantage of aNN may be attributed to the intrinsic properties of this machine learning method, able to explore and recognize complex and generally non-linear relationships among multiple variables, obviously going beyond the PET visual assessment alone.

Analyzing the relevant features selected by Boruta algorithm as input parameters, the metabolic features were the most numerous (8/13) and the first ones in order of importance: PET nodal staging (N0/N1/N2) in the first position, followed by PET nodal status (N0/N+) and semiquantitative parameters. We may suppose that PET nodal staging resulted as the most relevant feature since it appears intrinsically more linked to the target output (i.e., pathological nodal status) than other variables, providing direct and complete information on nodal assessment (even more detailed than dichotomous PET nodal status). When considering the PET semiquantitative tumor-related parameters, their relevance seems to be expected, being widely reported in literature as predictive factors of pathological nodal involvement in NSCLC (24–31).

TABLE 4 | Logistic regression model with stepwise selection based on AIC criteria.

Variable	Coefficient	Standard error	*p*-value
Intercept	−2.071	1.480	0.1
Tumor histology (*squamous cell carcinoma*)	−1.595	0.518	0.002
Tumor grading (*G3*)	1.121	0.309	0.0003
PET tumor result (*positive*)	2.318	1.032	0.02
PET nodal result (*positive*)	1.436	0.473	0.002
PET nodal staging (*N1*)	1.038	0.724	0.1
Patient age	−0.029	0.017	0.08

Visual analysis of primary lesion resulted the last relevant metabolic feature. This finding may be reasonably attributed to its dichotomous nature (uptake $\geq$ or $<$ mediastinal blood-pool activity) compared to the continuous nature of semiquantitative parameters (wide range of uptake levels), so providing less detailed information on tumor metabolism. Among the anatomic variables, tumor size resulted the only relevant feature: it was already reported to be a predictive factor for nodal involvement (26, 32) since reflecting the T-classificator in the TNM staging, and the risk of lymph node involvement increases with the increase of T stage. Lastly, among histological variables, the relevance of G3 (grading-feature) appears in line with the expectations: high grading, reflecting high tumor aggressiveness, increases the risk of metastatic nodal involvement (33), as also observed in our study, with a higher rate of nodal-metastatic patients in G3 group than in well or moderately differentiated groups (34.1 vs. 11.3%). Finally, regarding tumor histotype, more nodal metastases in adenocarcinomas than in squamous cell carcinomas were observed in our population (21.8 vs. 10.1%), supposing that adenocarcinoma type would be more informative for aNN regarding the risk of nodal involvement. Nevertheless, adenocarcinoma resulted a relatively weaker input parameter than the other one, in line with literature, as no concordant and definitive results on the greater or lesser predictive role of one or the other histotype have emerged (26, 27, 34, 35).

In our study, the LR results were only slightly lower compared to NN. A neural network is more complex than LR since one can think of it as a subset of a neural network classifier. LR model can always be simulated using a NN with one hidden node with the identity activation function and one output node with zero bias and logistic sigmoid activation. This finding can suggest that, when applying aNN to ^{18}F-FDG PET for predicting nodal metastases, the added value of modeling non-linear interactions is not sufficient to substantially increase the diagnostic performance, also given the strong association of input variables (primarily PET-related) with the outcome.

Few studies in literature evaluated the application of aNN to ^{18}F-FDG PET/CT in NSCLC for predicting nodal involvement, with several differences in clinical and procedural aspects among single studies and when compared to our work. In particular, Vesselle et al. (14) and Toney et al. (15), investigating 133 NSCLC patients, reported a NN accuracy higher than accuracy of PET expert reader (87.3 and 99.2% vs. 73.5 and 72.4%, respectively). This result seems to outperform the performance reported in our study. However, both authors reported an increased PET accuracy and closer to NN performance (up to 92.2%) when N status was dichotomized in N0+N1 vs. N2+N3 disease. Moreover, it has to be considered that both studies are not comparable to our work due to several aspects (smaller population, inclusion of non-surgically treated patients, heterogeneous reference standard, higher rate of nodal-metastatic patients, fewer input parameters and without PET-volumetric ones) and, mainly, to the criteria used for PET visual nodal analysis, that likely affect the comparison between PET and NN performance. Indeed, nodes have been interpreted as benign or malignant according on the expert reader's clinical experience, taking into account also size, location, and activity of primary tumor and size of the most metabolically active node. On the contrary, we used a strictly metabolic, more standardized, reproducible and objective criterion, interpreting nodes as benign or malignant only based on the mediastinal blood-pool activity. Anyway, the value of adding morphological nodal information for PET interpretation appears negligible in our population of clinically resectable patients, being almost all nodes with short axis $\leq$ 10 mm. Among other two studies focused on the same topic (16, 17), only one compared NN with PET visual performance, reporting similar accuracy, higher NN sensitivity and lower NN specificity for predicting nodal involvement. However, differences in population and/or methodological aspects make both studies not directly comparable to our paper. Finally, our study used the widest combination of clinical, anatomic, metabolic and histopathological data as input parameters, while only morpho-anatomic and/or metabolic features were considered in all the four previous studies; in addition, none of these studies reported LR model for comparison with aNN performance.

We acknowledge some limitations of our study, mainly represented by its retrospective nature. Moreover, a selection bias has to be considered, since only NSCLC patients candidate to surgical resection were included in our analysis, inherently lowering the prevalence of lymph nodal involvement. This aspect could have made our results generalizable only to similar cohorts of NSCLC patients, also affecting the diagnostic performance, especially in terms of PPV (due to the low rate of true positive patients). On the other hand, selecting only patients with surgical nodal evaluation allowed a reliable and robust verification of our results. Finally, external data validation was not applied.

In conclusion, the application of aNN to preoperative ^{18}F-FDG PET/CT, along with clinical, anatomic and histopathological features, provides overall good performance for predicting pathological nodal involvement in clinically resectable NSCLC patients, especially for ruling out nodal metastases. Compared to visual PET analysis, aNN seem able to reduce the chance of PET false negative results; this finding assumes particular relevance in a population of clinically resectable NSCLC patients, with low *a priori* probability of nodal involvement, when the identification of the relatively few and unexpected nodal-metastatic patients may change their planned treatment strategies and also impact on prognosis. From a practical point of view, our observations may support the additional use of aNN to the PET/CT reporting activity in case of visually negative images. The application of aNN for categorizing pathological nodal involvement in N1 vs. N2 disease is topic of further ongoing analyses.

DATA AVAILABILITY STATEMENT

The raw data supporting the conclusions of this article will be made available by the authors, without undue reservation.

ETHICS STATEMENT

The studies involving human participants were reviewed and approved by Comitato Etico Lazio 1. The ethics

committee waived the requirement of written informed consent for participation.

AUTHOR CONTRIBUTIONS

MC, GC, ST, and AP were involved in conception and design of the study. ST, VS, ML, SR, and FC were involved in acquisition of PET/CT and clinical data. ST, VS, and OA analyzed PET/CT data. LB and JL performed logistic regression and neural network analyses. ST and VS conducted a literature research. ST, LB, and JL drafted the manuscript. MC, GC, and AP critically revised the manuscript for important intellectual content. All authors revised the final manuscript and gave their final approval for manuscript submission.

REFERENCES

1. National Comprehensive Cancer Network Guidelines in Oncology. *Non-small Cell Lung Cancer*. Version 06.2020. Available online at: https://www.nccn.org/professionals/physician_gls/pdf/nscl.pdf (accessed July 20, 2020).
2. De Leyn P, Dooms C, Kuzdzal J, Lardinois D, Passlick B, Rami-Porta R, et al. Revised ESTS guidelines for preoperative mediastinal lymph node staging for non-small-cell lung cancer. *Eur J Cardiothorac Surg.* (2014) 45:787–98. doi: 10.1093/ejcts/ezu028
3. Lv YL, Yuan DM, Wang K, Miao XH, Qian Q, Wei SZ, et al. Diagnostic performance of integrated positron emission tomography/computed tomography for mediastinal lymph node staging in non-small cell lung cancer: a bivariate systematic review and meta-analysis. *J Thorac Oncol.* (2011) 6:1350–8. doi: 10.1097/JTO.0b013e31821d4384
4. Silvestri GA, Gonzalez AV, Jantz MA, Margolis ML, Gould MK, Tanoue LT, et al. Methods for staging non-small cell lung cancer: diagnosis and management of lung cancer, 3rd ed: American College of Chest Physicians evidence-based clinical practice guidelines. *Chest.* (2013) 143:e211S–e50S. doi: 10.1378/chest.12-2355
5. Schmidt-Hansen M, Baldwin DR, Hasler E, Zamora J, Abraira V, Roque IFM. PET-CT for assessing mediastinal lymph node involvement in patients with suspected resectable non-small cell lung cancer. *Cochrane Database Syst Rev.* (2014) 2014:CD009519. doi: 10.1002/14651858.CD009519.pub2
6. Zhao L, He ZY, Zhong XN, Cui ML. (18)FDG-PET/CT for detection of mediastinal nodal metastasis in non-small cell lung cancer: a meta-analysis. *Surg Oncol.* (2012) 21:230–6. doi: 10.1016/j.suronc.2011.11.001
7. Bertolaccini L, Solli P, Pardolesi A, Pasini A. An overview of the use of artificial neural networks in lung cancer research. *J Thorac Dis.* (2017) 9:924–31. doi: 10.21037/jtd.2017.03.157
8. Hyun SH, Ahn MS, Koh YW, Lee SJ. A machine-learning approach using PET-based radiomics to predict the histological subtypes of lung cancer. *Clin Nucl Med.* (2019) 44:956–60. doi: 10.1097/RLU.0000000000002810
9. Kirienko M, Sollini M, Silvestri G, Mognetti S, Voulaz E, Antunovic L, et al. Convolutional neural networks promising in lung cancer T-parameter assessment on baseline FDG-PET/CT. *Contrast Media Mol Imaging.* (2018) 2018:1382309. doi: 10.1155/2018/1382309
10. Avanzo M, Stancanello J, Pirrone G, Sartor G. Radiomics and deep learning in lung cancer. *Strahlenther Onkol.* (2020) 196:879–87. doi: 10.1007/s00066-020-01625-9
11. Sahiner B, Pezeshk A, Hadjiiski LM, Wang X, Drukker K, Cha KH, et al. Deep learning in medical imaging and radiation therapy. *Med Phys.* (2019) 46:e1–36. doi: 10.1002/mp.13264
12. Esteva A, Robicquet A, Ramsundar B, Kuleshov V, DePristo M, Chou K, et al. A guide to deep learning in healthcare. *Nat Med.* (2019) 25:24–9. doi: 10.1038/s41591-018-0316-z
13. Boldrini L, Bibault JE, Masciocchi C, Shen Y, Bittner MI. Deep learning: a review for the radiation oncologist. *Front Oncol.* (2019) 9:977. doi: 10.3389/fonc.2019.00977
14. Vesselle H, Turcotte E, Wiens L, Haynor D. Application of a neural network to improve nodal staging accuracy with 18F-FDG PET in non-small cell lung cancer. *J Nucl Med.* (2003) 44:1918–26.
15. Toney LK, Vesselle HJ. Neural networks for nodal staging of non-small cell lung cancer with FDG PET and CT: importance of combining uptake values and sizes of nodes and primary tumor. *Radiology.* (2014) 270:91–8. doi: 10.1148/radiol.13122427
16. Tau N, Stundzia A, Yasufuku K, Hussey D, Metser U. Convolutional neural networks in predicting nodal and distant metastatic potential of newly diagnosed non-small cell lung cancer on FDG PET images. *AJR Am J Roentgenol.* (2020) 215:192–7. doi: 10.2214/AJR.19.22346
17. Wang H, Zhou Z, Li Y, Chen Z, Lu P, Wang W, et al. Comparison of machine learning methods for classifying mediastinal lymph node metastasis of non-small cell lung cancer from (18)F-FDG PET/CT images. *EJNMMI Res.* (2017) 7:11. doi: 10.1186/s13550-017-0260-9
18. Brierley JD, Gospodarowicz MK, Wittekind C. *UICC TNM Classification of Malignant Tumours*, 8th edn. Oxford: Wiley-Blackwell (2017). p. 105–112.
19. Amin MB, Edge SB, Greene FL. *AJCC Cancer Staging Manual, 8th edn*. New York, NY: Springer (2017). p. 431–456.
20. Quak E, Le Roux PY, Hofman MS, Robin P, Bourhis D, Callahan J, et al. Harmonizing FDG PET quantification while maintaining optimal lesion detection: prospective multicentre validation in 517 oncology patients. *Eur J Nucl Med Mol Imaging.* (2015) 42:2072–82. doi: 10.1007/s00259-015-3128-0
21. Kursa MB, Jankowski A, Rudnicki WR. Boruta - a system for feature selection. *Fundam Inf.* (2010) 101:271–85. doi: 10.3233/FI-2010-288
22. Soret M, Bacharach SL, Buvat I. Partial-volume effect in PET tumor imaging. *J Nucl Med.* (2007) 48:932–45. doi: 10.2967/jnumed.106.035774
23. El-Sherief AH, Lau CT, Wu CC, Drake RL, Abbott GF, Rice TW. International association for the study of lung cancer (IASLC) lymph node map: radiologic review with CT illustration. *Radiographics.* (2014) 34:1680–91. doi: 10.1148/rg.346130097
24. Ghaly G, Rahouma M, Kamel MK, Nasar A, Harrison S, Nguyen AB, et al. Clinical predictors of nodal metastases in peripherally clinical T1a N0 non-small cell lung cancer. *Ann Thorac Surg.* (2017) 104:1153–8. doi: 10.1016/j.athoracsur.2017.02.074
25. Wang J, Welch K, Wang L, Kong FM. Negative predictive value of positron emission tomography and computed tomography for stage T1-2N0 non-small-cell lung cancer: a meta-analysis. *Clin Lung Cancer.* (2012) 13:81–9. doi: 10.1016/j.cllc.2011.08.002
26. Kaseda K, Watanabe K, Asakura K, Kazama A, Ozawa Y. Identification of false-negative and false-positive diagnoses of lymph node metastases in non-small cell lung cancer patients staged by integrated (18F-)fluorodeoxyglucose-positron emission tomography/computed tomography: a retrospective cohort study. *Thorac Cancer.* (2016) 7:473–80. doi: 10.1111/1759-7714.12358
27. Miyasaka Y, Suzuki K, Takamochi K, Matsunaga T, Oh S. The maximum standardized uptake value of fluorodeoxyglucose positron emission tomography of the primary tumour is a good predictor of pathological nodal involvement in clinical N0 non-small-cell lung cancer. *Eur J Cardiothorac Surg.* (2013) 44:83–7. doi: 10.1093/ejcts/ezs604
28. Nambu A, Kato S, Sato Y, Okuwaki H, Nishikawa K, Saito A, et al. Relationship between maximum standardized uptake value (SUVmax) of lung cancer and lymph node metastasis on FDG-PET. *Ann Nucl Med.* (2009) 23:269–75. doi: 10.1007/s12149-009-0237-5
29. Zhou X, Chen R, Huang G, Liu J. Potential clinical value of PET/CT in predicting occult nodal metastasis in T1-T2N0M0 lung cancer patients staged by PET/CT. *Oncotarget.* (2017) 8:82437–45. doi: 10.18632/oncotarget.19535
30. Ouyang ML, Xia HW, Xu MM, Lin J, Wang LL, Zheng XW, et al. Prediction of occult lymph node metastasis using SUV, volumetric parameters and intratumoral heterogeneity of the primary tumor in T1-2N0M0 lung cancer patients staged by PET/CT. *Ann Nucl Med.* (2019) 33:671–80. doi: 10.1007/s12149-019-01375-4
31. Park SY, Yoon JK, Park KJ, Lee SJ. Prediction of occult lymph node metastasis using volume-based PET parameters in small-sized peripheral non-small cell lung cancer. *Cancer Imaging.* (2015) 15:21. doi: 10.1186/s40644-015-0058-9
32. Aktas GE, Karamustafaoglu YA, Balta C, Sut N, Sarikaya I, Sarikaya A. Prognostic significance of fluorine-18 fluorodeoxyglucose positron

emission tomography/computed tomography-derived metabolic parameters in surgically resected clinical-N0 nonsmall cell lung cancer. *Nucl Med Commun.* (2018) 39:995–1004. doi: 10.1097/MNM.0000000000000903

33. Cerfolio RJ, Bryant AS, Ohja B, Bartolucci AA. The maximum standardized uptake values on positron emission tomography of a non-small cell lung cancer predict stage, recurrence, and survival. *J Thorac Cardiovasc Surg.* (2005) 130:151–9. doi: 10.1016/j.jtcvs.2004.11.007
34. Akthar AS, Ferguson MK, Koshy M, Vigneswaran WT, Malik R. Limitations of PET/CT in the detection of occult N1 metastasis in clinical stage I(T1-2aN0) non-small cell lung cancer for staging prior to stereotactic body radiotherapy. *Technol Cancer Res Treat.* (2017) 16:15–21. doi: 10.1177/1533034615624045
35. Yeh YC, Kadota K, Nitadori J, Sima CS, Rizk NP, Jones DR, et al. International Association for the Study of Lung Cancer/American Thoracic Society/European Respiratory Society classification predicts occult lymph node metastasis in clinically mediastinal node-negative lung adenocarcinoma. *Eur J Cardiothorac Surg.* (2016) 49:e9–15. doi: 10.1093/ejcts/ezv316

Conflict of Interest: The authors declare that the research was conducted in the absence of any commercial or financial relationships that could be construed as a potential conflict of interest.

frontiers in Medicine

ORIGINAL RESEARCH
published: 25 May 2021
doi: 10.3389/fmed.2021.662233

Multi-Atlas MRI-Based Striatum Segmentation for ^{123}I-FP-CIT SPECT (DAT-SPECT) Compared With the Bolt Method and SPECT-Atlas-Based Segmentation Method Toward the Accurate Diagnosis of Parkinson's Disease/Syndrome

Koji Sohara[1], Tetsuro Sekine[2], Amane Tateno[3], Sunao Mizumura[4], Masaya Suda[1], Takeshi Sakayori[3], Yoshiro Okubo[3] and Shin-ichiro Kumita[1]*

[1] Department of Radiology, Nippon Medical School Hospital, Tokyo, Japan, [2] Department of Radiology, Nippon Medical School Musashi Kosugi Hospital, Kanagawa, Japan, [3] Department of Neuropsychiatry, Nippon Medical School, Tokyo, Japan, [4] Department of Radiology, Omori Medical Center, Toho University, Tokyo, Japan

OPEN ACCESS

Edited by:
Désirée Deandreis, University of Turin, Italy

Reviewed by:
Bijoy Kundu, University of Virginia, United States
Kun Zheng, Peking Union Medical College Hospital (CAMS), China

***Correspondence:**
Koji Sohara
sohara@nms.ac.jp

Specialty section:
This article was submitted to Nuclear Medicine, a section of the journal Frontiers in Medicine

Received: *31 January 2021*
Accepted: *15 April 2021*
Published: *25 May 2021*

Citation:
Sohara K, Sekine T, Tateno A, Mizumura S, Suda M, Sakayori T, Okubo Y and Kumita S (2021) Multi-Atlas MRI-Based Striatum Segmentation for ^{123}I-FP-CIT SPECT (DAT-SPECT) Compared With the Bolt Method and SPECT-Atlas-Based Segmentation Method Toward the Accurate Diagnosis of Parkinson's Disease/Syndrome. Front. Med. 8:662233. doi: 10.3389/fmed.2021.662233

Aims: This study aimed to analyze the performance of multi-atlas MRI-based parcellation for ^{123}I-FP-CIT SPECT (DAT-SPECT) in healthy volunteers. The proposed method was compared with the SPECT-atlas-based and Bolt methods. ^{18}F-FE-PE2I-PET (DAT-PET) was used as a reference.

Methods: Thirty healthy subjects underwent DAT-SPECT, DAT-PET, and 3D-T1WI-MRI. We calculated the striatum uptake ratio (SUR/SBR), caudate uptake ratio (CUR), and putamen uptake ratio (PUR) for DAT-SPECT using the multi-atlas MRI-based method, SPECT-atlas-based method, and Bolt method. In the multi-atlas MRI-based method, the cerebellum, occipital cortex, and whole-brain were used as reference regions. The correlation of age with DAT-SPECT activity and the correlations of SUR/SBR, CUR, and PUR between DAT-SPECT and DAT-PET were calculated by each of the three methods.

Results: The correlation between age and SUR/SBR for DAT-SPECT based on the multi-atlas MRI-based method was comparable to that based on the SPECT-atlas-based method ($r = -0.441$ to -0.496 vs. -0.488). The highest correlation between DAT-SPECT and DAT-PET was observed using the multi-atlas MRI-based method with the occipital lobe defined as the reference region compared with the SPECT-atlas-based and Bolt methods (SUR, CUR, and PUR: 0.687, 0.723, and 0.676 vs. 0.698, 0.660, and 0.616 vs. 0.655).

Conclusion: Multi-atlas MRI-based parcellation with the occipital lobe defined as the reference region was at least comparable to the clinical methods.

Keywords: ^{123}I-FP-CIT, ^{18}F-FE-PE2I, positron emission tomography, semi-quantification, multi-atlas MRI based parcellation, Bolt method, single photon emission computed tomography, dopamine transporter

INTRODUCTION

^{123}I-FP-CIT-SPECT (DAT-SPECT) is widely used for the assessment of degenerative Parkinson's syndromes, such as Parkinson's disease (PD), multiple system atrophy, and progressive supranuclear palsy. The tracer accumulation in DAT-SPECT reflects the availability of dopamine transporter (DAT) and thus the functionality of the nigrostriatal dopaminergic neurons (1–4). As a semi-quantitative method for DAT-SPECT, the uptake ratios in the corpus striatum or in more detailed regions, such as putamen and caudate nucleus, have been used. These ratios can be obtained by dividing the uptake in the target regions (e.g., corpus striatum) by those in the reference areas (e.g., cerebellum, occipital cortex, or whole brain). Several approaches have been attempted to provide robust semi-quantification from DAT imaging. In clinical settings, two types of methods, the Bolt method and the SPECT atlas method, are widely used. The Bolt method can serve as a robust, easy-to-use semi-quantification method (5). However, some errors are inevitable in the case of abnormal brain shapes (6). In addition, this approach does not segment the caudate and putamen, resulting in no capability to evaluate the distribution of nigrostriatal dopaminergic neuron changes in the striatum. Compared with the Bolt method, the SPECT atlas method (e.g., DaTQUANT, GE Healthcare, Little Chalfont, UK) can segment the caudate and putamen (7, 8). However, the segmentation may not be accurate because single SPECT template is used. The volume and shape of the striatum vary among subjects. Generally, it is observed that significant volume reduction is proportional to aging (9). One previous study demonstrated that the effect of aging on dopamine receptor availability was overestimated due to the volume reduction (10). To overcome the disadvantages of the current methods described above, Perlaki et al. evaluated the utility of segmentation by using patient-specific T1WI (11). Their method is expected to be easily implemented into clinical workflows because 3D-T1WI-MRI is generally performed as a routine assessment for Parkinson's diseases and the scan time for it has decreased due to recently developed acceleration techniques (e.g., parallel imaging and compressed sensing). However, they did not compare MRI segmentation to current clinical methods (the Bolt method or SPECT-atlas-based method). In addition, in terms of MRI segmentation, they only used single MRI atlas. One can expect that the MRI segmentation using multi-atlas MRI can improve the accuracy of segmentation (12).

The purpose of this study was to analyze the performance of multi-atlas MRI-based parcellation for DAT-SPECT. The proposed method was compared with the Bolt method and SPECT-atlas-based method, both of which are currently used in clinical settings.

^{18}F-FE-PE2I ([18F]-(E)-N-(3-iodoprop-2-enyl)-2β-carbo fluoroethoxy-3β-(4′-methyl-phenyl) nortropane) for PET (DAT-PET) was used as a reference. ^{18}F-FE-PE2I showed high affinity and high selectivity for DAT, faster kinetics, more favorable metbolism and low production of a radio metabolite with intermediate lipophilicity (13–15). Several studies have confirmed its high correlation to age even in small regions such as caudate and putamen ($r = -0.845$ and -0.85, respectively) and high discriminative power between PD and healthy controls (16–19). Based on these previous reports, we expected that ^{18}F-FE-PE2I was an excellent imaging tool for *in vivo* DAT quantification in the entire nigrostriatal tract (17, 18, 20).

MATERIALS AND METHODS

Subjects

The study was approved by the institutional review board of our institution. Thirty healthy volunteers (HVs) aged 31–79 years (mean ± SD, 54.1 ± 14.5; six subjects per age group: 30s, 40s, 50s, 60s, and 70s) were enrolled. All studies were performed between January 2016 and March 2017. None of the subjects had a present or past history of psychiatric, neurological or somatic disorders or of alcohol- or drug-related problems. All subjects were non-smokers. After an explanation of the study, written informed consent was obtained from all participants. All participants underwent ^{123}I-FP-CIT-SPECT (DAT-SPECT), ^{18}F-PE2I-PET (DAT-PET) and 3D-T1WI-MRI within 85 days (21.4 ± 13.2 days).

SPECT Procedures

SPECT imaging was performed using a dual-head SPECT gamma camera (Infinia, GE Healthcare, Milwaukee, WI, USA) equipped with an extended low-energy general-purpose (ELEGP) collimator (12 mm full width at half maximum; FWHM). All subjects had received an intravenous injection of ^{123}I-FP-CIT (167 MBq) (^{123}I-Ioflupane, DaTScan™, Nihon Mediphysics Corporation, Nishinomiya, Japan) *via* the antecubital vein in the supine position. Three hours after tracer injection, SPECT data were acquired for 28.5 min over a 360° range in 4°-angular steps (90 views) with 855 s/cycle using circularly rotating gamma cameras. The radius of rotation was 14 cm. We used a 3-dimensional ordered subset expectation maximization (3D-OSEM) image reconstruction algorithm (iteration number, 6; subsets, 10) with an eighth-order Butterworth filter with a cut off of 0.55 cycles/cm. The final SPECT images were reconstructed with Chang's method (Chang's attenuation correction) into 3.0-mm isotropic voxels using a 128 × 128 matrix with 128 slices parallel to the orbitomeatal line (21, 22). Scatter correction was not used in this study.

PET Procedures

^{18}F-FE-PE2I was synthesized from its precursor, tosylethyl-PE2I, *via* a nucleophilic fluorination reaction in our cyclotron for PET (HM18, Sumitomo Heavy Industries, Ltd, Tokyo) at the Clinical Imaging Center for Healthcare, Nippon Medical School. PET scans were carried out with an Eminence SET-3000GCT-X scanner (Shimadzu Corp, Kyoto, Japan) to measure regional brain radioactivity. No arterial blood sampling or metabolite analysis was performed. This scanner provides 99 sections with an axial field of view (FOV) of 256 mm. The in-plane and axial spatial resolutions were 3.45 mm FWHM and 3.72 mm FWHM, respectively. A head fixation device was used during the scans. A 10-min transmission scan using a ^{137}Cs point source was performed to correct for attenuation. A dynamic PET scan was

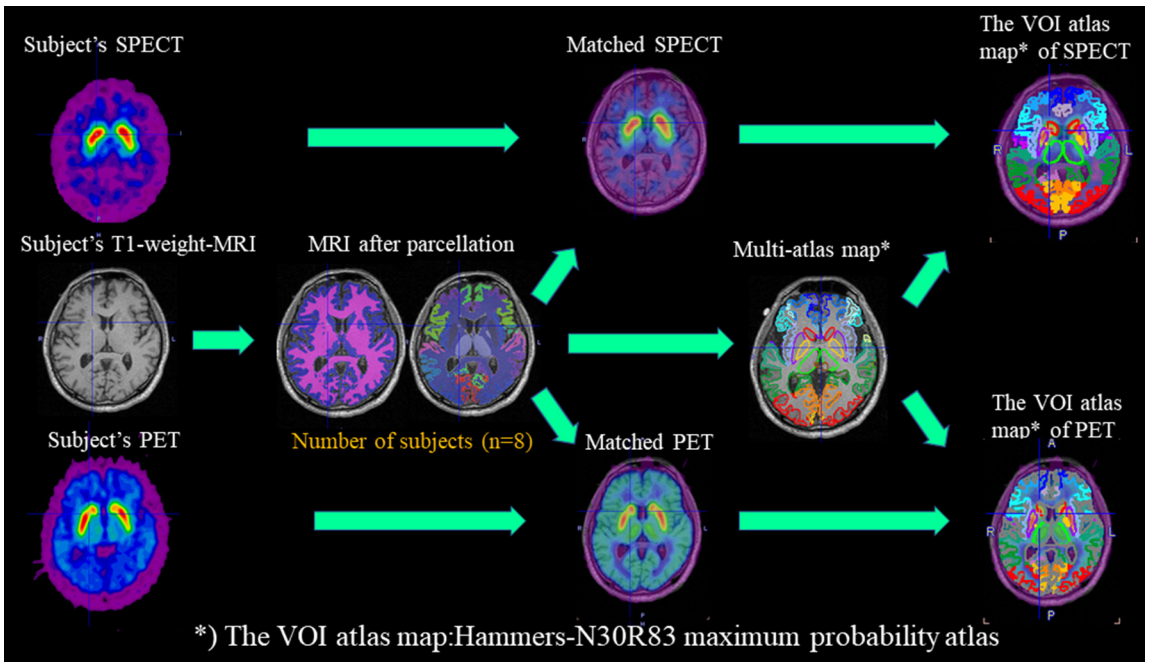

FIGURE 1 | Workflow for studies with DAT-SPECT/PET and T1-MRI in PNEURO. In the workflow, subject-specific images (DAT-PET and DAT-SPECT) and MRI images after parcellation with eight normal subjects are matched, and multi-atlas maps are generated.

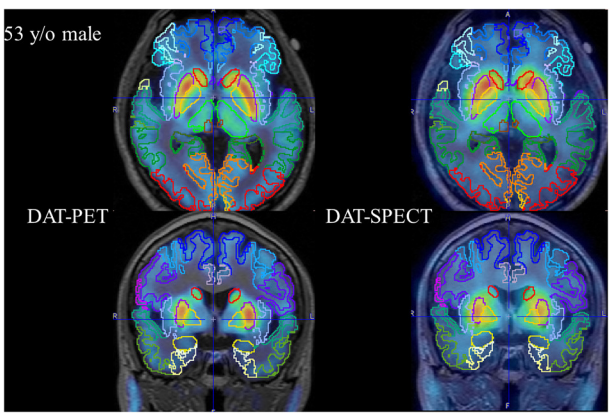

FIGURE 2 | Representative case (53-year-old male). Axial and coronal fused PET (left column) and fused SPECT (right column) are shown.

performed for 60 min (20 s × 9, 1 min × 5, 2 min × 4, 4 min × 11) after intravenous bolus injection of ^{18}F-FE-PE2I. The injected radioactivity was 175.0 to 194.0 (185.5 ± 4.2) MBq. We used a filtered back-projection (FBP) image reconstruction algorithm with a second-order Gaussian filter with a cut off of 0.8 mm. Scatter correction was carried out with the hybrid dual-energy window (HDE) method. Motion correction was not used in this study.

MRI Procedures

A 1.5 T magnetic resonance (MR) scanner (Intera 1.5 T Achieva Nova, Philips Medical Systems, Best, Netherlands) was used to acquire a high-resolution 3D fast spoiled gradient echo T1WI sequence (180 slices, 1 mm thickness, TR = 9.3 ms, TE = 4.6 ms, flip angle 10°, field of view 25 × 25 cm). The images were used as a reference for drawing volumes of interest (VOIs) on SPECT or PET images.

Image Analysis

One neuroradiologist (T.S.) confirmed that no brain abnormalities were present in the subjects. DAT-SPECT uptake was semi-quantified based on three methods: the multi atlas-based method using MRI, single atlas-based method using SPECT and Bolt method. In the first two methods, uptake ratios were calculated for DAT-SPECT in the striatum, caudate, and putamen. In the latter method, the specific-to-non-displaceable binding ratio (SBR) was measured as a substitute for specific uptake ratios. The uptake ratios were calculated for DAT-PET in the striatum, caudate, and putamen in a standard manner based on the multi atlas-based method using MRI (17). For subsequent analyses, the quantified values for DAT-PET were defined as the reference values. The details of the subsequent analyses are described next.

DAT-SPECT Images Analysis

Multi-Atlas-Based Method Using MRI (PNEURO)

The PNEURO tool (version 4.0, PMOD Technologies Ltd., Zurich, Switzerland) was used for the entire process. The whole processes described below can be performed semi-automatically, without any user interaction. It took ∼10 min to perform the analysis for each case. First, rigid transformation between DAT-SPECT and 3D-T1WI was performed. Then, automatic segmentation was performed using subject-specific T1 images,

TABLE 1 | The SUR/SBR, CUR, and PUR of DAT-SPECT and DAT-PET.

Radiopharmaceutical	Analysis tool	Reference area	CSF-C	SUR/SBR		CUR		PUR	
				Mean	SD	Mean	SD	Mean	SD
DAT-SPECT	PNEURO	Cerebellum	−	4.323	0.706	3.783	0.683	4.843	0.779
		Occipital lobe	−	3.768	0.540	3.298	0.540	4.220	0.577
		Whole brain	−	3.308	0.388	2.831	1.102	3.708	0.433
	DaTQUANT	Occipital lobe	−	2.696	0.573	2.952	0.598	2.550	0.574
	DaTView	Whole brain	−	7.151	1.683	−	−	−	−
		Whole brain	+	6.259	1.487	−	−	−	−
DAT-PET	PNEURO	Cerebellum	−	3.391	0.454	2.888	0.499	3.868	0.436

SUR, striatum uptake ratio; SBR, specific binding ratio; CUR, caudate uptake ratio; PUR, putamen uptake ratio; CSF-C, cerebrospinal fluid correction.

Table 2A | Age correlation with DAT activity, measured with DAT-SPECT and DAT-PET.

Radiopharmaceutical	Analysis tool	Reference area	CSF-C	SUR/SBR		CUR		PUR	
				r	*p*	*r*	*p*	*r*	*p*
DAT-SPECT	PNEURO	Cerebellum	−	−0.441	0.015	−0.539	0.002	−0.339	0.067
		Occipital lobe	−	−0.496	0.005	−0.589	0.001	−0.390	0.033
		Whole brain	−	−0.480	0.007	−0.608	<0.001	−0.331	0.074
	DaTQUANT	Occipital lobe	−	−0.488	0.006	−0.483	0.007	−0.481	0.007
	DaTView	Whole brain	−	−0.665	<0.001				
		Whole brain	+	−0.635	<0.001				
DAT-PET	PNEURO	Cerebellum	−	−0.701	<0.001	−0.743	<0.001	−0.601	<0.001

SUR, striatum uptake ratio; SBR, specific binding ratio; CUR, caudate uptake ratio; PUR, putamen uptake ratio; CSF-C, cerebrospinal fluid correction.

creating VOIs for each of the striatum and caudate, putamen, and an outline of the cerebellum, occipital cortex and whole brain (excluding the striatum, ventricles and cerebellum) as a reference in each individual participant. To set these VOIs, we used the 1 mm Hammers atlas-N30R83 maximum probability atlas. The atlas map comprised gray matter as determined from segmentation of the subjects' T1 images into 30 bilateral cortical areas (including the amygdala and hippocampus), five bilateral deep nuclei (caudate, putamen, ventral striatum, thalamus, and pallidum), the bilateral cerebellum and the brainstem. This was accomplished in PNEURO using a pre-defined database of eight normal T1 MRI scans, each of which was manually segmented by neuroanatomically trained operators, with the most comparable brain hemispheres to those in a specific subject's T1 images selected using anatomical landmarks (anterior/posterior commissure, inter-hemispheric point, and inter-caudate point) and a calculation of the average thickness of the frontal horn of the left and right ventricles (12). The selected knowledge-based hemispheres were then elastically matched to subject hemispheres using a hierarchical approach [(1) global affine transformation, (2) individual structure adjustment with a free-form deformation algorithm] to create a set of structure definitions that was combined with the gray and white matter segmentation to produce a maximum probability atlas of base structures (deep nuclei, gray matter, cerebellum), with the gray matter (at probability>0.3) being further parcellated *via* intersection with the specified cortical atlas (here, Hammers). After parcellation, the VOIs were warped to SPECT images. SPECT uptake values were measured using MR-based anatomical VOIs to limit the SPECT-active volume in a reproducible manner. VOI-based analysis was then performed to extract specific target uptakes in the striatum, caudate, and putamen. To calculate uptake ratios, we chose the following three regions as a reference region: the cerebellum, occipital cortex and whole brain (excluding deep nuclei, the brainstem, the cerebellum and ventricles). As a result, the uptake ratio of the striatum (SUR), uptake ratio of the putamen (PUR) and uptake ratio of the caudate (CUR) were calculated based on each of the three reference regions. In addition, we also measured the volumes of the striatum, caudate, and putamen; their volumes were calculated by summing the right and left sides. Each semi-quantitative uptake ratio was calculated using the following formula: semi-quantitative uptake ratio = (mean counts in the target VOI)/(mean counts in the reference VOI).

The workflow for studies with DAT-SPECT/PET and T1-MRI in PNEURO is shown in the upper part of **Figure 1**.

Single Atlas-Based Method Using SPECT (DaTQUANT)

DaTQUANT was used for the entire process (7). After SPECT reconstruction, the transaxial slices were used as input for the software. Non-rigid registration was applied to patient-specific SPECT data to match predefined SPECT-atlas data. Predefined template VOIs on the SPECT atlas were automatically positioned

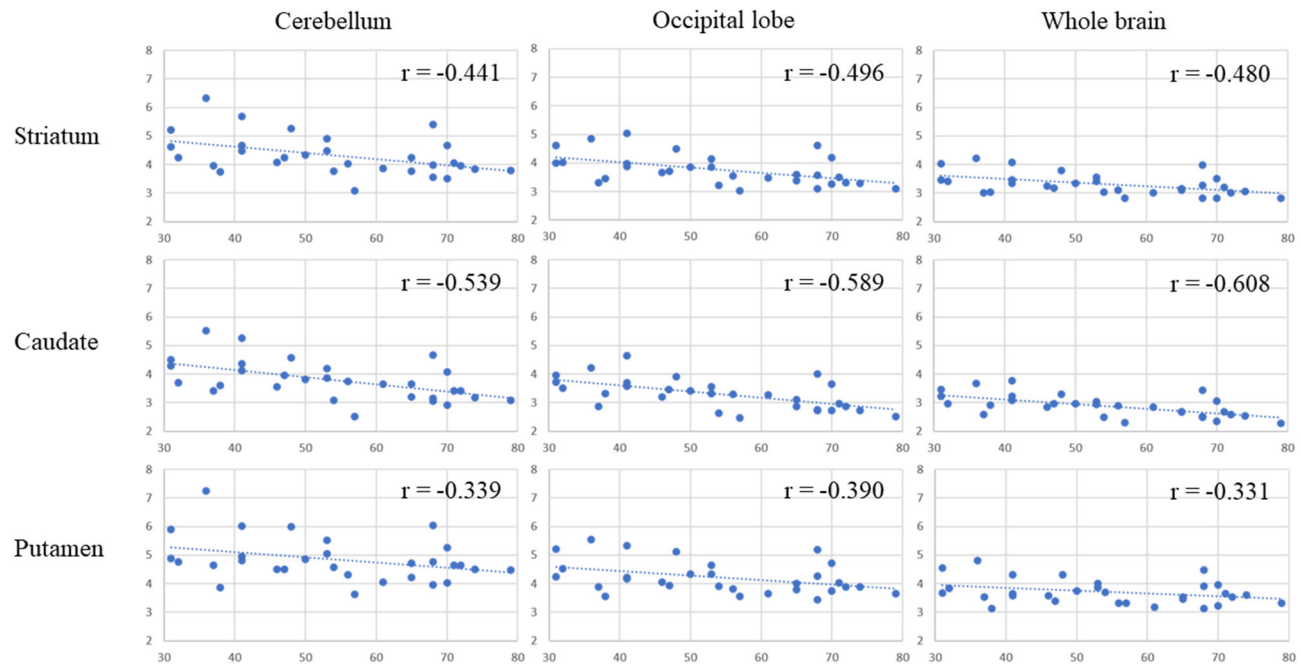

FIGURE 3 | Age correlation with DAT activity, measured with DAT-SPECT and DAT-PET in the multi-atlas MRI-based method. In each correlation figure, the vertical axis indicates the semi-quantitative uptake for DAT-SPECT measured by the multi-atlas MRI-based method, and the horizontal axis indicates age. There are 3 × 3 correlation figure patterns in two different cases: where the target region is the striatum, caudate, or putamen and where the reference area is the cerebellum, occipital lobe or whole brain.

TABLE 2B | Annual decline rate of DAT activity for Age, measured with DAT-SPECT and DAT-PET.

Radiopharmaceutical	Analysis tool	Reference area	CSF-C	SUR/SBR	CUR	PUR
DAT-SPECT	PNEURO	Cerebellum	–	−0.391	−0.491	−0.312
		Occipital lobe	–	−0.386	−0.488	−0.306
		Whole brain	–	−0.320	−0.432	−0.232
	DaTQUANT	Occipital lobe	–	−0.515	−0.494	−0.531
	DaTView	Whole brain	–	−0.680		
		Whole brain	+	−0.691		
DAT-PET	PNEURO	Cerebellum	–	−0.479	−0.598	−0.372

SUR, striatum uptake ratio; SBR, specific binding ratio; CUR, caudate uptake ratio; PUR, putamen uptake ratio; CSF-C, cerebrospinal fluid correction.

in the target regions, including the striatum, caudate, and putamen. The occipital cortex was also segmented as a reference region. The program calculated the SUR, CUR, and PUR as the ratio of each target region to the reference region.

DaTView (DAT-SPECT Analysis)

We used DaTView (Aze, Tokyo, Japan) for the entire process. The procedure was the same as the method proposed by Tossici-Bolt et al. (5). DaTView applies the whole brain, except a region around the basal ganglia, as a reference region. SBR was defined as

$$SBR = Cs/Cr,$$

where Cs is the count concentration in the striatum due to specific binding only and Cr is the count concentration in the reference region due to non-specific binding. SBR is calculated from a sufficiently large VOI, including all counts associated with striatal activity, to be independent from the size of the VOI and from the resolution of the SPECT system. In order to avoid extrastriatal heterogeneous tissue counts, an average striatum volume of 11.2 mL was applied. In addition, we also used the cerebrospinal fluid correction (CSF-c) developed by Mizumura and equipped in DaTView to calculate the SBR (23).

DAT-PET Images Analysis

We applied a simplified reference tissue model (14, 19, 24). To obtain semi-quantitative measures of SUR, CUR, and PUR for

TABLE 3 | Correlation between the SUR/SBR, CUR and PUR of DAT-SPECT and those of DAT-PET.

Analysis tool	Reference area	CSF-C	SUR/SBR		CUR		PUR	
			r	*p*	*r*	*p*	*r*	*p*
PNEURO	Cerebellum	–	0.648	<0.001	0.688	<0.001	0.639	<0.001
	Occipital lobe	–	0.687	<0.001	0.723	<0.001	0.676	<0.001
	Whole brain	–	0.642	<0.001	0.704	<0.001	0.621	<0.001
DaTQUANT	Occipital lobe	–	0.698	<0.001	0.660	<0.001	0.616	<0.001
DaTView	Whole brain	–	0.655	<0.001				
	Whole brain	+	0.659	<0.001				

UR, striatum uptake ratio; SBR, specific binding ratio; CUR, caudate uptake ratio; PUR, putamen uptake ratio; CSF-C, cerebrospinal fluid correction.

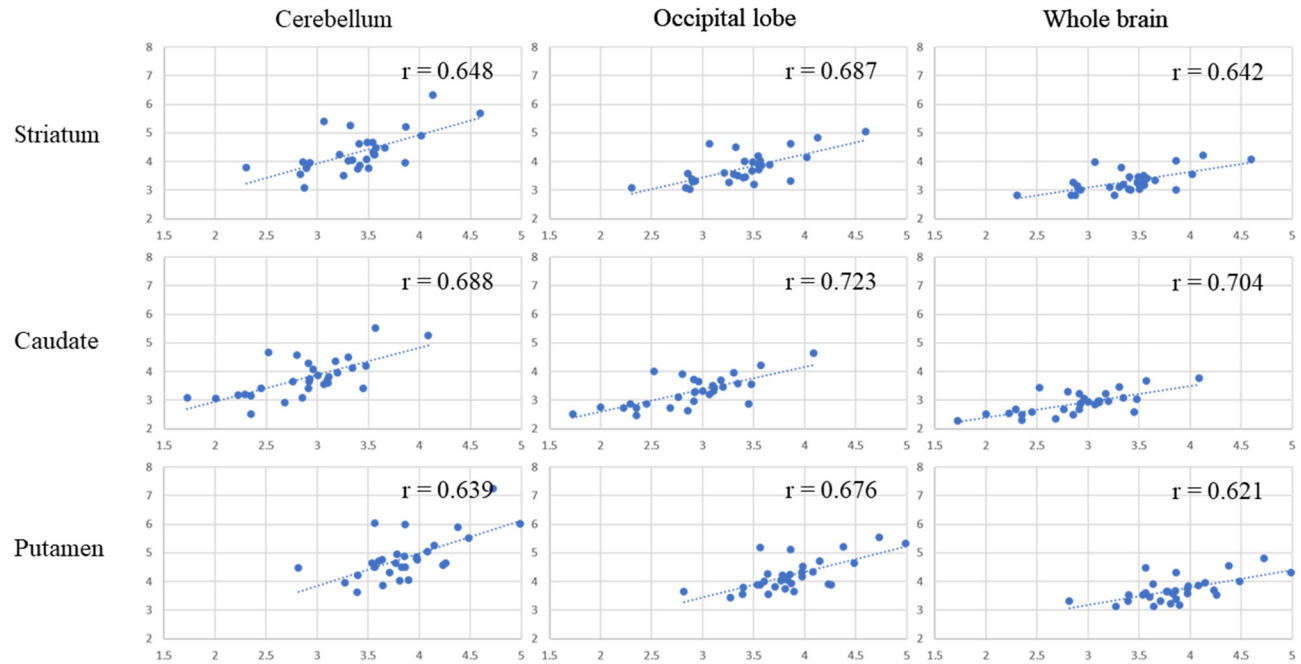

FIGURE 4 | Correlation between the SUR, CUR, and PUR of DAT-SPECT and those of DAT-PET in the multi-atlas MRI-based method. In each correlation figure, the vertical axis indicates the semi-quantitative uptake for DAT-SPECT, and the horizontal axis indicates the semi-quantitative uptake for DAT-PET. There are 3 × 3 correlation figure patterns in two different cases: where the target region is the striatum, caudate, or putamen and where the reference area is the cerebellum, occipital lobe or whole brain.

DAT-PET, static images were created by summing the dynamic scans between 32 and 60 min. The VOIs were created on these summed images with PNEURO. As in the the method used for the PNEURO DAT-SPECT analysis, after parcellation, the MRI and PET data were matched. PET activity values were applied to the MR-based anatomical VOIs to limit the PET-active volume in a reproducible manner. We also calculated 3 sets of semi-quantitative values with the cerebellum as a reference region (14, 17). The workflow for studies with DAT-PET and T1-MRI in PNEURO is shown in the lower part of **Figure 1**.

Statistical Analysis

To validate the accuracy of DAT-SPECT quantification, the three types of correlations were statistically tested. First, the correlation of age with DAT-SPECT activity in each of the three methods was calculated with Pearson's correlation coefficient. Second, the correlation between DAT-SPECT and the reference, DAT-PET, in each region (e.g., the striatum, caudate, and putamen) was calculated with Pearson's correlation coefficient. Third, the correlation between region volume and age and that between region volume and DAT-SPECT activity in each of the three methods were calculated with Pearson's correlation coefficient. All statistical analyses were performed using IBM SPSS Statistics (Version 25.0, IBM Corp, Armonk, NY, USA).

RESULTS

The PNEURO analysis after parcellation successfully matched MRI and SPECT/PET data for each of the 30 cases. A representative case (53-year-old male) is shown in **Figure 2**.

TABLE 4A | Volume (mL) of striatum, caudate, and putamen.

Striatum		Caudate		Putamen	
Mean	**SD**	**Mean**	**SD**	**Mean**	**SD**
20.941	2.873	8.691	1.449	12.250	1.582

TABLE 4B | Correlation between volume and age.

	r	*p*
Striatum	−0.529	0.003
Caudate	−0.367	0.046
Putamen	−0.342	0.064
Occipital lobe	−0.519	0.003
Cerebellum	−0.678	<0.001
Whole brain	−0.567	0.001

TABLE 4C | Annual decline rate (%) of volume for age.

Striatum	−0.393
Caudate	−0.343
Putamen	−0.261
Occipital lobe	−0.416
Cerebellum	−0.483
Whole brain	−0.425

Table 1 presents the results for the mean SUR/SBR, CUR and PUR from the DAT-SPECT and DAT-PET analyses. The correlation coefficients (*r* values) between age and SUR/SBR, CUR and PUR for DAT-SPECT and DAT-PET are presented in **Table 2A**; those between age and SUR, CUR and PUR for DAT-SPECT and DAT-PET in the PNEURO analyses are shown in **Figure 3**. Significant correlation between age and each semi-quantitative value was observed, except for SPECT-PUR, in the PNEURO analyses using the cerebellum or whole brain as the reference region. The annual decline rate of DAT activity with age was −0.232 to −0.691% depending on the measurement method (**Table 2B**). The *r* values for SUR/SBR, CUR and PUR between DAT-SPECT and DAT-PET are presented in **Table 3**; those between DAT-SPECT and DAT-PET in the PNEURO analyses are shown in **Figure 4**. All three types of SPECT semi-quantified values showed significant correlation to the values of PET ($r = 0.616$–0.723). In the PNEURO analyses, there was a tendency toward higher correlation when using the occipital lobe as the reference region than when using other regions (i.e., the cerebellum or whole brain). Regarding semi-quantification in the detailed regions (i.e., CUR or PUR), PNEURO using the occipital lobe as the reference region showed higher correlation than DaTQUANT (CUR 0.723 vs. 0.660, PUR 0.676 vs. 0.616). **Table 4A** shows the results for the mean volumes of the striatum, caudate and putamen. The *r* values indicated higher correlation of the volumes of the striatum, occipital lobe, cerebellum and whole brain to age ($r = -0.519$ to -0.678; **Table 4B**). The percentage volume decrease in these regions was −0.393 to −0.483% (**Table 4C**). The *r* values between volume and SUR/SBR, CUR and PUR are presented in **Table 4D**. The table shows that only one value in the DaTQUANT analysis, PUR, depended on volume, but only slightly ($r = 0.383$, $p = 0.037$).

DISCUSSION

In the current study, DAT-SPECT semi-quantification based on multi-atlas MRI-based methods showed comparable to higher correlation to age or DAT-PET values compared with clinically available methods. In multi-atlas-based MRI analyses, the occipital lobe can be used as a reference for more precise semi-quantification than the cerebellum or whole brain. To our knowledge, this is the first study to validate the performance of semi-automatic multi-atlas MRI-based parcellation for DAT-SPECT. Furthermore, in regard to the comparisons between DAT-SPECT and DAT-PET, the current study recruited more age-generalized healthy controls (i.e., a uniform distribution of younger to older ages) than any of the previous studies.

Correlation Between Age and DAT-SPECT

Significant correlation was observed between age and all types of semi-quantitative value for DAT-SPECT. The correlation coefficients (*r* values) in this study showed a tendency to be equal to those in previous studies. In this study, the *r* values between age and SUR/SBR, CUR, and PUR for DAT-SPECT were −0.441 to −0.665, −0483 to −0.608, and −0.331 to −0.481, respectively. In previous studies, the *r* values between age and SUR/SBR, CUR, and PUR for DAT-SPECT were −0.449 to −0.632, −0.496 and −0.400, respectively (18, 19, 21, 25, 26). The *r* values between age and SBR based on the Bolt method were relatively higher than those based on the other methods (−0.635 to −0.665 vs. −0.441 to −0.496). It is assumed that the SBR method overestimates the reduction with age because it does not take the age-dependent decline in striatal volume into account (21). We revealed that the striatal volume declined annually (0.393% per year) despite the fact that the Bolt method defines a fixed striatum volume (11.2 mL) (5). DaTQUANT is generally considered to also be vulnerable to atrophy of the target regions. This method transforms the subject's specific target tracer accumulation into a SPECT template. As a result, it could overestimate the decrease in DAT activity in patients because the putamen volume in Parkinson's disease and multiple system atrophy has a tendency to decrease (27, 28). Therefore, MRI-based VOI delineation is necessary for *in vivo* DAT quantification.

Correlation Between DAT-PET and DAT-SPECT

DAT-PET has been shown to be an excellent imaging tool for *in vivo* DAT quantification in the entire nigrostriatal tract (13, 14, 20). There are also some studies concerning the performance of DAT-PET for *in vivo* DAT quantification and comparisons of diagnostic value between normal subjects and those with Parkinson's disease/Parkinsonism (11, 17, 18).

TABLE 4D | Correlation between Volume and the SUR/SBR, CUR, and PUR of DAT-SPECT and DAT-PET.

Radiopharmaceutical	Analysis tool	Reference area	CSF-C	SUR/SBR		CUR		PUR	
				r	*p*	*r*	*p*	*r*	*p*
DAT-SPECT	PNUERO	Cerebellum	–	−0.014	0.942	0.175	0.354	−0.128	0.501
		Occipital lobe	–	−0.013	0.945	0.166	0.381	−0.136	0.475
		Whole_brain	–	0.021	0.913	0.130	0.494	−0.061	0.750
	DaTQUANT	Occipital lobe	–	−0.190	0.315	0.225	0.232	−0.383	0.037
	DaTView	Whole_brain	–	0.081	0.672				
		Whole_brain	+	0.108	0.569				
DAT-PET	PNEURO	Cerebellum	–	0.167	0.377	0.370	0.044	0.008	0.967

SUR indicates striatum uptake ratio; SBR, specific binding ratio; CUR, caudate uptake ratio; PUR, putamen uptake ratio; CSF-C, cerebrospinal fluid correction.

One of the expected merits of DAT-PET with higher spatial resolution is the segmentation of tracer accumulation into caudate and putamen regions. A detailed evaluation based on this segementation enables differentiation of neurodegenerative Parkinsonism (29, 30). However, in clinical practice, the use of DAT-PET entails higher costs and higher radiation exposure. It is necessary to enhance the utility of DAT-SPECT semi-quantification by combining several methodological approaches, such as accurate VOI delineation and the selection of appropriate reference tissue.

Regarding SUR, the correlation coefficient between the semi-quantitative values for DAT-SPECT and DAT-PET did not significantly differ among the three methods. The multi-atlas MRI-based method is at least comparable to clinical methods for the semi-quantification of this region. Regarding CUR and PUR, in particular, the method showed higher correlation than the SPECT-atlas method (0.723 and 0.676 vs. 0.660 and 0.616). The multi-atlas MRI-based method is expected to be utilized to detect subtle changes of DAT activity in the caudate and putamen, which may impact the diagnosis of Parkinson's disease/syndrome. This expectation is also supported by previous studies (17, 18).

Selection of the Reference Region in the Multi-Atlas MRI-Based Method

In the current study, we sought to determine the appropriate reference regions for accurate DAT-SPECT semi-quantification. The occipital cortex proved to be the best region, with stronger correlation to age and DAT-PET compared with the cerebellum or whole brain. In a study with a similar concept to that of the current study, Delva et al. investigated the location of the optimal reference tissues for DAT imaging (17). They recruited nine patients with early Parkinson's disease and 34 healthy volunteers. All participants underwent DAT-PET with simultaneous acquisition of MRI, which was further used for VOI delineation. The results showed that the occipital cortex may be preferable as the reference region compared with the cerebellum, which supports the results of the current study. Another of their studies also supported the results of the current study (17). It should be noted, however, that our result cannot be translated directly into clinical scans. In our study, only HVs were recruited. In cases with dementia (e.g., dementia with Lewy bodies and Alzheimer's disease), several brain morphological changes can be present (31–34). Even when complicated morphological changes occur, the multi-atlas MRI-based approach would be useful thanks to its flexibility with respect to multiple outputs. The pre-processing performed for accurate delineation of each brain region enables mapping of the output of the multiple semi-quantification results based on each reference region. In addition, the degree of the atrophy (net volume) in each corresponding target or reference region would be easily obtainable.

Limitations

The current study has some limitations. First, it is known that ^{18}F-FE-PE2I is a more selective ligand to DAT than ^{123}I-FP-CIT. There is concern regarding the difference between the pharmacokinetics of ^{123}I-FP-CIT and that of ^{18}F-FE-PE2I. However, previous studies supported high correlation for both of these ligands (17, 18). Second, we applied one of the standard co-registration methods, the mutual information matching algorithm, provided by a single tool (PNEURO) (35–37). Other co-registration algorithms, such as MRtrix and ANTs, may improve or lead to different results (38–41). Further investigations utilizing multiple pipelines should be conducted. Third, the clinical impact of the multi-atlas MRI-based method was not clarified, because we analyzed only normal volunteers and did not assess any subjects with Parkinson's disease or Parkinsonism. We used the correlation to age and to DAT-PET value as surrogate indices to validate the accuracy of the current method, and this method has been widely accepted in this kind of study (7, 8, 17–19, 21, 25, 26). The multi-atlas MRI-based method is expected to be more useful in disease conditions because it compensates for the difficulty in segmentation in patients with morphological changes or decreased uptake, but further studies should be conducted. Fourth, a PNEURO analysis takes relatively more time (i.e., ∼10 min), though the whole process is performed semi-automatically. This issue will undoubtedly be resolved when computer technology gets better. Fifth, the attenuation correction in DAT-PET was different from that in DAT-SPECT, which might have impacted the correlation between the two tracers. This is an inherent limitation of a comparison study between DAT-PET and DAT-SPECT (17, 18). Sixth, we performed DAT-PET quantification with a simplified reference tissue model without

motion correction, partial volume correction or dynamic data analysis (14, 19). We tried to maintain the uniformity of the methodology between DAT-PET and DAT-SPECT analysis. The accuracy of the DAT-PET data was partially validated in the current study, as there was sufficient age correlation of DAT-PET data ($r = -0.601$ to -0.743) compared with previous studies (18, 19).

CONCLUSION

Multi-atlas MRI-based parcellation for DAT-SPECT semi-quantification is at least comparable to the current clinical methods in terms of the correlation to age and to DAT-PET quantification. In this method, the occipital lobe is the best region to use as the reference. The method is expected to provide detailed and robust semi-quantification in the putamen and caudate nucleus regardless of abnormal brain shape or atrophy of brain tissue.

DATA AVAILABILITY STATEMENT

The raw data supporting the conclusions of this article will be made available by the authors, without undue reservation.

ETHICS STATEMENT

The studies involving human participants were reviewed and approved by Committee on Clinical Practice of Investigational New Drugs, Nippon Medical School. The patients/participants provided their written informed consent to participate in this study. Written informed consent was obtained from the individual(s) for the publication of any potentially identifiable images or data included in this article.

AUTHOR CONTRIBUTIONS

All authors listed have made a substantial, direct and intellectual contribution to the work, and approved it for publication.

FUNDING

This work was partially supported by Grant-in-Aid for Scientific Research (B), 15H04896, from Ministry of Education, Culture, Sports, Science and Technology (MEXT, Japan).

ACKNOWLEDGMENTS

We would like to thank the radiology technicians of the Division of Nuclear Medicine at the Department of Radiology of Nippon Medical School Hospital and the Nippon Medical School Imaging Center for Healthcare for their valuable support: Kuwako Tomoyuki, Kyoji Asano, Shinjiro Yoshida, Junya Tashiro, Satoshi Harashina, Toshio Maki, and Minoru Sakurai.

REFERENCES

1. Makinen E, Joutsa J, Jaakkola E, Noponen T, Johansson J, Pitkonen M, et al. Individual parkinsonian motor signs and striatal dopamine transporter deficiency: a study with [I-123]FP-CIT SPECT. *J Neurol.* (2019) 266:826–34. doi: 10.1007/s00415-019-09202-6
2. Kaasinen V, Vahlberg T. Striatal dopamine in Parkinson disease: a meta-analysis of imaging studies. *Ann Neurol.* (2017) 82:873–82. doi: 10.1002/ana.25103
3. Albert NL, Unterrainer M, Diemling M, Xiong G, Bartenstein P, Koch W, et al. Implementation of the European multicentre database of healthy controls for [(123)I]FP-CIT SPECT increases diagnostic accuracy in patients with clinically uncertain parkinsonian syndromes. *Euro J Nucl Med Mol Imaging.* (2016) 43:1315–22. doi: 10.1007/s00259-015-3304-2
4. Ba F, Martin WR. Dopamine transporter imaging as a diagnostic tool for parkinsonism and related disorders in clinical practice. *Parkinsonism Relat Disord.* (2015) 21:87–94. doi: 10.1016/j.parkreldis.2014.11.007
5. Tossici-Bolt L, Hoffmann SM, Kemp PM, Mehta RL, Fleming JS. Quantification of [123I]FP-CIT SPECT brain images: an accurate technique for measurement of the specific binding ratio. *Euro J Nucl Med Mol Imaging.* (2006) 33:1491–9. doi: 10.1007/s00259-006-0155-x
6. Iwabuchi Y, Nakahara T, Kameyama M, Yamada Y, Hashimoto M, Ogata Y, et al. Quantitative evaluation of the tracer distribution in dopamine transporter SPECT for objective interpretation. *Ann Nucl Med.* (2018) 32:363–71. doi: 10.1007/s12149-018-1256-x
7. Dickson JC, Tossici-Bolt L, Sera T, de Nijs R, Booij J, Bagnara MC, et al. Proposal for the standardisation of multi-centre trials in nuclear medicine imaging: prerequisites for a European 123I-FP-CIT SPECT database. *Euro J Nucl Med Mol Imaging.* (2012) 39:188–97. doi: 10.1007/s00259-011-1884-z
8. Varrone A, Dickson JC, Tossici-Bolt L, Sera T, Asenbaum S, Booij J, et al. European multicentre database of healthy controls for [123I]FP-CIT SPECT (ENC-DAT): age-related effects, gender differences and evaluation of different methods of analysis. *Eur J Nucl Med Mol Imaging.* (2013) 40:213–27. doi: 10.1007/s00259-012-2276-8
9. Raz N, Rodrigue KM. Differential aging of the brain: patterns, cognitive correlates and modifiers. *Neurosci Biobehav Rev.* (2006) 30:730–48. doi: 10.1016/j.neubiorev.2006.07.001
10. Smith CT, Crawford JL, Dang LC, Seaman KL, San Juan MD, Vijay A, et al. Partial-volume correction increases estimated dopamine D2-like receptor binding potential and reduces adult age differences. *J Cereb Blood Flow Metab.* (2019) 39:822–33. doi: 10.1177/0271678X17737693
11. Perlaki G, Szekeres S, Orsi G, Papp L, Suha B, Nagy SA, et al. Validation of an automated morphological MRI-based (123)I-FP-CIT SPECT evaluation method. *Parkinsonism Relat Disord.* (2016) 29:24–9. doi: 10.1016/j.parkreldis.2016.06.001
12. Douaud G, Gaura V, Ribeiro MJ, Lethimonnier F, Maroy R, Verny C, et al. Distribution of grey matter atrophy in Huntington's disease patients: a combined ROI-based and voxel-based morphometric study. *Neuroimage.* (2006) 32:1562–75. doi: 10.1016/j.neuroimage.2006.05.057
13. Fazio P, Svenningsson P, Cselenyi Z, Halldin C, Farde L, Varrone A. Nigrostriatal dopamine transporter availability in early Parkinson's disease. *Mov Disord.* (2018) 33:592–9. doi: 10.1002/mds.27316
14. Sasaki T, Ito H, Kimura Y, Arakawa R, Takano H, Seki C, et al. Quantification of dopamine transporter in human brain using PET with 18F-FE-PE2I. *J Nucl Med.* (2012) 53:1065–73. doi: 10.2967/jnumed.111.101626
15. Varrone A, Steiger C, Schou M, Takano A, Finnema SJ, Guilloteau D, et al. *In vitro* autoradiography and *in vivo* evaluation in cynomolgus monkey of [^{18}F]FE-PE2I, a new dopamine transporter PET radioligand. *Synapse.* (2009) 63:871–80. doi: 10.1002/syn.20670
16. Brumberg J, Kerstens V, Cselényi Z, Svenningsson P, Sundgren M, Fazio P, et al. Simplified quantification of [^{18}F]FE-PE2I PET in Parkinson's disease:

discriminative power, test-retest reliability and longitudinal validity during early peak and late pseudo-equilibrium. *J Cereb Blood Flow Metab*. (2020). doi: 10.1177/0271678X20958755. [Epub ahead of print].
17. Delva A, Van Weehaeghe D, van Aalst J, Ceccarini J, Koole M, Baete K, et al. Quantification and discriminative power of ^{18}F-FE-PE2I PET in patients with Parkinson's disease. *Eur J Nucl Med Mol Imaging.* (2020) 47:1913–26. doi: 10.1007/s00259-019-04587-y
18. Jakobson Mo S, Axelsson J, Jonasson L, Larsson A, Ogren MJ, Ogren M, et al. Dopamine transporter imaging with [^{18}F]FE-PE2I PET and [^{123}I]FP-CIT SPECT-a clinical comparison. *EJNMMI Res.* (2018) 8:100. doi: 10.1186/s13550-018-0450-0
19. Shingai Y, Tateno A, Arakawa R, Sakayori T, Kim W, Suzuki H, et al. Age-related decline in dopamine transporter in human brain using PET with a new radioligand [^{18}F]FE-PE2I. *Ann Nucl Med.* (2014) 28:220–6. doi: 10.1007/s12149-013-0798-1
20. Fazio P, Svenningsson P, Forsberg A, Jönsson EG, Amini N, Nakao R, et al. Quantitative analysis of [^{18}F]-(E)-N-(3-Iodoprop-2-Enyl)-2β-carbofluoroethoxy-3β-(4′-Methyl-Phenyl) nortropane binding to the dopamine transporter in Parkinson disease. *J Nucl Med.* (2015) 56:714–20. doi: 10.2967/jnumed.114.152421
21. Matsuda H, Murata M, Mukai Y, Sako K, Ono H, Toyama H, et al. Japanese multicenter database of healthy controls for [^{123}I]FP-CIT SPECT. *Euro J Nucl Med Mol Imaging.* (2018) 45:1405–16. doi: 10.1007/s00259-018-3976-5
22. Sohara K, Kiriyama T, Mizumura S, Ishiwata A, Yamazaki M, Kimura K, et al. Diagnostic utility and characteristics of CT-based attenuation correction in brain perfusion SPECT/CT in predicting the exacerbation of Alzheimer changes from mild cognitive impairment utilizing voxel-based statistical analysis in comparison with Chang's method. *Ann Nucl Med.* (2020) 34:502–11. doi: 10.1007/s12149-020-01477-4
23. Mizumura S, Nishikawa K, Murata A, Yoshimura K, Ishii N, Kokubo T, et al. Improvement in the measurement error of the specific binding ratio in dopamine transporter SPECT imaging due to exclusion of the cerebrospinal fluid fraction using the threshold of voxel RI count. *Ann Nucl Med.* (2018) 32:288–96. doi: 10.1007/s12149-018-1249-9
24. Ito H, Sudo Y, Suhara T, Okubo Y, Halldin C, Farde L. Error analysis for quantification of [(11)C]FLB 457 binding to extrastriatal D(2) dopamine receptors in the human brain. *Neuroimage.* (2001) 13:531–9. doi: 10.1006/nimg.2000.0717
25. Tossici-Bolt L, Dickson JC, Sera T, Booij J, Asenbaun-Nan S, Bagnara MC, et al. [^{123}I]FP-CIT ENC-DAT normal database: the impact of the reconstruction and quantification methods. *EJNMMI Phys.* (2017) 4:8. doi: 10.1186/s40658-017-0175-6
26. Yamamoto H, Arimura S, Nakanishi A, Shimo Y, Motoi Y, Ishiguro K, et al. Age-related effects and gender differences in Japanese healthy controls for [(123)I] FP-CIT SPECT. *Ann Nucl Med.* (2017) 31:407–12. doi: 10.1007/s12149-017-1168-1
27. Sako W, Murakami N, Izumi Y, Kaji R. MRI can detect nigral volume loss in patients with Parkinson's disease: evidence from a meta-analysis. *J Parkinsons Dis.* (2014) 4:405–11. doi: 10.3233/JPD-130332
28. Sako W, Murakami N, Izumi Y, Kaji R. The difference in putamen volume between MSA and PD: evidence from a meta-analysis. *Parkinsonism Relat Disord.* (2014) 20:873–7. doi: 10.1016/j.parkreldis.2014.04.028
29. Morbelli S, Arnaldi D, Cella E, Raffa S, Donegani MI, Capitanio S, et al. Striatal dopamine transporter SPECT quantification: head-to-head comparison between two three-dimensional automatic tools. *EJNMMI Res.* (2020) 10:137. doi: 10.1186/s13550-020-00727-w
30. Matesan M, Gaddikeri S, Longfellow K, Miyaoka R, Elojeimy S, Elman S, et al. I-123 DaTscan SPECT brain imaging in parkinsonian syndromes: utility of the putamen-to-caudate ratio. *J Neuroimaging.* (2018) 28:629–34. doi: 10.1111/jon.12530
31. Tagawa R, Hashimoto H, Nakanishi A, Kawarada Y, Muramatsu T, Matsuda Y, et al. The relationship between medial temporal lobe atrophy and cognitive impairment in patients with dementia with lewy bodies. *J Geriatr Psychiatry Neurol.* (2015) 28:249–54. doi: 10.1177/0891988715590210
32. Kril JJ, Macdonald V, Patel S, Png F, Halliday GM. Distribution of brain atrophy in behavioral variant frontotemporal dementia. *J Neurol Sci.* (2005) 232:83–90. doi: 10.1016/j.jns.2005.02.003
33. Sarro L, Senjem ML, Lundt ES, Przybelski SA, Lesnick TG, Graff-Radford J, et al. Amyloid-β deposition and regional grey matter atrophy rates in dementia with Lewy bodies. *Brain.* (2016) 139:2740–50. doi: 10.1093/brain/aww193
34. Ferreira D, Nordberg A, Westman E. Biological subtypes of Alzheimer disease: a systematic review and meta-analysis. *Neurology.* (2020) 94:436–48. doi: 10.1212/WNL.0000000000009058
35. Tateno A, Sakayori T, Kim WC, Honjo K, Nakayama H, Arakawa R, et al. Comparison of dopamine D3 and D2 receptor occupancies by a single dose of blonanserin in healthy subjects: a positron emission tomography study with [11C]-(+)-PHNO. *Int J Neuropsychopharmacol.* (2018) 21:522–7. doi: 10.1093/ijnp/pyy004
36. Sakayori T, Tateno A, Arakawa R, Kim WC, Okubo Y. Evaluation of dopamine D(3) receptor occupancy by blonanserin using [(11)C]-(+)-PHNO in schizophrenia patients. *Psychopharmacology.* (2021) 238:1343–50. doi: 10.1007/s00213-020-05698-3
37. Sekine T, Buck A, Delso G, Ter Voert EE, Huellner M, Veit-Haibach P, et al. Evaluation of atlas-based attenuation correction for integrated PET/MR in human brain: application of a head atlas and comparison to true CT-based attenuation correction. *J Nucl Med.* (2016) 57:215–20. doi: 10.2967/jnumed.115.159228
38. Tournier JD, Smith R, Raffelt D, Tabbara R, Dhollander T, Pietsch M, et al. MRtrix3: a fast, flexible and open software framework for medical image processing and visualisation. *Neuroimage.* (2019) 202:116137. doi: 10.1016/j.neuroimage.2019.116137
39. Tustison NJ, Cook PA, Klein A, Song G, Das SR, Duda JT, et al. Large-scale evaluation of ANTs and FreeSurfer cortical thickness measurements. *Neuroimage.* (2014) 99:166–79. doi: 10.1016/j.neuroimage.2014.05.044
40. Avants BB, Duda JT, Kim J, Zhang H, Pluta J, Gee JC, et al. Multivariate analysis of structural and diffusion imaging in traumatic brain injury. *Acad Radiol.* (2008) 15:1360–75. doi: 10.1016/j.acra.2008.07.007
41. Grossman M, Eslinger PJ, Troiani V, Anderson C, Avants B, Gee JC, et al. The role of ventral medial prefrontal cortex in social decisions: converging evidence from fmri and frontotemporal lobar degeneration. *Neuropsychologia.* (2010) 48:3505–12. doi: 10.1016/j.neuropsychologia.2010.07.036

Conflict of Interest: The authors declare that the research was conducted in the absence of any commercial or financial relationships that could be construed as a potential conflict of interest.

frontiers in Medicine

ORIGINAL RESEARCH
published: 29 July 2021
doi: 10.3389/fmed.2021.680072

The Utility of PET/CT Metabolic Parameters Measured Based on Fixed Percentage Threshold of SUVmax and Adaptive Iterative Algorithm in the New Revised FIGO Staging System for Stage III Cervical Cancer

Yun Zhang, Yuxiao Hu, Shuang Zhao and Can Cui*

Department of PET/CT Center, Jiangsu Cancer Hospital and Jiangsu Institute of Cancer Research and The Affiliated Cancer Hospital of Nanjing Medical University, Nanjing, China

OPEN ACCESS

Edited by:
Martin Huellner, University Hospital Zürich, Switzerland

Reviewed by:
Désirée Deandreis, University of Turin, Italy
Salvatore Annunziata, Catholic University of the Sacred Heart, Italy

***Correspondence:**
Yuxiao Hu
hyx_0102@yeah.net

Specialty section:
This article was submitted to Nuclear Medicine, a section of the journal Frontiers in Medicine

Received: *13 March 2021*
Accepted: *30 June 2021*
Published: *29 July 2021*

Citation:
Zhang Y, Hu Y, Zhao S and Cui C (2021) The Utility of PET/CT Metabolic Parameters Measured Based on Fixed Percentage Threshold of SUVmax and Adaptive Iterative Algorithm in the New Revised FIGO Staging System for Stage III Cervical Cancer. Front. Med. 8:680072. doi: 10.3389/fmed.2021.680072

Objectives: The main aim of this study was to evaluate the differences in metabolic parameters of positron emission tomography with 2-deoxy-2-[fluorine-18] fluoro-D-glucose integrated with computed tomography (^{18}F-FDG PET/CT) measured based on fixed percentage threshold of maximum standard uptake value (SUVmax) and adaptive iterative algorithm (AT-AIA) in patients with cervical cancer. Metabolic parameters in stage III patients subdivided into five groups according to FIGO and T staging (IIIB-T3B, IIIC1-T2B, IIIC1-T3B, IIIC2-T2B, IIIC2-T3B) were compared.

Methods: In total, 142 patients with squamous cell cervical cancer subjected to ^{18}F-FDG-PET/CT before treatment were retrospectively reviewed. SUVmax, mean standard uptake value (SUVmean), maximum glucose homogenization (GNmax), mean glucose homogenization (GNmean), metabolic tumor volume (MTV), total lesion glycolysis (TLG), and glucose homogenization total lesion glycolysis (GNTLG) values measured based on the above two measurement methods of all 142 patients (IIB-IVB) and 102 patients in the above five groups were compared.

Results: MTV measured based on fixed percentage threshold of SUVmax was lower than that based on AT-AIA ($p < 0.05$). $MTV_{40\%}$, $MTV_{0.5}$, $TLG_{0.5}$, $GNTLG_{40\%}$, and $GNTLG_{0.5}$ values were significantly different among the five groups ($p < 0.05$) while the rest parameters were comparable ($p > 0.05$). All metabolic parameters of group IIIB-T3B were comparable to those of the other four groups. $MTV_{40\%}$, $MTV_{0.5}$, $GNTLG_{40\%}$, and $GNTLG_{0.5}$ in group IIIC1-T2B relative to IIIC1-T3B and those of group IIIC2-T2B relative to group IIIC2-T3B were significantly different. All metabolic parameters of group IIIC1-T2B relative to IIIC2-T2B and those of group IIIC1-T3B relative to group IIIC2-T3B were not significantly different.

Conclusion: Metabolic parameters obtained with the two measurement methods showed a number of differences. Selection of appropriate methods for measurement of ^{18}F-FDG-PET/CT metabolic parameters is important to facilitate advances in laboratory research and clinical applications. When stage III patients had the same T stage, their metabolic parameters of local tumor were not significantly different, regardless of the presence or absence of lymph node metastasis, location of metastatic lymph nodes in the pelvic cavity or para-abdominal aorta. These results support the utility of the revised FIGO system for stage III cervical cancer, although our T-staging of stage III disease is incomplete.

Keywords: cervical cancer, 18F-FDG-PET/CT metabolic parameters, revised FIGO staging system, fixed percentage threshold of SUVmax, AT-AIA

INTRODUCTION

Globally, cervical cancer is one of the most common cancer types in females, ranking fourth after breast, colorectal, and lung cancer in terms of morbidity and mortality (1). Cervical cancer has been relatively well-controlled for several decades in high-income countries owing to efficient screening initiatives and cancer treatment services but remains the most common cause of cancer-related mortality in 42 countries, the majority of which are low income and lower-middle income countries (LMIC) (2), such as South Africa (SA), India, China, and Brazil.

Gynecologic cancers are staged according to the International Federation of Gynecology and Obstetrics (FIGO) system (3). Although a parallel TNM system has been described by the American Joint Committee on Cancer, the FIGO system continues to be predominantly used worldwide in clinical practice and for cancer database reporting (4). In 2018, FIGO revised the staging system for cervical cancer based on recent developments in imaging and increased use of minimally invasive surgery, which has changed the paradigm for management of this patient group. One of the modifications in the revised FIGO system is that nodal status is incorporated into the criteria for stage III disease. Consequently, cases of lymph node metastasis are designated stage IIIC disease, specifically, stage IIIC1 for pelvic lymph node metastasis only, and stage IIIC2 for para-aortic lymph node metastasis (3).

Imaging plays a central role in the 2018 FIGO staging system for uterine cervical cancer. ^{18}F-FDG-PET/CT has significant advantages in detecting lymph node metastases and distant metastases (5). For cervical cancer, ^{18}F-FDG-PET/CT metabolic parameters of primary tumors and lymph nodes, such as SUVmax, MTV, and TLG, have considerable value (6–14). Yilmaz et al. (6) identified pretreatment primary tumor SUVmax, TLG, pelvic lymph node SUVmax, and pretreatment para-aortic lymph node SUVmax as significant prognostic factors for disease-free survival (DFS) with different cut-off values. The group of Lima showed that pretreatment MTV and TLG values and nodal involvement were effective predictors of response to therapy in a cohort with locally advanced squamous cell cervical cancer (LACC) patients treated with computer-controlled radiation therapy (CCRT). MTV was identified as the best predictor of response (11). Xu et al. (14) reported a combination of tumor TLG, Dmin [obtained by the diffusion-related coefficient (D) map of MRI] and PET for lymph node diagnosis as a powerful prognostic factor for cervical cancer. TLG showed the best predictive performance in patients with PET-negative lymph nodes.

The most commonly used metabolic parameter to quantify ^{18}F-FDG uptake on PET is the SUVmax. The SUVmax was widely accepted and routinely clinical used owing to the ease of use and an excellent inter-observer reproducibility in association with promising results for SUVmax as a prognostic factor (15, 16). However, the use of SUVmax has many disadvantages, especially the variability caused by the high statistical noise associated with a single voxel analysis (17). TLG was proposed as an alternative quantitative metric in 1999, which take the SUV and the tracer uptake of the entire lesion into account. TLG is defined as the MTV multiplied with the SUVmean. The MTV is determined as the total number of voxels within a volume of interest (VOI) that have uptake above a predetermined SUV threshold (18). Various automated methods are currently used to segment regions of interest in PET/CT scans, such as fixed SUV threshold (e.g., SUV2.5), fixed percentage threshold of SUVmax (e.g., T42%), and gradient-based threshold (adaptive iterative algorithm, AT-AIA) (19). At present, the fixed percentage of the SUVmax threshold algorithm is commonly used, especially for target delineation of cervical cancer, lung cancer, and head and neck cancers (6, 11, 20–22). In 2006, Sebastian et al. (23) published the iterative adaptive segmentation algorithm. The adaptive iterative algorithm has an advantage over fixed threshold methods in accurate delineation of the target volume according to the individual metabolic activity. This method is usually based on the SUVmax uptake within the volume and the threshold defined according to the background uptake within the adjacent normal tissue using a mathematical algorithm.

In view of the wide application of the ^{18}F-FDG-PET/CT metabolic parameters in cervical cancer and the MTV and TLG are greatly affected by the different measurement methods, one of the major objectives of the current investigation was to compare the ^{18}F-FDG-PET/CT metabolic parameters obtained using the fixed percentage threshold of SUVmax and AT-AIA in patients with LACC.

According to the new revised FIGO staging system, Stage IIIC disease is directly correlated with pelvic and para-aortic metastatic lymph nodes regardless of the T stage. We additionally focused on differences in ^{18}F-FDG-PET/CT metabolic parameters of local tumors with different T-stages in patient groups of stage III cervical cancer.

PATIENTS AND METHODS

Patients

The clinical records of all patients referred to our center for cervical cancer from May 2016 to July 2020 were analyzed. In total, 142 patients with squamous cell cervical cancer confirmed via biopsy were included.

All patients underwent routine clinical staging, including physical and gynecological examinations, complete blood count, biochemical tests, and radiological imaging of the pelvis and abdomen with enhanced MRI or enhanced CT. Patients with histologically confirmed cervical cancer (FIGO stage IIB–IVB) underwent a ^{18}F-FDG-PET/CT examination before treatment.

PET/CT Imaging

All patients were imaged using an integrated PET/CT system (Discovery 710, GE Medical Systems, Waukesha, Wisconsin, USA). Patients fasted for at least 6 h before intravenous administration of 0.1–0.2 mCi/kg ^{18}F-FDG. Blood glucose concentrations were measured before the injection of radiopharmaceuticals to ensure a threshold <11 mmol/L. Patients were allowed to rest during distribution of the radiotracer in a comfortable, quiet room, and hydrated orally with 1,000 ml water. Patients were instructed to empty their bladder immediately before the scan. Combined image acquisition began about 50–70 min after ^{18}F-FDG injection. From the vertex to mid-thigh, CT was performed using the following parameters: 140 kV, Auto mA (noise index, 28.5), 0.8 s rotation time, and 3.75 mm slice thickness. A PET scan was performed with the same parameters. The emission scan time was 2 min/bed position and the scanning range covered 6–7 bed positions. PET image datasets were reconstructed iteratively using the ordered-subsets expectation maximization algorithm with CT-based attenuation correction. The following parameters were used: sharp IR algorithm with the VUE Point FX (fully 3D iterative reconstruction), 192×192 matrix, 24 subset/2 iteration, and 6.4 post-filter. Trans axial, sagittal, coronal, and fused images were analyzed on an Advanced Workstation AW 4.6 (GE Healthcare Bio-Sciences, NJ, USA).

PET/CT Image Analysis

Qualitative and quantitative (or semi-quantitative) image analyses were conducted by an experienced nuclear medicine physician with significant experience in ^{18}F-FDG-PET/CT scan analysis (average 150 reads/month individually). A VOI was placed around the primary tumor in such a way that the entire tumor activity was enclosed and regions of physiologically increased activity avoided. VOI placement was performed according to a previously published protocol (24). Within the selected VOI, SUVmax, SUVmean, GNmax, GNmean, MTV, TLG, and GNTLG [SUV is a measurement of the uptake in a tumor normalized on the basis of a distribution volume. GN is defined as SUV with plasma glucose correction. SUVmax and GNmax are the maximum SUV and GN. SUVmean and GNmean are the mean SUV and GN (15). The MTV is determined as the total number of voxels within a volume of interest that have uptake above a predetermined SUV threshold. TLG was defined as the MTV multiplied with the SUVmean (18). GNTLG was defined as the MTV multiplied with the GNmean.] were measured based on fixed percentage threshold (40% SUVmax) [All voxels with SUVs above or equal to 40% of the SUVmax were delineated inside the selected VOI (6, 8).] and AT-AIA [The VOI was segmented automatically using an iterative adaptive algorithm to detect the threshold level that separated the target volume from the background tissue by weighting the SUVmax and the SUVmean within the target volume with a weighting factor "w" ($0 \leq w \leq 1$)]. This weighting factor was automatically set at 0.5 (19, 21, 22, 25).

Statistical Analysis

Comparisons between the two groups were performed with the independent samples *t*-test or Mann-Whitney U-test depending on the homogeneity of variance. Multi-group comparisons were conducted with ANOVA. All hypotheses were two-tailed and $P < 0.05$ considered statistically significant. Statistical Package for Social Sciences (SPSS, version 22.0, IBM Corp, Armonk, NY, USA) was applied for data analysis.

RESULTS

Clinical Features and PET Metabolic Parameters of the Two Groups Measured Using Different Methods

^{18}F-FDG-PET/CT metabolic parameters obtained with the two methods were compared in 142 patients with squamous cell cervical cancer. The clinical characteristics of participants are listed in **Table 1**. Mean age of patients was 53.39 ± 9.61 years. The most common FIGO stage was IIIC1 ($n = 53$, 37.32%) followed by IIIC2 ($n = 32$, 22.50%), IVB ($n = 27$, 19.01%), IIIB ($n = 19$, 13.38%), IIB ($n = 9$, 6.34%), IIIA ($n = 1$, 0.70%), and IVA ($n = 1$, 0.70%).

PET parameters of the two groups are listed in **Table 2**. We observed no significant differences in SUVmean, GNmean, TLG, and GNTLG values between the groups. MTV measured based on fixed percentage threshold (40% SUVmax) was lower than that based on AT-AIA ($w = 0.5$, **Figure 1**).

Patient Characteristics and PET Parameters of IIIB-IIIC2 Groups

To establish whether metabolic ^{18}F-FDG-PET/CT parameters of local tumors at various T-stages differ among patients with stage III cervical cancer, 102 patients from groups IIIB-IIIC2 were analyzed. SUVmean, GNmean, MTV, TLG, GNTLG measured based on fixed percentage threshold (40% SUVmax) and AT-AIA ($w = 0.5$) were labeled $SUVmean_{40\%}$, $GNmean_{40\%}$, $MTV_{40\%}$, $TLG_{40\%}$, $GNTLG_{40\%}$, and $SUVmean_{0.5}$, $GNmean_{0.5}$, $MTV_{0.5}$,

TABLE 1 | Clinical characteristics of patients with squamous cell cervical cancer.

	IIB	IIIA	IIIB	IIIC1	IIIC2	IVa	IVb
Number, %	9 (6.34%)	1 (0.70%)	19 (13.38%)	53 (37.32%)	32 (22.54%)	1 (0.70%)	27 (19.01%)
Age (year)	55.89 ± 5.18	66	58.84 ± 11.49	51.77 ± 8.72	50.81 ± 10.11	49	54.67 ± 9.02
Stature (cm)	158.33 ± 7.04	152	157.95 ± 4.45	160.85 ± 5.18	159.38 ± 5.11	155	158.04 ± 5.41
Weight (kg)	60.56 ± 6.41	71	58.79 ± 8.44	60.11 ± 8.54	60.02 ± 9.31	49	59.06 ± 9.86
^{18}F-FDG dose (mCi/kg)	0.16 ± 0.02	0.14	0.18 ± 0.04	0.17 ± 0.03	0.17 ± 0.04	0.22	0.17 ± 0.03
Blood glucose (mmol/L)	5.54 ± 1.34	5.70	5.81 ± 1.51	5.62 ± 1.10	5.57 ± 0.63	6.10	5.61 ± 0.71

TABLE 2 | PET parameters of groups measured using the two different methods.

	Fixed percentage threshold	AT-AIA	*P*
SUVmean	9.32 ± 3.59	8.60 ± 3.21	0.074 ($t = -1.79$)
GNmean	9.31 ± 3.44	8.55 ± 3.14	0.051 ($t = -1.96$)
MTV (cm^3)	28.64 (15.40–50.71)	35.84 (21.17–60.91)	0.019 ($Z = -2.34$)
TLG	276.40 (121.24–500.10)	315.15 (145.55–535.43)	0.22 ($Z = -1.22$)
GNTLG	277.91 (124.04–503.02)	319.27 (151.13–559.39)	0.24 ($Z = -1.18$)

SUVmax = 15.48 ± 5.86.

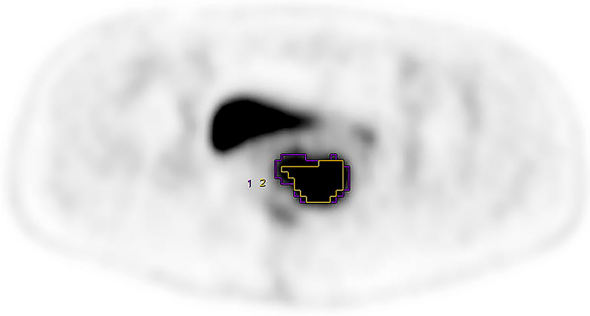

FIGURE 1 | FIGO stage was IIIB, purple VOI and yellow VOI were measured based on the AT-AIA($w = 0.5$) and fixed percentage threshold (40% SUVmax), respectively. $MTV_{0.5} = 32.16$, $MTV_{40\%} = 17.30$.

$TLG_{0.5}$, and $GNTLG_{0.5}$, respectively. Patients were subdivided into five groups according to FIGO system and T staging of the TNM system: IIIB-T3B, IIIC1-T2B, IIIC1-T3B, IIIC2-T2B, and IIIC2-T3B. Patient characteristics and PET parameters of IIIB-IIIC2 groups are listed in **Table 3**.

We observed no significant differences in age, stature, weight, ^{18}F-FDG dose, blood glucose, SUVmax, $SUVmean_{40\%}$, $SUVmean_{0.5}$, GNmax, $GNmean_{40\%}$, $GNmean_{0.5}$, and $TLG_{40\%}$ values among the groups, with (F, P) of (1.020, 0.401), (1.096, 0.363), (0.099, 0.983), (0.112, 0.978), (0.313, 0.869), (1.420, 0.233), (1.218, 0.308), (0.736, 0.570), (1.791, 0.137), (1.633, 0.172), (0.945, 0.441), and (2.395, 0.056), respectively. However, $MTV_{40\%}$, $MTV_{0.5}$, $TLG_{0.5}$, $GNTLG_{40\%}$, and $GNTLG_{0.5}$ were significantly different among the five groups, with (F, P) of (2.516, 0.046), (3.286, 0.014), (2.839, 0.028), (2.740, 0.033), and (3.082, 0.020), respectively.

All metabolic parameters of group IIIB-T3B were comparable to those of the other four groups. Metabolic parameters of group IIIC1-T2B relative to IIIC2-T2B and those of IIIC1-T3B relative to IIIC2-T3B were not significantly different. $MTV_{40\%}$, $MTV_{0.5}$, $GNTLG_{40\%}$, and $GNTLG_{0.5}$ values of group IIIC1-T2B were lower than those of IIIC1-T3B while the $TLG_{0.5}$ were comparable. $MTV_{40\%}$, $MTV_{0.5}$, $TLG_{0.5}$, $GNTLG_{40\%}$, and $GNTLG_{0.5}$ values of group IIIC2-T2B were lower than those of group IIIC2-T3B. All metabolic parameters of group IIIC1-T2B or IIIC2-T2B were comparable to those of the group IIIB-T3B. $MTV_{40\%}$ of group IIIC1-T2B were lower than those of group IIIC2-T3B while the other metabolic parameters were comparable. $MTV_{40\%}$, $MTV_{0.5}$, $TLG_{0.5}$, $GNTLG_{40\%}$, and $GNTLG_{0.5}$ values of group IIIC2-T2B were lower than those of group IIIC1-T3B (**Figure 2**).

DISCUSSION

MTV measured based on fixed percentage threshold (40% SUVmax) was lower than that based on the AT-AIA ($w = 0.5$). Weina Xu et al. (25) compared the accuracy of MTV by the iterative adaptive algorithm (MTViterative adaptive) with that of the fixed percentage SUVmax threshold method using gross tumor volume (GTV) as the gold standard and investigated the correlation between them. Significant differences were observed among the fixed percentage method and the optimal threshold percentage was inversely correlated with SUV max. MTViterative adaptive is independent of SUVmax, more accurate, and correlated with GTV in patients with early-stage cervical cancer (stage Ia–IIb). They speculated that iterative adaptive algorithm segmentation may be more suitable than the fixed percentage threshold method to estimate the tumor volume of cervical primary squamous cell carcinoma. The group of Xiao-Yi Wang investigated the suitable segmentation method in small, low uptake, and heterogeneous nodules of stage I

TABLE 3 | Patient characteristics and PET parameters (mean ± *SD*) of groups IIIB-IIIC2.

	IIIB-T3B	IIIC1-T2B	IIIC1-T3B	IIIC2-T2B	IIIC2-T3B	*P*
Number, %	19 (18.63%)	26 (25.49%)	25 (24.51%)	15 (14.71%)	17 (16.67%)	
Age (year)	56.58 ± 13.18	52.62 ± 9.88	52.08 ± 6.51	51.00 ± 12.85	50.65 ± 7.32	0.401 ($F = 1.020$)
Stature (cm)	158.63 ± 4.22	160.50 ± 5.60	161.48 ± 4.58	159.40 ± 5.11	159.35 ± 5.27	0.363 ($F = 1.096$)
Weight (kg)	60.53 ± 7.49	59.69 ± 7.23	60.20 ± 10.04	59.13 ± 10.85	60.79 ± 7.96	0.983 ($F = 0.099$)
^{18}F-FDG dose (mCi/kg)	0.17 ± 0.04	0.17 ± 0.03	0.17 ± 0.04	0.16 ± 0.03	0.17 ± 0.04	0.978 ($F = 0.112$)
Blood glucose (mmol/L)	5.75 ± 1.53	5.51 ± 1.15	5.79 ± 1.06	5.51 ± 0.65	5.62 ± 0.63	0.869 ($F = 0.313$)
SUVmax	14.56 ± 5.89	16.57 ± 6.64	17.56 ± 7.51	13.29 ± 5.18	15.29 ± 4.34	0.233 ($F = 1.420$)
GNmax	14.48 ± 4.04	16.28 ± 6.41	17.76 ± 7.27	13.04 ± 4.60	15.33 ± 4.16	0.137 ($F = 1.791$)
$SUVmean_{40\%}$	8.70 ± 3.50	9.94 ± 4.15	10.53 ± 4.58	8.19 ± 3.46	9.09 ± 2.66	0.308 ($F = 1.218$)
$SUVmean_{0.5}$	8.01 ± 3.20	9.13 ± 3.57	9.39 ± 4.03	7.94 ± 3.32	8.51 ± 2.49	0.570 ($F = 0.736$)
$GNmean_{40\%}$	8.64 ± 3.23	9.89 ± 3.87	10.65 ± 4.48	8.02 ± 3.06	9.11 ± 2.56	0.172 ($F = 1.633$)
$GNmean_{0.5}$	7.80 ± 3.01	8.94 ± 3.39	9.51 ± 3.98	7.78 ± 2.92	8.37 ± 2.84	0.441 ($F = 0.945$)
$MTV_{40\%}$ (cm^3)	42.02 ± 37.29	30.56 ± 14.41^{bd}	46.29 ± 28.50^{ac}	27.09 ± 21.51^{bd}	50.07 ± 32.21^{ac}	0.046 ($F = 2.516$)
$MTV_{0.5}$ (cm^3)	47.64 ± 36.49	39.75 ± 19.23^{b}	59.25 ± 36.78^{ac}	29.08 ± 21.67^{bd}	58.05 ± 31.85^{c}	0.014 ($F = 3.286$)
$TLG_{40\%}$	359.67 ± 355.08	315.89 ± 200.96	448.19 ± 270.73	226.46 ± 174.11	474.71 ± 344.02	0.056 ($F = 2.395$)
$TLG_{0.5}$	384.45 ± 353.89	368.74 ± 233.30	516.41 ± 311.47^{c}	237.74 ± 185.41^{bd}	519.57 ± 354.48^{c}	0.028 ($F = 2.839$)
$GNTLG_{40\%}$	356.30 ± 243.14	309.05 ± 193.24^{b}	466.29 ± 305.99^{ac}	220.03 ± 164.41^{bd}	475.66 ± 346.81^{c}	0.033 ($F = 2.740$)
$GNTLG_{0.5}$	380.26 ± 340.60	361.77 ± 225.32^{b}	530.76 ± 346.67^{ac}	231.08 ± 175.02^{bd}	515.06 ± 358.32^{c}	0.020 ($F = 3.082$)

[a]*significantly different from IIIC1-T2B.*
[b]*significantly different from IIIC1-T3B.*
[c]*significantly different from IIIC2-T2B.*
[d]*significantly different from IIIC2-T3B.*
no significant difference between group IIIB-T3B and other groups.

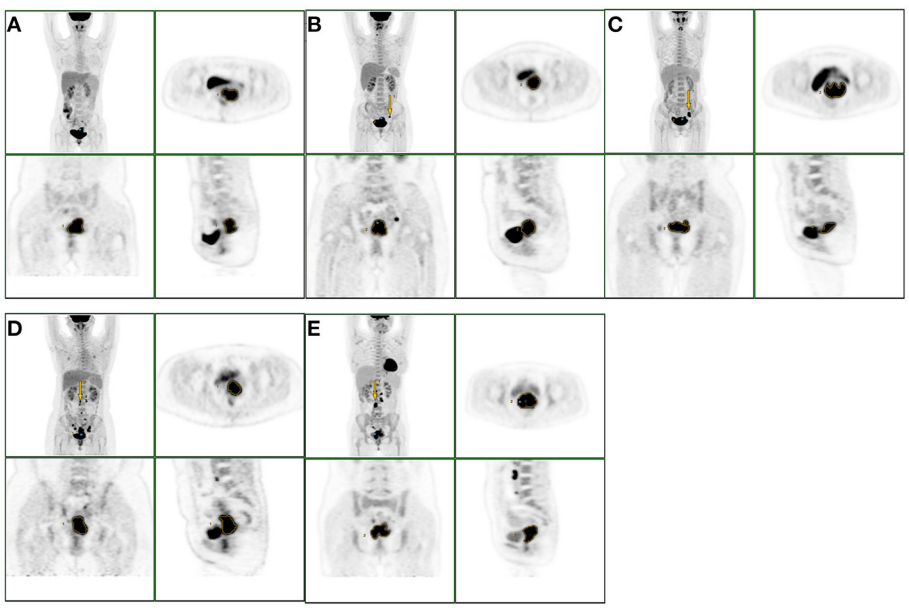

FIGURE 2 | The group of A, B, C, D, E were IIIB-T3B, IIIC1-T2B, IIIC1-T3B, IIIC2-T2B, IIIC2-T3B. The yellow arrows indicated the metastatic lymph nodes. When stage III patients had the same T stage, their metabolic parameters of local tumor were not significantly different, regardless of the presence or absence of lymph node metastasis, location of metastatic lymph nodes in the pelvic cavity or para-abdominal aorta.

lung adenocarcinoma and found that AT-AIA had the highest accuracy in large, high uptake, and solid nodules (19). This finding may be explained by phantom results showing that a fixed threshold can substantially underestimate MTV for lesions with high ^{18}F-FDG uptake (26). Recent studies have reported limitations of this threshold method in measurement of lesion activity and volume. MTV and TLG values obtained based on a fixed threshold using SUVmax (40%) can lead to underestimation

of lesional uptake with high activity and overestimation of lesions with SUVmax close to the background level (26). If the radiotherapy regimen is based on the measurement range of MTV with a fixed threshold using SUVmax, active tumor lesions are likely to be overestimated or underestimated.

On the other hand, the TLG and GNTLG values in our study were not significantly different between the two groups, the two measurement methods had no effect on TLG and GNTLG, which differs from the previous studies (26). This conclusion needs further study.

MTV measurements using different methods have been reported. Some studies have measured MTV in cervical cancer based on fixed percentage threshold (40% SUVmax) (6, 11, 21), while others have shown that MTV and TLG calculated using a threshold of 55% SUVmax and 32% SUVmax from pre- and per-treatment PET scans, respectively, could be effectively used to predict patient outcomes after CCRT for LACC (27). Burger and co-workers reported that PET volume metrics based on fixed SUVmax threshold (42%) led to significant bias and were not correlated with response to chemotherapy assessed via histopathologic examination, while PET volume metrics based on background-adapted measurements were correlated with tumor regression in non-small cell lung carcinoma (22). Other researchers used a fixed SUV threshold, most commonly 2.5 (27–30), with the obvious limitations of an arbitrary cutoff. However, lesions with low activity may have been consequently underestimated. In our study, MTV was also assessed with the fixed SUV threshold of 2.5 but bladder and rectum were incorporated into the VOI, which could potentially increase the value. Therefore we only compared the differences in ^{18}F-FDG-PET/CT metabolic parameters measured based on fixed percentage threshold of 40% SUVmax and AT-AIA ($w = 0.5$). Metabolic parameters obtained using the two measurement methods showed some variations.

Currently, validation of methods for tumor quantification against published MTV and TLG is a challenge due to the lack of a true gold standard. There are some differences in MTV and TLG obtained by different measurement methods. Therefore, selection of the right measurement method is crucial to facilitate advances in research or clinical application.

According to the new revised FIGO staging system, Stage IIIC disease is directly related to pelvic and para-aortic metastatic lymph nodes regardless of the T stage. This new staging system clearly reflects the importance of lymph node metastasis as a major prognostic factor in cervical cancer. Matsuo and co-workers reported that stage IIIC1 is independently associated with improved cause-specific survival compared to stage IIIA or stage IIIB disease (5-year survival rates of 46.0% for stage IIIA, 42.6% for stage IIIB, and 62.1% for stage IIIC1 disease). Survival of patients with stage IIIC1 disease varied in a manner dependent on T-stage (5-year cause-specific survival rates: 74.8% for T1 stage, 58.7% for T2 stage, and 39.3% for T3 stage), indicating that local tumor factors in addition to nodal status are important determinants of survival (31). Many studies showed MTV and TLG of primary tumor were predictors of response to therapy and prognosis (6, 9, 11, 27). In other studies, TLG of the primary tumor has been used to construct a predictive model of lymph node metastasis (14, 21). Their findings suggest that the internal metabolism of the primary tumor may exert an effect on lymph node metastasis.

Inspired by the above studies, we attempted to investigate the differences of metabolic parameters of primary tumor in stage III, considering the different T staging and lymph node metastasis. Since there was only one patient in the stage IIIA in our study, we included the patients in stage IIIB, IIIC1, and IIIC2 in our study, and subdivided the patients into five groups according to the new revised FIGO staging system and T staging of the TNM system: IIIB-T3B, IIIC1-T2B, IIIC1-T3B, IIIC2-T2B, and IIIC2-T3B. According to our results, when the stage III patients have the same T stage, their metabolic parameters of local tumor were not significantly different. The differences between them were the presence or absence of lymph node metastasis, location of metastatic lymph nodes in the pelvic cavity or para-abdominal aorta. In stage IIIC1 or stage IIIC2, all patients with lymph node metastasis, the lower the T stage, the lower the $MTV_{40\%}$, $MTV_{0.5}$, $GNTLG_{40\%}$, and $GNTLG_{0.5}$ of the primary tumor. In the group IIIC1-T2B or IIIC2-T2B with lymph node metastasis, although T staging was lower than that in the group IIIB-T3B without lymph node metastasis, the metabolic parameters of the local tumor were comparable. Even using two different measurement methods, we still got similar results. In other words, the difference between the group IIIC and the other groups was only the lymph node metastasis. Our study showed that the staging criteria for stage IIIC disease (Stage IIIC disease is directly related to pelvic and para-aortic metastatic lymph nodes regardless of the T stage) seemed to be more reasonable.

To our knowledge, this is the first study to evaluate the differences in the ^{18}F-FDGPET/CT metabolic parameters of primary tumors since the new staging system was revised. Our study was retrospective, FIGO staging was performed by clinicians according to imaging examinations while the invasive range of the primary tumor and lymph node metastasis were not confirmed by pathology, which could lead to inaccurate staging. This aspect is particularly important because histologic analysis generally shows higher sensitivity for detecting nodal metastasis than radiologic studies (32). Therefore, we did not test the correlation between metabolic parameters of the primary tumors and lymph node metastasis due to lacking of pathology as a gold standard. In addition, we had a shorter follow-up period, so we did not perform outcome analysis. The stage III was incomplete (Our study lacked samples for IIIA-T3a, IIIC1-T1, IIIC1-T3a, IIIC2-T1 and IIIC2-T3a, etc.). We only compared the differences between the above five groups, further follow-up studies with larger sample numbers are therefore warranted.

A number of limitations of this study should be acknowledged. Firstly, as mentioned above, it is difficult to validate any method of tumor quantification against the published MTV and TLG due to the lack of a true gold standard. Secondly, the retrospective nature of the analysis led to inconsistencies in uptake time and the injected ^{18}F-FDG dose varied over time. Thirdly, Moreover, outcome analysis was not performed. While we investigated differences in the ^{18}F-FDG PET/CT metabolic parameters of primary tumors among five groups

with stage III disease (IIIB-T3B, IIIC1-T2B, IIIC1-T3B, IIIC2-T2B, IIIC2-T3B), the patient population of stage IIIA was too small and heterogeneous (in terms of stage and histology) to allow meaningful assessment of potential correlation with progression-free and overall survival. To address this issue, follow-up studies on larger homogeneous patient cohorts are planned.

CONCLUSION

In this study, we compared the ^{18}F-FDG-PET/CT metabolic parameters measured based on fixed percentage threshold of SUVmax and AT-AIA in patients with LACC. Our data showed that MTV measured based on fixed percentage threshold was smaller than that based on AT-AIA. On the other hand, the TLG and GNTLG were not significantly different between the two groups, the two measurement methods had no effect on TLG and GNTLG, which differs from the previous studies. MTV assessment using various methods has been reported. Validation of methods for tumor quantification against the established MTV and TLG parameters is a significant challenge due to the lack of a true gold standard, and selection of the appropriate measurement method to obtain ^{18}F-FDG-PET/CT metabolic parameters is important.

Our results showed that when the stage III patients have the same T stage, their metabolic parameters of local tumor were not significantly different, regardless of the presence or absence of lymph node metastasis, location of metastatic lymph nodes in the pelvic cavity or para-abdominal aorta. In stage IIIC1 or stage IIIC2, all patients with lymph node metastasis, the lower the T stage, the lower the $MTV_{40\%}$, $MTV_{0.5}$, $GNTLG_{40\%}$, and $GNTLG_{0.5}$ of the primary tumor. In the group IIIC1-T2B or IIIC2-T2B with lymph node metastasis, although T staging was lower than that in the group IIIB-T3B without lymph node metastasis, the metabolic parameters of the local tumor were comparable. Staging according to the revised FIGO staging system, stage III patients with lymph node metastasis did not have higher ^{18}F-FDG uptake than those without lymph node metastasis when they had the same T stage. Even if the FIGO stage was the same in stage IIIC1 or IIIC2, there were significant differences in some metabolic parameters if the T stage is different. Although patients in the group IIIC1-T2B or IIIC2-T2B with lymph node metastasis had lower T stage than that in the group IIIB-T3B without lymph node metastasis, they did not have lower ^{18}F-FDG uptake. Even using two different measurement methods, we still got similar results. In other words, we speculated that the difference between the group IIIC and the other groups was only the lymph node metastasis in our study. The collective results imply that the revised FIGO staging system for stage III cervical cancer (Stage IIIC disease is directly related to pelvic and para-aortic metastatic lymph nodes regardless of the T stage) is more reasonable to an extent. Further research on larger patient cohorts is warranted to validate this conclusion.

DATA AVAILABILITY STATEMENT

The original contributions presented in the study are included in the article/supplementary material, further inquiries can be directed to the corresponding author/s.

ETHICS STATEMENT

Written informed consent was obtained from each participant. The studies involving human participants were reviewed and approved by Ethical Committee of Jiangsu Cancer Hospital.

AUTHOR CONTRIBUTIONS

YZ and YH: study concept and design, analysis, and interpretation of data. YZ and SZ: data collection. YZ, YH, and CC: drafting and critical revision of the manuscript. All authors contributed to the article and approved the submitted version.

FUNDING

This work was supported by the talents program of Jiangsu Cancer Hospital (Number: YC201801).

REFERENCES

1. Ferlay J, Soerjomataram I, Dikshit R, Eser S, Mathers C, Rebelo M, et al. Cancer incidence and mortality worldwide: sources, methods and major patterns in GLOBOCAN 2012. *Int J Cancer.* (2015) 136:E359–86. doi: 10.1002/ijc.29210
2. Bray F, Ferlay J, Soerjomataram I, Siegel RL, Torre LA, Jemal A. Global cancer statistics 2018: GLOBOCAN estimates of incidence and mortality worldwide for 36 cancers in 185 countries. *CA Cancer J Clin.* (2018) 68:394–424. doi: 10.3322/caac.21492
3. Bhatla N, Aoki D, Sharma DN, Sankaranarayanan R. Cancer of the cervix uteri. *Int J Gynaecol Obstet.* (2018) 143(Suppl 2):22–36. doi: 10.1002/ijgo.12611
4. American Joint Committee on Cancer. Cervix uteri. In: Amin MB, Edge S, Greene F, Byrd DR, Brookland RK, Washington MK, et al. editors. *AJCC Cancer Staging Manual. 8th ed.* New York, NY: Springer (2017). p. 649–59.
5. Lee SI, Atri M. 2018 FIGO staging system for uterine cervical cancer: enter cross-sectional imaging. *Radiology.* (2019) 292:15–24. doi: 10.1148/radiol.2019190088
6. Yilmaz B, Dag S, Ergul N, Cermik TF. The efficacy of pretreatment and after treatment 18F-FDG PET/CT metabolic parameters in patients with locally advanced squamous cell cervical cancer. *Nucl Med Commun.* (2019) 40:219–27. doi: 10.1097/MNM.0000000000000969
7. Hong CM, Park SH, Chong GO, Lee YH, Jeong JH, Lee SW, et al. Enhancing prognosis prediction using pre-treatment nodal SUVmax and HPV status in cervical squamous cell carcinoma. *Cancer Imaging.* (2019) 19:43. doi: 10.1186/s40644-019-0226-4
8. Son SH, Jeong SY, Chong GO, Lee YH, Park SH, Lee CH, et al. Prognostic value of pretreatment metabolic PET parameters in cervical cancer patients with metabolic complete response after concurrent chemoradiotherapy. *Clin Nucl Med.* (2018) 43:e296–303. doi: 10.1097/RLU.0000000000002188

9. Scher N, Castelli J, Depeursinge A, Bourhis J, Prior JO, Herrera FG, et al. ((18)F)-FDG PET/CT parameters to predict survival and recurrence in patients with locally advanced cervical cancer treated with chemoradiotherapy. *Cancer Radiother.* (2018) 22:229–35. doi: 10.1016/j.canrad.2017.10.003
10. Lucia F, Visvikis D, Desseroit MC, Miranda O, Malhaire JP, Robin P, et al. Prediction of outcome using pretreatment (18)F-FDG PET/CT and MRI radiomics in locally advanced cervical cancer treated with chemoradiotherapy. *Eur J Nucl Med Mol Imaging.* (2018) 45:768–86. doi: 10.1007/s00259-017-3898-7
11. Lima GM, Matti A, Vara G, Dondi G, Naselli N, De Crescenzo EM, et al. Prognostic value of posttreatment (18)F-FDG PET/CT and predictors of metabolic response to therapy in patients with locally advanced cervical cancer treated with concomitant chemoradiation therapy: an analysis of intensity- and volume-based PET parameters. *Eur J Nucl Med Mol Imaging.* (2018) 45:2139–46. doi: 10.1007/s00259-018-4077-1
12. Ueno Y, Lisbona R, Tamada T, Alaref A, Sugimura K, Reinhold C. Comparison of FDG PET metabolic tumour volume versus ADC histogram: prognostic value of tumour treatment response and survival in patients with locally advanced uterine cervical cancer. *Br J Radiol.* (2017) 90:20170035. doi: 10.1259/bjr.20170035
13. Lee WK, Chong GO, Jeong SY, Lee HJ, Park SH, Ryu JM, et al. Prognosis-predicting model based on [(18)F]fluorodeoxyglucose PET metabolic parameters in locally advanced cervical cancer patients treated with concurrent chemoradiotherapy: multi-center retrospective study. *J Clin Med.* (2020) 9:427. doi: 10.3390/jcm9020427
14. Xu C, Li X, Shi Y, Wang B, Sun H. Combinative evaluation of primary tumor and lymph nodes to predict pelvic lymphatic metastasis in cervical cancer: an integrated PET-IVIM MRI study. *Cancer Imaging.* (2020) 20:21. doi: 10.1186/s40644-020-00298-y
15. Boellaard R, O'Doherty MJ, Weber WA, Mottaghy FM, Lonsdale MN, Stroobants SG, et al. FDG PET and PET/CT: EANM procedure guidelines for tumour PET imaging: version 1.0. *Eur J Nucl Med Mol Imaging.* (2010) 37:181–200. doi: 10.1007/s00259-010-1458-5
16. Annunziata S, Cuccaro A, Tisi MC, Hohaus S, Rufini V. FDG-PET/CT at the end of immuno-chemotherapy in follicular lymphoma: the prognostic role of the ratio between target lesion and liver SUVmax (rPET). *Ann Nucl Med.* (2018) 32:372–7. doi: 10.1007/s12149-018-1243-2
17. Schwartz J, Humm JL, Gonen M, Kalaigian H, Schoder H, Larson SM, et al. Repeatability of SUV measurements in serial PET. *Med Phys.* (2011) 38:2629–38. doi: 10.1118/1.3578604
18. Larson SM, Erdi Y, Akhurst T, MazumdarM, Macapinlac HA, Finn RD, et al. Tumor treatment response based on visual and quantitative changes in global tumor glycolysis using PET-FDG imaging: the visual response score and the change in total lesion glycolysis. *Clin Positron Imaging.* (1999) 2:159–71. doi: 10.1016/s1095-0397(99)00016-3
19. Wang XY, Zhao YF, Liu Y, Yang YK, Zhu Z, Wu N. Comparison of different automated lesion delineation methods for metabolic tumor volume of 18F-FDG PET/CT in patients with stage I lung adenocarcinoma. *Medicine (Baltimore).* (2017) 96:e9365. doi: 10.1097/MD.0000000000009365
20. Sridhar P, Mercier G, Tan J, Truong MT, Daly B, Subramaniam RM. FDG PET metabolic tumor volume segmentation and pathologic volume of primary human solid tumors. *Am J Roentgenol.* (2014) 202:1114–9. doi: 10.2214/AJR.13.11456
21. Li K, Sun H, Guo Q. Combinative evaluation of primary tumor and lymph nodes in predicting pelvic lymphatic metastasis in early-stage cervical cancer: a multiparametric PET-CT study. *Eur J Radiol.* (2019) 113:153–7. doi: 10.1016/j.ejrad.2019.02.013
22. Burger IA, Casanova R, Steiger S, Husmann L, Stolzmann P, Huellner MW, et al. 18F-FDG PET/CT of Non-Small Cell Lung Carcinoma Under Neoadjuvant Chemotherapy: background-based adaptive-volume metrics outperform TLG and MTV in predicting histopathologic response. *J Nucl Med.* (2016) 57:849–54. doi: 10.2967/jnumed.115.167684
23. Sebastian TB, Manjeshwar RM, Akhurst TJ, Miller JV, editors. Objective PET lesion segmentation using a spherical mean shift algorithm. In: *Proceedings of the 9th international conference on Medical Image Computing and Computer-Assisted Intervention - Volume Part II.* Berlin, Heidelberg: Springer-Verlag (2006). doi: 10.1007/11866763_96
24. Burger IA, Vargas HA, Beattie BJ, Goldman DA, Zheng J, Larson SM, et al. How to assess background activity: introducing a histogram-based analysis as a first step for accurate one-step PET quantification. *Nucl Med Commun.* (2014) 35:316–24. doi: 10.1097/MNM.0000000000000045
25. Xu W, Yu S, Ma Y, Liu C, Xin J. Effect of different segmentation algorithms on metabolic tumor volume measured on 18F-FDG PET/CT of cervical primary squamous cell carcinoma. *Nucl Med Commun.* (2017) 38:259–65. doi: 10.1097/MNM.0000000000000641
26. Burger IA, Vargas HA, Apte A, Beattie BJ, Humm JL, Gonen M, et al. PET quantification with a histogram derived total activity metric: superior quantitative consistency compared to total lesion glycolysis with absolute or relative SUV thresholds in phantoms and lung cancer patients. *Nucl Med Biol.* (2014) 41:410–8. doi: 10.1016/j.nucmedbio.2014.02.006
27. Leseur J, Roman-Jimenez G, Devillers A, Ospina-Arango JD, Williaume D, Castelli J, et al. Pre- and per-treatment 18F-FDG PET/CT parameters to predict recurrence and survival in cervical cancer. *Radiother Oncol.* (2016) 120:512–8. doi: 10.1016/j.radonc.2016.08.008
28. Yuan H, Ai QY, Kwong DL, Fong DY, King AD, Vardhanabhuti V, et al. Cervical nodal volume for prognostication and risk stratification of patients with nasopharyngeal carcinoma, and implications on the TNM-staging system. *Sci Rep.* (2017) 7:10387. doi: 10.1038/s41598-017-10423-w
29. Park SY, Cho A, Bae MK, Lee CY, Kim DJ, Chung KY. Value of 18F-FDG PET/CT for predicting the world health organization malignant grade of thymic epithelial tumors: focused in volume-dependent parameters. *Clin Nucl Med.* (2016) 41:15–20. doi: 10.1097/RLU.0000000000001032
30. Chung HH, Kim JW, Han KH, Eo JS, Kang KW, Park NH, et al. Prognostic value of metabolic tumor volume measured by FDG-PET/CT in patients with cervical cancer. *Gynecol Oncol.* (2011) 120:270–4. doi: 10.1016/j.ygyno.2010.11.002
31. Matsuo K, Machida H, Mandelbaum RS, Konishi I, Mikami M. Validation of the 2018 FIGO cervical cancer staging system. *Gynecol Oncol.* (2019) 152:87–93. doi: 10.1016/j.ygyno.2018.10.026
32. Monk BJ, Tian C, Rose PG, Lanciano R. Which clinical/pathologic factors matter in the era of chemoradiation as treatment for locally advanced cervical carcinoma? Analysis of two Gynecologic Oncology Group (GOG) trials. *Gynecol Oncol.* (2007) 105:427–33. doi: 10.1016/j.ygyno.2006.12.027

Conflict of Interest: The authors declare that the research was conducted in the absence of any commercial or financial relationships that could be construed as a potential conflict of interest.

Publisher's Note: All claims expressed in this article are solely those of the authors and do not necessarily represent those of their affiliated organizations, or those of the publisher, the editors and the reviewers. Any product that may be evaluated in this article, or claim that may be made by its manufacturer, is not guaranteed or endorsed by the publisher.

frontiers in Medicine

ORIGINAL RESEARCH
published: 17 August 2021
doi: 10.3389/fmed.2021.715115

[^{18}F]FDG Positron Emission Tomography for Initial Staging and Healing Assessment at the End of Therapy in Lymph Nodes and Bone Tuberculosis

Laure Sarda-Mantel[1], Jidar Kaoutar[2], Toni Alfaiate[3], Amanda Lopes[4], Frédéric Paycha[1], Khadija Benali[5], Nidaa Mikail[5], Michael Soussan[6], Charles Lemarignier[7], Frédéric Méchaï[8], Sophie Le Nagat[9], Françoise Montravers[10], Ouda Deradji[11], Emmanuel Durand[12], Tiphaine Goulenok[13], Diane Ponscarme[14], Patrick Yéni[2], Cédric Laouénan[3,15] and Christophe Rioux[2]*

[1] Nuclear Medicine Department, Lariboisière Hospital, APHP, Paris, France, [2] Infectious Diseases Department, Bichat Hospital, APHP, Paris, France, [3] Université de Paris, INSERM, IAME UMR 1137, Paris, France, [4] Internal Medicine Department, Lariboisière Hospital, APHP, Paris, France, [5] Nuclear Medicine Department, Bichat Hospital, APHP, Paris, France, [6] Nuclear Medicine Department, Avicenne Hospital, APHP, Bobigny, France, [7] Nuclear Medicine Department, Saint-Louis Hospital, APHP, Paris, France, [8] Infectious Diseases Department, Avicenne Hospital, APHP, Bobigny, France, [9] Infectious Diseases Department, Tenon Hospital, APHP, Paris, France, [10] Nuclear Medicine Department, Tenon Hospital, APHP, Paris, France, [11] Internal Medicine Department, Bicêtre Hospital, APHP, Le Kremlin Bicêtre, France, [12] Nuclear Medicine Department, Bicêtre Hospital, APHP, Le Kremlin Bicêtre, France, [13] Internal Medicine Department, Bichat Hospital, APHP, Paris, France, [14] Infectious Diseases Department, Saint-Louis Hospital, APHP, Paris, France, [15] Université de Paris, INSERM, IAME UMR 1137, Paris, France

OPEN ACCESS

Edited by:
Martin Huellner,
University Hospital Zürich, Switzerland

Reviewed by:
Virginia Liberini,
University of Turin, Italy
Ismini C. Mainta,
Geneva University Hospitals (HUG), Switzerland

***Correspondence:**
Laure Sarda-Mantel
laure.sarda-mantel@aphp.fr

Specialty section:
This article was submitted to Nuclear Medicine, a section of the journal Frontiers in Medicine

Received: 26 May 2021
Accepted: 19 July 2021
Published: 17 August 2021

Citation:
Sarda-Mantel L, Kaoutar J, Alfaiate T, Lopes A, Paycha F, Benali K, Mikail N, Soussan M, Lemarignier C, Méchaï F, Nagat SL, Montravers F, Deradji O, Durand E, Goulenok T, Ponscarme D, Yéni P, Laouénan C and Rioux C (2021) [^{18}F]FDG Positron Emission Tomography for Initial Staging and Healing Assessment at the End of Therapy in Lymph Nodes and Bone Tuberculosis. Front. Med. 8:715115. doi: 10.3389/fmed.2021.715115

Objective: In extra-pulmonary tuberculosis, therapeutic management is difficult in the absence of reliable tool to affirm healing at the end of treatment. In this prospective multicenter study, we evaluated [^{18}F]FDG-PET for this purpose.

Methods: Forty-two patients out of 55 included patients could be analyzed. Additionally to usual biological, histological and morphological explorations, [^{18}F]FDG-PET was performed at diagnosis (PET1), at the end of treatment (PET2), indeed 6 months later. Then patients were followed until 12 months after end of prescribed treatment.

Results: PET1 was positive in 97.6% of patients and discovered unknown injured sites in 52.7% of cases. PET2 was positive in 83.3% of uncured patients, and in 82.3% of cured patients. The sum and mean value of SUV_{max} measured in PET/CT lesions decreased between PET1 and PET2 in all patients. Mean value of SUV_{max} (MSUV) and sum value of SUVmax on PET2 showed the highest AUC on ROC curves for the diagnosis of healing at the end of prescribed treatment; MSUV 3.5 on PET2 had a sensitivity of 76.5% and a specificity of 80.0% to affirm healing at the end of prescribed treatment.

Conclusions: [^{18}F]FDG-PET/CT was useful at diagnosis, discovering unknown lesions in 52.7% of cases. MSUV on PET2 was the best criteria to affirm healing at the end of prescribed treatment.

Keywords: tuberculosis, bone, lymph nodes, [^{18}F]FDG-PET, Positron emission tomography, antibiotherapy monitoring

INTRODUCTION

Tuberculosis remains a major public health problem worldwide with more than 9 million cases per year in 2009 (137/100,000 inhabitants). Its endemic evolution associated with the explosion of HIV in emerging countries, particularly in sub-Saharan Africa, has increased the number of new annual cases of the disease since 1990 from 6.6 to 9.4 million (1). Mortality remains worrying with 1.7 million deaths worldwide, more than half of them in Africa. The first region affected in metropolitan France is the Ile de France with 36% of reported cases, an incidence of 17.9/100,000 inhabitants. The two most affected departments are Paris and the department of Seine-Saint-Denis (respectively, 27.5 and 30.3/100,000 inhabitants). At-risk groups with higher incidence are identified: people from sub-Saharan Africa (159.1/100,000 inhabitants), homeless people (223.1/100,000 inhabitants), elderly people (16.9/100,000 inhabitants for the over 75 years). The data of the declaration in France concerning the anatomical localization of the tuberculosis are rather restricted. Also in 2008, it was pulmonary tuberculosis associated or not with another localization in 70.4% of the cases; of the remaining 27.8, 51.4% ($n = 824$) were pleural or intra-thoracic lymph nodes, 5.7% were tuberculous meningitis, and 7.7% were tuberculous miliaries (2).

The definitive diagnosis of tuberculosis can only be made on the identification of the mycobacterium in culture with the presence of one of the three species belonging to the tuberculosis complex: *Mycobacterium tuberculosis*, *M. africanum*, and *M. bovis*. In pulmonary tuberculosis, the diagnosis remains relatively easy. In extra-pulmonary forms, on the other hand, cultures are much more often negative. The few available French data show that in extra-pulmonary tuberculosis sites for which a puncture could be performed, the cultures are positive in, respectively, 38, 70, 25, and 42% of cases of lymph node, bone, pleural and meningeal injury; whereas in more than 90% of cases they are pulmonary forms (3).

In pulmonary tuberculosis, the negativation of BK tubages after a 3 months treatment is a good indicator of healing. While in pulmonary tuberculosis treatment and follow-up are well-codified (WHO 1997, UICT 2000, ATS 2002) (4), they are less clear in extra-pulmonary forms. Moreover, it is often impossible to confirm by bacteriology the sterilization of the initial sampling site when it has been informative. The management of radiological abnormalities [Computed Tomography (CT), Magnetic Resonance Imaging (MRI)] is not rigorously codified and their persistence at the end of treatment is not systematically synonymous with failure. Indeed, the evolution of imaging is often delayed compared to that of the clinic and radiological healing criteria are poorly defined. Thus, the recommendations in terms of duration of treatment of extra-pulmonary forms remain unclear: at least 6 months for lymph node tuberculosis, between 6 and 9 months for bone/articular tuberculosis, between 9 and 12 months for a neuro-meningeal injury (5). The total duration of treatment is left to the appreciation of the clinician, who in the absence of certainty tends to prolong treatment rather than shorten it. The consequences in terms of individual health (duration of treatment, side effects) and public health (mobilization in human and financial health resources) posed by the uncertainties which concern the positive diagnosis or the diagnosis of cure, as well as the duration of treatment, raise the need for other assessment tools in the management of extra-pulmonary tuberculosis.

During those last years, recommendations and uses of [18F]Fluoro-desoxy-glucose Positron Emission Tomography coupled with CT ([18F]FDG-PET/CT) have extended from oncological indications to imaging inflammatory diseases. Indeed activated inflammatory cells in infection foci as well as live bacterias have increased glucose metabolism and show increased [18F]FDG uptake on [18F]FDG-PET scans. [18F]FDG accumulation in active tuberculosis foci has been widely reported, as well as its decrease under antibiotic therapy (6, 7). [18F]FDG-PET/CT has an excellent predictive negative value for non-active lesions. But in extra-pulmonary tuberculosis, the few studies available report cases of residual [18F]FDG uptake in cured patients at the end of antibiotherapy. So the question whether [18F]FDG-PET/CT is a reliable tool or not for healing assessment is still unsolved (8, 9).

The aim of this study was to evaluate [18F]FDG-PET/CT before and after anti-tuberculosis treatment, assuming that this technique could provide useful data for therapeutic monitoring.

We described [18F]FDG-PET/CT evolution between initial diagnosis, end of antibiotherapy indeed 6 months after the end of therapy, and identified PET criteria to affirm or invalidate healing at the end of the therapeutic course.

METHODS

This is a French multicenter prospective pilot study conducted in the seven investigative centers, within the departments of infectious and tropical diseases, internal medicine, and rheumatology, registered in clinicaltrials.gov NCT01613196. The study has been approved by the French ethics committee CPP Ile-de-France 1 (and sponsored by Assistance Publique Hôpitaux de Paris) and the subjects gave informed consent to the work.

Patients

The inclusion criteria were: Male or Female over 18, Patient who has not been infected with HIV or has been infected with HIV with a CD4 count > 200/mm3 for at least 3 months, Patient with certain or probable lymph node or bone tuberculosis (certain: presence of bacillus acid-alcohol-resistant in collected samples (ganglionic puncture, bone biopsy puncture, but also other samples—in particular pulmonary—in case of associated extra-lymph nodes or bone localizations; probable: cluster of suggestive arguments among which epidemiological context and/or general clinical signs and/or extra respiratory and/or compatible biological and/or radiological abnormalities and start of antituberculous treatment and absence of argument for another etiology possible).

The patients whose tuberculosis was not confirmed on the evolution were secondary excluded.

Exclusion criteria were: Relapse of tuberculosis (patient having already been treated in the past), Suspicion of another concomitant systemic infection (bacterial, fungal or parasitic),

Severe immunodepression, Active or progressive neoplasia (solid cancer and hematology), Extended corticotherapy (corticosteroid therapy> 20 mg/day) for at least 3 months, Chronic inflammatory diseases, Pregnant or lactating woman or during periods of genital activity without contraception.

Treatment

The choice of treatment was made in accordance with the recommendations of the Superior Council of Public Hygiene and the High Authority of Health concerning the management of tuberculosis (10). It consisted in an association of 3 or 4 anti-tuberculosis agents for the first 2 months, followed by a dual therapy for 4–7 months for lymph node locations and 10 months for bone sites. Those are the expected theoretical durations of treatment. In the case of resistance to anti-tuberculosis drug, the treatment was adapted according to the antibiogram data, according to the recommendations (5, 11) and according to the opinion of the reference center of resistance to anti-tuberculosis drugs in case of multi-resistance. The duration and the decision to stop treatment was left to the discretion of the clinician.

[18F]FDG PET Imaging

[18F]FDG-PET/CT scans were performed on clinical PET/CT devices in five nuclear medicine departments of Assistance-Publique-Hopitaux de Paris. For each patient, initial, post-treatment, and delayed PET-scan procedures were identical (injected dose, PET/CT device).

Included patients underwent 2 or 3 successive [18F]FDG-PET/CT examinations: PET1 within 30 days after initial diagnosis and 15 days after antibiotherapy's initiation, PET2 within 15 days after the end of prescribed treatment, PET3 6 months after the end of treatment if PET2 was positive for tuberculosis.

Acquisitions

Patients were asked to fast at least during 8 h before the PET/CT scan. Upon their arrival in nuclear medicine departments, Capillary glycemia was measured before allowing (or not) the PET scan: a glycemia $\leq$9 nmol/ml was mandatory. [18F]FDG was injected intravenously at the dose of 3–5 MBq/Kg. Then the patients were asked to keep lying and calm during 1 h until the acquisition. The recording of the images was started 60 min after the injection and included CT acquisition followed by the PET recording. CT recording, necessary for the attenuation correction of PET images as well as the anatomical identification of lesions detected by PET, was performed without contrast injection with voltages around 100 kV and intensities of $\sim$140 mA, in order to obtain axial sections of adequate quality with a thickness ranging from 3 to 5 mm and a matrix 512 $\times$ 512. Static PET acquisitions were performed in 3D mode and with a spatial resolution of <5 mm. They were started at the level of the root of the thighs and included several consecutive recordings to cover the pelvis, the abdomen, the thorax and the head. The PET images were reconstructed using an iterative method (OSEM), with parameters allowing to obtain a voxel size $\leq$ 4 mm in the 3 dimensions of the space. PET images were analyzed using specific softwares, allowing the display of merged images.

[18F]FDG-PET/CT Analysis

The [18F]FDG foci were visually detected according to the criterion of a maximum activity clearly greater than that of the surrounding tissue activity. Only hypermetabolic abnormalities present on both uncorrected and attenuation corrected images were considered significant. Quantitative analysis of hypermetabolic abnormalities was performed using manually drawn regions of interest. The maximum activity in the regions of interest was determined [Maximal Standard Uptake Value (SUV_{max}) in g/ml]. The results of [18F]FDG-PET/CT at each time were transmitted to the clinician only after he had made his own diagnosis and had completed the results of his diagnosis in the observation book. At the end of the study, centralized reading of all anonymous PET/CT scans was done by four senior nuclear medicine physicians unaware of any other data. The results were recorded in the scorecard including both the number of detected lesions and the highest SUV_{max} measured in each following areas: cervical, axillary, mediastinal and abdominal lymph nodes areas, axial bone, peripheral bone, lungs, abdominal organs, brain, muscles, skin, and subcutaneous soft tissues. A consensus was made in case of discrepancy between the lecturers.

For each PET scanner, SUV_{max} was recorded for each anatomical regions where abnormal hot spot(s) was (were) seen. Then two quantitative criteria were determined on all PET scans: the sum of all recorded regional SUV_{max} ($\sum$SUV), the mean value of recorded regional SUV_{max} (MSUV). Additionally, a lesion by lesion analysis was performed in the patients for whom the information of healing or uncured disease at the end of treatment could be obtained. For such analysis, the highest SUV_{max} value measured on PET2 was considered.

Healing or Residual Disease Assessment at the End of Prescribed Therapy

Patients were followed up to 12 months after the end of treatment, i.e., 18–24 months after inclusion (duration of treatment: 6, 9, or 12 months depending on the type of injury). Each consultation (Cs1 at initial diagnosis, Cs2 at the end of treatment, Cs3 6 months then Cs4 12 months after the end of treatment) included an examination of the general condition and the general and local signs of infection, weight evaluation, and targeted assessments based on initial locations of tuberculosis. Patients benefited from the usual biological, histological, and morphological explorations at the time of diagnosis and during therapeutic follow-up.

Patients were considered cured if they have been treated for at least 80% of the prescribed time with BK-sensitive drugs, presented no biological or clinical sign of tuberculosis at the end of treatment and have not relapsed 1 year after the end of treatment.

Statistical Analysis

Descriptive Analysis

Patient's characteristics were described using frequency and percentage for categorical variables, and mean and standard deviation or median and inter-quartile range values for continuous variables, depending of the normality of their distribution.

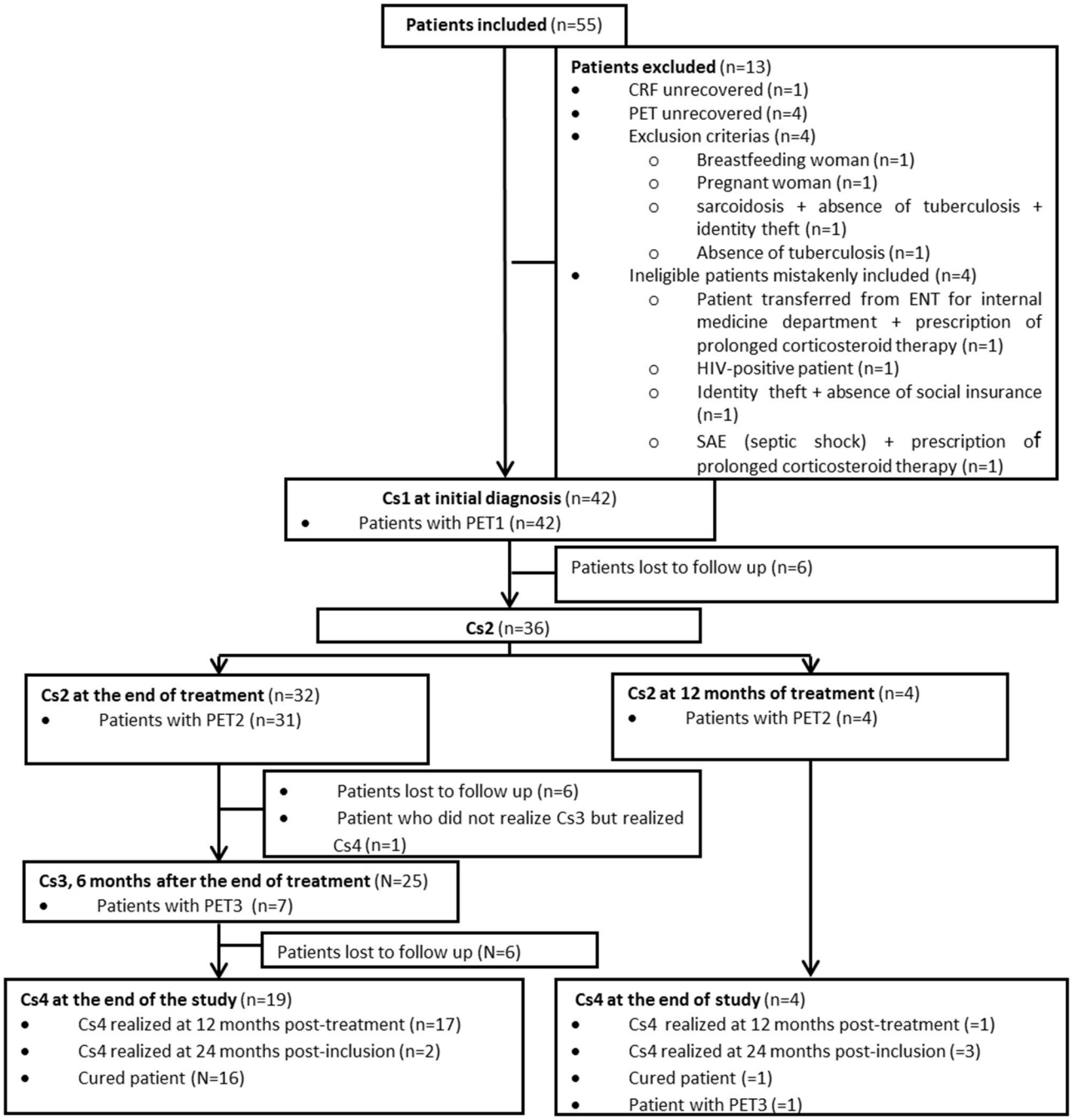

FIGURE 1 | Flowchart of the study. Cs, medical consultation; PET1, Pet performed at initial diagnosis; PET2, PET performed at the end of treatment; PET3, PET performed 6 months after the end of treatment.

Primary Analysis

∑SUM and MSUV were compared between PET1 and PET2 using Wilcoxon signed rank tests.

Secondary Analyses

Thepercentages of variation of ∑SUM ([∑SUM on PET2 – ∑SUV on PET1]/∑SUV on PET1) and MSUV were compared between cured and uncured patients using Wilcoxon tests. Pre-specified subgroup analyses were performed in patients with lymph node lesions, and bone lesions. Comparisons also involved Wilcoxon tests.

The evolutions of ∑SUM and MSUV for each patient were described with spaghetti plots. Thus, we analyzed these using a linear mixed effect model. These models had two

parameters, one for the baseline sum or mean of the SUV_{max}, and one for the slope of evolution of sum or mean of SUV_{max}, both with random effects. Parameters were estimated using the REstricted Maximum Likehood (REML) algorithm implemented in SAS 9.4. For each parameter we reported the estimated mean and standard deviation (SD) of inter-individual variability. The predictions of these models were represented in the spaghetti plots. A first analysis was performed among cured patients and followed by a second analysis among uncured patients.

The ROC test curve analysis and the Youden Index were performed for determining the optimal cut-off value for $\sum$SUM and MSUV at the end of treatment (PET2) to diagnose the recovery.

A p-value of <0.05 was considered statistically significant.

All the analyses were performed using SAS V.9.4 (SAS Institute Inc., Cary, North Carolina, USA).

RESULTS

Patients

Flow-Chart of the Study

The flow-chart of the study is presented in **Figure 1**. Globally, 55 patients were enrolled in the study from May 2012 to August 2014. Thirteen of them were secondarily excluded (HIV confirmed in one case, tuberculosis not confirmed in two cases, prolonged corticotherapy >20 mg/day established in two cases, CRF unrecovered in one case, PET unrecovered in four cases, absence of social insurance in one case, one breastfeeding woman, and one pregnant woman) so 42 of the 55 included patients could be analyzed. Also, the assessment of healing or residual disease at the end of therapy was not possible in 19 patients either because they were lost to follow-up (no Cs4) or because they did not undergo TEP2 or because they did not undergo Cs2. Also only eight patients with positive PET2 underwent PET3.

The characteristics of analyzed patients are presented in **Table 1**.

Healing or Residual Disease Status at the End of Prescribed Therapy

Three of 23 patients (13.0%) had recurrence during the 12-months follow-up after the end of treatment, related to bacterial resistance. According to the criteria indicated in the methods section, 17 patients were cured (including six patients who underwent PET3) and six uncured at the end of treatment (none of them underwent PET3). Lesion by lesion analysis in healed and uncured patients revealed that 16 of 18 initial lymph nodes lesions (88.8%), 10 of 12 initial bone lesions (83.3%), 5 of 6 initial lung lesions (83.3%) were cured at the end of treatment.

TABLE 1 | Description of the study population.

Inclusion	*N* = 42
Sex	F: 14 (33.3%), M: 28 (66.7%)
Age	39.0 [31.0–49.0]
Type of tuberculosis	Lymph nodes: 17 (40.5%)
	Bone: 5 (11.9%)
	Lymph nodes + Bone: 6 (14.3%)
	Lymph nodes + Lung: 6 (14.3%)
	Bone + Lung: 4 (9.5%)
	Lymph nodes + Bone + Lung: 4 (9.5%)
Associated disease	Diabetes Type II: 3 (7.1%)
	Chronic inflammatory disease (controlled): 2 (4.8%)
	Cancer: 1 (2.4%)
Temperature	37.0 [36.8–37.2]
Body weight, kg	63.0 [55.0–80.0]
Symptoms	Sweats: 13 (31.0%): Cough: 7 (16.7%); Pain related to tuberculosis: 23 (54.8%)
Biology	Hb: 12.1 [11.1–13.7]; WBC: 7.1 [5.6–9.0]; Platelets: 309.0 [265.0–371.0]
	ALAT: 25.0 [16.0–38.0]; ASAT: 26.0 [21.0–37.0]; PAL: 96.0 [73.0–126.0]; ϒGT: 64.0 [29.0–107.0]
	Creatinin: 70.0 [61.0–83.0]
	CRP: 19.0 [8.5–79.0]
Microbiology	Lung: positive in 10/34 (29.4%) patients
	Lymph nodes: positive in 11/21 (52.4%) patients
	Bone: positive in 11/14 (78.6%) patients
	Other: positive in 6/9 (66.7%) patients
Imaging data (other than PET)	Thoracic radiography: abnormal in 9/31 (29.0%) patients
	Thoracic CT: abnormal in 28/33 (84.8%) patients
	Abdominal CT: abnormal in 13/27 (48.1%) patients
	Bone MRI: abnormal in 19/19 (100%) patients
Antibiotherapy	Isoniazide: 100% of patients
	Rifampicine: 97.6% of patients
	Ethambutol: 95.2% of patients
	Pyrazinamide: 95.2% of patients
	Moxifloxacin: 2.4% of patients
Treatment duration (months)	9.0 [9.0–12.0]
Treatment observance > 80%	34/36 (94.4%) patients

Results are expressed as median [IQR] or n (%).

[18F]FDG-PET/CT

Overall Study Population

PET1 performed at initial diagnosis was completed in 42 Patients. PET2 performed at the end of therapy was completed in 35 Patients. PET3 performed 6 months after the end of therapy was completed in eight Patients. The results of PET1, PET2 and PET3 in all included patients are recorded in **Table 2**. PET1

TABLE 2 | Tuberculosis locations according to [18F]FDG-PET/CT data and values of PET/CT quantitative criteria ∑SUV and MSUV at 3 time points.

		PET 1 ($n = 42$)	PET2 ($n = 35$)	PET3 ($n = 8$)
Presence of [18F]FDG abnormal Hot spots evocative of TB lesions		41 (97.6%)	29 (82.8%)	7 (87.5%)
Lymph nodes	Cervical	24 (58.5%)	10 (34.5%)	3 (42.9%)
	Mediastinal	27 (65.9%)	10 (34.5%)	3 (42.9%)
	Axillary	8 (19.5%)	4 (13.8%)	0 (0.0%)
	Abdominal, pelvic	16 (39.0%)	4 (13.8%)	0 (0.0%)
	Inguinal	3 (7.3%)	1 (3.4%)	0 (0.0%)
Bone	Spine	14 (34.1%)	4 (13.8%)	0 (0.0%)
	Bassin	6 (14.6%)	1 (3.4%)	0 (0.0%)
	Sup	1 (2.4%)	0 (0.0%)	0 (0.0%)
	Inf	3 (7.3%)	2 (6.9%)	0 (0.0%)
	Other	5 (12.2%)	0 (0.0%)	1 (14.3%)
Lungs		11 (26.8%)	5 (17.2%)	1 (14.3%)
Liver		3 (7.3%)	0 (0.0%)	0 (0.0%)
Spleen		3 (7.3%)	0 (0.0%)	0 (0.0%)
GUT		3 (7.3%)	1 (3.4%)	0 (0.0%)
ENT		2 (4.9%)	0 (0.0%)	0 (0.0%)
Muscular		16 (39.0%)	6 (26.7%)	0 (0.0%)
Skin		4 (9.8%)	1 (3.4%)	0 (0.0%)
Abdominal abcess		1 (2.4%)	0 (0.0%)	1 (14.3%)
Other		4 (9.8%)	2 (6.9%)	3 (42.9%)
∑SUV	Mean (std)	39.0 (28.7%)	8.9 (8.2%)	4.7 (3.1%)
(Patients with abnormal PET)	Median (IQR)	32.0 [21.1–47.8]	6.1 [3.1–12.5]	4.0 [2.3–8.0]
MSUV	Mean (std)	7.0 (2.8)	3.3 (2.1)	2.8 (2.6)
(Patients with abnormal PET)	Median (IQR)	6.6 [4.9–9.2]	3.1 [2.0–5.0]	2.1 [1.1–4.0]
∑SUV	Mean (std)	38.1 (29.0)	7.3 (8.1)	4.1 (3.3)
All patients	Median (IQR)	31.5 [19.6–47.8]	5.4 [0–11.2]	3.8 [1.1–7.1]
MSUV	Mean (std)	6.8 (2.9)	2.7 (2.3)	2.4 (2.6)
All patients	Median (IQR)	6.5 [4.8–9.2]	2.7 [0.0–4.7]	1.6 [0.6–3.4]

PET1, [18F]FDG-PET/CT performed at initial diagnosis; PET2, [18F]FDG-PET/CT performed at the end of treatment; PET3, [18F]FDG-PET/CT performed 6 months after the end of treatment.

was positive in 41 of 42 (97.6%) patients (ΣSUV: 32 [21.1–47.8], MSUV: 6.6 [4.9–9.2]). As compared to data obtained on chest and abdominal CT and MRI (such analysis was possible in 36 of 42 patients), PET1 retrieved unknown additional injured site in 19/36 (52.7%) patients, which were cutaneous lesions in 4/19 (21.0%), liver lesions in 4/19 (21.0%), spleen lesion in 1/19 (5.2%), lung lesions in 2/19 (10.5%), mediastinal lymph nodes in 2/19 (10.5%), and abdominal lymph nodes in 6/19 (31.6%) of cases. Also, among 14 patients with known bone injury, additional bone lesions were discovered on PET1 in three of them (21.4%). Such findings induced a modification of therapy duration in 2/42 (4.7%) patients. Type of medications was not modified and additional CT or MRI examinations were not performed in those two patients. PET2 was positive in 29/35 (82.8%) patients (ΣSUV: 6.1 [3.1–12.5], MSUV 3.1 [2.0–5.0]), and retrieved unknown lymph nodes cervical lesions which were not present at initial diagnosis in 2 of them (5.7%). Such findings did not induce modification of patient management. PET3 was positive in 7 of 8 (87.5%) patients (ΣSUV: 4.0 [2.3–8.0]; MSUV: 2.1 [1.1–4.0]. In the patients who underwent both TEP1 and TEP2, ∑SUV and MSUV values on TEP2 were significantly lower than those calculated on TEP1: 5.4 [0.0–11.2] vs. 30.1 [18.9–43.6] and 2.8 [0.0–4.7] vs. 6.4 [4.7–8.9], respectively, $p < 0.0001$ for both criteria. In the patients who underwent both TEP2 and TEP3, ∑SUV and MSUV on PET2 and PET3 were: 8.0 [3.8–10.9] vs. 3.8 [1.2–7.2] (NS) and 2.8 [2.1–3.8] vs. 1.7 [0.6–3.5] (NS), respectively.

Patients With Available Healed or Residual Disease Assessment at the End of Initially Prescribed Therapy

The results of PET1 and PET2 in cured patients ($n = 17$) and uncured ($n = 6$) patients at the end of therapy are recorded in **Figures 2**, **3**. PET1 ∑SUV and MSUV were higher in uncured than in cured patients but the difference was not statistically significant ($p = 0.55$ and 0.19, respectively). Five of six uncured patients had abnormal PET2. Fourteen of 17 cured patients

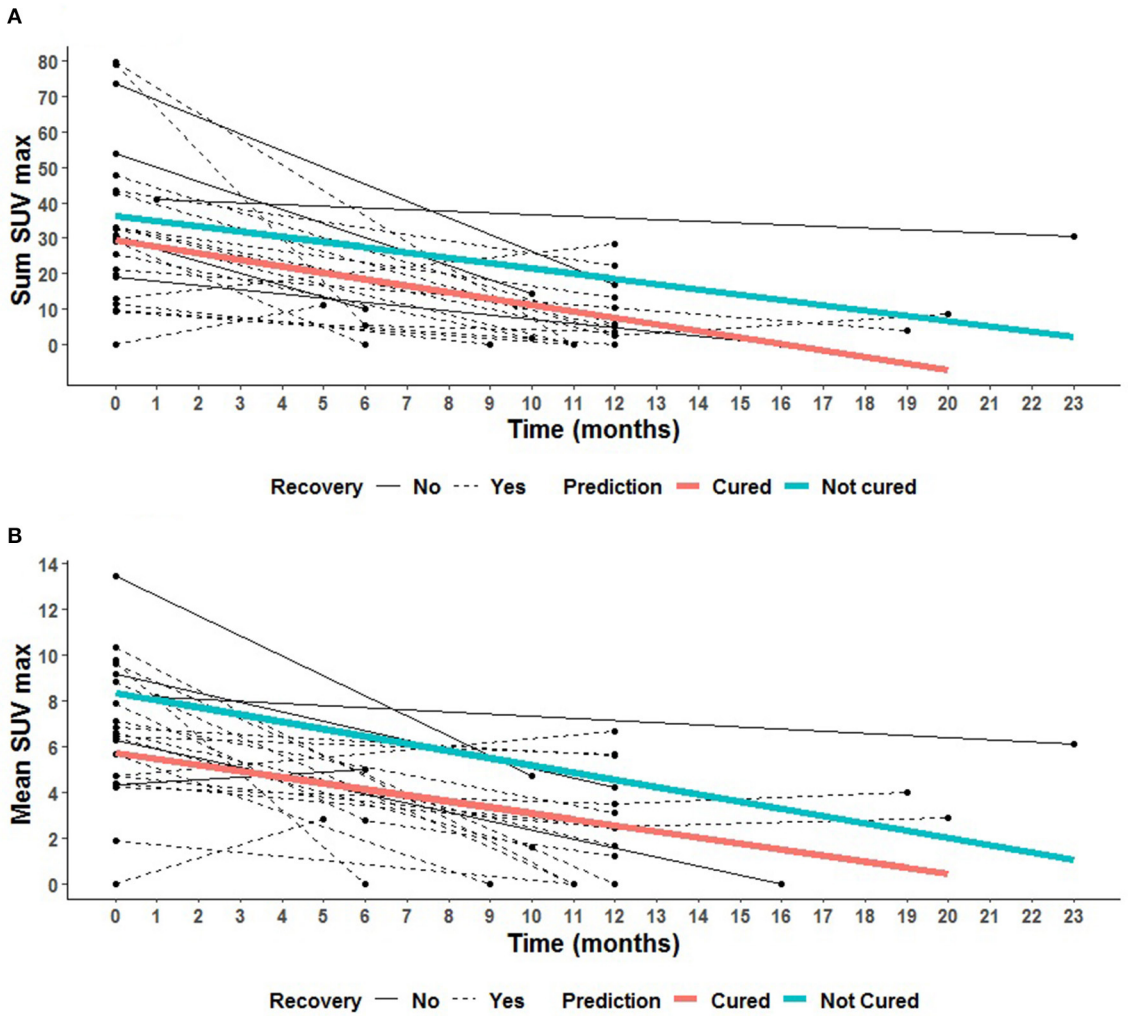

FIGURE 2 | Spaghetti plots of the 23 patients with final diagnosis at the end of treatment. Description of the evolution of the PET parameters with time for each patient, for cured patients (black dotted line) at the end of treatment (red slope, mean prediction), and for uncured patients (black solid line) at the end of treatment (blue slope, mean prediction). **(A)** Description of the evolution of ΣSUV for each patient. **(B)** Description of the evolution of MSUV for each patient.

(82.3%) showed persistent [^{18}F]FDG uptake in at least one lesion on PET2 (**Figure 3**). In cured bone lesions, persistent [^{18}F]FDG uptake on PET2 was observed in the presence of bone lysis on CT, but not when bone CT was normal. $\Delta\sum$SUV and ΔMSUV between PET1 and PET2 were higher but not significantly different between cured and uncured patients: −92.9 [−100.0; −72.3] vs. −73.7 [−77.1; −66.8] ($p = 0.26$), and −70.0 [−100.0; −30.8] vs. −54.3 [−64.9; −25.5] ($p = 0.47$). Lymph node lesions demonstrated a decrease in MSUV (−87.5% [−100.0%; −32.4%]) in cured patient, and conversely an increase in MSUV in uncured patients (+16.3% [−59.7; +37.1]) between TEP1 and TEP2 ($p = 0.04$). Such analysis could not be done with bone lesions since all but 1 bone lesions were cured at the time of TEP2. The variation slope of both criteria ($\Delta\sum$SUV and ΔMSUV per month) was not different in cured and uncured patients (**Figure 2**). On PET3 performed in six cured patients $\Delta\sum$SUV and ΔMSUV decreased as compared to PET2, but the differences were not significant.

ROC curves were performed for all quantitative criteria. $\sum$SUV and MSUV on PET2 showed the highest AUC on ROC curves for the diagnosis of healing or residual disease at the end of treatment (0.73 [0.42–1.00] and 0.72 [0.42–1.00], respectively) (**Figure 4**). MSUV under 3.5 had a sensitivity of 76.5% [56.3–96.6%], and a specificity of 80.0% [44.9%; 100.0%] to affirm healing at the end of treatment. The probability to be healed at the end of treatment for a patient with MSUV < 3.5 on PET2 was 92.9%. The probability to have residual disease at the end of treatment for a patient with MSUV ≥ 3.5 on PET2 was 50%.

The lesion by lesion analysis of PET2 in healed and uncured patients at the end treatment showed that when the highest SUV_{max} value was considered with a threshold of 3.5, healing could be correctly affirmed ($SUV_{max} < 3.5$) on PET2 for 11/16

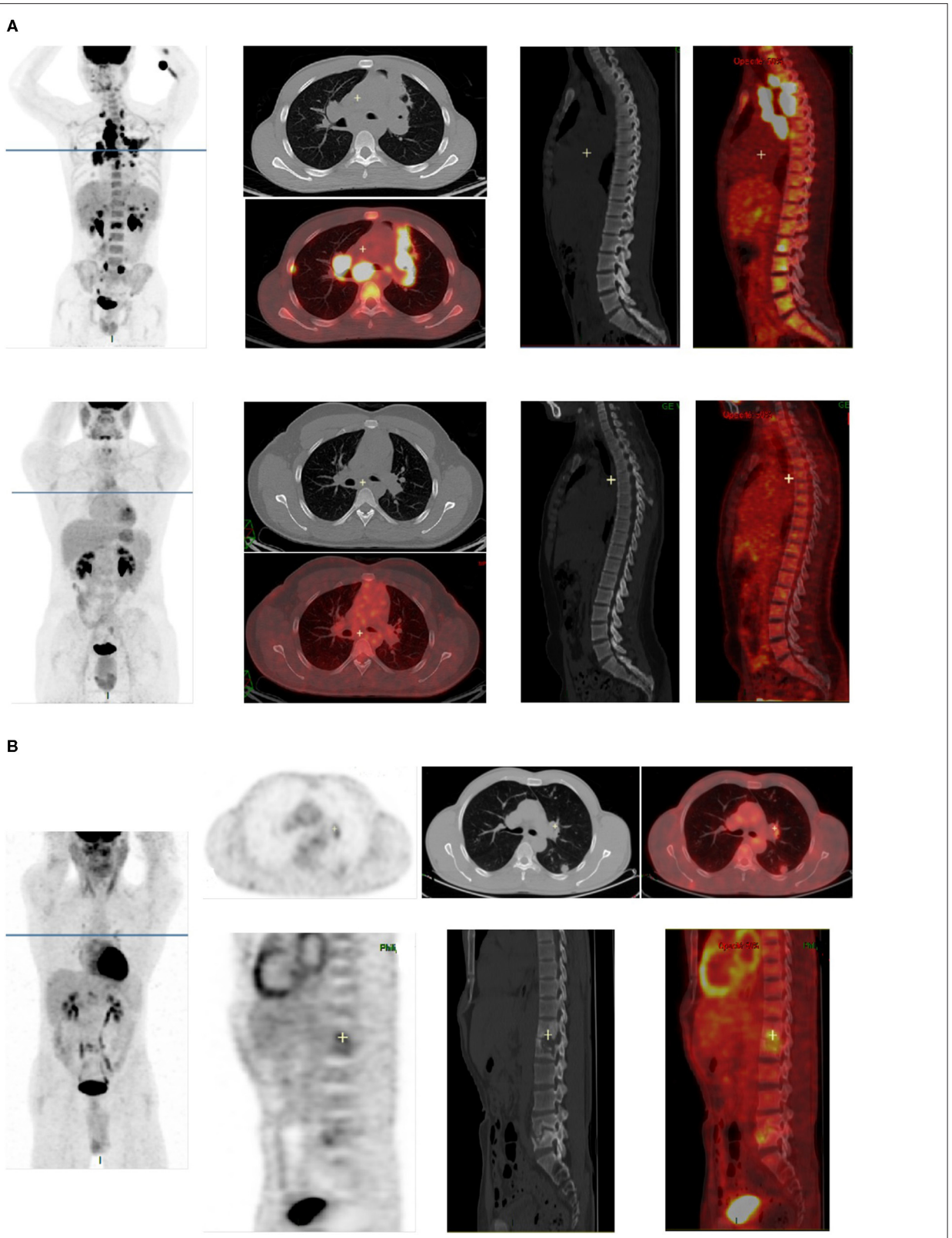

FIGURE 3 | Examples of [^{18}F]FDG-PET/CT images in two patients cured at the end of treatment. **(A)** PET1 and PET2 images of a patient cured at the end of treatment. All abnormalities seen on PET1 (lung lesions, mediastinal lymph nodes, bone lesions in dorsal and lumbar spine) completely disappeared on PET2. **(B)** PET2 images of a patient cured at the end of antibiotherapy, showing residual FDG uptake in cured lesions [left lung, left hilar lymph node, and spine (T12, L1, and L5)].

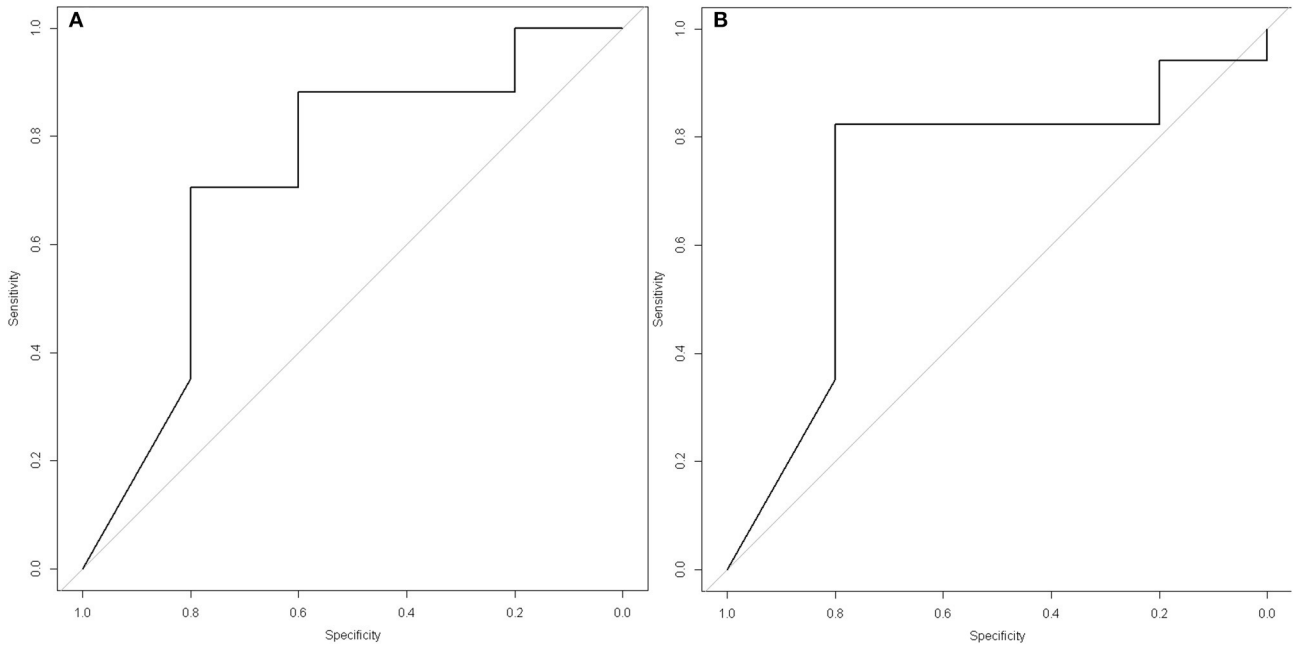

FIGURE 4 | ROC curves with best PET/CT criteria for the diagnosis of healing or residual disease at the end of treatment. **(A)** ΣSUV on PET2 (at the end of prescribed treatment): AUC = 0.73 [0.42–1.00]), Youden index: 5.6, Sensitivity = 64.7 [42.0–87.4], Specificity = 80.0 [44.9–100.0], Positive Predictive Value of ΣSUV < 5.6 for the diagnosis of healing = 91.7 [76.0–100.0], Negative Predictive Value of ΣSUV ≥ 5.6 for the diagnosis of healing= 40.0 [9.6–70.4]. **(B)** MSUV on PET2: AUC = 0.72 [0.42–1.00]), Youden index: 3.5, Sensitivity = 76.5 [56.3–96.6], Specificity = 80.0 [44.9–100.0], Positive Predictive Value of MSUV < 3.5 for the diagnosis of healing = 92.9 [79.4–100.0], Negative Predictive Value of MSUV ≥ 3.5 for the diagnosis of healing = 50.0 [15.3–84.6].

(68.7%) patients, 13/16 (81.2%) lymph node lesions, 8/10 (80.0%) bone lesions, 5/5 (100%) lung lesions, and 3/5 (60%) muscular lesions; and residual disease could be correctly detected (SUV_{max} ≥ 3.5) in 4/5 (80%) uncured patients. In uncured patients, all initial lymph nodes (n = 4) and bone (n = 2) lesions showed SUV_{max} > 3.5 on PET2, whereas all initial muscular lesions (n = 5) showed SUVmax < 3.5 on PET2. This suggests that residual disease was still present at the end of treatment in all initial lymph nodes and bone lesions, whereas all muscular lesions had cured. The probability for a patient to be healed when SUV_{max} was < 3.5 on PET2 was 11/13 (84.6%). The probability for a patient to be uncured when SUV_{max} was ≥ 3.5 on PET2 was 4/10 (40%).

DISCUSSION

[18F]FDG-PET/CT at diagnosis was positive in 97.6% of the patients and discovered unknown lesions in 52.7% of cases. $\sum$SUV and MSUV clearly decreased on PET2 at the end of treatment in cured patients, but abnormal hot spots persisted in 82.3% of them. $\sum$SUV and MSUV did not decrease between PET2 and PET3 in cured patients. MSUV under 3.5 on PET2 was the best criteria to diagnose healing at the end of treatment.

The sensitivity of [18F]FDG-PET/CT at initial diagnosis in our study is comparable to those previously reported (97–100%) (8, 9, 12–14). Additional unknown injured sites were discovered on PET1 in 52.7% of cases. Such parameter is highly variable in the literature, from 10 to 69%, probably depending on the study population (disseminated or local tuberculosis). Discovered additional sites mainly concerned cutaneous lesions, liver lesions and abdominal lymph nodes not detected on CT. As compared to data of the literature (8, 9, 12–14), the percentage of residual [18F]FDG uptake in lesions at the end of antibiotherapy is higher in our study (82 vs. about 40–50% in most studies). This may be explained by the characteristics of the study population: only extra-pulmonary and mostly disseminated tuberculosis in our study when other studies included both pulmonary and other types of tuberculosis. The cured lesions which remained positive on PET2 were lymph nodes, bone, lung, muscle lesions or subcutaneous abcesses. In cured bone lesions residual [18F]FDG uptake was observed in the presence of bone lysis on CT but not when bone CT was normal. This is concordant with residual [18F]FDG uptake being related to bone repair after sterilization. The data observed in lung lesions are surprising and emphasize the role of BK tubage to monitor therapy in pulmonary locations.

Despite the small number of patients analyzed during post-treatment follow-up (n = 8, 6 cured at the end of therapy), we could conclude that [18F]FDG-PET/CT does not normalize 6 months after the end of antibiotic therapy: in seven patients TEP3 remained positive, with comparable MSUV as compared to PET2. Many reasons may explain such data: long healing process with [18F]FDG uptake by activated fibroblasts, latent tuberculosis with the persistence of live but non replicating bacteria, the persistence of dead bacteria or of products of bacterial lysis inducing persistent immune-reactive inflammation. It is

probable that a 6 months delay is too short and that a more delayed [18F]FDG-PET/CT scan would have returned negative. This is supported from previous data of our department in six patients cured since 3 years who had all a negative [18F]FDG-PET/CT scans. However, a longer delay than 6 months after treatment to confirm healing is not applicable in the clinical situation since most of the patients are difficult to follow. With this regards, it is worth noting that only 23 of 42 patients completed the entire study course, many of being absent to 1 or 2 of the 3 [18F]FDG-PET/CT appointments.

Six of the 23 patients who completed entire follow-up were not cured at the end of initial antibiotic therapy. Non observance of treatment can be incriminated in 1 of those. This confirms a posteriori the need for a marker of healing at the end of treatment. Also, lesion by lesion analysis in healed and uncured patients revealed that 16 of 18 initial lymph nodes lesions (88.8%), 10 of 12 initial bone lesions (83.3%), and 5 of 6 initial lung lesions (83.3%) were cured at the end of treatment. This suggests that the location (lymph nodes, bone, or lung) of initial lesions is not related to the persistence of residual disease at the end of treatment.

Despite this small number of uncured patient we could identify $SUV_{max} \geq 3.5$ on PET2 as a criteria to identify uncured patients with good sensitivity (76.5%) and specificity (80.0%). SUV_{max} on PET2 was also previously reported as a valuable criteria for healing assessment by Sathekge et al. (15). However these authors found a threshold value of 4.5 for SUV_{max}. This emphasizes the need of other studies to confirm the value of this criteria, and refine the value of the threshold to be considered. $\sum$SUV on PET2 also showed a high AUC on ROC curves for the diagnosis of healing or residual disease at the end of treatment (0.73 [0.42–1.00]) (**Figure 4**). This suggests that the extension of initial disease plays a role in healing or not, the patients with extensive disease being more at risk for residual disease at the end of treatment. Other criteria which had to be further studied are the $\sum$SUV per month and the ΔMSUV per month which theoretically take into account the problems of non-observance, but they were not different in cured and uncured patients (**Figure 2**). It is worth noting that the variation of $\sum$SUV and MSUV between initial diagnosis and end of antibiotic therapy did not appear as reliable criteria according to ROC curves. This may be related to statistical reason related to the small number of patients.

Also we found that $\sum$SUV has no additional value as compared to MSUV, despite it takes into account the extension of the disease. This is probably due to the facts that only one active lesion is enough for the patient to be uncured, and that there is no relation between the number of lesions at initial diagnosis and the number of uncured lesions at the end of therapy.

We did not use other PET criteria than SUV_{max} (sum and mean) because other PET criteria such as MTV and TLG need to determine the volume of each lesion: this was not feasible for technical reasons in most patients who demonstrated multiple (especially lymph node) lesions. Also SUVpeak was not available in all analysis software at the time of the study so we could not use it.

Overall this study, like others in this field, support present interest for new radiotracers more specific for infection, especially those specifically targeting live bacteria (8, 16). Unfortunately until now no specific marker of mycobacterium has been radiolabeled for *in-vivo* imaging. Authors suggest that [18F]fluoro-choline may be of interest in this setting (12). It showed lower uptake in BK lesions than [18F]FDG but was never evaluated in therapeutic response assessment. Maybe the number of falsely positive sites at the end of treatment would be lower with [18F]fluoro-choline than with [18F]FDG.

Limitations of the Study

This study is hampered by the small effective of patients who completed the entire protocol, affecting the strength of statistical tests. This is probably due to the social characteristics of most patients whose follow-up was difficult (foreign origin with language barrier, homeless patients).

Additionally the study was performed at five different nuclear medicine centers, using three different PET/CT tomographs. Unless each PET/CT tomograph was calibrated according to manufacturers' specifications, harmonization of the data through a phantom study was not performed. Therefore, despite being very promising, the cut-off values identified on PET2 may be currently only preliminary data, which need further validation in the future.

Finally, the evaluation of other PET quantitative criteria, such as MTV and TLG could not be performed at the time of the study, which could be of interest in this setting.

CONCLUSION

[18F]FDG-PET/CT at diagnosis was positive in 97.6% of patients with confirmed lymph node or bone tuberculosis, and discovered unknown lesions in 53.7% of cases. $\sum$SUV and MSUV clearly decreased on PET2 at the end of treatment in cured patients, but abnormal hot spots persisted in 82.3% of cases. SUV_{max} on PET2 was the best criteria to discriminate between healing and residual disease at the end of treatment, with a threshold of 3.5 in our study which needs further validation in the future.

DATA AVAILABILITY STATEMENT

The original contributions presented in the study are included in the article/supplementary files, further inquiries can be directed to the corresponding author/s.

ETHICS STATEMENT

The studies involving human participants were reviewed and approved by the French Ethic Committee CCP Ile-de-France 1 Hôtel Dieu, 1 place du parvis Notre Dame, 75004 Paris (ID-RCB: 2011-A01658-33). The patients/participants provided their written informed consent to participate in this study.

AUTHOR CONTRIBUTIONS

LS-M, JK, CR, PY, and CLa designed the study and obtained funding. AL, FMé, SN, OD, TG, and DP included and followed the patients. LS-M, KB, NM, MS, and CLe performed centralized interpretation and scoring of PET/CT scanners. TA and CLa performed statistical analyses. LS-M, TA, and CLa wrote the manuscript. LS-M, TA, CLa, CR, FMo, and ED reviewed and validated the manuscript. All authors contributed to the article and approved the submitted version.

FUNDING

The French Health Ministry funded the study (PHRCI, No AOM 11080).

ACKNOWLEDGMENTS

We thank Aline Dechanet, from Bichat hospital's Clinical Trial Unit (URC PNVS), for her very helpful contribution to study's setting-up and monitoring.

REFERENCES

1. Global Tuberculosis Control. *WHO Report*. (2010). Available online at: http://www.who.int/tb/data (accessed June 15, 2020).
2. Antoine D, Che D. Les cas de tuberculose maladie déclarés en France en 2007. *Bull Epidémiol Hebdomad.* (2009) 12–13:106-109.
3. Fain O, Lortholary O, Lascaux VV, Amoura II, Babinet P, Beaudreuil J, et al. Extrapulmonary tuberculosis in the northeastern suburbs of Paris: 141 cases. *Eur J Intern Med.* (2000) 11:145–50. doi: 10.1016/S0953-6205(00)00076-5
4. Prévention et prise ne charge de la tuberculose en France. Synthèse et recommandations du groupe de travail du Conseil Supérieur d'Hygiène Publique de France (2002-2003). *Rev Mal Respir*. (2003) 20:7S3–S4.
5. Blumberg HM, Burman WJ, Chaisson RE, Daley CL, Etkind SC, Friedman LN, et al. American Thoracic Society/Centers for Disease Control and Prevention/Infectious Diseases Society of America: treatment of tuberculosis. *Am J Respir Crit Care Med*. (2003) 167:603–20. doi: 10.1164/rccm.167.4.603
6. Gambhir S, Ravina M, Rangan K, Dixit M, Barai S, Bomanji J. International Atomic Energy Agency Extra-pulmonary TB Consortium. Imaging in extrapulmonary tuberculosis. *Int J Infect Dis.* (2017) 56:237–47. doi: 10.1016/j.ijid.2016.11.003
7. Ankrah AO, Glaudemans AWJM, Maes A, Van de Wiele C, Dierckx RAJO, Vorster M, et al. Tuberculosis. *Semin Nucl Med.* (2018) 48:108–30. doi: 10.1053/j.semnuclmed.2017.10.005
8. Lefebvre N, Argemi X, Meyer N, Mootien J, Douiri N, Sferrazza-Mandala S, et al. Clinical usefulness of (18)F-FDG PET/CT for initial staging and assessment of treatment efficacy in patients with lymph node tuberculosis. *Nucl Med Biol.* (2017) 50:17–24. doi: 10.1016/j.nucmedbio.2017.04.003
9. Yu WY, Lu PX, Assadi M, Huang XL, Skrahin A, Rosenthal A, et al. Updates on (18)F-FDG-PET/CT as a clinical tool for tuberculosis evaluation and therapeutic monitoring. *Quant Imaging Med Surg.* (2019) 9:1132–46. doi: 10.21037/qims.2019.05.24 (accessed June 15, 2020).
10. Guide Affection de Longue Durée: Tuberculose Active. *Recommandations de la Haute Autorité de Santé, France*. (2007). Available online at: http://www.has-sante.fr/portail/upload/docs/application/pdf/07-029_tuberculoseguide_edite_sans_lap.pdf (accessed June 15, 2020).
11. Société de Pneumologie de Langue Française: guidelines for the management of tuberculosis in France. *Rev Mal Respir*. (2004) 21:414–20. doi: 10.1016/S0761-8425(04)71306-6
12. Ankrah AO, van der Werf TS, de Vries EF, Dierckx RA, Sathekge MM, Glaudemans AW. PET/CT imaging of *Mycobacterium tuberculosis* infection. *Clin Transl Imaging.* (2016) 4:131–44. doi: 10.1007/s40336-016-0164-0
13. Bomanji J, Sharma R, Mittal BR, Gambhir S, Qureshy A, Begum SMF, et al. PET/CT features of extrapulmonary tuberculosis at first clinical presentation: a cross-sectional observational 18F-FDG imaging study across six countries. *Eur Respir J.* (2020) 55:1901959. doi: 10.1183/13993003.01959-2019
14. Martinez V, Castilla-Lievre MA, Guillet-Caruba C, Grenier G, Fior R, Desarnaud S, et al. (18)F-FDG PET/CT in tuberculosis: an early non-invasive marker of therapeutic response. *Int J Tuberc Lung Dis.* (2012) 16:1180–5. doi: 10.5588/ijtld.12.0010
15. Sathekge M, Maes A, D'Asseler Y, Vorster M, Gongxeka H, Van de Wiele C. Tuberculous lymphadenitis: FDG PET and CT findings in responsive and nonresponsive disease. *Eur J Nucl Med Mol Imaging.* (2012) 39:1184–90. doi: 10.1007/s00259-012-2115-y
16. Ordonez AA, Weinstein EA, Bambarger LE, Saini V, Chang YS, DeMarco VP, et al. A systematic approach for developing bacteria-specific imaging tracers. *J Nucl Med.* (2017) 58:144–50. doi: 10.2967/jnumed.116.181792

Conflict of Interest: The authors declare that the research was conducted in the absence of any commercial or financial relationships that could be construed as a potential conflict of interest.

Publisher's Note: All claims expressed in this article are solely those of the authors and do not necessarily represent those of their affiliated organizations, or those of the publisher, the editors and the reviewers. Any product that may be evaluated in this article, or claim that may be made by its manufacturer, is not guaranteed or endorsed by the publisher.

frontiers in Medicine

REVIEW
published: 27 August 2021
doi: 10.3389/fmed.2021.723748

Radiation Therapy Planning of Thoracic Tumors: A Review of Challenges Associated With Lung Toxicities and Potential Perspectives of Gallium-68 Lung PET/CT Imaging

François Lucia[1]*, *Martin Rehn*[1], *Frédérique Blanc-Béguin*[2] and *Pierre-Yves Le Roux*[2]

[1] Radiation Oncology Department, University Hospital, Brest, France, [2] Service de médecine nucléaire, CHRU de Brest, EA3878 (GETBO), Université de Brest, Brest, France

Despite the introduction of new radiotherapy techniques, such as intensity modulated radiation therapy or stereotactic body radiation therapy, radiation induced lung injury remains a significant treatment related adverse event of thoracic radiation therapy. Functional lung avoidance radiation therapy is an emerging concept in the treatment of lung disease to better preserve lung function and to reduce pulmonary toxicity. While conventional ventilation/perfusion (V/Q) lung scintigraphy is limited by a relatively low spatial and temporal resolution, the recent advent of ^{68}Gallium V/Q lung PET/CT imaging offers a potential to increase the accuracy of lung functional mapping and to better tailor lung radiation therapy plans to the individual's lung function. Lung PET/CT imaging may also improve our understanding of radiation induced lung injury compared to the current anatomical based dose–volume constraints. In this review, recent advances in radiation therapy for the management of primary and secondary lung tumors and in V/Q PET/CT imaging for the assessment of functional lung volumes are reviewed. The new opportunities and challenges arising from the integration of V/Q PET/CT imaging in radiation therapy planning are also discussed.

Keywords: radiation—adverse effects, PET perfusion map, radiation planning, lung cancer, stereotactic body radiation therapy, intensity modulated radiation therapy, volumetric modulated arc therapy

OPEN ACCESS

Edited by:
Martin Huellner,
University Hospital Zürich, Switzerland

Reviewed by:
Taiki Magome,
Komazawa University, Japan
Chunhui Han,
City of Hope National Medical Center, United States

***Correspondence:**
François Lucia
francois.lucia@gmail.com
orcid.org/0000-0001-7286-1350

Specialty section:
This article was submitted to Nuclear Medicine, a section of the journal Frontiers in Medicine

Received: *11 June 2021*
Accepted: *09 August 2021*
Published: *27 August 2021*

Citation:
Lucia F, Rehn M, Blanc-Béguin F and Le Roux P-Y (2021) Radiation Therapy Planning of Thoracic Tumors: A Review of Challenges Associated With Lung Toxicities and Potential Perspectives of Gallium-68 Lung PET/CT Imaging. Front. Med. 8:723748. doi: 10.3389/fmed.2021.723748

INTRODUCTION

Radiation therapy has an increasing role in the treatment of both primary and secondary lung cancer (1, 2). In recent years, there has been a technologic revolution in radiation therapy (RT) with the introduction of new techniques, like intensity modulated radiation therapy (IMRT), image guided radiation therapy (IGRT), and stereotactic body radiation therapy (SBRT), which have improved the conformation with the target volumes.

However, radiation induced lung injury (RILI) remains a significant treatment related adverse event of thoracic RT (3). Indeed, the incidence of grade $\geq$ 2 lung toxicities is about 15-20% (3). Accordingly, a current major challenge of thoracic RT is to better preserve lung function and to reduce pulmonary toxicity.

Radiotherapy for the management of pulmonary lesions is currently based on the so-called anatomical planning. Lung volumes are delineated on CT images, and dose constraints are applied

to these anatomical volumes, based on the simplistic assumption that the lungs are functionally homogeneous. However, it is well-established that the distribution of regional function into the lungs is non-uniform, especially in patients with lung cancer who frequently present with tobacco-related lung diseases and cancer treatment induced pulmonary disease.

Functional lung avoidance RT is an emerging concept in the treatment of lung disease.

The technique aim at personalizing RT treatment planning to individual's lung functional distribution, by prioritizing delivery of higher dose in non-functional pulmonary regions while sparing functional areas (4). In that purpose, establishing a functional map of the regional ventilation and perfusion in the lungs is required. Several groups have proposed to use conventional lung ventilation/perfusion scintigraphy and showed a potential interest of functional lung avoidance RT to reduce the dose to the functional lung (4). However, the low spatial and temporal resolution of conventional V/Q scintigraphy has limited accurate mapping of lung functional volumes and restrained its use in daily practice (5).

Ventilation/perfusion (V/Q) positron emission tomography/computed tomography (PET/CT) is a novel imaging modality for regional lung function assessment. As compared with conventional V/Q scan, V/Q PET/CT is inherently a vastly superior technology for image acquisition, with higher sensitivity, higher spatial and temporal resolution, superior quantitative capability, and a greater access to respiratory gated acquisition (5, 6). As a consequence, V/Q PET imaging offers an opportunity to improve the accuracy of lung functional mapping and its use for thoracic radiation therapy planning.

The advent of both advanced radiotherapy techniques and high resolution lung functional mapping is a real opportunity to personalize lung radiation therapy plans to an individual's own lung function and to minimize lung toxicity. Lung PET/CT imaging may also improve our understanding of radiation induced lung injury compared to the current anatomical based dose–volume constraints.

In this review, we will discuss recent developments in radiation therapy for the management of primary and secondary lung tumors, and in V/Q PET/CT imaging for the assessment of functional lung volumes. We will also review the new opportunities and challenges arising from the integration of V/Q PET/CT imaging in radiation therapy planning.

CURRENT ROLES OF THORACIC RADIATION THERAPY

NSCLC

Lung cancer is the leading cancer in terms of frequency and mortality, with more than 1.6 million deaths per year (7). The role of curative-intent RT is well-recognized in both early stage (8) and locally advanced (9) non-small cell lung cancer (NSCLC).

In recent years, there have been efforts to diagnose lung cancers at earlier and more curable stages using annual low-dose computed tomography (CT) for at-risk populations (10). In the United States, these screening efforts have resulted in up to 30% of lung cancer cases being diagnosed at an early stage, i.e., stage I or II (11). These early tumors are amenable to surgical treatment, with local control rates of up to 96% and overall survival (OS) rates of ∼50-60% at 3 years (12). Unfortunately, an important limitation to surgical treatment of these patients is that many have underlying pulmonary or cardiac comorbidities (13). In current practice, RT is the preferred alternative for these patients with early stage (preferably stage I disease with tumor size $\leq$ 3 cm) NSCLC who are unfit or refuse radical surgery (13).

Approximately 30% of NSCLC patients are diagnosed with locally advanced disease (stage III). This is a heterogeneous group that includes a large number of clinical presentations, often with a significant tumor burden (T3-T4 and N2-N3). Their management requires consultation within a multidisciplinary team. Radical chemoradiation, especially concurrent chemoradiation, and maintenance immune checkpoint-inhibitors (durvalumab) is the standard of care of unresectable stage III NSCLC (14, 15).

Metastasis

Historically, patients diagnosed with distant metastases secondary to solid tumors were considered incurable and the gold standard of treatment was systemic chemotherapy. Hellman and Weichselbaum suggested that a subset of patients with limited metastatic disease might benefit from aggressive local therapy (16, 17). These patients with a small number (five or fewer) of low volume metastatic lesions were classified as having oligometastatic disease. The management of oligometastatic disease has become a frequent question (18) because increasing evidence has shown that surgical resection or radiation therapy can lead to better outcomes (2). One of the main sites where radiotherapy is used in this setting is in the treatment of lung metastases. Stereotactic body radiation therapy (SBRT) is an excellent therapeutic modality, with control rates of >90% reported in prospective and retrospective series (19–21).

MODERN RADIATION THERAPY

3D-CRT

The 1980s saw the advent of three-dimensional conformal radiotherapy (3D-CRT) with the use of computed tomography (CT) for treatment planning and the replacement of Cerrobend blocking with multi-leaf collimators (MLC). These advances have allowed for the automation of radiation field formation and treatment planning that shapes the fields to the tumor volume. For the past decade, 3D-CRT has been the standard of care to treat unresectable local advanced lung cancer. In recent years there has been an increasing use of intensity-modulated radiation therapy (IMRT) (22). IMRT is a form of 3D-CRT where treatment planning system (TPS) determines non-uniform fluence to attain customized dose distribution, where dose is sculpted to target the tumor while sparing proximal organs at risk (OARs). IMRT is carried out by delivery of multiple beamlets of non-uniform fluence. The calculation of fluence is done by high performance computers using algorithms taking an iterative approach, called inverse planning. The inverse planning starts

with desired result and works backwards to achieve best possible beam shape and fluence pattern.

IMRT itself has taken many forms including step-and-shoot that delivers discrete intensity levels and sliding window IMRT that delivers continuous intensity levels. Recently, there has been a growing interest in the rotating gantry IMRT techniques, tomotherapy and volumetric-modulated arc therapy (VMAT), that deliver radiation with MLCs and gantry both in motion. This type of radiation therapy allows the patient to be treated with the full 360° beam angle as the radiation source rotates around the patient during the irradiation. A higher modulation of the beam fluence in the whole arc is obtained thanks to the continuous movement of the leaf and the rotating gantry. The different IMRT techniques are equivalent except for a reduction in treatment time with VMAT (23–25).

However, to ensure full exploitation of this technique, it is necessary to monitor changes in tumor and OAR volume and/or position during treatment with image-guided radiation therapy (IGRT), such as cone-beam CT (CBCT) (26). Indeed, IGRT allows ensuring adequate target coverage while improving treatment outcome (27–30).

Since a secondary analysis of RTOG 0617, a randomized phase III trial comparing 60-74 Gy with concurrent chemotherapy in the treatment of inoperable stage III NSCLC in 544 patients, IMRT has become the gold standard technique (31). Indeed, IMRT was associated with similar survival and tumor control outcomes with a significant decrease in grade $\geq$ 3 radiation-induced lung fibrosis (RILF) compared with RTC3D (3.5% vs. 7.9) despite larger tumors and higher V5s (lung volume receiving 5 Gy or more) but similar V20s and mean lung doses (MLD) (31).

SBRT

In the mid-1990s, stereotactic "body" radiotherapy (SBRT), also called stereotactic ablative radiotherapy (SABR), was first introduced by researchers at the Karolinska Institute in Stockholm by applying the principles of cranial stereotactic radiosurgery to extracranial tumor sites, particularly to the lung (32). Then, this technique was developed by several centers in the world (33–35). SBRT consists of delivering very high doses per fraction in a small number of sessions (usually between 3 and 8 fractions over 1-2 weeks) corresponding to a so-called hypofractionated scheme. Thus, radiation oncologists can perform an even more precise and tumor conformal radiation therapy with a rapid dose falloff in the lung parenchyma and adjacent structures leading to a higher biological effective dose (aiming at a BED10 of at least 100 Gy) directed to the tumors and to a more important destruction of the tumor cells (36–38).

A randomized trial comparing SBRT (54 Gy in 3 fractions or 48 Gy in 4 fractions) with conventional (66 Gy in 33 fractions) or moderate hypofractionation (50 Gy in 20 fractions) was conducted by the Trans-Tasmanian Radiation Oncology Group (TROG), known as the CHISEL trial. A total of 101 participants were included (2:1 with $n = 66$ SBRT and $n = 35$ conventional). Results showed superior local control (hazard ratio = 0.32, 95% CI 0.13-0.77, $p = 0.0077$) of the primary disease without an increase in major toxicity (3).

Multiple randomized controlled trials have sought to compare SBRT with surgery (lobar or sublobar resection) for stage I NSCLC, either in an unselected population or in a high-risk population (39–41). Unfortunately, all trials were stopped prematurely due to low inclusion rates, despite multiple adjustments of inclusion criteria to increase patient recruitment. However, a survival analysis including two phase III trials (STARS and ROSEL) by Chang et al. (39) demonstrated similar 3-year recurrence-free survival with SBRT or resection (86 and 80%, respectively, $p = 0.54$). OS was in favor of SBRT [95 vs. 79%, hazard ratio = 0.14, 95% confidence interval (CI) 0.017-1.190, $p = 0.037$]. However, these results should be interpreted with great caution because of the presence of numerous biases, including small patient numbers, unbalance cohorts in these two studies, the risk of type I inference error, and the relatively short follow-up. Based on these data, many international scientific societies and networks now consider SBRT as the best treatment strategy for medically inoperable patients with stage I NSCLC (40, 41).

In light of these results with lung SBRT in NSCLC, studies concerning the possible benefit of SBRT in patients with oligometastatic disease in the lung have been initiated (42–45). Recently, results of ongoing trials using SBRT in oligometastatic disease have been presented. They report improved overall survival and progression-free survival compared to standard therapy, confirming the benefit of local ablative therapy in limited systemic disease (46, 47). Thus, it is very likely that the treatment strategy and prognosis of these patients will change significantly. Indeed, more of them will be future candidates eligible for SBRT for lung metastases before and after multiple lines of immunotherapy and/or targeted agents.

RADIATION INDUCED LUNG TOXICITIES

Radiation exposure of the lungs is common during a course of therapeutic radiation for thoracic malignancies. Radiation-induced lung injury (RILI) encompasses radiation-induced pneumonitis (RIP), inflammation of the lung which may manifest as a dose-limiting acute or subacute toxicity, and radiation-induced lung fibrosis (RILF), a late effect of lung exposure to radiation. The diagnosis of RIP and RILF is based on clinical presentation and may be supported by associated imaging findings. Various grading scales are used (**Tables 1**, **2**).

Despite the introduction of new radiotherapy techniques, RILI remains a significant treatment related morbidity of thoracic radiation therapy (3).

The occurrence of grade $\geq$ 2 RIP in the treatment of lung cancer has gradually decreased from 30–35% with 3D-radiotherapy (48) to 29–32% with IMRT (48). Grade $\geq$ 3 RIP was seen in about 10-15% with IMRT (49). Grade $\geq$ 2 and grade $\geq$3 RILF were seen in about 29 and 15% of patients with IMRT, respectively (50, 51).

Although quality of life after SBRT represents an important issue in assessing the effective impact of this radiation modality on patient management, it has been evaluated in few studies. Indeed, the majority of patients receiving SBRT have poor lung function at the time of diagnosis making them unfit for surgery,

TABLE 1 | Overview about grading scales for radiation-induced pneumonitis.

Grading scale	Grade 1	Grade 2	Grade 3	Grade 4	Grade 5
CTCAE v5.0	Asymptomatic; clinical or diagnostic observations only; intervention not indicated	Symptomatic; medical intervention indicated; limiting instrumental ADL	Severe symptoms; limiting self-care ADL; oxygen indicated	Life-threatening respiratory compromise; urgent intervention indicated (e.g., tracheotomy or intubation)	Death
RTOG	Asymptomatic or mild symptoms (dry cough); slight radiographic appearances	Moderate symptomatic pneumonitis (severe cough); low grade fever; patchy radiographic appearances	Severe symptomatic pneumonitis; dense radiographic changes	Severe respiratory insufficiency/Continuous O2/Assisted ventilation	Death
LENT-SOMA (EORTC)	Asymptomatic or mild symptoms; slight imaging changes	Moderate symptoms; moderate imaging changes	Severe symptoms; increased density imaging changes	Severe symptoms requiring continuous O2 or assisted ventilation	Death

CTCAE v5.0, Common terminology criteria for adverse events, version 5.0; RTOG, Radiation Therapy Oncology Group; EORTC, European Organization for Research and Treatment of Cancer; LENT-SOMA, Late effects in normal tissue-subjective objective management analysis.

TABLE 2 | Overview about grading scales for radiation-induced lung fibrosis.

Grading scale	Grade 1	Grade 2	Grade 3	Grade 4	Grade 5
CTCAE v5.0	Radiologic pulmonary fibrosis < 25% of lung volume associated with hypoxia	Evidence of pulmonary hypertension; radiographic pulmonary fibrosis 25–50% associated with hypoxia	Severe hypoxia; evidence of right-sided heart failure; radiographic pulmonary fibrosis > 50–75%	Life-threatening consequences (e.g., hemodynamic/pulmonary complications); intubation with ventilatory support indicated; radiographic pulmonary fibrosis > 75% with severe honeycombing	Death
RTOG	Asymptomatic or mild symptoms (dry cough); slight radiographic appearances	Moderate symptomatic fibrosis (severe cough); low grade fever; patchy radiographic appearances	Severe symptomatic fibrosis; dense radiographic changes	Severe respiratory insufficiency/ Continuous O2/ Assisted ventilation	Death
LENT-SOMA (EORTC)	Asymptomatic or mild symptoms; radiological abnormalities; 10–25% reduction of respiration volume and/or diffusion capacity	Moderate symptoms; patchy dense abnormalities in imaging; > 25–50% reduction of respiration volume and/or diffusion capacity	Severe symptoms; dense confluent radiographic changes limited to irradation field; > 50–75% reduction of respiration volume and/or diffusion capacity	Severe symptoms requiring continuous O2 or assisted ventilation; dense fibrosis, severe scarring and major retraction of normal lung; > 75% reduction of respiration volume and/or diffusion capacity	Death

CTCAE v5.0, Common terminology criteria for adverse events, version 5.0; RTOG, Radiation Therapy Oncology Group; EORTC, European Organization for Research and Treatment of Cancer; LENT-SOMA, Late effects in normal tissue-subjective objective management analysis.

so it is crucial to know the effect of SBRT on lung function. The occurrence of RIP grade $\geq$ 2 and grade $\geq$ 3 are about 17-20% and 6-7%, respectively. The incidences of grade $\geq$ 2 and grade $\geq$ 3 RILF are about 15-20% and 5-6% with SBRT, respectively (3).

Thus, the thorax remains a challenging anatomical site for RT delivery, especially for patients with lung comorbidities, and the reduction of pulmonary side effects (and spare lung function) while achieving reasonable local control and sustaining its curative potential is an ongoing challenge faced by radiation oncologists and interdisciplinary treatment teams (3).

CONVENTIONAL (ANATOMICALLY BASED) PLANNING

Currently, radiotherapy planning is anatomical for the treatment of lung tumors. Indeed, only CT images are used to define the lung volumes to which dose constraints are applied. To minimize toxicity to the OARs, in particular to the "healthy lung," treatment planning system (TPS) are used to optimize the beam arrangements in order to respect the planning constraints. TPS allows to evaluate the dose delivered to each voxel in a volume of interest. Among the multiple plan options provided by TPS, the plan with the best therapeutic ratio (maximum tumor control with the least possible complications for normal tissues) is chosen. The dose-volume histogram (DVH) is used as a tool for comparison between plans.

In IMRT, the most important modifiable risk factors for RILF are the radiation dose and anatomical volume of lung irradiated, with lung V20 (volume of lung receiving 20 Gy or more) and mean lung dose (MLD) being validated in early studies. Consistency in lung volumes is important for reporting purposes, with the preferred method being total lung volume minus Gross Tumor Volume (GTV). In one of the most comprehensive analyses, a multi-institutional individual patient data meta-analysis investigated dosimetric predictors for RILF

in patients treated with concurrent chemoradiation. This study reported symptomatic RILF in 30% of treated patients, with fatal RILF reported in 2% (52). The most important predictors for RILF included V20, older age, and carboplatin/paclitaxel chemotherapy. V20 as a continuous variable was also validated in a subgroup analysis of RTOG 0617 (31). In this analysis, treatment with IMRT was associated with a significantly lower risk of RILF despite having a higher V5, which had been associated with RILF in prior studies. Thus, the goal for radiation treatment planning is to achieve the lowest V20 and MLD possible, while V5 does not appear to be a critical variable. Commonly cited metrics include a V20 <35% and MLD <20 Gy, but lower doses are often achievable with modern treatment planning strategies. Patients with interstitial lung disease (ILD) should be treated with caution, as higher rates of symptomatic and fatal pneumonitis have been reported in this patient population (53).

In SBRT, there is few data about dose-effect relationship between lung anatomical volumes irradiated and the risk or the grade of toxicities. Saha et al. found that lower lobe tumor location, larger tumor size, PTV, mean lung dose, V20, and V12.5 were significant predictors of symptomatic RILF (54). Tumor size has been found to predict toxicity in previous studies (55–57). The only clinical factor associated with symptomatic RIP found was subclinical interstitial lung disease (45 vs. 1.6%) in the study of Okubo et al. (58). A recent review of 97 studies evaluated clinical and dosimetric predictors of RILI. Unfortunately, no threshold level of "tolerance dose volume" was found. However, the results seemed to show that the risk of symptomatic RILI was relatively low (<10-15%) with an MLD of 8 Gy and a V20 of 10-15% (59).

FUNCTIONAL LUNG AVOIDANCE PLANNING

Current conventional anatomically-based planning simplistically assumes that the lungs are functionally homogeneous. However, it is well-known that the regional distribution of pulmonary function is heterogeneous, especially in patients with lung cancer, who frequently present with tobacco-related lung diseases such as chronic obstructive pulmonary disease (COPD) or emphysema, and treatment induced pulmonary disease from surgery, radiotherapy, or systemic therapies. In order to decrease pulmonary toxicities and preserve lung function, it has been proposed to personalize radiation therapy treatment planning to individual's lung functional distribution, i.e., to limit as far as possible the dose to the functional lung to the detriment of regions with already impaired lung function (4). Recent advances in radiotherapy techniques, with the use of inverse planning and TPS optimization algorithms, has made possible to add a constraint on a "functional lung" volume.

For that purpose, establishing a functional map of the regional function in the lungs is required. In that respect, the principle underlying Ventilation/Perfusion (V/Q) scintigraphy is very attractive. Indeed, lung scintigraphy allows to assess the regional distribution of ventilation and perfusion in the lungs. Ventilation is imaged after inhalation of inert gases or radiolabeled aerosols that reach terminal bronchioles and alveoli in proportion to regional distribution of ventilation. Perfusion is imaged after intravenous administration of macro-aggregated albumin (MAA) particles, which are trapped in the lung capillaries according to the regional blood flow.

Several studies showed that lung scintigraphy may provide additional information to assist in identifying patients at greater risk of radiation pneumonitis (60–62). Furthermore, studies have demonstrated the potential for lung SPECT imaging to be integrated into treatment planning to improve functional dose metrics (4). Several studies reported a reduction of mean functional volumes and mean lung dose when plans were optimized to spare functional lung (4). However, functional lung avoidance planning using SPECT imaging has not yet been adopted in daily clinical practice. Indeed, no clinical benefit has been clearly established so far (4). Furthermore, there are a wide variety of thresholds used for lung functional volumes delineation. This may be explained by the low spatial and temporal resolution of conventional V/Q scintigraphy, which prevents an accurate and reproducible mapping of lung functional volumes.

V/Q PET/CT IMAGING: A NEW IMAGING TOOL FOR FUNCTIONAL LUNG AVOIDANCE PLANNING

V/Q PET/CT is a novel imaging modality for regional lung function assessment. The same carrier molecules as conventional V/Q scintigraphy are used, but they are labeled with ^{68}Gallium, a ß+ isotope, instead of ^{99m}Tc, allowing acquisition of images with PET technology (5, 63, 64). Similar physiological processes are therefore imaged using conventional V/Q scan or V/Q PET/CT, but PET is a vastly superior technology for image acquisition, with higher sensitivity, higher spatial and temporal resolution, superior quantitative capability, and a greater access to respiratory gated acquisition (5, 65). The test has already shown promising results in a variety of pulmonary conditions, such as pulmonary embolism diagnosis (63, 66) or pre-surgical assessment of lung cancer patients (67). Similarly, V/Q PET imaging offers an opportunity to improve the accuracy and utility of lung functional mapping for thoracic radiotherapy.

Besides improving the accuracy of lung functional volume delineation, pulmonary PET/CT imaging is also appealing for several reasons (5, 68). The acquisition time is much lower (5 min) than with conventional V/Q scan. V/Q PET imaging is a simple and non-invasive test, with no contraindication or side-effects, especially related to the injection of contrast media (allergy, renal dysfunction). No special procedure such as fasting or diet is required. The effective radiation dose of the scan is low, similar to the dose of conventional V/Q scan (∼2-3 mSv for the PET acquisition), PET and CT respiratory-gated acquisition can be readily performed, which may further improve the accuracy of lung functional volumes delineation and improve the co-registration with the CT used for radiotherapy planning. In nuclear medicine facilities that routinely perform

V/Q scans with Technegas, and equipped with a ^{68}Ga generator, performing V/Q PET/CT does not require additional resources. ^{68}Ga is an extremely convenient radiotracer for clinical use. ^{68}Ga generators are increasingly available in nuclear medicine facilities owing to growing use for prostate cancer and neuroendocrine tumor imaging.

Le Roux et al. studied, in 30 lung cancer patients, the correlation between ^{68}Ga V/Q PET/CT functional volumes and pulmonary function tests (PFTs) indices (69). The results showed that a percentage of lung volume with normal ventilation and perfusion >90% correctly identified impaired lung function in 93% of patients. A high degree of correlation between all functional lung volumes on V/Q PET/CT imaging and lung function as assessed by PFTs was also demonstrated. These results support the possible use of ^{68}Ga V/Q PET/CT to predict potential consequences and side effects of treatments that may alter regional function, such as RT.

Although V/Q PET/CT is a very attractive test tool for functional lung avoidance planning, only few studies has been published on the topic so far. A first study simulated a 4D PET/CT perfusion-based radiotherapy plan in a cohort of NSCLC patients (70). These patients were planned to receive curative 3D-CRT at a dose of 60 Gy in 30 fractions. In this study, the definition of "perfused" or "well-perfused" lung on ^{68}Ga-MAA PET/CT was based on an automated contour encompassing any ^{68}Ga-MAA uptake or a maximum standardized uptake value (SUVmax) cutoff of 30%, respectively. To exclude any areas of clumping or other artifacts, automated contours were manually corrected. This PET/CT-guided planning improved the functional parameters V30, V40, V50, and V60 (all p-values < 0.05), and the mean functional dose to the lung was improved by a median value of 0.86 Gy ($p < 0.01$) for well-perfused lungs.

The same team evaluated the value of ventilation in addition to perfusion for functional lung volume sparing in IMRT. Perfusion-guided IMRT planning alone was able to decrease the functional lung dose while maintaining a consistent plan quality (71).

In the same population, changes in perfusion, ventilation, and CT lung density were assessed (72). The authors used deformable registration to register the functional images with RT planning (73). Then, they averaged the isodose volumes in 10 Gy bins intervals. Finally, the relative SUV loss was analyzed for ventilation and perfusion for each dose bin. They showed an almost perfectly linear negative dose-response relationship for perfusion ($r2 = 0.99$, $P < 0.01$) with a strongly negative correlation for ventilation ($r2 = 0.95$, $P < 0.01$). In some patients, peritumoral reperfusion/reventilation occurred. These results suggest that the effects of postradiotherapy may be closely correlated with impairments in perfusion, more so than ventilation. Thus, it would be necessary to preserve primarily the function of perfused lungs. In ^{68}Ga V/Q PET/CT planning optimization, the aim would be to increase the weight of the radiation beams through the non-perfused lung regions and avoid the perfused lung regions without compromising the plan in terms of satisfying the established criteria for tumor coverage and preservation of other normal tissue (e.g., **Figure 1**).

PERSPECTIVE AND FUTURE CHALLENGES

For several years, radiotherapy in lung cancer has seen major technological advances, with the advent of motion management control (4D-CT, respiratory gating), image guidance, intensity modulated volumetric techniques or SBRT, which have led to an improvement in efficacy and tolerance. Nevertheless, further improvements in radiation therapy planning to spare lung function would be of interest for several reasons.

First, most of patients referred for thoracic radiation therapy have poor pulmonary function or have been heavily pretreated. Limiting the risk of high grade/fatal radiation pneumonitis remains therefore a major challenge. Second, multiple subsequent treatments are likely to be necessary for both primary NSCLC (second tumors) and lung metastases (oligo-progression). In these patients, toxicity should be kept as low as possible from the first treatment to preserve the possibility of re-irradiation, especially in SBRT. Third, patients with larger tumors or tumors close to critical structures would probably benefit the most from high-precision SBRT (74, 75), given the absence of other options and the higher risk of toxicity with current technology.

Moreover, V/Q PET/CT could be useful to better assess the relationship between radiation dose and lung toxicity. Indeed, in previous studies, the normal lung volume definitions for dose-volume histogram calculation are highly variable (76, 77). Usually, lung volume was defined as the bilateral lung excluding the planning target volume (Lung-PTV) (78–80) or excluding the gross tumor volume (Lung-GTV) (81–83). However, in RTOG 0617, lung volume was defined as the bilateral lung volume excluding the CTV (Lung-CTV). Currently, both RTOG and ESTRO-ACROP guidelines recommend using Lung-GTV delineation instead of Lung-PTV to standardize lung volume definition among different institutions (84, 85). However, there is only limited clinical evidence on which normal lung definition is better for symptomatic RILF prediction. The definition of a functional lung volume may be of interest to better predict toxicity.

Before implementation of functional lung avoidance planning using lung PET/CT imaging, a number of issues need to be resolved. Firstly, the definition of functional lung volumes was not consistent throughout publications. There is no consensus on the definition of the optimal functional region of the lung. The majority of current planning systems require the definition of a functional threshold, but continuum-based planning is possible (14, 32). Another possibility could be to define multiple levels of functional lung regions that do not overlap, with the most important dosimetric goals assigned to the most functional regions. Secondly, the dose constraints to the functional lung must be clarified. In the two studies that evaluated PET-guided functional lung avoidance planning, the functional lung dose constraints used were the same as those for anatomy-based planning. Most importantly, there is currently no publication that demonstrated the clinical benefit of functional lung imaging over anatomical lung imaging for radiotherapy planning. Indeed, no randomized interventional

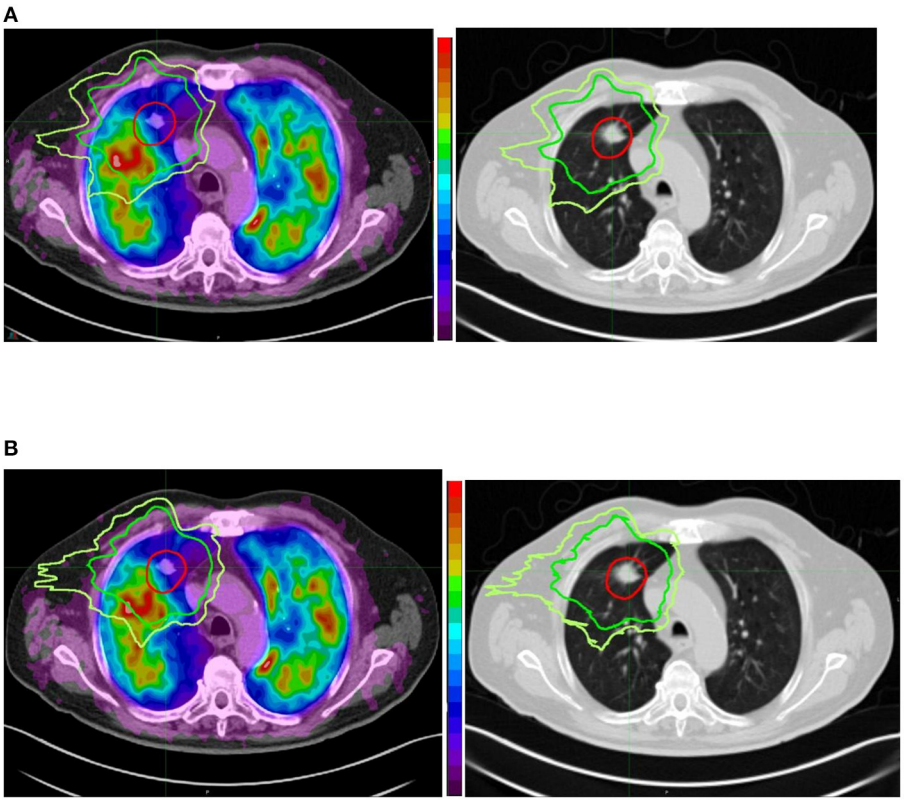

FIGURE 1 | Comparison between conventional (anatomically based) planning **(A)** and functional lung avoidance planning guided by ^{68}Ga Q PET/CT **(B)** in a patient treated for a lung tumor by stereotactic body radiation therapy. Both planning show optimal coverage (red isodose line) of the tumor but the functional planning shows a decrease of the dose (20 Gy isodose in green and 16 Gy isodose in yellow) to the functional lung (in red the most functional areas and in blue the least functional areas). We can also see that on the corresponding anatomical images we cannot see any difference between the functional and non-functional areas.

study has evaluated this question. Thus, it is necessary to test this hypothesis in a phase 3 randomized trial with appropriate statistical power to demonstrate a possible decrease in RILI using functional lung imaging.

Finally, there are currently different options for lung ventilation and perfusion imaging (SPECT, MR, ventilation CT and PET/CT) for the implementation of image-guided functional planning.

The availability and cost of the gas, the expertise required for gas imaging, including access to specialized equipment, and the need for image registration to the planning CT have been perceived as limitations to the clinical implementation of MR hyperpolarized gas imaging techniques in radiotherapy (86–88).

4D CT based methods have also shown promising results to estimate regional ventilation lung function (89, 90). However, high quality CT imaging is a key requirement given the potential for artifacts (90, 91). Furthermore, data in the literature seem to favor the use of perfusion data rather than ventilation for functional optimization of dose delivery to the lung. Indeed, perfusion defects are more frequent than ventilation defects, and both are more frequent than CT changes (92).

Thus, ^{68}Ga Q PET/CT seems to be the imaging technique that can provide interesting functional data to guide radiotherapy with a fast and cost-effective imaging.

Two ongoing prospective trials should provide important data to support the initiation of such large scale randomized controlled trials.

Bucknell et al. are investigating a prospective dose escalation study with PET-guided radiotherapy planning that aims to show the value of PET-guided radiotherapy for IMRT stage III NSCLC (93). The HI-FIVE trial is a single arm interventional trial integrating ^{68}Ga V/Q PET/CT respiratory-gated (four-dimensional) into radiation treatment planning to identify highly functioning lung volumes and avoidance of these using VMAT planning (NCT03569072). The aim is to evaluate the possibility for moderate dose escalation to the primary tumor only, while respecting conventional normal tissue toxicity constraints. For each patient, his radiation plan will be tailored to the location of his tumor and his lung functional mapping. Feasibility of this study is defined as meeting all dosimetric criteria for $\geq$15 of 20 patients. Thus, the purpose of this study is to provide valuable information on the feasibility of a larger-scale randomized trial and not to show a possible reduction in pulmonary toxicity or improvement in tumor control.

Our group has recently launched the PEGASUS trial, a single arm monocenter study in patients treated with SBRT for primary or secondary lung lesions (NCT04942275). Initially, patients will receive standard, "anatomical" planning, blinded to the results of

the ^{68}Ga Q PET/CT. In a second phase, patients will benefit from functional planning guided by ^{68}Ga Q PET/CT. Each patient will be his own control. The doses to the functional lung will be calculated and compared for the two treatment planning. The primary aim is to estimate the percentage of patients for whom the dose to the functional lung can be reduced while respecting the standard constraints. Patients will have a clinical follow-up at 1 month and then every 3 months for 1 year. They will also undergo PFTs and repeated ^{68}Ga Q PET/CT at 3 months and 1 year to assess the impact of SBRT on global and regional lung function.

CONCLUSION

Technological advances in radiation modalities have revolutionized the treatment of primary and secondary lung tumors. The advent of lung PET/CT imaging opens new perspectives for functional lung avoidance planning, in order to improve the therapeutic index, the technique may allow to decrease the dose to the functional lung and to reduce pulmonary toxicity, which may increase the possibility of dose escalation and re-irradiation. Results from ongoing clinical trials should help to guide future research and further push the boundaries of radiation therapy for years to come.

AUTHOR CONTRIBUTIONS

FL and MR: clinical experiment in lung cancer and radiation therapy and manuscript writing/editing. FB-B and P-YL: clinical experiment in PET/CT and manuscript writing/editing. All authors contributed to the article and approved the submitted version.

REFERENCES

1. Chansky K, Detterbeck FC, Nicholson AG, Rusch VW, Vallieres E, Groome P, et al. The IASLC lung cancer staging project: external validation of the revision of the TNM stage groupings in the eighth edition of the TNM classification of lung cancer. *J Thorac Oncol.* (2017) 12:1109–21. doi: 10.1016/j.jtho.2017.04.011
2. Timmerman RD, Bizekis CS, Pass HI, Fong Y, Dupuy DE, Dawson LA, et al. Local surgical, ablative, and radiation treatment of metastases. *CA Cancer J Clin.* (2009) 59:145–70. doi: 10.3322/caac.20013
3. Ball D, Mai GT, Vinod S, Babington S, Ruben J, Kron T, et al. Stereotactic ablative radiotherapy versus standard radiotherapy in stage 1 non-small-cell lung cancer (TROG 09.02 CHISEL): a phase 3, open-label, randomised controlled trial. *Lancet Oncol.* (2019) 20:494–503. doi: 10.1016/S1470-2045(18)30896-9
4. Bucknell NW, Hardcastle N, Bressel M, Hofman MS, Kron T, Ball D, et al. Functional lung imaging in radiation therapy for lung cancer: a systematic review and meta-analysis. *Radiother Oncol.* (2018) 129:196–208. doi: 10.1016/j.radonc.2018.07.014
5. Le Roux PY, Hicks RJ, Siva S, Hofman MS. PET/CT lung ventilation and perfusion scanning using Galligas and Gallium-68-MAA. *Semin Nucl Med.* (2019) 49:71–81. doi: 10.1053/j.semnuclmed.2018.10.013
6. Le Roux PY, Robin P, Salaun PY. New developments and future challenges of nuclear medicine and molecular imaging for pulmonary embolism. *Thromb Res.* (2018) 163:236–41. doi: 10.1016/j.thromres.2017.06.031
7. Bray F, Ferlay J, Soerjomataram I, Siegel RL, Torre LA, Jemal A. Global cancer statistics 2018: GLOBOCAN estimates of incidence and mortality worldwide for 36 cancers in 185 countries. *CA Cancer J Clin.* (2018) 68:394–424. doi: 10.3322/caac.21492
8. Postmus PE, Kerr KM, Oudkerk M, Senan S, Waller DA, Vansteenkiste J, et al. Early and locally advanced non-small-cell lung cancer (NSCLC): ESMO Clinical Practice Guidelines for diagnosis, treatment and follow-up. *Ann Oncol.* (2017) 28(suppl_4):iv1–iv21. doi: 10.1093/annonc/mdx222
9. Eberhardt WE, De Ruysscher D, Weder W, Le Pechoux C, De Leyn P, Hoffmann H, et al. 2nd ESMO Consensus Conference in Lung Cancer: locally advanced stage III non-small-cell lung cancer. *Ann Oncol.* (2015) 26:1573–88. doi: 10.1093/annonc/mdv187
10. Moyer VA, Force USPST. Screening for lung cancer: U.S. Preventive Services Task Force recommendation statement. *Ann Inter Med.* (2014) 160:330–8. doi: 10.7326/M13-2771
11. Marshall HM, Bowman RV, Yang IA, Fong KM, Berg CD. Screening for lung cancer with low-dose computed tomography: a review of current status. *J Thorac Dis.* (2013) 5(Suppl 5):S524–39. doi: 10.3978/j.issn.2072-1439.2013.09.06
12. Crabtree TD, Denlinger CE, Meyers BF, El Naqa I, Zoole J, Krupnick AS, et al. Stereotactic body radiation therapy versus surgical resection for stage I non-small cell lung cancer. *J Thorac Cardiovasc Surg.* (2010) 140:377–86. doi: 10.1016/j.jtcvs.2009.12.054
13. Altorki NK. Stereotactic body radiation therapy versus wedge resection for medically inoperable stage I lung cancer: tailored therapy or one size fits all? *J Clin Oncol.* (2010) 28:905–7. doi: 10.1200/JCO.2009.26.5157
14. Auperin A, Le Pechoux C, Rolland E, Curran WJ, Furuse K, Fournel P, et al. Meta-analysis of concomitant versus sequential radiochemotherapy in locally advanced non-small-cell lung cancer. *J Clin Oncol.* (2010) 28:2181–90. doi: 10.1200/JCO.2009.26.2543
15. Bezjak A, Temin S, Franklin G, Giaccone G, Govindan R, Johnson ML, et al. Definitive and adjuvant radiotherapy in locally advanced non-small-cell lung cancer: American Society of Clinical Oncology Clinical Practice Guideline Endorsement of the American Society for Radiation Oncology Evidence-Based Clinical Practice Guideline. *J Clin Oncol.* (2015) 33:2100–5. doi: 10.1200/JCO.2014.59.2360
16. Weichselbaum RR, Hellman S. Oligometastases revisited. *Nat Rev Clin Oncol.* (2011) 8:378–82. doi: 10.1038/nrclinonc.2011.44
17. Hellman S, Weichselbaum RR. Oligometastases. *J Clin Oncol.* (1995) 13:8–10. doi: 10.1200/JCO.1995.13.1.8
18. Ahmed KA, Torres-Roca JF. Stereotactic body radiotherapy in the management of oligometastatic disease. *Cancer Control.* (2016) 23:21–9. doi: 10.1177/107327481602300105
19. Milano MT, Katz AW, Zhang H, Okunieff P. Oligometastases treated with stereotactic body radiotherapy: long-term follow-up of prospective study. *Int J Radiat Oncol Biol Phys.* (2012) 83:878–86. doi: 10.1016/j.ijrobp.2011.08.036
20. Salama JK, Hasselle MD, Chmura SJ, Malik R, Mehta N, Yenice KM, et al. Stereotactic body radiotherapy for multisite extracranial oligometastases: final report of a dose escalation trial in patients with 1 to 5 sites of metastatic disease. *Cancer.* (2012) 118:2962–70. doi: 10.1002/cncr.26611
21. Binkley MS, Trakul N, Jacobs LR, von Eyben R, Le QT, Maxim PG, et al. Colorectal histology is associated with an increased risk of local failure in lung metastases treated with stereotactic ablative radiation therapy. *Int J Radiat Oncol Biol Phys.* (2015) 92:1044–52. doi: 10.1016/j.ijrobp.2015.04.004
22. Harris JP, Murphy JD, Hanlon AL, Le QT, Loo BW, Jr., Diehn M. A population-based comparative effectiveness study of radiation therapy techniques in stage III non-small cell lung cancer. *Int J Radiat Oncol Biol Phys.* (2014) 88:872-84. doi: 10.1016/j.ijrobp.2013.12.010
23. Chan C, Lang S, Rowbottom C, Guckenberger M, Faivre-Finn C, Committee IART. Intensity-modulated radiotherapy for lung cancer: current status and future developments. *J Thorac Oncol.* (2014) 9:1598–608. doi: 10.1097/JTO.0000000000000346
24. Jiang X, Li T, Liu Y, Zhou L, Xu Y, Zhou X, et al. Planning analysis for locally advanced lung cancer: dosimetric and efficiency comparisons between intensity-modulated radiotherapy (IMRT), single-arc/partial-arc volumetric modulated arc therapy (SA/PA-VMAT). *Radiat Oncol.* (2011) 6:140. doi: 10.1186/1748-717X-6-140

25. Yom SS, Liao Z, Liu HH, Tucker SL, Hu CS, Wei X, et al. Initial evaluation of treatment-related pneumonitis in advanced-stage non-small-cell lung cancer patients treated with concurrent chemotherapy and intensity-modulated radiotherapy. *Int J Radiat Oncol Biol Phys.* (2007) 68:94–102. doi: 10.1016/j.ijrobp.2006.12.031
26. Korreman S, Rasch C, McNair H, Verellen D, Oelfke U, Maingon P, et al. The European Society of Therapeutic Radiology and Oncology-European Institute of Radiotherapy (ESTRO-EIR) report on 3D CT-based in-room image guidance systems: a practical and technical review and guide. *Radiother Oncol.* (2010) 94:129–44. doi: 10.1016/j.radonc.2010.01.004
27. Kwint M, Conijn S, Schaake E, Knegjens J, Rossi M, Remeijer P, et al. Intra thoracic anatomical changes in lung cancer patients during the course of radiotherapy. *Radiother Oncol.* (2014) 113:392–7. doi: 10.1016/j.radonc.2014.10.009
28. Knap MM, Hoffmann L, Nordsmark M, Vestergaard A. Daily cone-beam computed tomography used to determine tumour shrinkage and localisation in lung cancer patients. *Act Oncol.* (2010) 49:1077–84. doi: 10.3109/0284186X.2010.498434
29. Persoon LC, Egelmeer AG, Ollers MC, Nijsten SM, Troost EG, Verhaegen F. First clinical results of adaptive radiotherapy based on 3D portal dosimetry for lung cancer patients with atelectasis treated with volumetric-modulated arc therapy (VMAT). *Act Oncol.* (2013)52:1484–9. doi: 10.3109/0284186X.2013.813642
30. Kilburn JM, Soike MH, Lucas JT, Ayala-Peacock D, Blackstock W, Isom S, et al. Image guided radiation therapy may result in improved local control in locally advanced lung cancer patients. *Pract Radiat Oncol.* (2016) 6:e73–80. doi: 10.1016/j.prro.2015.10.004
31. Chun SG, Hu C, Choy H, Komaki RU, Timmerman RD, Schild SE, et al. Impact of intensity-modulated radiation therapy technique for locally advanced non-small-cell lung cancer: a secondary analysis of the NRG oncology RTOG 0617 randomized clinical trial. *J Clin Oncol.* (2017) 35:56–62. doi: 10.1200/JCO.2016.69.1378
32. Blomgren H, Lax I, Naslund I, Svanstrom R. Stereotactic high dose fraction radiation therapy of extracranial tumors using an accelerator. Clinical experience of the first thirty-one patients. *Acta Oncol.* (1995) 34:861–70. doi: 10.3109/02841869509127197
33. Uematsu M, Shioda A, Tahara K, Fukui T, Yamamoto F, Tsumatori G, et al. Focal, high dose, and fractionated modified stereotactic radiation therapy for lung carcinoma patients: a preliminary experience. *Cancer.* (1998) 82:1062–70.
34. Wulf J, Hadinger U, Oppitz U, Olshausen B, Flentje M. Stereotactic radiotherapy of extracranial targets: CT-simulation and accuracy of treatment in the stereotactic body frame. *Radiother Oncol.* (2000) 57:225–36. doi: 10.1016/S0167-8140(00)00226-7
35. Timmerman R, Papiez L, McGarry R, Likes L, DesRosiers C, Frost S, et al. Extracranial stereotactic radioablation: results of a phase I study in medically inoperable stage I non-small cell lung cancer. *Chest.* (2003) 124:1946–55. doi: 10.1016/S0360-3016(03)01131-3
36. Videtic GM, Stephans KL. The role of stereotactic body radiotherapy in the management of non-small cell lung cancer: an emerging standard for the medically inoperable patient? *Curr Oncol Rep.* (2010) 12:235–41. doi: 10.1007/s11912-010-0108-1
37. Chua KLM, Sin I, Fong KW, Chua MLK, Onishi H. Stereotactic body radiotherapy for early stage lung cancer-historical developments and future strategies. *Chin Clin Oncol.* (2017) 6(Suppl 2):S20. doi: 10.21037/cco.2017.08.02
38. Nagata Y, Kimura T. Stereotactic body radiotherapy (SBRT) for Stage I lung cancer. *Jpn J Clin Oncol.* (2018) 48:405–9. doi: 10.1093/jjco/hyy034
39. Chang JY, Senan S, Paul MA, Mehran RJ, Louie AV, Balter P, et al. Stereotactic ablative radiotherapy versus lobectomy for operable stage I non-small-cell lung cancer: a pooled analysis of two randomised trials. *Lancet Oncol.* (2015) 16:630–7. doi: 10.1016/S1470-2045(15)70168-3
40. Ettinger DS, Wood DE, Aggarwal C, Aisner DL, Akerley W, Bauman JR, et al. NCCN guidelines insights: non-small cell lung cancer, Version 1.2020. *J Natl Compr Cancer Netw.* (2019) 17:1464–72. doi: 10.6004/jnccn.2019.0059
41. McGarry RC, Papiez L, Williams M, Whitford T, Timmerman RD. Stereotactic body radiation therapy of early-stage non-small-cell lung carcinoma: phase I study. *Int J Radiat Oncol Biol Phys.* (2005) 63:1010–5. doi: 10.1016/j.ijrobp.2005.03.073
42. Agolli L, Bracci S, Nicosia L, Valeriani M, De Sanctis V, Osti MF. Lung metastases treated with stereotactic ablative radiation therapy in oligometastatic colorectal cancer patients: outcomes and prognostic factors after long-term follow-up. *Clin Colorectal Cancer.* (2017) 16:58–64. doi: 10.1016/j.clcc.2016.07.004
43. Carvajal C, Navarro-Martin A, Cacicedo J, Ramos R, Guedea F. Stereotactic body radiotherapy for colorectal lung oligometastases: preliminary single-institution results. *J BUON.* (2015) 20:158–65.
44. Milano MT, Katz AW, Schell MC, Philip A, Okunieff P. Descriptive analysis of oligometastatic lesions treated with curative-intent stereotactic body radiotherapy. *Int J Radiat Oncol Biol Phys.* (2008) 72:1516–22. doi: 10.1016/j.ijrobp.2008.03.044
45. Rieber J, Streblow J, Uhlmann L, Flentje M, Duma M, Ernst I, et al. Stereotactic body radiotherapy (SBRT) for medically inoperable lung metastases-A pooled analysis of the German working group "stereotactic radiotherapy." *Lung Cancer.* (2016) 97:51–8. doi: 10.1016/j.lungcan.2016.04.012
46. Gomez DR, Blumenschein GR, Jr., Lee JJ, Hernandez M, Ye R, Camidge DR, et al. Local consolidative therapy versus maintenance therapy or observation for patients with oligometastatic non-small-cell lung cancer without progression after first-line systemic therapy: a multicentre, randomised, controlled, phase 2 study. *Lancet Oncol.* (2016) 17:1672–82. doi: 10.1016/S1470-2045(16)30532-0
47. Palma DA, Olson R, Harrow S, Gaede S, Louie AV, Haasbeek C, et al. Stereotactic ablative radiotherapy verus standard of care palliative treatment in patients with oligometastatic cancers (SABR-COMET): a randomised, phase 2, open-label trial. *Lancet.* (2019) 393:2051–8. doi: 10.1016/S0140-6736(18)32487-5
48. Kasmann L, Dietrich A, Staab-Weijnitz CA, Manapov F, Behr J, Rimner A, et al. Radiation-induced lung toxicity - cellular and molecular mechanisms of pathogenesis, management, and literature review. *Radiat Oncol.* (2020) 15:214. doi: 10.1186/s13014-020-01654-9
49. Bradley JD, Paulus R, Komaki R, Masters G, Blumenschein G, Schild S, et al. Standard-dose versus high-dose conformal radiotherapy with concurrent and consolidation carboplatin plus paclitaxel with or without cetuximab for patients with stage IIIA or IIIB non-small-cell lung cancer (RTOG 0617): a randomised, two-by-two factorial phase 3 study. *Lancet Oncol.* (2015) 16:187–99. doi: 10.1016/S1470-2045(14)71207-0
50. Wijsman R, Dankers F, Troost EGC, Hoffmann AL, van der Heijden E, de Geus-Oei LF, et al. Comparison of toxicity and outcome in advanced stage non-small cell lung cancer patients treated with intensity-modulated (chemo-)radiotherapy using IMRT or VMAT. *Radiother Oncol.* (2017) 122:295–9. doi: 10.1016/j.radonc.2016.11.015
51. Jiang ZQ, Yang K, Komaki R, Wei X, Tucker SL, Zhuang Y, et al. Long-term clinical outcome of intensity-modulated radiotherapy for inoperable non-small cell lung cancer: the MD Anderson experience. *Int J Radiat Oncol Biol Phys.* (2012) 83:332–9. doi: 10.1016/j.ijrobp.2011.06.1963
52. Palma DA, Senan S, Tsujino K, Barriger RB, Rengan R, Moreno M, et al. Predicting radiation pneumonitis after chemoradiation therapy for lung cancer: an international individual patient data meta-analysis. *Int J Radiat Oncol Biol Phys.* (2013) 85:444–50. doi: 10.1016/j.ijrobp.2012.04.043
53. Bahig H, Filion E, Vu T, Chalaoui J, Lambert L, Roberge D, et al. Severe radiation pneumonitis after lung stereotactic ablative radiation therapy in patients with interstitial lung disease. *Pract Radiat Oncol.* (2016) 6:367–74. doi: 10.1016/j.prro.2016.01.009
54. Saha A, Beasley M, Hatton N, Dickinson P, Franks K, Clarke K, et al. Clinical and dosimetric predictors of radiation pneumonitis in early-stage lung cancer treated with Stereotactic Ablative radiotherapy (SABR) - an analysis of UK's largest cohort of lung SABR patients. *Radiother Oncol.* (2021) 156:153–9. doi: 10.1016/j.radonc.2020.12.015
55. Nakamura M, Nishimura H, Nakayama M, Mayahara H, Uezono H, Harada A, et al. Dosimetric factors predicting radiation pneumonitis after CyberKnife stereotactic body radiotherapy for peripheral lung cancer. *Br J Radiol.* (2016) 89:20160560. doi: 10.1259/bjr.20160560
56. Parker SM, Siochi RA, Wen S, Mattes MD. Impact of tumor size on local control and pneumonitis after stereotactic body radiation therapy for lung tumors. *Pract Radiat Oncol.* (2019) 9:e90–7. doi: 10.1016/j.prro.2018.09.003

57. Allibhai Z, Taremi M, Bezjak A, Brade A, Hope AJ, Sun A, et al. The impact of tumor size on outcomes after stereotactic body radiation therapy for medically inoperable early-stage non-small cell lung cancer. *Int J Radiat Oncol Biol Phys.* (2013) 87:1064–70. doi: 10.1016/j.ijrobp.2013.08.020
58. Okubo M, Itonaga T, Saito T, Shiraishi S, Mikami R, Nakayama H, et al. Predicting risk factors for radiation pneumonitis after stereotactic body radiation therapy for primary or metastatic lung tumours. *Br J Radiol.* (2017) 90:20160508. doi: 10.1259/bjr.20160508
59. Kong FS, Moiseenko V, Zhao J, Milano MT, Li L, Rimner A, et al. Organs at risk considerations for thoracic stereotactic body radiation therapy: what is safe for lung parenchyma? *Int J Radiat Oncol Biol Phys.* (2021) 110:172–87. doi: 10.1016/j.ijrobp.2018.11.028
60. Dhami G, Zeng J, Vesselle HJ, Kinahan PE, Miyaoka RS, Patel SA, et al. Framework for radiation pneumonitis risk stratification based on anatomic and perfused lung dosimetry. *Strahlenther Onkol.* (2017) 193:410–8. doi: 10.1007/s00066-017-1114-0
61. Farr KP, Kallehauge JF, Moller DS, Khalil AA, Kramer S, Bluhme H, et al. Inclusion of functional information from perfusion SPECT improves predictive value of dose-volume parameters in lung toxicity outcome after radiotherapy for non-small cell lung cancer: a prospective study. *Radiother Oncol.* (2015) 117:9–16. doi: 10.1016/j.radonc.2015.08.005
62. Wang D, Sun J, Zhu J, Li X, Zhen Y, Sui S. Functional dosimetric metrics for predicting radiation-induced lung injury in non-small cell lung cancer patients treated with chemoradiotherapy. *Radiat Oncol.* (2012) 7:69. doi: 10.1186/1748-717X-7-69
63. Hofman MS, Beauregard JM, Barber TW, Neels OC, Eu P, Hicks RJ. 68Ga PET/CT ventilation-perfusion imaging for pulmonary embolism: a pilot study with comparison to conventional scintigraphy. *J Nucl Med.* (2011) 52:1513–9. doi: 10.2967/jnumed.111.093344
64. Blanc-Beguin F, Elies P, Robin P, Tripier R, Kervarec N, Lemarie CA, et al. (68)Ga-Labelled carbon nanoparticles for ventilation PET/CT imaging: physical properties study and comparison with Technegas(R). *Mol Imaging Biol.* (2021) 23:62–9. doi: 10.1007/s11307-020-01532-6
65. Hicks RJ, Hofman MS. Is there still a role for SPECT-CT in oncology in the PET-CT era? *Nat Rev Clin Oncol.* (2012) 9:712–20. doi: 10.1038/nrclinonc.2012.188
66. Le Roux PY, Iravani A, Callahan J, Burbury K, Eu P, Steinfort DP, et al. Independent and incremental value of ventilation/perfusion PET/CT and CT pulmonary angiography for pulmonary embolism diagnosis: results of the PECAN pilot study. *Eur J Nucl Med Mol Imaging.* (2019) 46:1596–604. doi: 10.1007/s00259-019-04338-z
67. Le Roux PY, Leong TL, Barnett SA, Hicks RJ, Callahan J, Eu P, et al. Gallium-68 perfusion positron emission tomography/computed tomography to assess pulmonary function in lung cancer patients undergoing surgery. *Cancer Imaging.* (2016) 16:24. doi: 10.1186/s40644-016-0081-5
68. Bailey DL, Eslick EM, Schembri GP, Roach PJ. (68)Ga PET ventilation and perfusion lung imaging-current status and future challenges. *Semin Nucl Med.* (2016) 46:428–35. doi: 10.1053/j.semnuclmed.2016.04.007
69. Le Roux PY, Siva S, Steinfort DP, Callahan J, Eu P, Irving LB, et al. Correlation of 68Ga ventilation-perfusion PET/CT with pulmonary function test indices for assessing lung function. *J Nucl Med.* (2015) 56:1718–23. doi: 10.2967/jnumed.115.162586
70. Siva S, Devereux T, Ball DL, MacManus MP, Hardcastle N, Kron T, et al. Ga-68 MAA perfusion 4D-PET/CT scanning allows for functional lung avoidance using conformal radiation therapy planning. *Technol Cancer Res Treat.* (2016) 15:114–21. doi: 10.1177/1533034614565534
71. Siva S, Thomas R, Callahan J, Hardcastle N, Pham D, Kron T, et al. High-resolution pulmonary ventilation and perfusion PET/CT allows for functionally adapted intensity modulated radiotherapy in lung cancer. *Radiother Oncol.* (2015) 115:157–62. doi: 10.1016/j.radonc.2015.04.013
72. Siva S, Hardcastle N, Kron T, Bressel M, Callahan J, MacManus MP, et al. Ventilation/perfusion positron emission tomography–based assessment of radiation injury to lung. *Int J Radiat Oncol Biol Phys.* (2015) 93:408–17. doi: 10.1016/j.ijrobp.2015.06.005
73. Hardcastle N, Hofman MS, Hicks RJ, Callahan J, Kron T, MacManus MP, et al. Accuracy and utility of deformable image registration in (68)Ga 4D PET/CT assessment of pulmonary perfusion changes during and after lung radiation therapy. *Int J Radiat Oncol Biol Phys.* (2015) 93:196–204. doi: 10.1016/j.ijrobp.2015.05.011
74. Louie AV, Haasbeek CJ, Mokhles S, Rodrigues GB, Stephans KL, Lagerwaard FJ, et al. Predicting overall survival after stereotactic ablative radiation therapy in early-stage lung cancer: development and external validation of the amsterdam prognostic model. *Int J Radiat Oncol Biol Phys.* (2015) 93:82–90. doi: 10.1016/j.ijrobp.2015.07.241
75. Koshy M, Malik R, Weichselbaum RR, Sher DJ. Increasing radiation therapy dose is associated with improved survival in patients undergoing stereotactic body radiation therapy for stage I non-small-cell lung cancer. *Int J Radiat Oncol Biol Phys.* (2015) 91:344–50. doi: 10.1016/j.ijrobp.2014.10.002
76. Wang W, Xu Y, Schipper M, Matuszak MM, Ritter T, Cao Y, et al. Effect of normal lung definition on lung dosimetry and lung toxicity prediction in radiation therapy treatment planning. *Int J Radiat Oncol Biol Phys.* (2013) 86:956–63. doi: 10.1016/j.ijrobp.2013.05.003
77. Kabolizadeh P, Kalash R, Huq MS, Greenberger JS, Heron DE, Beriwal S. Dosimetric definitions of total lung volumes in calculating parameters predictive for radiation-induced pneumonitis. *Am J Clin Oncol.* (2015) 38:401–4. doi: 10.1097/COC.0b013e3182a2588f
78. Graham MV, Purdy JA, Emami B, Harms W, Bosch W, Lockett MA, et al. Clinical dose-volume histogram analysis for pneumonitis after 3D treatment for non-small cell lung cancer (NSCLC). *Int J Radiat Oncol Biol Phys.* (1999) 45:323–9. doi: 10.1016/S0360-3016(99)00183-2
79. Jenkins P, Watts J. An improved model for predicting radiation pneumonitis incorporating clinical and dosimetric variables. *Int J Radiat Oncol Biol Phys.* (2011) 80:1023–9. doi: 10.1016/j.ijrobp.2010.03.058
80. De Ruysscher D, Wanders S, Minken A, Lumens A, Schiffelers J, Stultiens C, et al. Effects of radiotherapy planning with a dedicated combined PET-CT-simulator of patients with non-small cell lung cancer on dose limiting normal tissues and radiation dose-escalation: a planning study. *Radiother Oncol.* (2005) 77:5–10. doi: 10.1016/j.radonc.2005.06.014
81. Hernando ML, Marks LB, Bentel GC, Zhou SM, Hollis D, Das SK, et al. Radiation-induced pulmonary toxicity: a dose-volume histogram analysis in 201 patients with lung cancer. *Int J Radiat Oncol Biol Phys.* (2001) 51:650–9. doi: 10.1016/S0360-3016(01)01685-6
82. Rodrigues G, Lock M, D'Souza D, Yu E, Van Dyk J. Prediction of radiation pneumonitis by dose - volume histogram parameters in lung cancer–a systematic review. *Radiother Oncol.* (2004) 71:127–38. doi: 10.1016/j.radonc.2004.02.015
83. Kong FM, Hayman JA, Griffith KA, Kalemkerian GP, Arenberg D, Lyons S, et al. Final toxicity results of a radiation-dose escalation study in patients with non-small-cell lung cancer (NSCLC): predictors for radiation pneumonitis and fibrosis. *Int J Radiat Oncol Biol Phys.* (2006) 65:1075–86. doi: 10.1016/j.ijrobp.2006.01.051
84. Kong FM, Ritter T, Quint DJ, Senan S, Gaspar LE, Komaki RU, et al. Consideration of dose limits for organs at risk of thoracic radiotherapy: atlas for lung, proximal bronchial tree, esophagus, spinal cord, ribs, and brachial plexus. *Int J Radiat Oncol Biol Phys.* (2011) 81:1442–57. doi: 10.1016/j.ijrobp.2010.07.1977
85. Nestle U, De Ruysscher D, Ricardi U, Geets X, Belderbos J, Pottgen C, et al. ESTRO ACROP guidelines for target volume definition in the treatment of locally advanced non-small cell lung cancer. *Radiother Oncol.* (2018) 127:1–5. doi: 10.1016/j.radonc.2018.02.023
86. Castillo R, Castillo E, Martinez J, Guerrero T. Ventilation from four-dimensional computed tomography: density versus Jacobian methods. *Phys Med Biol.* (2010) 55:4661–85. doi: 10.1088/0031-9155/55/16/004
87. Vinogradskiy YY, Castillo R, Castillo E, Chandler A, Martel MK, Guerrero T. Use of weekly 4DCT-based ventilation maps to quantify changes in lung function for patients undergoing radiation therapy. *Med Phys.* (2012) 39:289–98. doi: 10.1118/1.3668056
88. Yamamoto T, Kabus S, Bal M, Keall P, Benedict S, Daly M. The first patient treatment of computed tomography ventilation functional image-guided radiotherapy for lung cancer. *Radiother Oncol.* (2016) 118:227–31. doi: 10.1016/j.radonc.2015.11.006

89. Kipritidis J, Hofman MS, Siva S, Callahan J, Le Roux PY, Woodruff HC, et al. Estimating lung ventilation directly from 4D CT Hounsfield unit values. *Med Phys.* (2016) 43:33. doi: 10.1118/1.4937599
90. Eslick EM, Kipritidis J, Gradinscak D, Stevens MJ, Bailey DL, Harris B, et al. CT ventilation imaging derived from breath hold CT exhibits good regional accuracy with Galligas PET. *Radiother Oncol.* (2018) 127:267–73. doi: 10.1016/j.radonc.2017.12.010
91. Ireland RH, Tahir BA, Wild JM, Lee CE, Hatton MQ. Functional image-guided radiotherapy planning for normal lung avoidance. *Clin Oncol.* (2016) 28:695–707. doi: 10.1016/j.clon.2016.08.005
92. Evans ES, Hahn CA, Kocak Z, Zhou SM, Marks LB. The role of functional imaging in the diagnosis and management of late normal tissue injury. *Semin Radiat Oncol.* (2007) 17:72–80. doi: 10.1016/j.semradonc.2006.11.003
93. Bucknell N, Hardcastle N, Jackson P, Hofman M, Callahan J, Eu P, et al. Single-arm prospective interventional study assessing feasibility of using gallium-68 ventilation and perfusion PET/CT to avoid functional lung in patients with stage III non-small cell lung cancer. *BMJ Open.* (2020) 10:e042465. doi: 10.1136/bmjopen-2020-042465

Conflict of Interest: The authors declare that the research was conducted in the absence of any commercial or financial relationships that could be construed as a potential conflict of interest.

frontiers in Medicine

ORIGINAL RESEARCH
published: 04 October 2021
doi: 10.3389/fmed.2021.748683

^{68}Ga-DOTA-FAPI-04 PET/CT as a Promising Tool for Differentiating Ovarian Physiological Uptake: Preliminary Experience of Comparative Analysis With ^{18}F-FDG

Qixin Wang[1,2], *Songsong Yang*[1,2], *Wenxin Tang*[1,2], *Lin Liu*[1,2] *and Yue Chen*[1,2]*

[1] *Department of Nuclear Medicine, The Affiliated Hospital of Southwest Medical University, Luzhou, China,* [2] *Nuclear Medicine and Molecular Imaging Key Laboratory of Sichuan Province, Luzhou, China*

Objectives: This study aimed to investigate the physiological distribution characteristics of ^{68}Ga-DOTA-FAPI-04 in the ovary, and assess the feasibility of early diagnosis of primary ovarian disease with ^{68}Ga-DOTA-FAPI-04 PET/CT.

Methods: We retrospectively analyzed the data of patients who received ^{18}F-FDG and ^{68}Ga-DOTA-FAPI-04 PET/CT scanning in the Nuclear Medicine Department of our hospital within 3 days from September 2020 to January 2021. We selected the data in which ovaries showed abnormal FDG activity. Patients with abnormal ovarian FDG uptake with focus confirmed by pathological biopsy or clinical follow-up as pathological changes were excluded. The uptake of tracers (^{18}F-FDG and ^{68}Ga-FAPI) was semi-quantitatively analyzed.

Results: This study included 14 patients (average age was 38.6). Physiological ovarian uptake was mostly unilateral, and there was no significant difference in SUVmax between the left and right sides (FDGt = 0.272, FAPIt = 0.592). The ovary SUVmax of FDG (4.89 ± 1.84) was statistically significantly higher than that of FAPI (1.53 ± 0.37). The Le/Li ratio on FDG is 3.38 ± 1.81, TBR is 5.81 ± 1.98, while the Le/Li ratio on FAPI is 3.57 ± 1.26, TBR is 0.94 ± 0.19.

Conclusion: Our research shows that ovarian functional or pathological changes can be manifested as FDG avid, while ^{68}Ga-DOTA-FAPI-04 has no physiological accumulation in the ovary and is not affected by the menstrual cycle. Therefore, ^{68}Ga-DOTA-FAPI-04 has unique advantages in the diagnosis of ovarian diseases, and can identify them early and accurately.

Keywords: ^{18}F-FDG, ^{68}Ga-DOTA-FAPI-04, PET/CT, ovary, physiological metabolism

OPEN ACCESS

Edited by:
Désirée Deandreis, University of Turin, Italy

Reviewed by:
Laura Evangelista, University of Padua, Italy
Salvatore Annunziata, Fondazione Policlinico Universitario Agostino Gemelli IRCCS, Italy

***Correspondence:**
Yue Chen
chenyue5523@126.com

Specialty section:
This article was submitted to Nuclear Medicine, a section of the journal Frontiers in Medicine

Received: *28 July 2021*
Accepted: *09 September 2021*
Published: *04 October 2021*

Citation:
Wang Q, Yang S, Tang W, Liu L and Chen Y (2021) ^{68}Ga-DOTA-FAPI-04 PET/CT as a Promising Tool for Differentiating Ovarian Physiological Uptake: Preliminary Experience of Comparative Analysis With ^{18}F-FDG. Front. Med. 8:748683. doi: 10.3389/fmed.2021.748683

INTRODUCTION

2-deoxy-2-[^{18}F]fluoro-D-glucose (^{18}F-FDG), known as "the century molecule," is currently the most widely used oncological tracer. ^{18}F-FDG positron emission tomography/computed tomography (PET/CT) is a valuable molecular imaging method widely used in the clinical diagnosis, staging and efficacy monitoring of various diseases. However, due to the pathological

characteristics of glucose metabolism, ^{18}F-FDG is highly distributed in normal organs including the brain, heart, and liver (1–3). Many physiological variations and pitfalls of whole-body ^{18}F-FDG PET/CT imaging have been reported (4–6). In the pelvic region, activity retention within the urinary tract and ^{18}F-FDG uptake in the normal intestine over very short segments are common sources of false-positives (7). At the same, ^{18}F-FDG PET/CT lacks specificity in differentiating inflammation (8–10).

The menstrual cycle complicates the imaging of the female reproductive system. Gynecologic malignancies, including cervical, endometrial, vulvar, and ovarian carcinoma show ^{18}F-FDG activity (11–13). ^{18}F-FDG uptake in follicular ovarian cysts or hemorrhagic luteal cysts has previously been reported (13–15)]. In recent years, there have been reports of focal ^{18}F-FDG uptake in the ovaries and uterus associated with the menstrual cycle in premenopausal women (14, 16–18), which may result in false positives on ^{18}F-FDG PET imaging or malignancy being overlooked for physical uptake. This may be a challenge to nuclear medicine physicians. In order to identify if ovarian ^{18}F-FDG uptake is physiological or pathological, the traditional method requires ^{18}F-FDG PET/CT in different menstrual periods, which is not conducive to early clinical diagnosis. This has led to the development of more tracers.

Quinoline-based ligands targeting cancer-associated fibroblasts are promising radiopharmaceuticals in multiple tumors. Fibroblast activation protein (FAP) is a type II transmembrane glycoprotein expressed in dimer form on the surface of the tumor-associated cell matrix (CAFs) (19, 20). Evidence indicates that FAP is highly expressed in a variety of tumors, especially colorectal, ovarian, pancreatic, and hepatocellular carcinomas characterized by a strong desmoplastic reaction (21). CAFs with high FAP expression are associated with an adverse prognosis by promoting invasion, angiogenesis, micro-environmental immune suppression, and metastasis (22). ^{68}Ga-DOTA-FAPI-04 showed the most favorable PET imaging properties, including low nanomolar affinity to FAP, near-complete internalization of FAP-bound radioactivity, and rapid blood clearance (23). This is a promising diagnostic and therapeutic target because of its low uptake in normal tissues and high target/non-target ratio.

To our knowledge, there have been no systematic investigations of ovarian FAPI metabolism. Herein, we present the results of a retrospective study of FAPI ovarian uptake patterns, which could help identify physiological and pathological changes for disease staging and formulate optimal treatment strategies.

MATERIALS AND METHODS

This is a retrospective analysis of a sub-cohort of patients from a previously acquired prospective database. Data were screened from the study previously registered at the clinical trial center and approved by the Clinical Research Ethics Committee of our Hospital. The study was conducted in accordance with the 1964 declaration of Helsinki and its subsequent amendments or similar ethical standards. In all cases, PET/CT scans were performed according to clinical needs or other protocols approved by our institutional review committee.

Patients

We retrospectively analyzed the images of patients who simultaneously underwent ^{18}F-FDG and ^{68}Ga-DOTA-FAPI-04 PET/CT examination in the Department of Nuclear Medicine in our institution between September of 2020 and January of 2021. We selected the patients whose ovary demonstrated ^{18}F-FDG uptake and reviewed their medical records and imaging findings. We then clarified any vague information to determine the reason for the increased FDG uptake. Pathological or imaging follow-up was the final determinant. The inclusion criteria were as follows: (1) female patients over 18 years old; (2) The inspection interval between FDG and FAPI is <3 days; (3) ovarian abnormal uptake on ^{18}F-FDG; and (4) ovarian lesions were excluded by imaging and clinical follow-up or pathological results. The exclusion criteria were as follows: (1) history of ovarian tumors or related diseases and (2) patients without menstrual records or who failed to follow up. The first day of the menstrual cycle was recorded and all menstrual cycles were converted to a standardized 28 days for comparison.

PET/CT Imaging

^{18}F-FDG was manufactured per the standard method using the coincidence ^{18}F-FDG synthesis module [FDG-N, PET (Beijing) Science and Technology, Beijing, China]. We purchased the precursor FAPI-04 from MedChemExpress LLC (Shanghai, China) with a purity of 98%. Radiolabeling of DOTA-FAPI-04 was performed by adding 1 mL sodium acetate (0.25 M) and 4 mL ^{68}Ga-solution (370 MBq) to a reactor with a 25μg precursor FAPI-04. The final pH was ∼4.0. The reaction was heated at 95°C for 10 min and the product was purified using a Sep-pak18C column. The final product was diluted with saline and sterilized by passing through a 0.22μm Millipore filter. The radiochemical purity was over 98% for ^{18}F-FDG and ^{68}Ga-DOTA-FAPI-04.

All patients were required to fast for at least 6 h before the ^{18}F-FDG PET/CT examination. Serum glucose values were normal before the injection. No special preparation was required before ^{68}Ga-DOTA-FAPI-04 PET/CT imaging (such as fasting or normal blood glucose levels). The dosage of intravenously injected ^{18}F-FDG and ^{68}Ga-DOTA-FAPI-04 was calculated based on the patient's weight (5.55 MBq [0.15mCi]/kg for FDG; 1.85 MBq [0.05mCi]/kg for FAPI).

Acquisition of ^{18}F-FDG and ^{68}Ga-DOTA-FAPI-04 imaging was started ∼60 min after intravenous injection. The whole-body inspection scope was from the base of the skull to the base of the thigh. CT scan parameters included a tube voltage of 120 kV, a current of 120 mA, and a slice thickness of 3 mm. A PET scan in 3D acquisition mode was immediately performed after the CT scan and 5–6 beds were used depending on body length (90 s/bed for FDG and 3 min/bed for FAPI).

Imaging Review

The Advantage Workstation was used to reviewed PET, CT, and fused PET/CT images. ^{18}F-FDG and ^{68}Ga-DOTA-FAPI-04 PET/CT scans were interpreted by two experienced board-certified nuclear medicine physicians. To prevent any bias, the research was reviewed in groups by study type: all ^{18}F-FDG PET/CT images were reviewed by Tang W. and Wang Q. as group 1, and all ^{68}Ga-DOTA-FAPI-04 PET/CT images were reviewed by Yang S. and Liu L. as group 2. Reviews were performed without other imaging data.

For a semi-quantitative analysis, regions of interest were manually drawn on transaxial images around the metabolic lesions of the uterine adnexa. The maximum standardized uptake value (SUVmax) was automatically calculated by the Advanced Workstation. The SUVmax of adjacent pelvic muscle was selected as the activity background, and the SUVmax of the ovary was divided by this muscle SUVmax to calculate target-to-background ratio (TBR). The mean standardized uptake value (SUVmean) of a round sphere with a diameter of 2 cm was selected from the liver to calculate Le/Li ratio (Le = ovary Li = Liver).

Statistical Analysis

Statistical software package SPSS (IBM SPSS Statistics, Version 22) was used for data analysis and description. Descriptive statistics such as absolute and relative frequencies for discrete parameters and mean and standard deviation for continuous parameters were computed. Pearson correlation coefficient was

TABLE 1 | The demographic and clinical characteristics of patients.

Patient no.	Age (years)/Gender	Height (cm)	Weight (kg)	Primary diagnosis	Treatment
1	19/female	152	38	Lymphoma	Radiotherapy and chemotherapy
2	27/female	155	56	Thyroid Ca	Surgery
3	29/female	162	55	Unknown fever	Conservative treatment
4	30/female	159	58	Trichoblastoma	Surgery
5	33/female	163	64	Lung Ca	Surgery
6	38/female	157	54	Thyroid Ca	Surgery
7	39/female	152	52	Stomach Ca	Surgery
8	42/female	162	61	Lung Ca	Surgery
9	45/female	158	60	Breast Ca	Surgery and chemotherapy
10	45/female	164	74	Lymphoma	Chemotherapy
11	46/female	156	72	Cervical Ca	Radiotherapy and chemotherapy
12	48/female	155	48	Breast Ca	Chemotherapy and Interventional therapy
13	48/female	165	78	Lung Ca	Surgery
14	52/female	158	69	Thyroid Ca	Surgery

TABLE 2 | Summary of ^{18}F-FDG and ^{68}Ga-DOTA-FAPI-04 PET/CT images.

Patient no.	Lesion size (mm^2)	FDG				FAPI			
		Menstrual cycle (days)	SUVmax of ovary	Le/Li ratio	TBR	Menstrual cycle (days)	SUVmax of ovary	Le/Li ratio	TBR
1	10.2 × 8.9	−14	4.1	4.6	8.2	−12	1.2	3.0	0.8
2	9.5 × 13.1	−17	3.9	3.3	5.6	−14	1.2	2.4	0.8
3	10.3 × 9.6	−12	4.6	3.5	6.6	−11	1.4	3.5	0.8
4	13.0 × 12.0	−11	8.5	8.5	9.4	−10	2.1	4.2	1.2
5	8.9 × 7.2	−13	3.6	2.6	6.0	−11	1.8	3.6	1.1
6	11.4 × 9.6	−8	3.3	2.5	4.1	−7	1.6	2.7	0.8
7	21.1 × 19.0	−11	8.2	5.5	9.1	−10	1.9	3.2	0.9
8	12.2 × 10.3	−12	4.6	2.4	4.6	−11	1.3	2.6	0.7
9	10.3 × 11.0	−16	4.6	2.2	4.2	−14	1.1	3.7	0.9
10	19.5 × 20.2	−15	2.7	1.5	3.0	−13	1.0	2.5	0.7
11	7.9 × 7.6	−10	5.4	2.6	5.4	−9	1.7	5.7	1.2
12	11.8 × 9.3	−14	2.8	1.8	3.5	−13	1.2	2.4	1.1
13	10.0 × 15.2	−11	5.2	3.5	5.8	−9	1.9	3.8	1
14	20.0 × 12.8	−13	7.0	2.9	5.8	−12	2.0	6.7	1.2

used to describe the relationship between FDG-dose/FAPI-dose and total SUV. Results with a *P*-value <5% were statistically significant.

RESULTS

A total of 78 female patients underwent ^{18}F-FDG and ^{68}Ga-DOTA-FAPI-04 PET/CT examination within 3 days. Ovarian uptake was observed on ^{18}F-FDG PET/CT images in 29 patients, 15 of whom were confirmed by pathology ($n = 11$) or follow-up ($n = 4$). This retrospective analysis included 14 patients with a mean age of 38.6 (range, 19–52 years). They were mainly in secretory phase (11/14 for FDG, 12/14 for FAPI) and proliferative phase (3/14 for FDG, 2/14 for FAPI). The demographic and clinical characteristics of the subjects are summarized in **Table 1**.

The FDG and FAPI PET/CT images showed that there were significant differences in the ovarian uptake between the two groups, most being unilateral. There was no significant difference

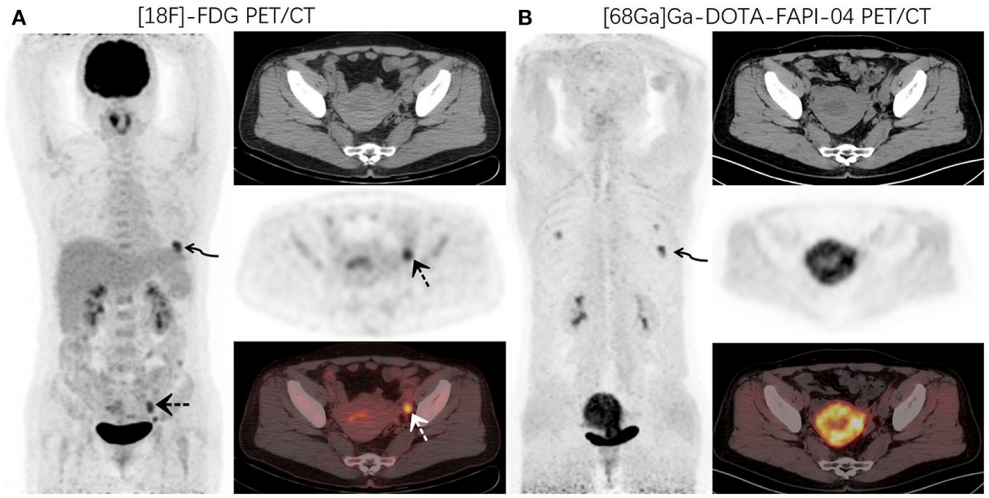

FIGURE 1 | A 48-year-old woman with newly diagnosed lung cancer underwent a PET/CT scan for tumor staging. ^{18}F-FDG PET/CT **(A)** images revealed increased FDG uptake in the left lung (curved arrow, SUVmax9.1). Abnormal activity was also observed in the endometrium and left adnexal area (dotted arrow, SUVmax 5.2). ^{68}Ga-DOTA-FAPI-04 PET/CT **(B)** showed increased FAPI uptake in the left lung lesion (curved arrow, SUVmax10.6) and uterus. No other abnormal lesions were observed.

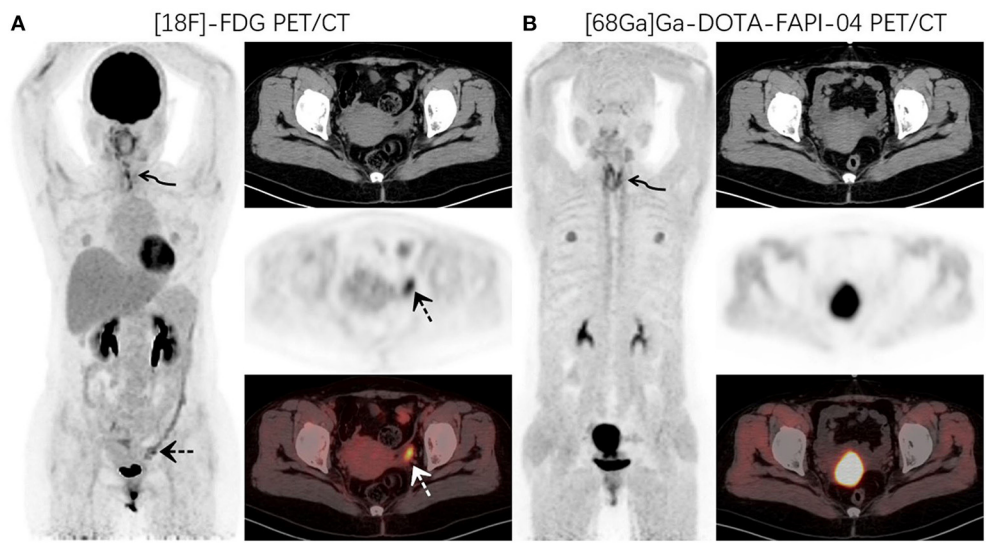

FIGURE 2 | PET/CT was performed for restaging in a 52-year-old woman who underwent thyroidectomy for thyroid cancer 1 year prior. ^{18}F-FDG PET/CT **(A)** images showed increased FDG uptake in the thyroidectomy area (curved arrow, SUVmax7.4) and left adnexal region (dotted arrow, SUVmax7.0). ^{68}Ga-DOTA-FAPI-04 PET/CT **(B)** images demonstrated increased uptake of imaging agents in the thyroid area (curved arrow, SUVmax8.9), but no abnormal uptake was observed in the left adnexal region.

in SUV between the left and right ovary ($t = 0.272$ for FDG, and $t = 0.592$ for FAPI). For the FDG group, the ovary SUVmax (4.89 ± 1.84) was statistically significantly higher than that of liver (1.57 ± 0.44) and pelvic muscle (0.86 ± 0.19) ($P < 0.05$). The average Le/Li ratio and TBR were 3.38 ± 1.81, and 5.81 ± 1.98, respectively. Physiological FDG uptake is associated with the menstrual cycle and occurs mainly in late hyperplasia and early secretion (**Table 2**). There was no significant difference between the two phases ($t = 1.26$, $p = 0.23$). Focal endometrial FDG uptake was observed in 4 patients (median SUVmax4.5, **Figure 1**). For the FAPI group, the average SUV of ovary, liver and muscle were 1.53 ± 0.37, 0.45 ± 0.10, and 1.64 ± 0.29, respectively. The difference between ovary and liver was statistically significant ($t = 11.108$, $p < 0.05$), while the difference between ovary and muscle was not ($t = -1.33$, $p = 0.21$). The average Le/Li ratio and TBR were 3.57 ± 1.26, and 0.94 ± 0.19, respectively. The uterus of the 14 subjects showed intense FAPI activity (average SUVmax 12.7, **Figure 2**). In addition, abnormal FAPI uptake in the broad ligament of the uterus was observed in a patient, which was manifested as a stripe of increased FAPI-avid (SUVmax 3.9). The TBR of the two groups was statistically different ($t = 9.42$, $p < 0.05$), while Le/Li ratio was not (**Table 3**). This is because normal liver has a high FDG uptake and a low FAPI uptake (one of the advantages of FAPI in displaying lesions, **Figure 3**).

DISCUSSION

Both pathological and functional ovarian lesions can show abnormal FDG uptake. Physiologically, FDG accumulates in the female reproductive system, with a high SUV, making it difficult to obtain a clear image with high tumor-background contrast and increasing the diagnostic difficulty. In 2002, Chander et al. confirmed the physiological uptake of the endometrium and ovary in a serial PET/CT follow-up of a patient, and suggested that this performance varies with the menstrual cycle (17, 24, 25). Glucose phosphorylation is an important rate-limiting step in the estrogenic stimulation of uterine glycolysis (14). Hughes assessed endometrial enzymes activity in 252 patients with normal menstrual histories and found that, in normal endometrial tissue, glycogen synthetase activity synthesizes glycogen from glucose in increasing amounts until the midcycle (26). Glycogen phosphorylase then-breaks down glucose during the regressive stage of endometrial activity, causing decreased glycogen levels at the end of the cycle. Increased metabolic demands and inflammatory responses before and after ovulation may lead

TABLE 3 | Comparison of indicators between FDG and FAPI.

	Ovary SUVmax	Liver SUVmax	Muscle SUVmax	Le/Li ratio	TBR
FDG	4.89 ± 1.84	1.57 ± 0.44	0.86 ± 0.19	3.38 ± 1.81	5.81 ± 1.98
FAPI	1.53 ± 0.37	0.45 ± 0.10	1.64 ± 0.29	3.57 ± 1.26	0.94 ± 0.19
t	7.97	−8.30	8.39	−0.34	9.42
P-value	<0.05	<0.05	<0.05	0.74	<0.05

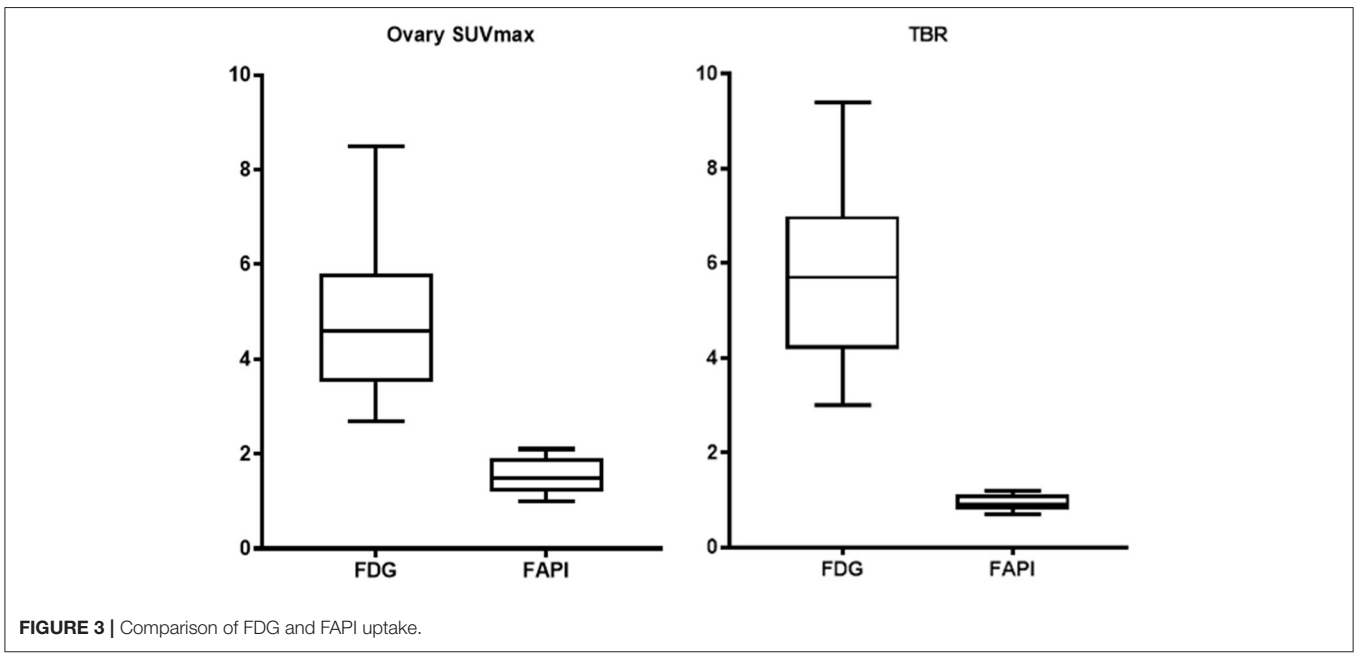

FIGURE 3 | Comparison of FDG and FAPI uptake.

to increased ovarian FDG uptake. However, not all women with active menstruation experience increased FDG uptake for reasons that remain unclear. This physiological FDG uptake mainly occurs during the late follicular to early luteal phase of the menstrual cycle and is usually round or elliptical, mostly unilateral, and with a SUVmax >3 (25). Subsequent research has evaluated the characteristics of physiological FDG uptake in the ovaries, including other imaging methods and the differential diagnostic value of delayed imaging (17, 24, 25).

Cook et al. warn that a high uptake in the periphery of a benign cyst, such as a follicular ovarian cyst, may mimic a necrotic lymph node (15). Therefore, it is crucial to differentiate between physiological and pathological uptake. Measurement of the serum levels of menstrual cycles or ovarian hormones may help diagnose false positives but does not rule out pathological metabolism. The traditional method to distinguish the physiological and pathological uptake of the ovary requires repeated FDG examination in different physiological cycles, which may delay diagnosis.

SUVmax is the most commonly used index for evaluating metabolism on PET/CT, but differences in nuclides, patients, and equipment may cause certain differences. Therefore, using the target/non-target ratio is obviously more comparable. TBR can better perform semi-quantitative analysis of the uptake of different patients and imaging agents. Research has demonstrated that TBR has independent prognostic abilities for many lesions (27).

This retrospective analysis sought to evaluate the benefit and impact of ^{68}Ga-FAPI-PET/CT in a small cohort of patients harboring suspicious ovarian lesions. We retrospectively analyzed the PET/CT images of 14 patients with suspected FDG false-positive ovaries. In contrast to ^{18}F-FDG, ^{68}Ga-DOTA-FAPI-04 has no physiological accumulation in the ovaries and is not affected by the physiological cycle, resulting in higher image contrast and better lesion delineation in the adnexal area of the uterus (**Figure 3**). ^{68}Ga-DOTA-FAPI-04 positron emission tomography produces accurate and comprehensive imaging that can help determine the best treatment strategy. It may improves tumor staging, relapse monitoring, and necessary therapeutic interventions. Tumor lesions exceeding 1–2 mm in size require a supporting stroma (28). As the stroma volume can be larger than the tumor volume, stroma-targeted PET imaging may be more sensitive than glycolysis PET imaging for detecting small lesions with sufficient FAP-expressing stroma (22, 28). In 2019, Clemens et al. quantified the tumor-uptake in FAPI-PET/CT of various primary and metastatic tumors and found that ovarian cancer showed a moderate uptake of FAPI (SUVmax 6-12) (29).

Limitations

This study has some limitations. First, the sample size was small and the patients varied greatly by primary disease (heterogeneity). Patient demographic characteristics may not reflect the general population. Second, this was a retrospective study. Some lesions might have been mistaken as physiological ingestion due to no obvious symptoms during follow-up. Currently, there is no literature evaluating FAPI's role in the ovaries. Therefore, prospective studies involving more patients are warranted to further explore ovarian FAPI uptake patterns.

CONCLUSIONS

Both malignant and functional ovarian lesions can exhibit abnormal FDG uptake. ^{68}Ga-DOTA-FAPI-04 has no physiological uptake and is not affected by the physiological cycle. It has a unique advantage in the diagnosis of ovarian diseases and can accurately differentiate physiological and pathological ovarian lesions in the early stage.

DATA AVAILABILITY STATEMENT

The original contributions presented in the study are included in the article/supplementary material, further inquiries can be directed to the corresponding author.

ETHICS STATEMENT

Written informed consent was obtained from the individual(s) for the publication of any potentially identifiable images or data included in this article.

AUTHOR CONTRIBUTIONS

QW, SY, WT, LL, and YC: conception and design. QW: methodology, formal analysis, and writing–original draft. All the authors revised the paper, agreed to the submission of the final version of the manuscript, vouch for the accuracy and completeness of the data, analyses and for the fidelity of this report.

ACKNOWLEDGMENTS

The authors are grateful to the members of Department of Nuclear Medicine, The Affiliated Hospital, Southwest Medical University and Nuclear Medicine and Molecular Imaging Key Laboratory of Sichuan Province for their technical guidance, cooperation and assistance in completing this report.

REFERENCES

1. Nakamoto Y, Tatsumi M, Hammoud D, Cohade C, Osman MM, Wahl RL. Normal FDG distribution patterns in the head and neck: PET/CT evaluation. *Radiology*. (2005)234:879–85. doi: 10.1148/radiol.2343030301
2. Morita K, Katoh C, Yoshinaga K, Noriyasu K, Mabuchi M, Tsukamoto T, et al. Quantitative analysis of myocardial glucose utilization in patients with left ventricular dysfunction by means of 18F-FDG dynamic positron tomography and three-compartment analysis. *Eur J Nucl Med Mol Imaging*. (2005) 32:806–12. doi: 10.1007/s00259-004-1743-2
3. Choi Y, Hawkins RA, Huang SC, Brunken RC, Hoh CK, Messa C, et al. Evaluation of the effect of glucose ingestion and kinetic model configurations of FDG in the normal liver. *J Nucl Med.* (1994) 35:8 18–23.

4. Tripathy S, Subudhi TK, Kumar R. Stoma site infection mimicking lymphoma recurrence: potential pitfall on (18)F FDG positron emission tomography-computed tomography. *Indian J Nucl Med.* (2019) 34:233–4. doi: 10.4103/ijnm.IJNM_5_19
5. Yang M, Rosenthal AC, Ashman JB, Craig FE. The role and pitfall of F18-FDG PET/CT in surveillance of high grade pulmonary lymphomatoid granulomatosis. *Curr Probl Diagn Radiol.* (2021) 50:443–9. doi: 10.1067/j.cpradiol.2019.02.002
6. Parida GK, Roy SG, Kumar R. FDG-PET/CT in skeletal muscle: pitfalls and pathologies. *Semin Nucl Med.* (2017) 47:362–72. doi: 10.1053/j.semnuclmed.2017.02.003
7. Nishimura M, Tamaki N, Matsushima S, Kiba M, Kotani T, Bamba C, et al. Dynamic whole-body (18)F-FDG PET for differentiating abnormal lesions from physiological uptake. *Eur J Nucl Med Mol Imaging.* (2020) 47:2293–300. doi: 10.1007/s00259-020-04726-w
8. Chuang TL, Tseng CE, Huang SW, Wang YF. Scrotal fibroepithelial polyp with acute and chronic inflammation mimics malignancy on 18F-FDG PET/CT imaging. *Clin Nucl Med.* (2019) 44:920–2. doi: 10.1097/RLU.0000000000002771
9. Shen G, Kuang A. Abdominal wall granulomatous inflammation mimicking malignancy on FDG PET/CT. *Clin Nucl Med.* (2020) 45:234–5. doi: 10.1097/RLU.0000000000002868
10. Ha JW, Lee JD, Kim YJ, Yun MJ, Chung N. Pulmonary artery aneurysm due to systemic vasculitis: assessment of vascular inflammation using F-18 FDG positron emission tomography. *Eur Heart J.* (2007) 28:779. doi: 10.1093/eurheartj/ehl253
11. Burger IA, Vargas HA, Donati OF, Andikyan V, Sala E, Gonen M, et al. The value of 18F-FDG PET/CT in recurrent gynecologic malignancies prior to pelvic exenteration. *Gynecol Oncol.* (2013) 129:586–92. doi: 10.1016/j.ygyno.2013.01.017
12. Scarsbrook A, Vaidyanathan S, Chowdhury F, Swift S, Cooper R, Patel C. Efficacy of qualitative response assessment interpretation criteria at 18F-FDG PET-CT for predicting outcome in locally advanced cervical carcinoma treated with chemoradiotherapy. *Eur J Nucl Med Mol Imaging.* (2017) 44:581–8. doi: 10.1007/s00259-016-3537-8
13. Tanizaki Y, Kobayashi A, Shiro M, Ota N, Takano R, Mabuchi Y, et al. Diagnostic value of preoperative SUVmax on FDG-PET/CT for the detection of ovarian cancer. *Int J Gynecol Cancer.* (2014) 24:454–60. doi: 10.1097/IGC.0000000000000074
14. Lerman H, Metser U, Grisaru D, Fishman A, Lievshitz G, Even-Sapir E. Normal and abnormal 18F-FDG endometrial and ovarian uptake in pre- and postmenopausal patients: assessment by PET/CT. *J Nucl Med.* (2004) 45:266–71.
15. Ho KC, Ng KK, Yen TC, Chou HH. An ovary in luteal phase mimicking common iliac lymph node metastasis from a primary cutaneous peripheral primitive neuroectodermal tumour as revealed by 18-fluoro-2-deoxyglucose positron emission tomography. *Br J Radiol.* (2005) 78:343–5. doi: 10.1259/bjr/95232584
16. Short S, Hoskin P, Wong W. Ovulation and increased FDG uptake on PET: potential for a false-positive result. *Clin Nucl Med.* (2005) 30:707. doi: 10.1097/01.rlu.0000178248.98702.9e
17. Kim SK, Kang KW, Roh JW, Sim JS, Lee ES, Park SY. Incidental ovarian 18F-FDG accumulation on PET: correlation with the menstrual cycle. *Eur J Nucl Med Mol Imaging.* (2005) 32:757–63. doi: 10.1007/s00259-005-1771-6
18. Nishizawa S, Inubushi M, Okada H. Physiological 18F-FDG uptake in the ovaries and uterus of healthy female volunteers. *Eur J Nucl Med Mol Imaging.* (2005) 32:549–56. doi: 10.1007/s00259-004-1703-x
19. Altmann A, Haberkorn U, Siveke J. The latest developments in imaging of fibroblast activation protein. *J Nucl Med.* (2021) 62:160–7. doi: 10.2967/jnumed.120.244806
20. Hicks RJ, Roselt PJ, Kallur KG, Tothill RW, Mileshkin L. FAPI PET/CT: will it end the hegemony of (18)F-FDG in oncology? *J Nucl Med.* (2021) 62:296–302. doi: 10.2967/jnumed.120.256271
21. Chen H, Pang Y, Wu J, Zhao L, Hao B, Wu J, et al. Comparison of [(68)Ga]Ga-DOTA-FAPI-04 and [(18)F] FDG PET/CT for the diagnosis of primary and metastatic lesions in patients with various types of cancer. *Eur J Nucl Med Mol Imaging.* (2020) 47:1820–32. doi: 10.1007/s00259-020-04769-z
22. Moradi F, Iagaru A. Will FAPI PET/CT replace FDG PET/CT in the next decade? counterpoint-no, not so fast! *Am J Roentgenol.* (2021) 216:307–8. doi: 10.2214/AJR.20.23794
23. Calais J. FAP: the next billion dollar nuclear theranostics target? *J Nucl Med.* (2020) 61:163–5. doi: 10.2967/jnumed.119.241232
24. Nishizawa S, Inubushi M, Ozawa F, Kido A, Okada H. Physiological FDG uptake in the ovaries after hysterectomy. *Ann Nucl Med.* (2007) 21:345–8. doi: 10.1007/s12149-007-0029-8
25. Navve D, Kaidar-Person O, Keidar Z. Physiological (18)F-FDG uptake patterns in female reproductive organs before and after chemotherapy treatments: assessment by PET/CT. *Med Oncol.* (2013) 30:598. doi: 10.1007/s12032-013-0598-4
26. Hughes EC. The effect of enzymes upon metabolism, storage, and release of carbohydrates in normal and abnormal endometria. *Cancer.* (1976) 38:487–502. doi: 10.1002/1097-0142(197607)38:1<487::aid-cncr2820380173>3.0.co;2-h
27. Annunziata S, Cuccaro A, Tisi MC, Hohaus S, Rufini V. FDG-PET/CT at the end of immuno-chemotherapy in follicular lymphoma: the prognostic role of the ratio between target lesion and liver SUV(max) (rPET). *Ann Nucl Med.* (2018) 32:372–7. doi: 10.1007/s12149-018-1243-2
28. Guo W, Pang Y, Yao L, Zhao L, Fan C, Ke J, et al. Imaging fibroblast activation protein in liver cancer: a single-center post hoc retrospective analysis to compare [(68)Ga]Ga-FAPI-04 PET/CT versus MRI and [(18)F]-FDG PET/CT. *Eur J Nucl Med Mol Imaging.* (2021) 48:1604–17. doi: 10.1007/s00259-020-05095-0
29. Kratochwil C, Flechsig P, Lindner T, Abderrahim L, Altmann A, Mier W, et al. (68)Ga-FAPI PET/CT: tracer uptake in 28 different kinds of cancer. *J Nucl Med.* (2019) 60:801–5. doi: 10.2967/jnumed.119.227967

Conflict of Interest: The authors declare that the research was conducted in the absence of any commercial or financial relationships that could be construed as a potential conflict of interest.

frontiers in Medicine

ORIGINAL RESEARCH
published: 10 November 2021
doi: 10.3389/fmed.2021.734476

Reducing Calibration Time in PET Systems Based on Monolithic Crystals

*Marta Freire, Gabriel Cañizares, Sara Echegoyen, Andrea Gonzalez-Montoro and Antonio J. Gonzalez**

Instituto de Instrumentación para Imagen Molecular, Centro Mixto CSIC—Universitat Politècnica de València, Valencia, Spain

In the past years, the gamma-ray detector designs based on the monolithic crystals have demonstrated to be excellent candidates for the design of high-performance PET systems. The monolithic crystals allow to achieve the intrinsic detector resolutions well below state-of-the-art; to increase packing fraction thus, increasing the system sensitivity; and to improve lesion detectability at the edges of the scanner field of view (FOV) because of their intrinsic depth of interaction (DOI) capabilities. The bottleneck to translate to the clinical PET systems based on a large number of monolithic detectors is eventually the requirement of mechanically complex and time-consuming calibration processes. To mitigate this drawback, several methods have been already proposed, such as using non-physically collimated radioactive sources or implementing the neuronal networks (NN) algorithms trained with simulated data. In this work, we aimed to simplify and fasten a calibration process of the monolithic based systems. The *Normal* procedure consists of individually acquiring a 11×11 ^{22}Na source array for all the detectors composing the PET system and obtaining the calibration map for each module using a method based on the Voronoi diagrams. Two reducing time methodologies are presented: (i) *TEST1*, where the calibration map of one detector is estimated and shared among all others, and (ii) *TEST2*, where the calibration map is slightly modified for each module as a function of their detector uniformity map. The experimental data from a dedicated prostate PET system was used to compare the standard calibration procedure with both the proposed methods. A greater similarity was exhibited between the *TEST2* methodology and the *Normal* procedure; obtaining spatial resolution variances within 0.1 mm error bars and count rate deviations as small as 0.2%. Moreover, the negligible reconstructed image differences (13% deviation at most in the contrast-to-noise ratio) and almost identical contrast values were reported. Therefore, this proposed method allows us to calibrate the PET systems based on the monolithic crystals reducing the calibration time by approximately 80% compared with the *Normal* procedure.

Keywords: positron emission tomography, monolithic crystals, calibration, total-body PET, whole-body PET

OPEN ACCESS

Edited by:
Martin Huellner,
University Hospital Zürich, Switzerland

Reviewed by:
Amirhossein Sanaat,
Geneva University Hospitals (HUG), Switzerland
Junwei Du,
University of California, Davis, United States

****Correspondence:***
Antonio J. Gonzalez
agonzalez@i3m.upv.es

Specialty section:
This article was submitted to Nuclear Medicine, a section of the journal Frontiers in Medicine

Received: *01 July 2021*
Accepted: *11 October 2021*
Published: *10 November 2021*

Citation:
Freire M, Cañizares G, Echegoyen S, Gonzalez-Montoro A and Gonzalez AJ (2021) Reducing Calibration Time in PET Systems Based on Monolithic Crystals. Front. Med. 8:734476. doi: 10.3389/fmed.2021.734476

INTRODUCTION

In the PET detectors, two main types of scintillator crystals are usually employed namely, pixelated and monolithic. The advantages and disadvantages of each one are extensively described elsewhere (1). They offer intrinsic resolutions that are well below the state-of-the-art and an improvement of the system sensitivity, as they do not contain zero detection zones, unlike the pixelated crystals. But the most significant feature of monolithic crystals is their inherent access to the light distribution (LD) profile of the scintillation events which allows to retrieve, in addition to the planar impact coordinates (*x,y*), accurate photon depth of interaction (DOI) information, unlike the pixelated crystals that require additional components to provide 3D positioning information (2, 3). The DOI information permits to correct for the parallax errors, which strongly affect the systems with small apertures (i.e., small animal and organ dedicated scanners), but also at the edges of the field of view (FOV) in the human size scanners. Both width and position of the source profile improve when applying the DOI correction independently of the system diameter (4, 5). Recently, the monolithic crystals are employed in the PET scanners achieving high sensitivity and spatial resolution (6–8). Moreover, regarding cost, analyzing the different providers for scintillator crystals and studying the price differences between the several pixel arrays and monolithic crystals with similar volumes, it can be concluded that they are cheaper than the traditional pixelated scintillators for the pixel sizes smaller than 1.5 mm × 1.5 mm, as the ones used in the pre-clinical PET imaging.

To accurately determine the energy and 3D impact position in the monolithic-based PET detectors, the calibration processes accounting for the possible non-uniformities or edge effects are required (9). The non-uniformities arise from different gains in the photosensors or readout channels, and eventually by the crystal light yields abnormalities. The edge effects result from the scintillation light truncation toward the crystal edges, reducing the accuracy of the photon impact coordinates determination and energy discrimination. For the pixelated-based detectors, the flood maps are easily and quickly found, since one source can be placed at the center of the PET scanner providing information of all the pixel elements. However, for the monolithic-based detectors, the calibration processes are typically based on scanning a collimated small size source across the entire monolithic surface while recording the measured and mechanical/known source positions (1). This procedure must be applied for each detector module of the PET scanner, which results in the time-consuming calibrations and requires using entangled hardware set-ups (9). For one single detector, the measurement for obtaining reference data might last about 30 min even when using the high activity sources.

Multiple methods have been proposed to ease the calibration processes in the monolithic assemblies; such as using reference data corresponding to a line of irradiation points instead of singular points (10 −13), utilizing an array of collimated sources (10), or using non-physically collimated sources (11, 12). An alternative approach, not requiring the calibration for each detector block of the PET system, is to carry out an accurate simulation of the detector responses either for Neural Networks (NN) training (13, 14) or for the generation of look-up-tables (LUTs) to be applied using the maximum likelihood expectation maximization methods (MLEM) (15).

In this work, we propose an approach to apply the detector calibration process based on the Voronoi diagrams (10) in the PET scanners based on a large number of monolithic detectors. The proposed methodology significantly reduces the calibration times while accounts and corrects for the possible differences among each individual detector module. Shortly, the method suggests using the combined accurate calibration of few detectors, to be applied after some tuning provided by uniform radiation, to all the other detectors. In the following, we describe this rather simple methodology, but never studied before in detail, and its experimental validation employing data from a prostate dedicated clinical PET scanner (16).

MATERIALS AND METHODS

Materials

Data were experimentally acquired using a clinical PET specifically designed for prostate imaging. The scanner is composed of a single ring with 24 detectors (16), each one comprising a LYSO:Ce ($Lu_{1.8}Y_2SiO_5$:Ce) monolithic crystal of 50 × 50 × 15 mm with the lateral surfaces black painted (absorbent paint) and the entrance face, such as a retro-reflector layer (10, 17), as shown in the images of the system in **Figure 1**. Each scintillation crystal is coupled to a photosensor array of 12 × 12 silicon photomultipliers (SiPMs) with 3 × 3 mm active area and 4.2 mm pitch (52% active are coverage) by means of optical grease (BC-630, Saint Gobain, France). The readout scheme provides the row and column SiPM signals, thus allowing to determine the 3D photon impact coordinates within the crystal (4, 18). The detector output signals are fed into a data acquisition (DAQ) system based on the 12-bit analog-to-digital converters (ADCs) with 1 GB ethernet connection, and the summed signal of either all SiPM rows or columns, was fed into a trigger board that allows coincidences within a 5 ns coincidence window. Further details about the system can be found in the reference (16).

The planar impact coordinates (*x*, *y*) were calculated using the rows and column SiPM signals by applying a modified version of the center of gravity algorithm (COG) in which the row and column values are risen to the power of 2 to improve the system linearity (19). The DOI value was estimated as E/I_{max} where E is the energy calculated as the sum of the rows or columns, and I_{max} is the maximum value of the row or column, respectively (12).

Calibration Process

Instead of sequentially moving individual radioactive sources across the crystal surface, which requires long calibration times, we used an array of 11 × 11 ^{22}Na radioactive sources (4.6 mm pitch and 1 mm in diameter, total activity ∼10 μCi) placed at the known positions. A 30 mm thick tungsten collimator, with drilled holes of 1.2 mm in diameter, was accurately aligned with the sources and placed at each crystal entrance. The acquired reference data were later post-processed using a software collimation method (defined as a trade-off between

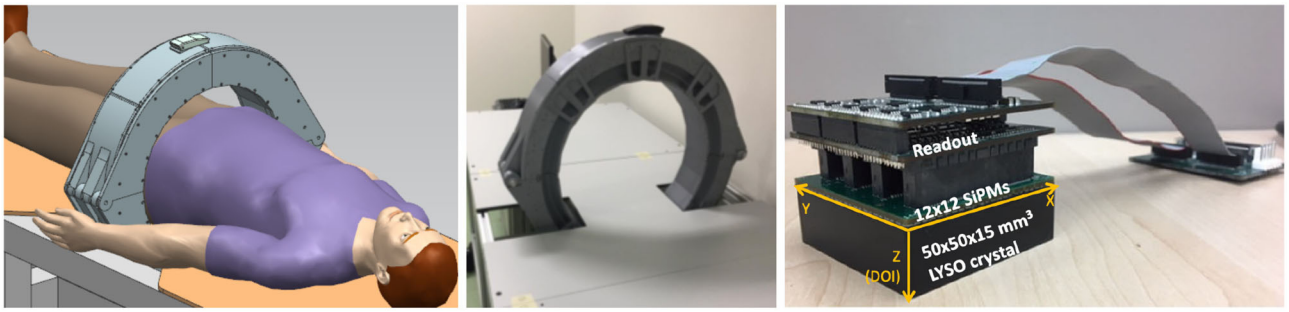

FIGURE 1 | The sketch (left) and photograph (right) of the prostate dedicated PET system used during the calibration tests.

the statistics and spatial resolution) that rejects the lines of response (LORs) with angles larger than 1.2 degrees measured from the detector normal (2). These two-steps, acquisition and collimation, resulted in the accurate flood maps composed by 121 measured positions as those shown in **Figure 2** (left).

The calculated 3D photon impact position and energy were calibrated using a method based on the Voronoi diagrams. The flood map of the 11 × 11 ^{22}Na sources (as shown in **Figure 2**) is used to generate a Voronoi diagram, thus permitting the partition of the crystal surface into 121 Voronoi cells and the extraction of five Voronoi factors for each cell (10). The VoronoiFactor$_X$ and VoronoiFactor$_Y$ were calculated as the deviation of the measured source position to the mechanical position and the VoronoiFactor$_E$ was determined as the deviation of the energy photopeak value in the channels to the value corresponding to the central Voronoi cell. Finally, we determined the lower and upper limits (a and b parameters) and sigma (σ_{int}) of the E/I$_{max}$ histogram for each Voronoi region using the DOI analytical expression extracted from the reference (14) (as shown in **Figure 2**). Two Voronoi factors were calculated corresponding to the limits a-σ_{int} and b+σ_{int} and then, considered to be equal to 0 and 15 mm (crystal thickness) to calibrate the measured E/I$_{max}$ into millimeters. As shown in the reference (10) for more detail of the process. These Voronoi factors were used to obtain five LUTs: two corresponding to the planar XY coordinates {LUT$_X$, LUT$_Y$}, two to the DOI {LUT$_{DOI1}$, LUT$_{DOI2}$}, and another one corresponding to the energy {LUT$_{Energy}$}. These LUTs are finally used to calibrate every impact. Data from the subjects or phantoms are off-line calibrated applying the calculated LUTs in an event-by-event process that includes a correction to the true LOR (parallax error compensation).

We have tested three different calibration methods, a conventional one detector-by-detector calibration, and two proposed modifications to shorten the calibration times:

(i) *Normal*, the 24 detectors of the PET scanner were individually calibrated as described above. This means, that a set of 5 individuals {LUT$_{X,Y,DOI1,DOI2,Energy}$} is generated from the flood map of each detector module. This calibration is considered as the ground-truth for comparison purposes. **Figure 2** shows the flood map of the 11 × 11 ^{22}Na sources, the energy and DOI histograms for one detector module of the prostate dedicated PET before (top panels) and after (bottom panels) calibration. Acquisition using the described array and activity might last about 2–3 h per detector, thus 48–72 h for the whole system without stop (at least 6 working days). Notice that the higher activities and the use of non-encapsulated sources, such as ^{18}F could accelerate these processes but potentially increase the radiation associated risk.

(ii) *TEST1*, the calibration set of only one random detector is carried out and, therefore only its {LUT$_{X,Y,DOI1,DOI2,Energy}$} are generated and shared among the other detectors without further corrections. With this approach, a total process calibration time of ∼ 3 h for the entire scanner was required. We have evaluated this method for two random detectors: *T1* and *T1B*, corresponding to the detectors M2 and M6, respectively.

(iii) *TEST2*, three random detectors of the PET scanner were individually calibrated and, to avoid an outlier detector performance, an averaged reference calibration map was obtained using the mean values of the calibration positions of the three detectors (as shown in **Figure 3** left). Thereafter, the calibration maps for each other detector were determined applying a shift map to such reference calibration map. The shift map was generated for each detector using their uniformity maps (as shown in **Figure 3**) acquired placing a relatively large uniform activity phantom at the center of the scanner FOV. Event accumulation can be observed at the edges of the uniform map due to the truncation of the LD closer to the edge of the monolithic crystal. The x and y coordinates for these regions were plotted, as shown in **Figure 2**, and a linear fit was used to estimate the slope following that event accumulation. The intersection of the lines allowed us to calculate the coordinates of the four corners. Then, four shift factors with respect to the reference ones were calculated and a natural neighbor interpolation methodology considering the four corners was applied to obtain the shift map for the entire surface. The shift map for each module was applied to the reference calibration map to obtain the new calibration map corresponding to each detector. Finally, the calibration maps were used to determine the Voronoi factors according to the reference (20). The Voronoi factors corresponding to the DOI and energy, were calculated using the uniformity measurements. A total

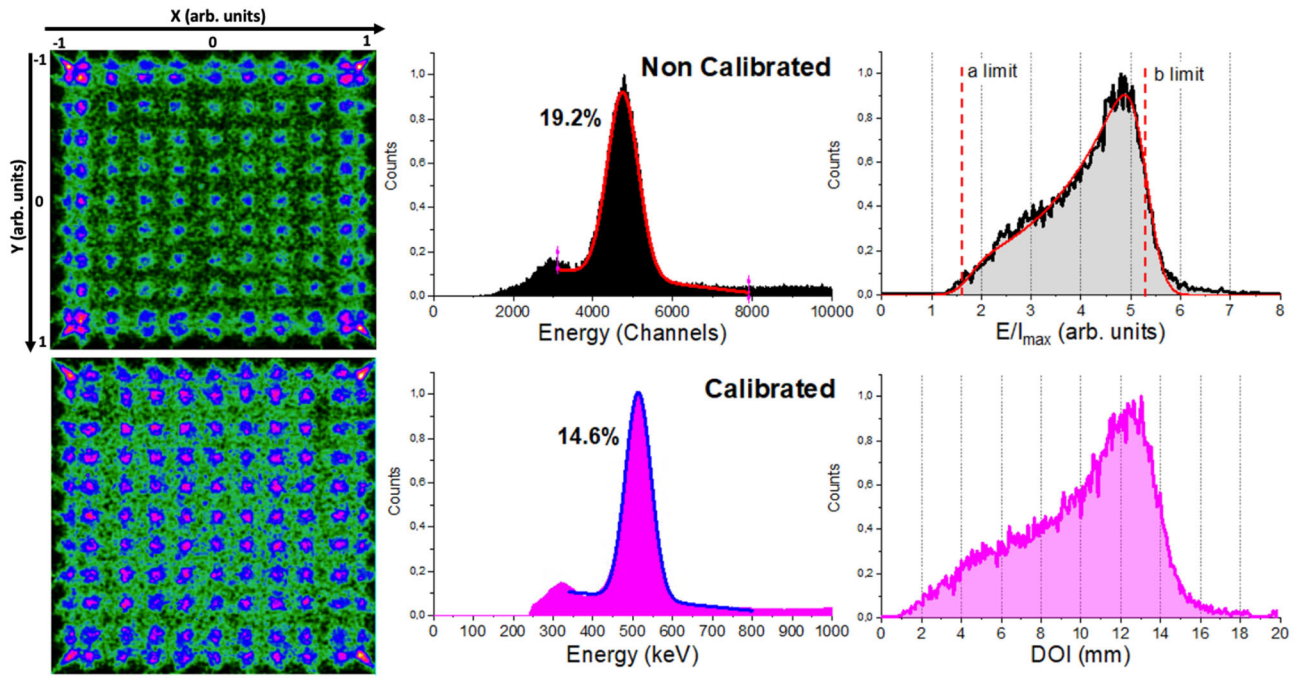

FIGURE 2 | From left to right, the image flood maps of the 11 × 11 ^{22}Na collimated sources before (top) and after (bottom) calibration using the *Normal* method, energy spectra, and depth of interaction (DOI) distribution for the whole detector.

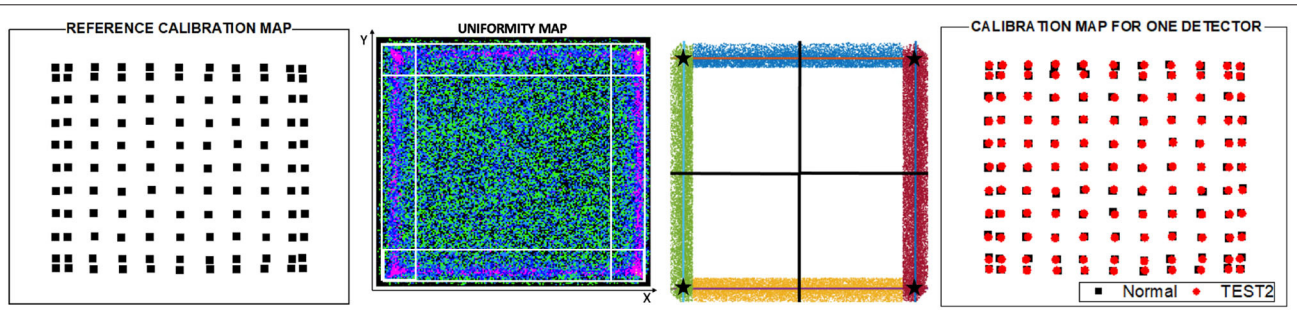

FIGURE 3 | From left to right, a reference calibration map obtained as the average of the calibration positions of three random detectors, example of a detector uniform map for one detector used to obtain the calibration map in *TEST2*, surface partition obtained from the four corners calculated as the intersection of the lines following the event accumulation and calibration positions obtained for one detector in the Normal calibration and after applying the TEST2.

calibration time of ∼ 10 h was consumed as: the uniformity acquisition (∼1 h) plus the three detectors calibration maps (6–9 h). For this case, three sets of three different detectors were used defining: *T2*, *T2B*, and *T2BB*, in particular detectors [M1, M9, and M21], [M5, M18, and M24], and [M7, M15, and M20] were used, respectively.

Evaluation of the Calibration Processes

The calibration accuracy of the proposed methods was evaluated by comparing the LUTs for *TEST1* and *TEST2* with the ground truth provided by the *Normal* case for each detector module of the prostate PET system. Thus, the correlation factors (CF) corresponding to X, Y, DOI1, DOI2, and energy, respectively, were determined for each detector module as:

$$CF^{i}_{X,Y,DOI1,DOI2,Energy} = \frac{(VoronoiFactor\ value^{i}_{X,Y,DOI1,DOI2,Energy})_{TEST}}{(VoronoiFactor\ value^{i}_{X,Y,DOI1,DOI2,Energy})_{Normal}} \quad (1)$$

where, i goes from 1 to 121 (each Voronoi diagram contains 121 values because 11 × 11 sources array was used for the calibration). Notice that, the range of values for the VoronoiFactor$_X$ and VoronoiFactor$_Y$ is [−1, 1] in arb. units; for the VoronoiFactor$_E$ it is [0, ∼10000] in channels and for the VoronoiFactor$_{DOI1,DOI2}$, it is [1, 8] in arb. units (as shown in **Figure 2** top). The mean of the 121 CF^i values was calculated,

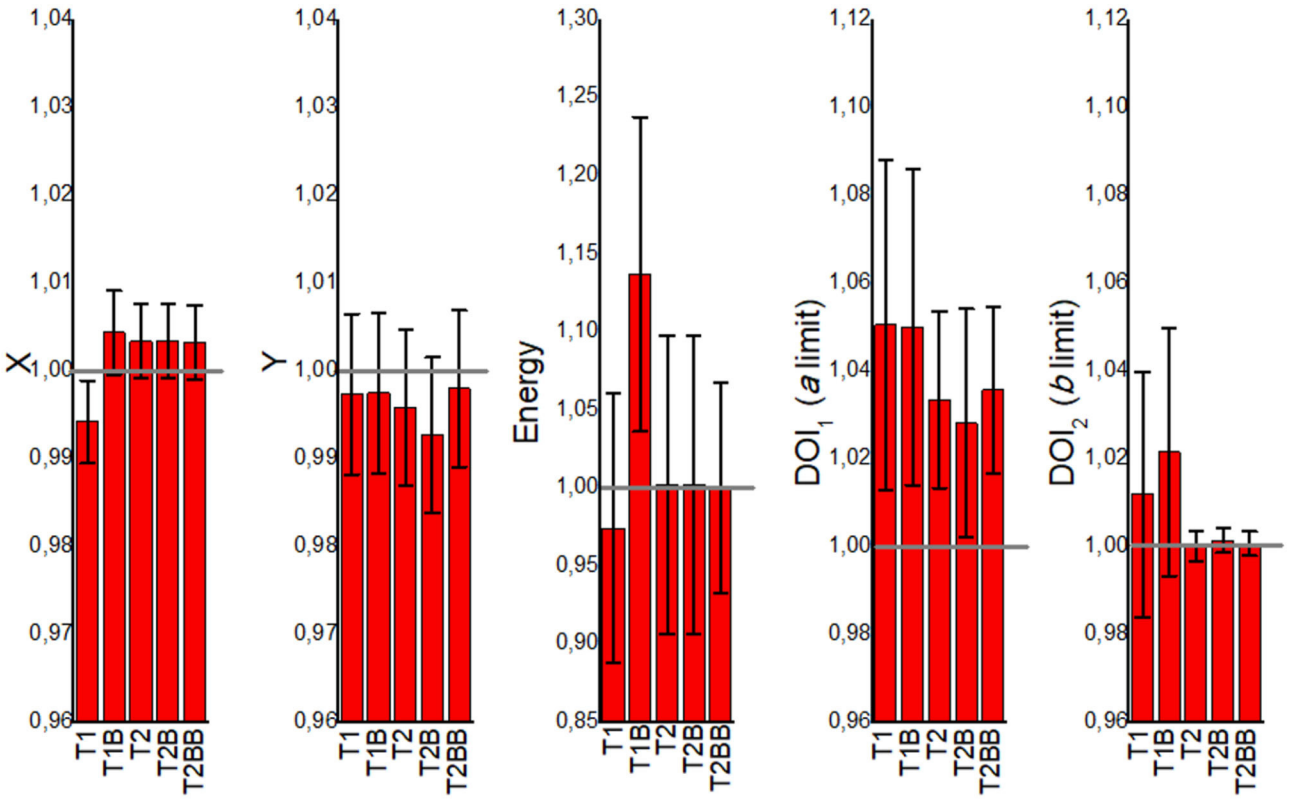

FIGURE 4 | The mean correlation factor (CF^i) values obtained from the VoronoiFactor$_X$, VoronoiFactor$_Y$, VoronoiFactor$_E$, VoronoiFactor$_{DOI1}$, and VoronoiFactor$_{DOI2}$ for all the detectors and calibration positions, and for all the proposed calibration cases.

obtaining five *CF* values corresponding to X, Y, DOI1, DOI2, and energy for each detector module. Finally, the mean of the $CF_{X,Y,DOI1,DOI2,Energy}$ values of all detector modules were calculated and considered as a good estimator of the validity of the two proposed approaches.

In addition, the three calibration methods were compared using the reconstructed images from the following datasets:

(i) Data of a small size ^{22}Na source (0.25 mm in diameter and $\sim$ 22 μCi activity) scanned across the radial axis of the scanner. The spatial resolution was estimated as the full width at half of the maximum (FWHM) of the source profiles.

(ii) Data acquired during the evaluation of the noise equivalent count rate (NECR) of the system. This dataset was used to provide hints about the count rates capabilities of the system as a function of the calibration method. Sub-optimal calibration of the detectors might lead to a decrease in the count rates.

(iii) Data acquired using a custom designed image quality (IQ) phantom made out of Polymethyl methacrylate (PMMA) with an outer diameter of 135 and 103 mm height. The IQ phantom contains six capillaries with diameters of 20, 15, 12, 9, 6, and 4.5 mm and 60 mm height each placed inside a warm background. A capillaries-to-background concentration ratio of 38 was used.

The reconstruction of the acquired data was performed using the Customizable and Advanced Software for Tomographic Reconstruction (CASToR) platform (21) and the ordered subset expectation maximization (OSEM) algorithm, with voxels sizes of 1 × 1 × 1 mm and virtual detector pixels of 1 × 1 mm. During the reconstruction process, three iterations and two subsets were used when the small size sources were imaged, whereas eight iterations and two subsets were employed for the image quality phantom. Additionally, both the attenuation and normalization corrections were applied. For the attenuation correction, the transmission information of a previous CT acquisition was used. The normalization was applied using data of an annulus filled with fluorodeoxyglucose (FDG) [as shown in reference (11)] and processed using the three different calibration approaches.

We have quantitatively evaluated the reconstructed IQ phantom calculating the contrast-to-noise ratio (CNR) and the contrast for all cases as:

$$CNR = \frac{Mean\ hot\ spot\ VOI - BackGround\ level}{Background\ standard\ deviation} \quad (2)$$

$$Contrast\ (\%) = 100 \times \frac{Mean\ hot\ spot\ VOI - Background\ level}{Mean\ hot\ spot} \quad (3)$$

where VOI stands for the Volume of Interest selected. Then, 12 VOIs were drawn distributed along the uniform warm area of the phantom to obtain the *background level* and *SD*. To calculate the

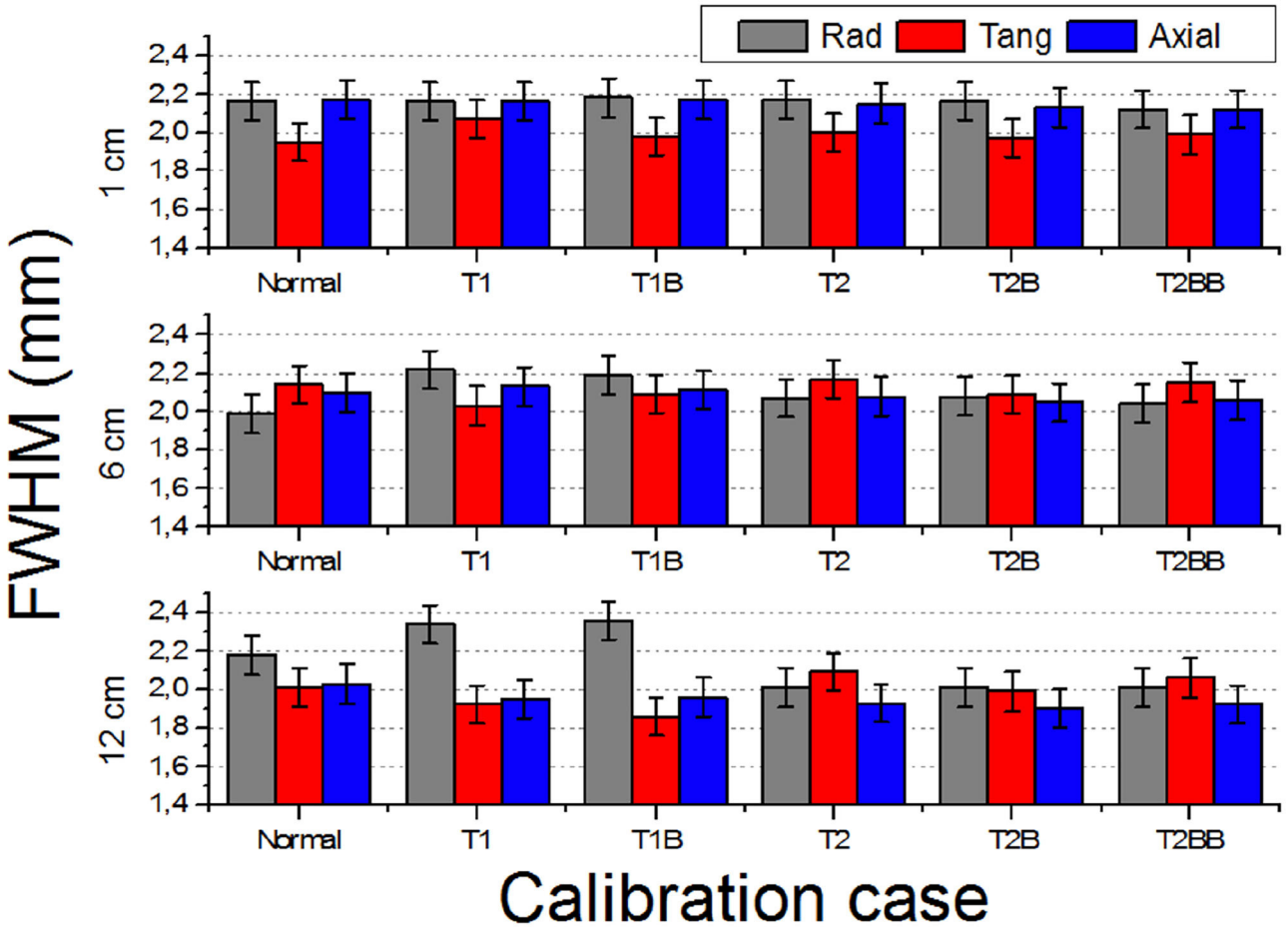

FIGURE 5 | Reconstructed full width at half of the maximum (FWHM) (three components: radial, tangential, and axial) of the 1 mm in diameter source at off-radial positions 1, 6, and 12 cm.

mean hot spot values, six VOIs were defined fitting each capillary dimension but with a centered height of 25 mm.

RESULTS

Detector Accuracy

Figure 4 shows the mean values for the CF^i parameters namely X and Y positions, energy, and DOI limits. The mean values are calculated for all 24 detector and for all 121 calibration positions within each detector block. The error bars are calculated as the SD of all these 24 × 121 values. The *T2*, *T2B*, and *T2BB* cases are typically close to 1, meaning that they reflect well the ground truth. However, the *T1* and *T1B* cases are in general further from 1.

Reconstructed Images

Figure 5 depicts the FWHM values (radial, tangential, and axial) of the reconstructed images of the ^{22}Na source versus the off-radial position. For the case closer to the center of the FOV (1 cm), all the cases exhibit very similar values. However, worse FWHM values are observed for the *T1* and *T1B* cases at radial positions far from the center, especially at the edges (12 cm) resulting in an elliptical shape of the sources.

Figure 6 depicts the count rate capabilities of the system for each calibration method. In general, there is a better agreement for the *TEST2* approaches with respect to the *Normal* case. Some deviations are observed for the NECR curves regarding the *TEST1* cases (also for the True and Scatter/random ones but not shown here) at high activities. We have calculated the ratios of the NECR for the *Normal* case with respect to all others. The average ratio for the *T2*, *T2B,* and *T2BB* cases is as small as 0.2, 0.1, and 0.1%, respectively, with SDs of about 1% only. However, we found the ratios of 7 and 2% for the *T1* and *T1B*, respectively.

Figure 7 shows the reconstructed IQ phantom after applying the described calibration processes for all the cases. Qualitatively, the images and profiles are very similar. Slightly less uniform background is observed for the *TEST1* cases, as it can also be appreciated in the shown slice and projection at the bottom panels.

We observe the CNR values that are in general poor, most likely due to low acquisition times (**Figure 8**). Comparing the results obtained between *Normal* and the other methods, the

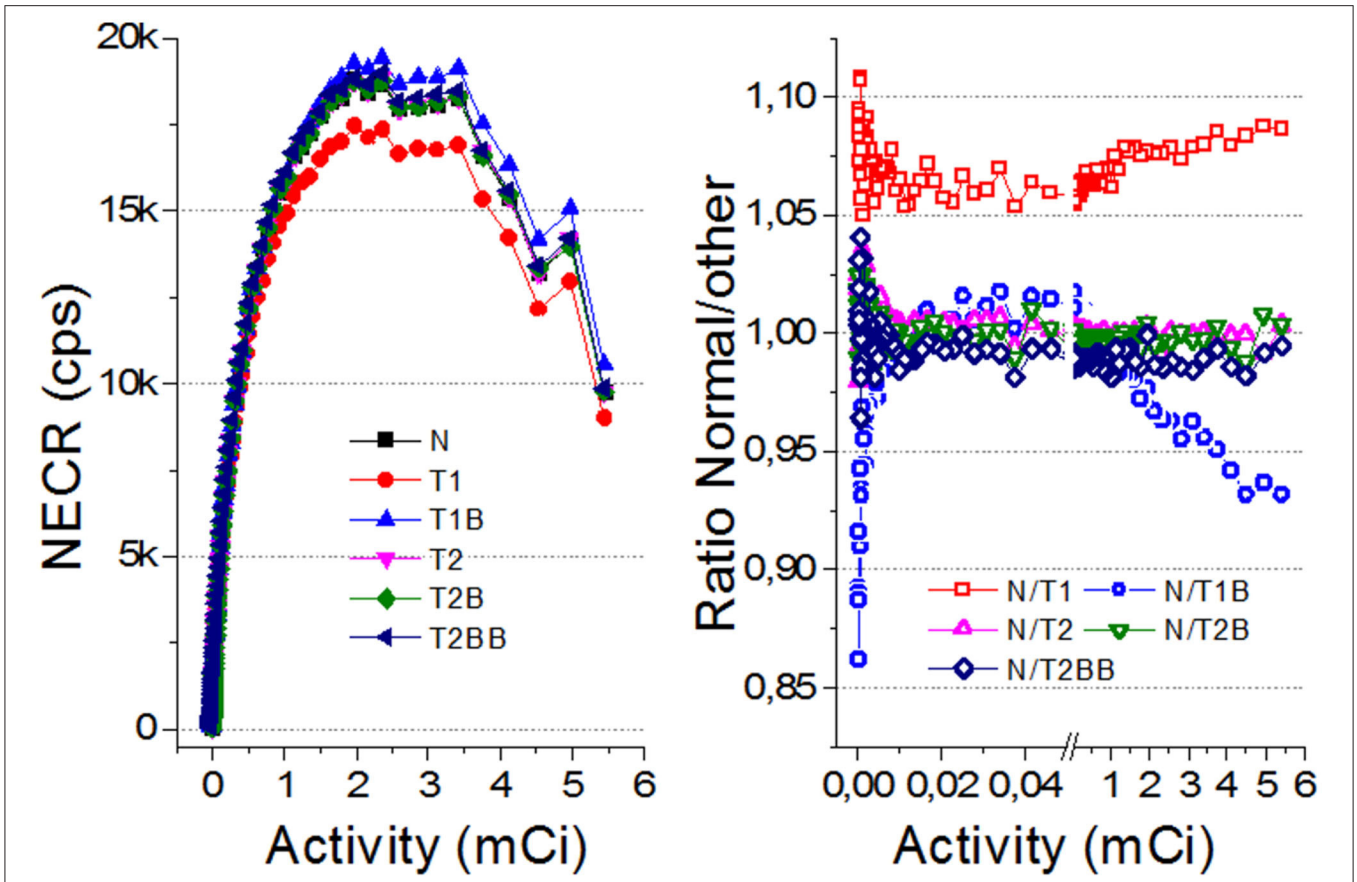

FIGURE 6 | (Left) The noise equivalent count rate (NECR) curves for all the evaluated cases. (Right) Ratio of the NECR values for *Normal* with respect to all others. Notice there is a break between 0.5 and 0.6 mCi to expand the axis for lower values.

CNR for *T1* and *T1B* are, on average, 28.5% lower. However, the *TEST2* cases exhibit similar values for the 4.5- and 6-mm rods, and better for the larger capillaries. An average improvement for all rods and tests of 8.4% is observed. We hypothesize that the improvement of CNR for the *TEST2* cases might be due to an improvement in the background uniformity caused by the averaging of three detector blocks.

DISCUSSION

In this work, we have studied the possibility to reduce the calibration time for monolithic-based PET systems. Different works are proposed to obtain reference dataset using the line sources and slit collimators or uncollimated sources without detector performance degradation, avoiding irradiating the crystal at a large number of known entry points across the entire surface, and thus, reducing the time calibration (6–11, 20, 22–24). Moreover, the use of simulated data for NN training or for LUT generation for ML position estimation (12, 13) allows for calibration time reduction. However, most of these methods demand higher computational requirements to be efficient.

In our approach, the calibration data are acquired using an array of collimated sources, instead of sequentially scanning individual radioactive sources across the crystal surface, which reduce the calibration times somewhat; however, in the *Normal* procedure each detector needs to be independently calibrated, which still leads to high time-consuming. Therefore, we have proposed two new calibration routines named *TEST1* and *TEST2* that reduce the calibration time from standard calibration of all 24 detectors of our prostate PET system (∼72 h) to just 10 h in the case of *TEST2* and 3 h in the case of *TEST1* (as shown in **Table 1**). Notice that the times were estimated considering the activity of a source that can be typically found in the instrumentation laboratories and, therefore, higher activity sources would linearly improve the process. Using the high radioactivity sources and two screw bar and step motors would allow to create a robotic instrument to speed up the calibration acquisition and to prevent the radiation hazard at the same time. However, for the PET systems already installed in the research laboratories or clinical sites, introducing such a hardware setup is sometimes difficult.

An important implication of this reduction is that allow one to perform the calibration in one single working journey without the requirement of stopping, thus avoiding the additional complications. The uniform flood maps are obtained routinely during the PET calibration processes when for instance the normalization is performed. By reducing the calibration time

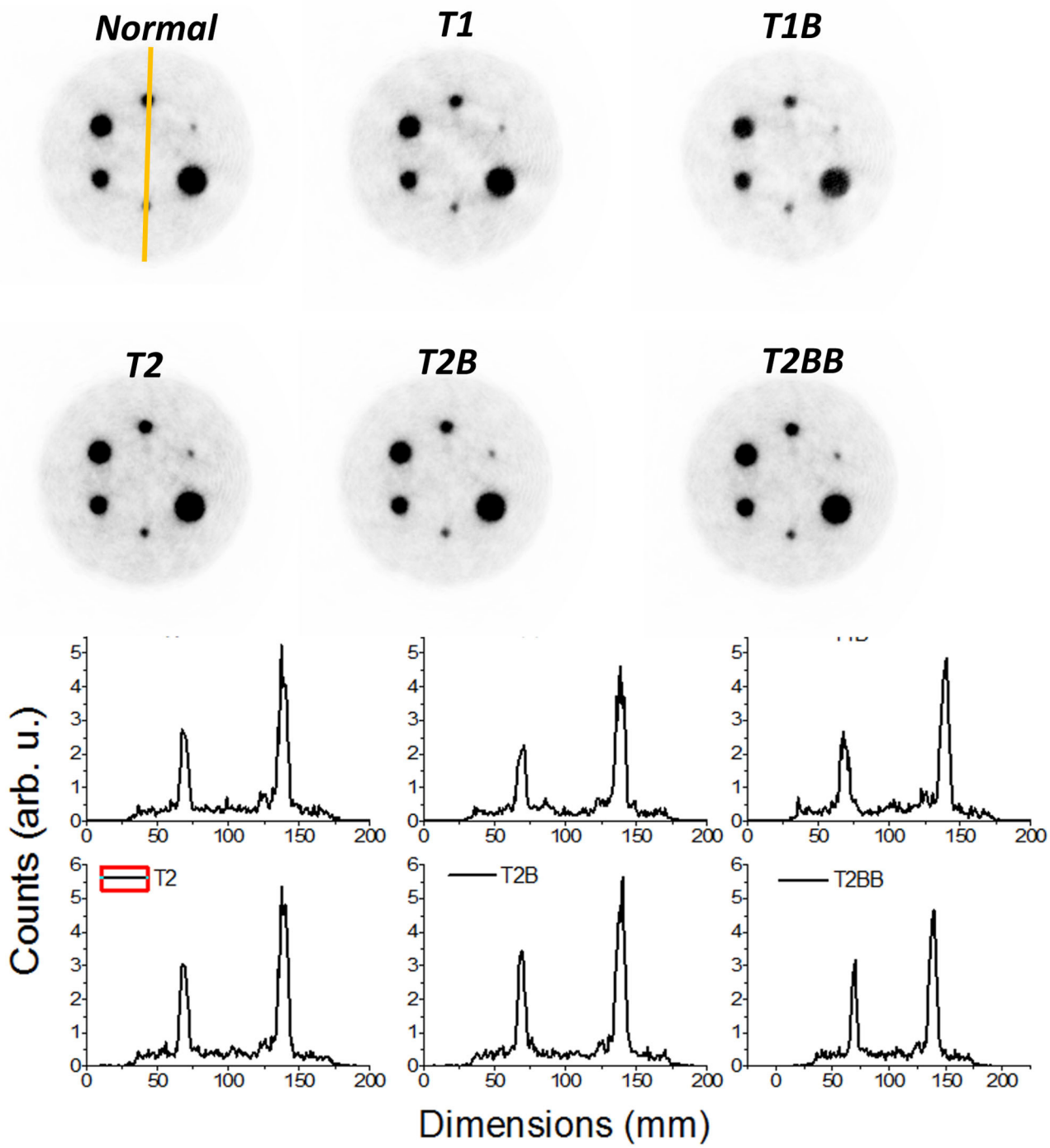

FIGURE 7 | Top panels, reconstructed images of the image quality (IQ) phantom. Only 15% of the low color scale was used. Bottom panels, profiles along the smallest marked rods in the *Normal* case.

without impacting the PET system performance, on the one hand, we are also minimizing the technical personnel exposure to radiation and, on the other hand, reducing the calibration cost associated to the supply of radioactive sources. An FDG dose used for calibration (370 MBq) costs approximately 275 € at our institution and lasts only for 1 day. Moreover, the proposed methodology simplifies the associated hardware, even if a low percentage of detectors are to be normally calibrated, such as in the *TEST2* (3/24 detectors), in comparison with calibrating all of them individually.

Our findings when comparing the results of the *TEST1* tests with the *Normal* case, showed some underperformance, as

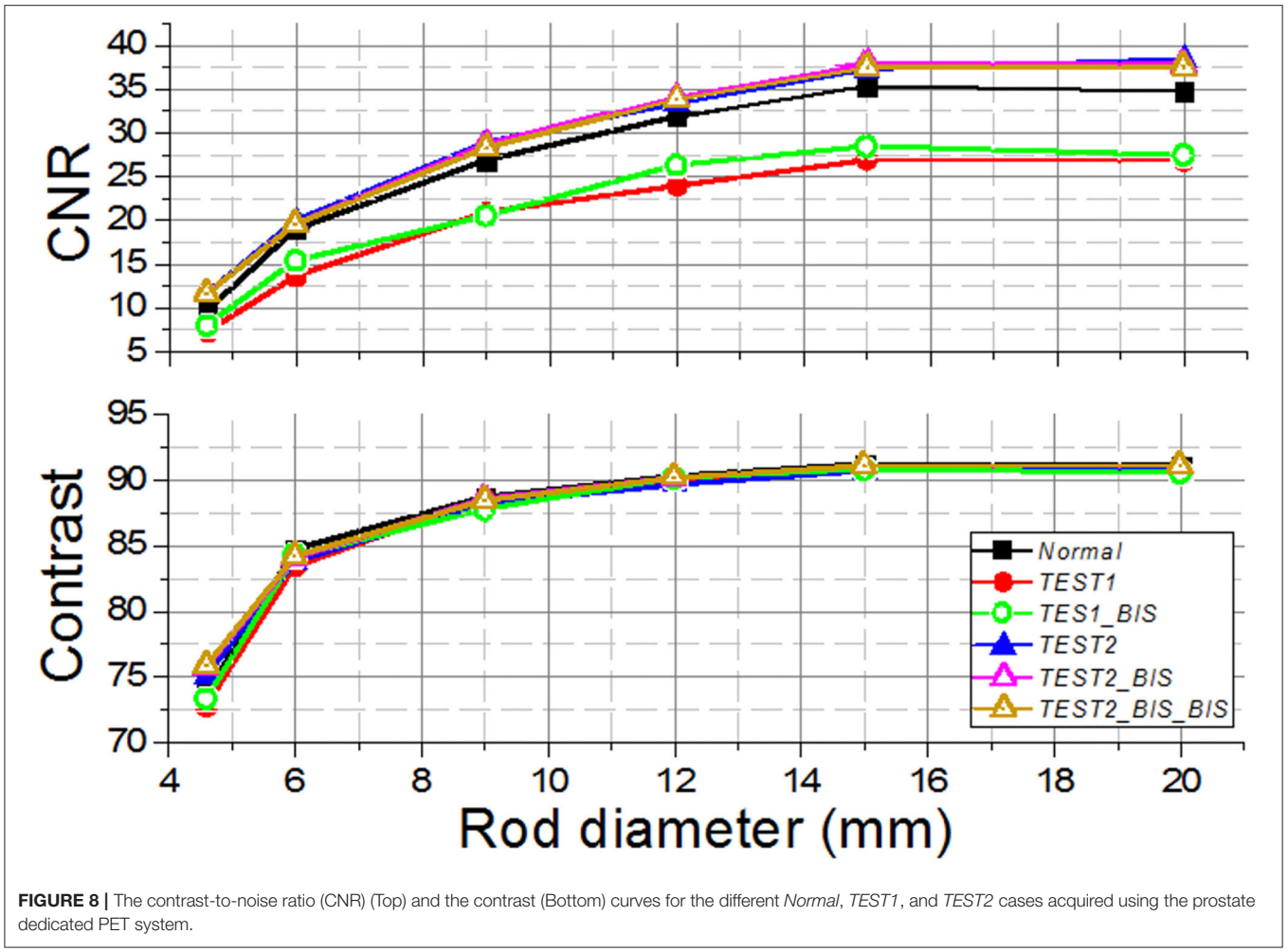

FIGURE 8 | The contrast-to-noise ratio (CNR) (Top) and the contrast (Bottom) curves for the different *Normal*, *TEST1*, and *TEST2* cases acquired using the prostate dedicated PET system.

TABLE 1 | Estimation of calibration time processes for the different methods.

	Steps/Tasks				Maximum calibration time
	Acquisitions		Computational time		
	11 × 11 ^{22}Na sources array. (∼10 μCi in total)	***Uniformity***	***Shift map***	***LUT generation***	
Normal	24 detectors × (2–3 h/detector) ≈ 72 h	1 h	–	24 detectors × (1 min/detector) ≈ 20 min	72.3 h
TEST1	2–3 h	1 h	–	1 min	3 h
TEST2	3 detectors × (2–3 h/detector) ≈ 9 h	1 h	24 detectors × (24 sec/detector) ≈ 10 min	24 detectors × (1 min/detector) ≈ 20 min	10.5 h

expected. Using one-detector calibration induces some errors due to many factors in the other 23 blocks, such as non-uniformities in the light collection, wrong coupling alignments of the photosensor and crystal, to name but a few. We observed that the reconstructed 1 mm sources show a worst performance for *T1* and *T1B* when they are far from the center FOV. Regarding the CNR, with the three different sets of detectors chosen for the *TEST2* cases, always a comparable performance to the *Normal* one case is found. Moreover, and somehow still to be understood, the CNR values outperformed those exhibited the *Normal* calibration. The *TEST1* cases are about 28% worst on average.

The *TEST2* methodology might be the key to exploit the use of large PET scanners based on the monolithic crystals

because it has demonstrated the capabilities to significantly reduce the calibration times without system degradation, enabling to calibrate a system with very low computational cost and in a reasonable time-period in a clinical domain. For a system, such as the MINDView PET insert with 60 detectors blocks of 50 × 50 × 20 mm monolithic LYSO crystals (13), we struggled with a 10 days calibration process using the high activities of FDG sources, when calibrating 2–3 detectors simultaneously.

Obviously, the proposed methods require the detectors of each system to behave relatively similar, which is the case of commercially available PET scanners, since they go through the quality assessment tests during the manufacturing process. In our case, the assembly of all 24 detectors building the PET system was carried out following the same procedure, the readout electronics components have very small tolerances, and all the crystals and SiPM arrays are provided by the same manufacturer.

CONCLUSION

We have proposed two new methodologies to reduce the calibration times for the monolithic-based PET systems and validated them using data acquired in a dedicated system for prostate imaging built of 24 monolithic crystals with 15 mm thickness each. The *TEST2* method, based on calibrating few detector blocks and then, making some fine tuning using the uniform calibration maps (routinely obtained when the corrections based on uniform radiation are applied), has shown the possibility of simplifying and accelerating the calibration process without system performance degradation and without high computational cost. Therefore, this proposed method allows to solve one of the obstacles to translate to the clinics large monolithic-based PET scanners.

DATA AVAILABILITY STATEMENT

The raw data supporting the conclusions of this article will be made available by the authors, without undue reservation.

AUTHOR CONTRIBUTIONS

MF has designed the experiments, the calibration of all detectors, and elaborated the draft manuscript. SE has analyzed part of the data. GC has taken care of the normalization correction and reconstruction of the data. AG-M has supervised the calibration processes and conducted the experimental data acquisitions. AG has managed the different contributions, wrote the final manuscript, and interpreted the results. All authors contributed to the article and approved the submitted version.

FUNDING

This work was supported in part by the Spanish Ministerio de Ciencia e Innovacion under Grant No. PID2019-107790RB-C21 and co-funded by the European Union ERDF funds (European Regional Development Fund [ERDF]) of the Comunitat Valenciana 2014-2020, with reference IDIFEDER/2018/032 (High-Performance Algorithms for the Modeling, Simulation, and early Detection of diseases in Personalized Medicine). This work was in part also supported by the Imagen Molecular de Alta Sensibilidad (IMAS) project launched by the Conselleria de Sanitat Universal i Salut Publica of the Goverment of Valencia Region, announced in the BOE 328, December 28, 2020, co-funded at 50% by the ERDF. AG-M was supported by Valid Program for Researchers in Postdoctoral Phase of the Ministry of Labor and Social Economy (Generalitat de Valencia) and the EU Social Fund. MF was supported by the Program for Researchers in Predoctoral Phase of the Ministry of Labor and Social Economy (Generalitat de Valencia) and the EU Social Fund.

REFERENCES

1. Gonzalez-Montoro A, Gonzalez AJ, Pourashraf S, Miyaoka RS, Bruyndonckx P, Chinn G, et al. Evolution of PET detectors and event positioning algorithms using monolithic scintillation crystals. *IEEE Trans Rad Plasma Med Sci.* (2021) 5:282. doi: 10.1109/TRPMS.2021.3059181
2. Gonzalez-Montoro A, Pierce LA, Hunter WJC, Gonzalez AJ, Miyaoka R. Validation of photon collimation techniques for monolithic PET detector calibration. *IEEE Trans Rad Plasma Med Sci.* (2020). doi: 10.1109/TRPMS.2020.3043397
3. Du J, Ariño-Estrada G, Bai X. and Cherry SR Performance comparison of dual-ended readout depth-encoding PET detectors based on BGO and LYSO crystals. *Phys Med Biol.* (2020) 65:5030. doi: 10.1088/1361-6560/abc365
4. Gonzalez AJ, Aguilar A, Conde P, Hernandez L, Moliner L, Vidal LF, et al. A PET Design Based on SiPM and Monolithic LYSO Crystals: Performance Evaluation. *IEEE Trans Nucl Scie.* (2016) 63:2471–77. doi: 10.1109/TNS.2016.2522179
5. Mohammadi I, Castro JFC, Correia PMM, Silva ALM. and Veloso FCA Minimization of parallax error in positron emission tomography using depth of interaction capable detectors: methods and apparatus. *Biomed Phys Eng Express.* (2019) 5:06200. doi: 10.1088/2057-1976/ab4a1b
6. Mikhaylova E, Tabacchini V, Borghi G, Mollet P, D'Hoe E, Schaart DR. Optimization of an ultralow-dose high-resolution pediatric PET scanner design based on monolithic scintillators with dual-sided digital SiPM readout: a simulation study. *Phys Med Biol.* (2017) 62:8402. doi: 10.1088/1361-6560/aa8eb2
7. Sanaat A, Ashrafi-Belgabad A, Zaidi H. Polaroid-PET: a PET scanner with detectors fitted with Polaroid for filtering unpolarized optical photons—a Monte Carlo simulation study. *Phys Med Biol.* (2020) 65:235044. doi: 10.1088/1361-6560/abaeb8
8. Sanaat A, Arabi H, Ay MR, Zaidi H. Novel preclinical PET geometrical concept using a monolithic scintillator crystal offering concurrent enhancement in spatial resolution and detection sensitivity: a simulation study. *Phys Med Biol.* (2020) 65:045013. doi: 10.1088/1361-6560/ab63ef
9. España S, Marcinkowski R, Keereman V, Vandenberghe S, Van Holen R. DigiPET: Sub-millimeter spatial resolution small-animal PET imaging using thin monolithic scintillators. *Phys Med Biol.* (2014) 59:3405–20. doi: 10.1088/0031-9155/59/13/3405
10. Freire M, Gonzalez-Montoro A, Sanchez F, Benlloch JM, Gonzalez AJ. Calibration of gamma ray impacts in monolithic-based detectors using voronoi diagrams. *IEEE Tran Rad Plasma Med Sci.* (2019) 4:350–60. doi: 10.1109/TRPMS.2019.2947716

11. España SK, Deprez van Holen R, Vandenberghe S. Fast calibration of SPECT monolithic scintillation detectors using un-collimated sources. *Phys Med Biol.* (2013) 58:4807–25. doi: 10.1088/0031-9155/58/14/4807
12. Fan P, Wang S, Wu Z, Liu Y, Ma T. *Monolithic PET detector calibration using uncollimated source and gamma interaction position distribution constrain*. In: Proc. IEEE NSS/MIC (2017). p. 1–5. doi: 10.1109/NSSMIC.2017.8532720
13. Iborra A, Gonzalez AJ, Gonzalez-Montoro A, Bousse A. and Visvikis D Ensemble of neural networks for 3D position estimation in monolithic PET detectors. *Phys Med Biol.* (2019) 64:5010–3. doi: 10.1088/1361-6560/ab3b86
14. Sanaat A, Zaidi H. Depth of interaction estimation in a preclinical PET scanner equipped with monolithic crystals coupled to SiPMs using a deep neural network. *Appl Sci.* (2020) 10:4753. doi: 10.3390/app10144753
15. Park JH, Lee S. Monte carlo simulations-based maximum-likelihood position estimation for monolithic scintillation detectors. *J Korean Phys Soc.* (2019) 74:812–5. doi: 10.3938/jkps.74.812
16. Cañizares G, Gonzalez-Montoro A, Freire M, Lamprou E, Barrio J, Sanchez F, et al. Pilot performance of a dedicated prostate PET suitable for diagnosis and biopsy guidance. *EJNMMI Phys.* (2020) 7:38. doi: 10.1186/s40658-020-00305-y
17. Gonzalez-Montoro A, Aguilar A, Cañizares G, Conde P, Hernandez L, Vidal LF, et al. Performance study of a large monolithic LYSO PET detector with accurate photon DOI using retroreflector layers. *IEEE Trans Rad Plasma Med Scie.* (2017) 1:229–37. doi: 10.1109/TRPMS.2017.2692819
18. Gonzalez AJ. Gonzalez-Monotoro, A, Vidal LF, Barbera J, Aussenhofer S, Hernandez L, et al. Initial Results on the MINDView PET Insert Inside the 3T mMR. *IEEE Trans Rad Plasma Med Sci.* (2019) 3:343–51. doi: 10.1109/TRPMS.2018.2866899
19. Pani R, Bettiol M, Preziosi E, Cinti MN, Borrazzo C, Pellegrini R et al. Position algorithm for monolithic scintillation crystals based on charge projection readout. *J Inst.* (2016) 11:C01061. doi: 10.1088/1748-0221/11/01/C01061
20. Solovov VN, Belov VA, Akimov DY, Araujo HM, Barnes EJ, Burenkov AA, et al. Position reconstruction in a dual phase xenon scintillation detector. *IEEE Trans Nucl Sci.* (2012) 59:3286–93. doi: 10.1109/TNS.2012.2221742
21. Merlin T, Stute S, Benoit D, Bert J, Carlier T, Comtat C, et al. CASToR: a generic data organization and processing code framework for multi-modal and multi-dimensional tomographic reconstruction. *Phys Med Biol.* (2018) 63:5505. doi: 10.1088/1361-6560/aadac1
22. van Dam HT, Seifert S, Vinke R, Dendooven P, Lohner H, Beekman FJ, Schaart DR. Improved nearest neighbor methods for gamma photon interaction position determination in monolithic scintillator PET detectors. *IEEE Trans Rad Plasma Med Scie.* (2011) 58:2139–47. doi: 10.1109/TNS.2011.2150762
23. Borghi G, Tabacchini V, Seifert S, Schaart DR. Experimental validation of an efficient fan-beam calibration procedure for *k*-nearest neighbor position estimation in monolithic scintillator detectors. *IEEE Trans Rad Plasma Med Scie.* (2015) 62:57–67. doi: 10.1109/TNS.2014.2375557
24. Müller F, Schug D, Hallen P, Grahe J, Schulz V. Gradient tree boosting-based positioning method for monolithic scintillator crystals in positron emission tomography. *IEEE Trans Rad Plasma Med Scie.* (2018) 2:411–21. doi: 10.1109/TRPMS.2018.2837738

Conflict of Interest: The authors declare that the research was conducted in the absence of any commercial or financial relationships that could be construed as a potential conflict of interest.

Publisher's Note: All claims expressed in this article are solely those of the authors and do not necessarily represent those of their affiliated organizations, or those of the publisher, the editors and the reviewers. Any product that may be evaluated in this article, or claim that may be made by its manufacturer, is not guaranteed or endorsed by the publisher.

frontiers in Medicine

ORIGINAL RESEARCH
published: 22 November 2021
doi: 10.3389/fmed.2021.725387

Short 2-[^{18}F]Fluoro-2-Deoxy-D-Glucose PET Dynamic Acquisition Protocol to Evaluate the Influx Rate Constant by Regional Patlak Graphical Analysis in Patients With Non-Small-Cell Lung Cancer

Luca Indovina[1], Valentina Scolozzi[2], Amedeo Capotosti[1], Stelvio Sestini[3], Silvia Taralli[2], Davide Cusumano[1], Romina Grazia Giancipoli[2], Gabriele Ciasca[1,4], Giuseppe Cardillo[5] and Maria Lucia Calcagni[2,6]*

[1] Fondazione Policlinico Universitario A. Gemelli IRCCS, Rome, Italy, [2] Unità Operativa Complessa (UOC) di Medicina Nucleare, Dipartimento di Diagnostica per Immagini, Radioterapia Oncologica ed Ematologia, Fondazione Policlinico Universitario A. Gemelli IRCCS, Rome, Italy, [3] Nuclear Medicine Unit, NOP S. Stefano, Prato, Italy, [4] Università Cattolica del Sacro Cuore, Rome, Italy, [5] Unit of Thoracic Surgery, San Camillo Forlanini Hospital, Rome, Italy, [6] Dipartimento Universitario di Scienze Radiologiche ed Ematologiche, Università Cattolica del Sacro Cuore, Rome, Italy

OPEN ACCESS

Edited by:
Ronan Abgral,
Centre Hospitalier Regional Universitaire (CHU) de Brest, France

Reviewed by:
Nicolas A. Karakatsanis,
Cornell University, United States
Virginia Liberini,
University of Turin, Italy

***Correspondence:**
Valentina Scolozzi
valentina.scolozzi@gmail.com

Specialty section:
This article was submitted to Nuclear Medicine, a section of the journal Frontiers in Medicine

Received: 15 June 2021
Accepted: 04 October 2021
Published: 22 November 2021

Citation:
Indovina L, Scolozzi V, Capotosti A, Sestini S, Taralli S, Cusumano D, Giancipoli RG, Ciasca G, Cardillo G and Calcagni ML (2021) Short 2-[^{18}F]Fluoro-2-Deoxy-D-Glucose PET Dynamic Acquisition Protocol to Evaluate the Influx Rate Constant by Regional Patlak Graphical Analysis in Patients With Non-Small-Cell Lung Cancer. Front. Med. 8:725387. doi: 10.3389/fmed.2021.725387

Purpose: To test a short 2-[^{18}F]Fluoro-2-deoxy-D-glucose (2-[^{18}F]FDG) PET dynamic acquisition protocol to calculate K_i using regional Patlak graphical analysis in patients with non-small-cell lung cancer (NSCLC).

Methods: 24 patients with NSCLC who underwent standard dynamic 2-[^{18}F]FDG acquisitions (60 min) were randomly divided into two groups. In group 1 ($n = 10$), a population-based image-derived input function (pIDIF) was built using a monoexponential trend (10–60 min), and a leave-one-out cross-validation (LOOCV) method was performed to validate the pIDIF model. In group 2 ($n = 14$), K_i was obtained by standard regional Patlak plot analysis using IDIF (0–60 min) and tissue response (10–60 min) curves from the volume of interests (VOIs) placed on descending thoracic aorta and tumor tissue, respectively. Moreover, with our method, the Patlak analysis was performed to obtain $K_{i,s}$ using $IDIF_{Fitted}$ curve obtained from PET counts (0–10 min) followed by monoexponential coefficients of pIDIF (10–60 min) and tissue response curve obtained from PET counts at 10 min and between 40 and 60 min, simulating two short dynamic acquisitions. Both IDIF and $IDIF_{Fitted}$ curves were modeled to assume the value of 2-[^{18}F]FDG plasma activity measured in the venous blood sampling performed at 45 min in each patient. Spearman's rank correlation, coefficient of determination, and Passing–Bablok regression were used for the comparison between K_i and $K_{i,s}$. Finally, $K_{i,s}$ was obtained with our method in a separate group of patients (group 3, $n = 8$) that perform two short dynamic acquisitions.

Results: Population-based image-derived input function (10–60 min) was modeled with a monoexponential curve with the following fitted parameters obtained in group 1: $a = 9.684$, $b = 16.410$, and $c = 0.068$ min^{-1}.

The LOOCV error was 0.4%. In patients of group 2, the mean values of K_i and $K_{i,S}$ were 0.0442 ± 0.0302 and 0.33 ± 0.0298, respectively ($R^2 = 0.9970$). The Passing–Bablok regression for comparison between K_i and $K_{i,S}$ showed a slope of 0.992 (95% CI: 0.94–1.06) and intercept value of −0.0003 (95% CI: −0.0033–0.0011).

Conclusions: Despite several practical limitations, like the need to position the patient twice and to perform two CT scans, our method contemplates two short 2-[^{18}F]FDG dynamic acquisitions, a population-based input function model, and a late venous blood sample to obtain robust and personalized input function and tissue response curves and to provide reliable regional K_i estimation.

Keywords: PET dynamic acquisition, Patlak graphical analysis, non-small-cell lung cancer, influx rate constant, 2-[^{18}F]Fluoro-2-deoxy-D-glucose

INTRODUCTION

The 2-[^{18}F]Fluoro-2-deoxy-D-glucose (2-[^{18}F]FDG) Positron Emission Tomography/Computed Tomography (PET/CT) is a well-established imaging modality for staging, restaging, and monitoring treatment response in patients with malignancy (1–3). Absolute quantification of 2-[^{18}F]FDG concentration, related to the local metabolic rate of glucose consumption measured with full kinetic analysis of time-activity curves, has proven to better characterize the tumor cell behavior and to correlate with histopathological data and prognosis (4–6). Nevertheless, some key points of full kinetic analysis, mainly the long dynamic acquisition and arterial blood sampling, limit the use of such an approach in a clinical setting. For these reasons, less-invasive approaches, including measurements of semiquantitative parameters such as the most common standard uptake value (SUV), are extensively used routinely (7–9). However, it has shown that the accuracy of SUV depends on several factors, including the standardization of technical parameters (e.g., acquisition protocol, glucose blood level, scan time window, recovery coefficient, partial volume effect, region-of-interest definition, and different PET scanners), which can affect the reliability of uptake values (10–13).

The Patlak graphical analysis is a valid alternative to full kinetic analysis for radioligands with irreversible kinetics as 2-[^{18}F] FDG since the activity of the phosphatases is considered negligible (14). The Patlak analysis provides the value of the influx rate constant K_i [min^{-1}] related to the metabolic rate of glucose in tissue. The K_i parameter is calculated from the slope of a straight line that correlates the integral radioligand activity in the blood pool with radioligand activity in the tissue (15). For this purpose, a long PET dynamic acquisition lasting at least 60 min is considered mandatory to calculate the time-activity curves of 2-[^{18}F]FDG in the blood (input function) and tissue (tissue response). Several efforts have been made to simplify the input function estimation with less- or non-invasive methods, such as the arterialized venous blood sampling (16), the image-derived input function (IDIF) estimation (17–20), the population input function modeling (21–24), the image segmentation methods (25, 26), and to overcome difficulties related to the long-lasting dynamic acquisition (27–30).

To reduce the dynamic 2-[^{18}F]FDG PET acquisition time (28–30), the aim of this study was to test a short dynamic protocol to obtain the input function and the tissue response curves to calculate K_i using the Patlak analysis and to compare it with K_i obtained using the standard long dynamic acquisition protocol in patients with non-small cell lung cancer (NSCLC).

MATERIALS AND METHODS

Patients

24 patients (15 male patients, mean age 69 ± 11 years) with histologically proven NSCLC, referred for staging to PET/CT center of Fondazione Policlinico Universitario A. Gemelli IRCCS in Rome by the local Thoracic Surgery Unit of San Camillo Forlanini Hospital, were enrolled. All patients ($n = 24$) underwent standard long (0–60 min) dynamic PET acquisition over the thorax followed by a total body scan. Patients were randomly divided into two groups: group 1 ($n = 10$; six male patients, mean age 70 ± 12 years) was used to extrapolate and validate the population-based image-derived input function (pIDIF); group 2 ($n = 14$; nine male patients, mean age 69 ± 10 years) was used to compare K_i obtained with our method (simulating two short dynamic acquisition and using the pIDIF validated in group 1) with K_i obtained using the standard long dynamic acquisition. Finally, a separate third group of patients ($n = 8$; seven male patients, mean age 71 ± 11 years) with histologically proven NSCLC were enrolled to test the feasibility of our method in clinical practice. All patients ($n = 8$) underwent two separate short dynamic PET acquisitions over the thorax followed by a total body scan. The local institution's ethics committee (Comitato Etico Lazio 1) approved this retrospective study, waiving written informed consent for participation.

2-[^{18}F]FDG PET/CT: Acquisition and Reconstruction Parameters

All patients were fasted for at least 6 h and in normoglycemic (glucose level < 150 mg/dl) conditions before PET acquisition. PET/CT studies were performed using a full-ring CT and PET-integrated tomograph (3D Biograph mCT, Siemens Healthineers, Chicago, Illinois). Patients were placed in a supine position with the thorax in the field of view and the arms placed over the head.

The acquisition protocol started with a CT scout including the thoracic aorta and lungs. A low-dose CT was performed (90 mA, 120 kV) for the attenuation correction of emission data and morphological information with a field of view of 21 cm. The transaxial CT matrix size was 512 × 512 (1 × 1 × 3 mm).

Standard Long Dynamic Acquisition

Patients of groups 1 and 2 were intravenously injected with 134–507 MBq of 2-[^{18}F]FDG, using an infusion pump (model RADInject; Tema Sinergie, Faenza, RA, Italy); 10 ml of 2-[^{18}F]FDG was administered at a rate of 4.32 ml/s followed by a 10-ml saline flush. After 2-[^{18}F]FDG injection, a thorax dynamic list-mode acquisition lasting 60 min was started with the following framing: 24 frames of 5 s each, 12 frames of 15 s each, and 11 frames of 5 min each. A venous blood sampling was performed at 45 min post-injection. Dynamic PET data were corrected for random events, dead time, and attenuation. PET data were reconstructed with the ordered subset expectation maximization (OSEM) algorithm, including time-of-flight and UltraHD recovery with 21 subsets and two iterations. The transaxial PET matrix size was 256 × 256 (3.18m × 3.18 × 3 mm).

Two Short Dynamic Acquisitions

Patients of group 3 were intravenously injected with 205–320 MBq of 2-[^{18}F]FDG using the same infusion pump and protocol of groups 1 and 2. After 2-[^{18}F]FDG injection, early thorax dynamic list-mode acquisition lasting 10 min was started with the following framing: 24 frames of 5 s each, 12 frames of 15 s each, and one frame of 5 min each; late thorax dynamic list-mode acquisition lasting 20 min was started at 40 min post-injection with the following framing: four frames of 5 min each. Two low-dose CTs were performed for each acquisition to assess an accurate attenuation correction of the two PET images. Patients left the examination PET/CT room in the period between early and late PET/CT examinations. A venous blood sampling was performed at 45-min post-injection. The same algorithm and reconstruction parameters of the standard long dynamic acquisition were used.

Input Function

In each patient of group 1 (n = 10), the standard input function was obtained drawing a volume of interest (VOI) on the descending thoracic aorta during the summed first nine frames of dynamic acquisition (45 s) and superimposing it on all subsequent frames of dynamic acquisition (0–60 min) (31). For each patient, the venous blood sampling performed at 45 min after injection was centrifuged for 5 min (Rotofix 32A; Hettich Italia S.r.l., Milano, Italy) to separate the plasma from the cellular components. The 2-[^{18}F]FDG activity in 1 ml of plasma was measured in a gamma counter (Wallac Wizard 1480−3″; PerkinElmer, Waltham, Massachusetts) cross-calibrated with the tomograph. The IDIF curve was modeled to assume the value of 2-[^{18}F]FDG activity measured in the plasma (32); in particular, a scale factor equal to the ratio between the plasma activity measured in 1 ml of plasma, and the activity measured in the IDIF at 45 min was used to impose the IDIF activity value at 45 min equal to the plasma activity measured in the blood sample, considering the plasma activity as the gold standard value and avoiding any problem regarding spillover effect or partial volume effect in the VOI signal.

To extrapolate and validate the input function used in our method, it was reconstructed taking into account only data from 0 to 10 min of the standard long dynamic acquisition, simulating an early short dynamic acquisition (pIDIF). In particular, for each patient of group 1 (n = 10), the early phase of the input function was built taking into account the first 10 min of the patient's input function curve of the standard long dynamic acquisition. The remaining part was reconstructed with a monoexponential function (23, 33) since all input function curves obtained from standard dynamic protocol showed a trend that can be well represented by a monoexponential function (1):

$$C_p(t) = a + b \cdot e^{(-c \cdot t)} \quad (1)$$

where a, b, and c coefficient values were obtained as mean values of monoexponential fit of each 10 IDIF, measured from 10 to 60 min in patients of group 1.

Then, a specific patient input function was built imposing the pIDIF 2-[^{18}F]FDG activity value at 45 min equal to the plasma activity in each patient measured at 45 min from the venous sample ($IDIF_{Fitted}$).

Lastly, the LOOCV method was performed to validate the method of pIDIF reconstruction.

K_i Estimation Using the Standard Dynamic Protocol

The K_i parameter was estimated using the following formula (2):

$$K_i = \frac{C_T(T)}{\int_0^T C_p(t) \cdot dt} - V_D \cdot \frac{C_p(T)}{\int_0^T C_p(t) \cdot dt} \quad (2)$$

where K_i, is the influx rate constant, $C_T(t)$ is the mean value for the radioligand concentration in tissue during the time (tissue response), T is the time of dynamic acquisition, V_D is the distribution volume, $C_p(t)$ is the radioligand concentration in plasma during the time (i.e., the IDIF), and the integral symbol represents the area under the curve of the IDIF. Since both C_T and C_p are obtained from the VOI in tumor tissue and in descending thoracic aorta, respectively, the proposed analysis is based on regional and not voxel-based Patlak parametric imaging method.

For each patient of group 2 (n = 14), K_i was estimated with the Patlak analysis using the IDIF (0–60 min) and the tissue response (10–60 min) curves. The IDIF was obtained as described in the previous paragraph. The tissue response curve was obtained by drawing VOI on the tumor in the last frame of the dynamic acquisition and superimposing it on all previous frames (10–60 min). VOIs for the input function and tissue response were automatically placed over three consecutive slices to include the five hottest pixels within the VOI (34, 35).

K_i Estimation Simulating the Short Dynamic Protocol ($K_{i,s}$)

For each patient of group 2 (n = 14), K_i was estimated using data from 0 to10 min and from 40 to 60 min of the long standard

acquisition to obtain the $IDIF_{Fitted}$ and the tissue response curves simulating two short dynamic acquisitions.

In particular, for each patient, the early phase of the input function was built taking into account the first 10 min of the patient's input function curve of the standard dynamic protocol. The remaining part was reconstructed with the previous reported monoexponential function (1) using the *a*, *b*, and *c* coefficients of pIDIF obtained and validated in patients of group 1, then modeled to assume at 45 min the value of 2-[^{18}F]FDG activity in the plasma measured at 45 min from the venous sample ($IDIF_{Fitted}$), as previously described.

For each patient, the tissue response curve was reconstructed taking into account data measured at 10 min and those measured between 40 and 60 min of the patient's tissue response curve of the standard protocol.

Finally, the influx rate constant ($K_{i,s}$) was estimated with the Patlak analysis according to the well-known formula (2) using the $IDIF_{Fitted}$ and the tissue response curves as described.

K_i Estimation Using the Short Dynamic Protocol ($K_{i,s}$)

For each patient of group 3 ($n = 8$), K_i was estimated using two short dynamic acquisitions performed to obtain the $IDIF_{Fitted}$ and the tissue response curves.

In particular, the $IDIF_{Fitted}$ was built drawing a VOI on the descending thoracic aorta during the summed first nine frames of early dynamic acquisition (45 s) and superimposing it on all subsequent frames of the early dynamic acquisition (0–10 min); the remaining part (10–60 min) was reconstructed using the *a*, *b*, and *c* coefficients values of pIDIF obtained and validated in patients of group 1, then modeled to assume at 45 min the value of 2-[^{18}F]FDG activity in the plasma measured at 45 min from the venous sample ($IDIF_{Fitted}$), as previously described.

The tissue response curve was obtained drawing a VOI on the tumor in the last frame of the late dynamic acquisition and superimposing it on all previous frames (40–60 min); another VOI was drawn on the tumor in the last frame of the early dynamic examinations (10 min). VOIs for input function and tissue response were automatically placed over three consecutive slices to include the five hottest pixels within the VOI (34, 35). Being a VOI-based analysis method and therefore limited to specific regions (not voxel-wise), the co-registration between early and late PET images was not necessary.

Finally, the influx rate constant ($K_{i,s}$) was estimated using the Patlak analysis according to the well-known formula (2) using the $IDIF_{Fitted}$ and the tissue response curves as described.

Standardized Uptake Value

Standard uptake value was calculated as following formula (3):

$$SUV = \frac{C_T(T)}{A_0/bw} \quad (3)$$

where $C_T(T)$ is the value of radioligand concentration at T equal to 55-min post-injection measured using a VOI drawn on tumor tissue (tissue response) in the last frame, A_0 is the injected activity, and bw is the bodyweight of the patient (36).

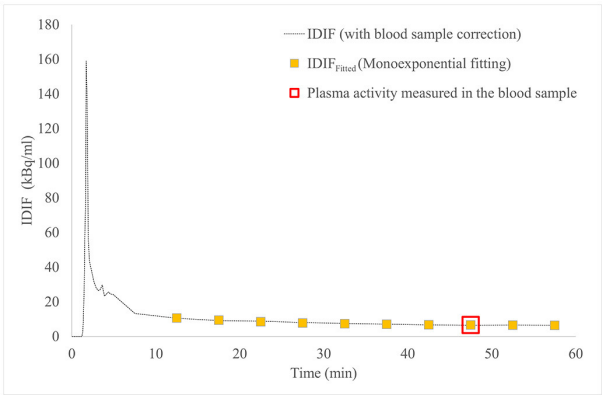

FIGURE 1 | IDIF curve (dashed line) and $IDIF_{Fitted}$ curve (yellow square boxes), both modeled to pass through the 2-[^{18}F]FDG activity in plasma measured in the venous blood sample at 45 min post-injection (red square box), in patient #4. 2-[^{18}F]FDG, 2-[^{18}F]Fluoro-2-deoxy-D-glucose; IDIF, image-derived input function.

Statistical Analysis

R (analytical software) was used for calculations. The mean square percentage error (MSEP) between standard IDIF (0–60 min) and $IDIF_{fitted}$ was calculated, and $LOOCV_{error}$ was computed to perform the leave-one-out cross-validation. The concordance between K_i and $K_{i,s}$ was evaluated using the Passing–Bablok regression. The Spearman's rank correlation coefficient (ρ) and coefficient of determination (R^2) were used to assess the correlation between K_i estimated using standard dynamic protocol and $K_{i,s}$ estimated with short dynamic protocol, and between $K_{i,s}$ and SUV.

RESULTS

In 24 patients with NSCLC who performed the standard long dynamic protocol (groups 1 and 2), the input function curves showed a monoexponential trend from 10 min after 2-[^{18}F]FDG injection up to the end of acquisition (60 min), as reported in a representative patient (**Figure 1**).

The mean values of *a*, *b*, and *c* coefficients obtained from monoexponential fittings of 10 input function curves (group 1) were 9.684, 16.410, and 0.068 min^{-1}, respectively.

Figure 1 shows IDIF obtained with standard long dynamic protocol and $IDIF_{Fitted}$ obtained with short dynamic protocol and reconstructed with monoexponential fit in a representative patient (#4): both curves were imposed to pass through the measured 2-[^{18}F]FDG activity in plasma at 45 min.

The $LOOCV_{error}$ between standard IDIF (0–60 min) and $IDIF_{fitted}$ was 0.4%.

Table 1 reports demographic data and PET parameters values (K_i, $K_{i,s}$, SUV) for all patients of group 2 ($n = 14$).

The mean values (±SD) of K_i obtained with standard long dynamic protocol and $K_{i,s}$ obtained simulating the short dynamic protocol for patients of group 2 ($n = 14$) were 0.0442 min^{-1} (±0.0302) and 0.0433 min^{-1} (±0.0298), respectively. The

TABLE 1 | Demographic data and PET parameters values in patients of group 2 ($n = 14$).

Patients	Age	Sex	K_i	R^2 (K_i)	$K_{i,s}$	R^2 ($K_{i,s}$)	SUV
2	75	M	0.0314	0.9838	0.0291	0.9748	7.69
4	74	M	0.0381	0.9900	0.0377	0.9873	11.28
6	73	M	0.0385	0.9475	0.0361	0.9808	7.86
9	77	M	0.0468	0.9820	0.0485	0.9833	14.32
11	73	F	0.0403	0.9983	0.0418	0.9965	10.29
13	70	M	0.0383	0.9572	0.0349	0.9545	8.75
15	74	F	0.0222	0.9342	0.0222	0.9364	9.10
18	72	F	0.0165	0.9812	0.0166	0.9839	5.88
21	81	M	0.0310	0.9640	0.0290	0.9593	5.97
24	40	F	0.0303	0.9952	0.0313	0.9953	5.83
25	74	M	0.0764	0.9813	0.0733	0.9859	15.20
26	61	M	0.0656	0.9906	0.0654	0.9951	11.60
27	64	M	0.1306	0.9941	0.1287	0.9936	25.92
31	58	F	0.0123	0.9782	0.0117	0.9877	4.46

K_i, influx rate constant obtained with the Patlak graphical analysis using the standard long dynamic protocol; R^2 (K_i), Patlak plot linear regression coefficient for K_i; $K_{i,s}$, influx rate constant obtained with the Patlak graphical analysis using the short dynamic protocol; R^2 ($K_{i,s}$), Patlak plot linear regression coefficient for $K_{i,s}$; SUV, standardized uptake value.

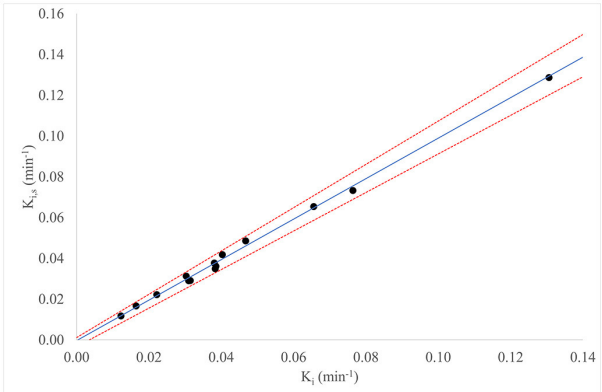

FIGURE 2 | Passing–Bablok regression for comparison of K_i and $K_{i,s}$, for all patients in group 2 ($n = 14$).

TABLE 2 | Demographic data and PET parameters values in patients of group 3 ($n = 8$).

Patients	Age	Sex	$K_{i,s}$	R^2 ($K_{i,s}$)	SUV
1	64	M	0.0646	0.9985	11.56
2	80	M	0.1018	0.9915	19.64
3	76	M	0.0374	0.9920	9.26
4	73	M	0.1188	0.9954	19.89
5	84	M	0.0614	0.9939	12.61
6	71	F	0.0697	0.9902	15.35
7	72	M	0.0485	0.9446	7.15
8	47	M	0.0971	0.9183	14.96

$K_{i,s}$, influx rate constant obtained with the Patlak graphical analysis using the short dynamic protocol; R^2($K_{i,s}$), Patlak plot linear regression coefficient for $K_{i,s}$; SUV, standardized uptake value.

correlation coefficient and coefficient of determination between the two parameters were $\rho = 0.974$ and $R^2 = 0.9970$, respectively.

Figure 2 reports for all patients of group 2 ($n = 14$) the Passing–Bablok regression for the comparison between K_i and $K_{i,s}$: the comparison between the two methods showed a slope value of 0.992 (95% CI: 0.94–1.06) and intercept value of −0.0003 (95% CI: −0.0033 to 0.0011).

Table 2 reports demographic data and PET parameters values ($K_{i,s}$, SUV) for all patients in group 3 ($n = 8$).

In patients of group 2 ($n = 14$, standard long dynamic acquisition) and those of group 3 ($n = 8$, two short dynamic acquisitions), the overall mean value (±SD) of SUV of the primary tumor was 11.57 (±5.37). The correlation coefficient and coefficient of determination between SUV and $K_{i,s}$ values were $\rho = 0.923$; $R^2 = 0.8746$ ($n = 22$), respectively, as reported in **Figure 3**.

Figure 4 shows 2-[^{18}F]FDG uptake at 2 min (**Figure 4A**), 30 min (**Figure 4B**), and 60 min (**Figure 4C**) in the thoracic aorta and primary tumor after tracer injection in a representative patient (#4).

DISCUSSION

The Patlak graphical analysis has been used in dynamic PET to estimate the influx rate constant (K_i) of tracers with irreversible uptake including 2-[^{18}F]FDG (14, 15, 37). Among several quantification methods, the Patlak analysis is a reliable and robust approach providing an accurate measure of K_i that is less affected by technical parameters and by tissue heterogeneity (38, 39).

Nevertheless, the kinetics of 2-[^{18}F]FDG requires a long dynamic PET acquisition lasting at least 60 min with consequent discomfort for the patient, limiting its use in clinical routine (40). To overcome such limitations, in this study a shorter dynamic acquisition protocol has been proposed to estimate K_i by Patlak

analysis in patients with NSCLC. The input function and the tissue response curves were reconstructed taking into account data (0–10 min and 40–60 min) from standard long dynamic acquisition, simulating two short dynamic PET acquisitions.

Regarding input function, it is well known that its accurate determination is a key point for kinetic modeling. The Patlak analysis requires the knowledge of the full course of input function time–activity curve, from the tracer injection to the end of dynamic acquisition of 60 min (41). In our method, the first part of each input function curve was built using data obtained from injection up to 10 min of the standard long dynamic acquisition, simulating a short early dynamic acquisition. The remaining part was reconstructed with monoexponential fitting using the mean value of *a*, *b*, and *c* coefficients obtained from standard input function values of a separate group of patients. Indeed, we observed that all curves of the standard long dynamic acquisition showed a monoexponential trend from the 10-min post-injection to the end. Finally, each input function curve so obtained was modeled to assume the value of 2-[^{18}F]FDG activity measured in the venous blood sample at 45 min post-injection. Indeed, at late times, an equilibrium between 2-[^{18}F]FDG concentration in arterial and venous blood is reached (35, 42). Moreover, the radioligand activity measured in blood better represents the "real" 2-[^{18}F]FDG concentration compared to that measured using only VOI. The reliability of this method is supported by the very low $LOOCV_{error}$ value between standard IDIF and $IDIF_{fitted}$. Therefore, a short dynamic acquisition plus a late venous blood sample can be sufficient to construct a robust input function that can be considered "personalized" since it uses data that are, largely, patients own data (counts in first 10 min of dynamic acquisition and counts in a venous blood sample) plus reconstructed data (monoexponential fitting). Therefore, we underline that the input function curve has to be as accurate as possible taking also into account the physio- and pathological characteristics of each patient representing the "true" tracer bioavailability. Regarding the tissue response, it was built using data obtained from 40 to 60 min of the standard long dynamic acquisition, simulating a late-short dynamic acquisition, plus counts of the last frame (10 min) of the simulated early-short dynamic acquisition, useful to well estimate the slope of Patlak plot.

Finally, the reliability of $K_{i,s}$ values calculated using the input function and tissue response curves obtained with the short protocol is supported by the high correlation with K_i obtained with the standard long dynamic acquisition. This finding suggests the feasibility of the short protocol in clinical practice, requiring only two short dynamic PET acquisitions (0–10 min and 40–60 min) instead of the longer standard one (60 min), plus a late venous blood sampling. In addition, such a method that contemplates two dynamic acquisitions (one including a large vessel for input function; the other including the neoplastic lesion for tissue response) can be applied to evaluate the influx rate constant (and other quantitative parameters) of neoplastic lesion located in everybody site. Recently, Wu et al. (43) investigated the feasibility of generating K_i for 2-[^{18}F]FDG PET from dual-time-point imaging data (5 min per scan) by using a population-based input function. Differently from our study, they did not extrapolate K_i from a linear regression but the angular coefficient

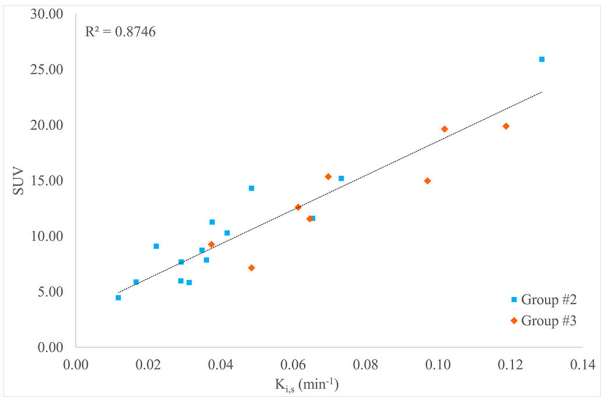

FIGURE 3 | Scatter plot, linear regression, and R^2 value for the comparison between $K_{i,S}$ and standard uptake value (SUV) for all patients in groups 2 and 3 ($n = 22$).

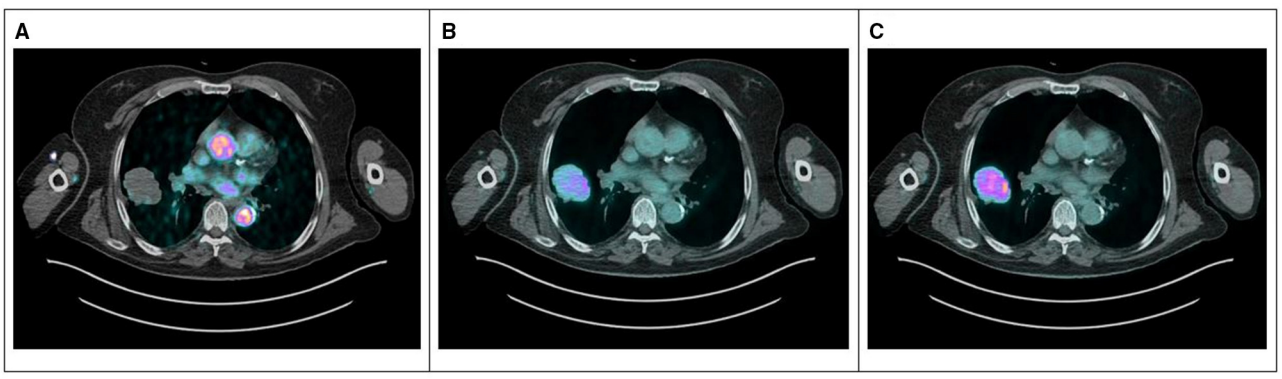

FIGURE 4 | PET/CT images at 2 min **(A)**, 30 min **(B)**, and 60 min **(C)** after 2-[^{18}F]FDG injection for a representative patient (#4) showing the blood pool in the early phase and the increasing uptake in the lesion during the time. 2-[^{18}F]FDG, 2-[^{18}F]Fluoro-2-deoxy-D-glucose.

of a straight line passing through two points. Moreover, the scaling factor for the population-based curve was determined on the summation of the input function values at the middle time points of the early and the late scans.

Regarding semiquantitative PET parameters, SUV showed a good (even if not excellent) correlation with $K_{i,s}$ obtained both in patients in whom the two short dynamic acquisitions were simulated and in patients in whom two short dynamic acquisitions were performed. This result confirms that semiquantitative parameters, even if less accurate, well represent the glucose metabolism only if all technical and procedural aspects in patient preparation and scan acquisition are strictly respected. Indeed, especially when several PET/CT examinations are repeated over time for the evaluation of response to oncological treatment (44–46), the difficulty in strictly respecting all technical aspects can make the semiquantitative parameters unreliable. Moreover, it is important to remind that the accuracy of semiquantitative parameters may be affected by non-controlled aspects such as the oncological therapies that can modify the tracer bioavailability (especially the news antiangiogenic drugs), the cancer cells biological characteristics (tracer uptake), and other unknown biologic and patients factors (47, 48). Furthermore, we have to take into account that semiquantitative parameters, such as SUV, perform relatively poorly when the tumor-to-background ratio is low as in liver lesions, in small and less 2-[^{18}F]FDG avid tumors (49) or post-treatment evaluation when the uptake in tumors may be suppressed after therapy (19). Therefore, the use of kinetic parameters seems preferable to semiquantitative ones, not only for therapy monitoring (50–52) but also for evaluating glucose metabolism of tumor regions with relatively high background activity (19). Moreover, it was recently showed that oncologic whole-body (WB) Patlak K_i imaging may improve lesion detectability reducing false-positive rates when complementing SUV (53). This potential improvement in specificity may support the use of kinetic parameters in other clinical settings, such as for differential diagnosis between pulmonary tumors and inflammatory lesions, and between progression and pseudoprogression during immunotherapy.

Regarding practical aspects of our method, to come in and out of the PET scanner twice to perform two separate acquisitions did not determine a discomfort for patients of group 3 who performed the short dynamic protocol. Indeed, the short lasting of PET acquisitions (compared to the long standard one) seems preferable for patients who have to maintain the correct position with the arms over the head on the scanner for a shorter time. In addition, the method does not require a rigid repositioning of the patient on the PET scanner, since a co-registration of early and late dynamic images was not needed. However, this could be a limitation if a voxel-wise Patlak analysis method would be explored; in that case, a similar approach may not be feasible due to the need for co-registration between early and late dynamic PET frames. Finally, this procedure that requires two separate short acquisitions, between which the patient leaves the scanner free for other patients PET acquisition, may result in several practical limitations, increasing the complexity in the scheduling of the daily clinical workflow, the time involvement of the staff in repositioning the patient on the scanner table, and the risk of propagating delay or cancellations of one exam on the following ones. Moreover, we have to take into account that the need for two low-dose CT scans for accurate attenuation correction of the two dynamic PET acquisitions introduces additional radiation exposure for the patient and increases the time involvement for patients and staff, reducing the time between the early and late acquisitions in which the scanner is available for another exam. However, this proposed method cannot replace the standard-of-care WB PET acquisitions, but it can allow quantifying K_i in few selected cases (maximum three per day for clinical or research aims), even in PET centers that do not have advanced technologies, scheduling them at the beginning of the end of the daily workflow, reducing the impact on daily clinical activities as much as possible. However, we have to take into account that there are currently commercially available products that provide fully automated WB parametric PET images. Their diffusion in the next future will allow acquiring dynamic WB PET studies with the arms in the down position, improving the comfort of patients and limiting the possibility of motion-induced artifacts in the PET images, with minimal control and time involvement requirements for the staff.

Beyond the practical aspects, the main limitations of this study are the relatively small sample size, the absence of arterial blood samples as the reference standard (being invasive and not feasible in clinical practice) to validate the input function time–activity curve, and the application of the short protocol only in patients with NSCLC. Moreover, the application of a single-scale factor to impose the IDIF activity value at 45 min equal to the plasma activity measured in the blood sample could be a potential limitation due to the different partial volume effects during time scan; in the early phase, the activity in the vessel is very high causing spill-out of activity outside the vessel wall boundaries and lead to a possible underestimation of the IDIF peak. On the contrary, in the late phase, the activity inside the vessel is expected to be very small, whereas the activity from the surrounding tissue is relatively larger, thus causing a possible overestimation of the IDIF value. In addition, the use of two short dynamic acquisitions could not be adequate to apply the generalized Patlak methods developed and employed in K_i quantification when considering a mild degree of reversibility of 2-[^{18}F]FDG kinetics, since these methods require multiple measurements at both early and late time points (23, 54–56). Nevertheless, the robustness of the performance of our method in the K_i evaluation using two short acquisitions (compared to the standard one) supports its use, aware that with the simplicity of our method, a good estimate of the value of the constant influx rate was obtained. Finally, the use of 4D reconstruction algorithms (30, 57–59), recently available in some PET scanners, but not applied in our PET scans, would mitigate statistical noise levels, improving image quality and K_i estimation.

CONCLUSION

In conclusion, our proposed method may provide a reliable quantification of regional estimates of influx rate constant for

tissues not expressing 2-[^{18}F]FDG uptake reversibility. Two short dynamic PET acquisitions obtained at an early and late time point post-injection plus a population-based input function model scaled according to a late venous blood sample may be enough to obtain a robust and personalized temporal integral of the input function, which is necessary to estimate the net influx rate constant by regional Patlak analysis. This short dynamic protocol of two scan sessions at 0–10 min and 40–60 min post-injection may have some potential advantages when compared with the standard dynamic WB long 60-min acquisition protocols; it can reduce the total time spent inside the scanner for each patient, but not its total exam time involvement. The scan time reduction could therefore mitigate their discomfort for some patients if exiting and entering the scanner twice per exam is not an issue; however, this reduction in acquisition time comes at the cost of additional radiation exposure for the patient with a second low-dose WB CT scan. Despite several practical limitations, such as the increase in CT radiation dose from the need for a second low-dose WB CT exam, the complexity of scheduling daily exams with interleaved sessions between different patients and the risk of propagating time delays and other problems from one exam session to the exams of other patients in the same day, the proposed dynamic PET/CT scan protocol can theoretically allow performing more dynamic PET acquisitions daily; furthermore, similarly to other WB dynamic PET scan protocols, it allows to obtain regional estimates of highly quantitative parameters in tumor regions located in distant organs scanned at different bed positions. Moreover, data analysis is not more time-consuming and does not require additional expertise compared to other dynamic WB PET/CT protocols. From the clinical point of view, the use of dynamic WB PET acquisitions assumes more significance in oncological patients in whom the quantification is more relevant than semiquantification, especially in treatment monitoring and prognostic assessment. Our proposed method, along with other recent dynamic WB PET/CT studies (28, 29, 43, 58), aims to facilitate the clinical adoption of dynamic PET and regional parametric analysis by shortening the total PET scan times often required in these protocols.

DATA AVAILABILITY STATEMENT

The raw data supporting the conclusions of this article will be made available by the authors, without undue reservation.

ETHICS STATEMENT

The studies involving human participants were reviewed and approved by Comitato Etico Lazio 1. The ethics committee waived the requirement of written informed consent for participation.

AUTHOR CONTRIBUTIONS

MC and LI contributed to the conception and design of the study. VS, ST, RG, and GCa were involved in the acquisition of PET/CT and clinical data. LI and AC performed data analysis. LI, VS, AC, SS, DC, GCi, and MC were involved in data interpretation. LI, VS, AC, and SS drafted the manuscript. MC critically revised the manuscript for important intellectual content. All authors revised the final manuscript and gave their final approval for the manuscript submission.

REFERENCES

1. Boellaard R, Delgado-Bolton R, Oyen WJ, Giammarile F, Tatsch K, Eschner W, et al. FDG PET/CT: EANM procedure guidelines for tumour imaging: version 20. *Eur J Nucl Med Mol Imaging.* (2015) 42:328–54. doi: 10.1007/s00259-014-2961-x
2. Gambhir SS. Molecular imaging of cancer with positron emission tomography. *Nat Rev Cancer.* (2002) 2:683–93. doi: 10.1038/nrc882
3. Czernin J, Allen-Auerbach M, Schelbert HR. Improvements in cancer staging with PET/CT: literature-based evidence as of september 2006. *J Nucl Med.* (2007) 48:78S—88.
4. Nishiyama Y, Yamamoto Y, Monden T, Sasakawa Y, Kawai N, Satoh K, et al. Diagnostic value of kinetic analysis using dynamic FDG PET in immunocompetent patients with primary CNS lymphoma. *Eur J Nucl Med Mol Imaging.* (2007) 34:78–86. doi: 10.1007/s00259-006-0153-z
5. Dimitrakopoulou-Strauss A, Pan L, Sachpekidis C. Kinetic modeling and parametric imaging with dynamic PET for oncological applications: general considerations, current clinical applications, and future perspectives. *Eur J Nucl Med Mol Imaging.* (2020) 48:21–39. doi: 10.1007/s00259-020-04843-6
6. Lammertsma AA. Forward to the past: the case for quantitative pet imaging. *J Nucl Med.* (2017) 58:1019–24. doi: 10.2967/jnumed.116.188029
7. Sadato N, Tsuchida T, Nakaumra S, Waki A, Uematsu H, Takahashi N, et al. Non-invasive estimation of the net influx constant using the standardized uptake value for quantification of FDG uptake of tumours. *Eur J Nucl Med Mol Imaging.* (1998) 25:559–64. doi: 10.1007/s002590050256
8. Naqa IE. The role of quantitative PET in predicting cancer treatment outcomes. *Clin Transl Imaging.* (2014) 2:305–20. doi: 10.1007/s40336-014-0063-1
9. Hofheinz F, Bütof R, Apostolova I, Zöphel K, Steffen IG, Amthauer H, et al. An investigation of the relation between tumor-to-liver ratio (TLR) and tumor-to-blood standard uptake ratio (SUR) in oncological FDG PET. *EJNMMI Res.* (2016) 6:19. doi: 10.1186/s13550-016-0174-y
10. Adams MC, Turkington TG, Wilson JM, Wong TZ. A systematic review of the factors affecting accuracy of SUV measurements. *AJR Am J Roentgenol.* (2010) 195:310–20. doi: 10.2214/AJR.10.4923
11. Zaidi H, Karakatsanis N. Towards enhanced PET quantification in clinical oncology. *Br J Radiol.* (2018) 91:20170508. doi: 10.1259/bjr.20170508
12. Keyes JW, SUV. Standard uptake or silly useless value? *J Nucl Med.* (1995) 36:1836–9.
13. Marin A, Murchison JT, Skwarski KM, Tavares AAS, Fletcher A, Wallace WA, et al. Can dynamic imaging, using 18F-FDG PET/CT and CT perfusion differentiate between benign and malignant pulmonary nodules? *Radiol Oncol.* (2021) 55:259–67. doi: 10.2478/raon-2021-0024
14. Patlak CS, Blasberg RG, Fenstermacher JD. Graphical evaluation of blood-to-brain transfer constants from multiple-time uptake data. *J Cereb Blood Flow Metab.* (1983) 3:1–7. doi: 10.1038/jcbfm.1983.1
15. Patlak CS, Blasberg RG. Graphical evaluation of blood-to-brain transfer constants from multiple-time uptake data. generalizations. *J Cereb Blood Flow Metab.* (1985) 5:584–90. doi: 10.1038/jcbfm.1985.87
16. van der Weerdt AP, Klein LJ, Visser CA, Visser FC, Lammertsma AA. Use of arterialised venous instead of arterial blood for measurement of myocardial

glucose metabolism during euglycaemic-hyperinsulinaemic clamping. *Eur J Nucl Med Mol Imaging.* (2002) 29:663–9. doi: 10.1007/s00259-002-0772-y
17. Liptrot M, Adams KH, Martiny L, Pinborg LH, Lonsdale MN, Olsen NV, et al. Cluster analysis in kinetic modelling of the brain: a noninvasive alternative to arterial sampling. *Neuroimage.* (2004) 21:483–93. doi: 10.1016/j.neuroimage.2003.09.058
18. Croteau E, Lavallée E, Labbe SM, Hubert L, Pifferi F, Rousseau JA, et al. Image-derived input function in dynamic human PET/CT: methodology and validation with 11C-acetate and 18F-fluorothioheptadecanoic acid in muscle and 18F-fluorodeoxyglucose in brain. *Eur J Nucl Med Mol Imaging.* (2010) 37:1539–50. doi: 10.1007/s00259-010-1443-z
19. Karakatsanis NA, Lodge MA, Tahari AK, Zhou Y, Wahl RL, Rahmim A. Dynamic whole body PET parametric imaging: I. concept, acquisition protocol optimization and clinical application. *Phys Med Biol.* (2013) 58:7391. doi: 10.1088/0031-9155/58/20/7391
20. Karakatsanis NA, Lodge MA, Zhou Y, Wahl RL, Rahmim A. Dynamic whole body PET parametric imaging: II. task-oriented statistical estimation. *Phys Med Biol.* (2013) 58:7419–45. doi: 10.1088/0031-9155/58/20/7419
21. Takikawa S, Dhawan V, Spetsieris P, Robeson W, Chaly T, Dahl R, et al. Noninvasive quantitative fluorodeoxyglucose PET studies with an estimated input function derived from a population-based arterial blood curve. *Radiology.* (1993) 188:131–6. doi: 10.1148/radiology.188.1.8511286
22. Zanotti-Fregonara P, Hines CS, Zoghbi SS, Liow J-S, Zhang Y, Pike VW, et al. Population-based input function and image-derived input function for [11C](R)-rolipram PET imaging: methodology, validation and application to the study of major depressive disorder. *Neuroimage.* (2012) 63:1532–41. doi: 10.1016/j.neuroimage.2012.08.007
23. Karakatsanis N, Zhou Y, Lodge M, Casey M, Wahl R, Subramaniam R, et al. Clinical whole-body PET patlak imaging 60-90min postinjection employing a population-based input function. *J Nucl Med.* (2015) 56(Supplement 3):1786.
24. Naganawa M, Gallezot J-D, Shah V, Mulnix T, Young C, Dias M, et al. Assessment of population-based input functions for Patlak imaging of whole body dynamic 18F-FDG PET. *EJNMMI Phys.* (2020) 7:67. doi: 10.1186/s40658-020-00330-x
25. Novikov M. Multiparametric quantitative and texture 18 F-FDG PET/CT analysis for primary malignant tumour grade differentiation. *Eur Radiol Exp.* (2019) 3:48. doi: 10.1186/s41747-019-0124-3
26. Hu J, Panin V, Smith AM, Spottiswoode B, Shah V, von Gall CCA, et al. Design and implementation of automated clinical whole body parametric pet with continuous bed motion. *IEEE Trans Radiat Plasma Med Sci.* (2020) 4:696–707. doi: 10.1109/TRPMS.2020.2994316
27. Braune A, Hofheinz F, Bluth T, Kiss T, Wittenstein J, Scharffenberg M, et al. Comparison of static and dynamic ^{18}F-FDG PET/CT for quantification of pulmonary inflammation in acute lung injury. *J Nucl Med.* (2019) 60:1629–34. doi: 10.2967/jnumed.119.226597
28. Karakatsanis N, Lodge M, Zhou Y, Casey M, Wahl R, Subramaniam R, et al. Novel multi-parametric SUV/Patlak FDG-PET wholebody imaging framework for routine application to clinical oncology. *J Nucl Med.* (2015) 56(Supplement 3):625.
29. Karakatsanis NA, Casey ME, Knesaurek K, Fayad ZA, Kostakoglu L. SUV/Patlak-4D whole-body PET/CT dynamic and parametric imaging: clinical demonstration and validation of SUV synthesis from dynamic passes. *IEEE Nucl Sci Symp Med Imaging Conf.* (2017) 1–6. doi: 10.1109/NSSMIC.2017.8532712
30. Karakatsanis N, Lodge M, Wahl R, Rahmim A. Direct 4D whole-body PET/CT parametric image reconstruction: concept and comparison vs. indirect parametric imaging. *J Nucl Med.* (2013) 54(Supplement 2):2133.
31. Velasco C, Mota-Cobián A, Mateo J, España S. Explicit measurement of multi-tracer arterial input function for PET imaging using blood sampling spectroscopy. *EJNMMI Physics.* (2020) 7:7. doi: 10.1186/s40658-020-0277-4
32. Berradja K, Boughanmi N, Bentourkia M. Kinetic modeling of brain FDG data with input function derived from images by independent component analysis. *2009 IEEE Nucl Sci Symp Conf Rec.* (2009) 2920–3. doi: 10.1109/NSSMIC.2009.5401614
33. Hunter GJ, Hamberg LM, Alpert NA, Choi NC, Fischman AJ. Simplified measurement of deoxyglucose utilization rate. *J Nuc Med.* (1996) 37:950–95.
34. Fahey FH, Kinahan PE, Doot RK, Kocak M, Thurston H, Poussaint TY. Variability in PET quantitation within a multicenter consortium. *Med Phys.* (2010) 37:3660–6. doi: 10.1118/1.3455705
35. Laffon E, Calcagni ML, Galli G, Giordano A, Capotosti A, Marthan R, et al. Comparison of three-parameter kinetic model analysis to standard Patlak's analysis in ^{18}F-FDG PET imaging of lung cancer patients. *EJNMMI Res.* (2018) 8:24. doi: 10.1186/s13550-018-0369-5
36. Strauss LG, Conti PS. The application of PET in clinical oncology. *J Nucl Med.* (1991) 32:623–48.
37. Mintun MA, Raichle ME, Kilbourn MR, Wooten GF, Welch MJ. A quantitative model for the in vivo assessment of drug binding sites with positron emission tomography. *Ann Neurol.* (1984) 15:217–27. doi: 10.1002/ana.410150302
38. Mori K, Schmidt K, Jay T, Palombo E, Nelson T, Lucignani G, et al. Optimal duration of experimental period in measurement of local cerebral glucose utilization with the deoxyglucose method. *J Neurochem.* (1990) 54:307–19. doi: 10.1111/j.1471-4159.1990.tb13316.x
39. Zhuang M, Karakatsanis NA, Dierckx RAJO, Zaidi H. Quantitative Analysis of Heterogeneous[^{18}F]FDG Static (SUV) vs. *Patlak (Ki) Whole-body PET Imaging Using Different Segmentation Methods: a Simulation Study Mol Imaging Biol.* (2019) 21:317–27. doi: 10.1007/s11307-018-1241-8
40. Aide N, Lasnon C, Veit-Haibach P, Sera T, Sattler B, Boellaard R. EANM/EARL harmonization strategies in PET quantification: from daily practice to multicentre oncological studies. *Eur J Nucl Med Mol Imaging.* (2017) 44:17–31. doi: 10.1007/s00259-017-3740-2
41. Zuo Y, Qi J, Wang G. Relative Patlak plot for dynamic PET parametric imaging without the need for early-time input function. *Phys Med Biol.* (2018) 63:165004. doi: 10.1088/1361-6560/aad444
42. Galli G, Indovina L, Calcagni ML, Mansi L, Giordano A. The quantification with FDG as seen by a physician. *Nucl Med Biol.* (2013) 40:720–30. doi: 10.1016/j.nucmedbio.2013.06.009
43. Wu J, Liu H, Ye Q, Gallezot J-D, Naganawa M, Miao T, et al. Generation of parametric $K_i$images for FDG PET using two 5-min scans. *Med Phys.* (2021) 48:5219–31. doi: 10.1002/mp.15113
44. de Geus-Oei L-F, van der Heijden HFM, Visser EP, Hermsen R, van Hoorn BA, Timmer-Bonte JNH, et al. Chemotherapy response evaluation with ^{18}F-FDG PET in patients with non-small cell lung cancer. *J Nucl Med.* (2007) 48:1592–8. doi: 10.2967/jnumed.107.043414
45. La Fontaine MD, Bruin NM, van Kranen S, Knegjens JL, van de Kamer JB, Vogel WV, et al. The dynamics and prognostic value of FDG PET-metrics in weekly monitoring of (chemo)radiotherapy for NSCLC. *Radiother Oncol.* (2021) 160:107–14. doi: 10.1016/j.radonc.2021.04.009
46. Yang D-M, Palma DA, Kwan K, Louie AV, Malthaner R, Fortin D, et al. Predicting pathological complete response (pCR) after stereotactic ablative radiation therapy (SABR) of lung cancer using quantitative dynamic [^{18}F]FDG PET and CT perfusion: a prospective exploratory clinical study. *Radiat Oncol.* (2021) 16:11. doi: 10.1186/s13014-021-01747-z
47. Chen K, Chen X. Positron emission tomography imaging of cancer biology: current status and future prospects. *Semin Oncol.* (2011) 38:70–86. doi: 10.1053/j.seminoncol.2010.11.005
48. Hoekstra CJ, Hoekstra OS, Stroobants SG, Vansteenkiste J, Nuyts J, Smit EF, et al. Methods to monitor response to chemotherapy in non-small cell lung cancer with 18F-FDG PET. *J Nucl Med.* (2002) 43:1304–9.
49. Yang M, Lin Z, Xu Z, Li D, Lv W, Yang S, et al. Influx rate constant of ^{18}F-FDG increases in metastatic lymph nodes of non-small cell lung cancer patients. *Eur J Nucl Med Mol Imaging.* (2020) 47:1198–208. doi: 10.1007/s00259-020-04682-5
50. Mankoff DA, Muzi M, Krohn KA. Quantitative positron emission tomography imaging to measure tumor response to therapy: what is the best method? *Mol Imaging Biol.* (2003) 5:281–5. doi: 10.1016/j.mibio.2003.09.002
51. Kroep JR, Van Groeningen CJ, Cuesta MA, Craanen ME, Hoekstra OS, Comans EF, et al. Positron emission tomography using 2-deoxy-2-[^{18}F]-fluoro-D-glucose for response monitoring in locally advanced gastroesophageal cancer: a comparison of different analytical methods. *Mol Imaging Biol.* (2003) 5:337–46. doi: 10.1016/j.mibio.2003.09.007

52. van Elmpt W, Das M, Hüllner M, Sharifi H, Zegers CML, Reymen B, et al. Characterization of tumor heterogeneity using dynamic contrast enhanced CT and FDG-PET in non-small cell lung cancer. *Radiother Oncol.* (2013) 109:65–70. doi: 10.1016/j.radonc.2013.08.032
53. Fahrni G, Karakatsanis NA, Di Domenicantonio G, Garibotto V, Zaidi H. Does whole-body Patlak ^{18}F-FDG PET imaging improve lesion detectability in clinical oncology? *Eur Radiol.* (2019) 29:4812–21. doi: 10.1007/s00330-018-5966-1
54. Karakatsanis NA, Zhou Y, Lodge MA, Casey ME, Wahl RL, Rahmim A. Quantitative whole-body parametric PET imaging incorporating a generalized Patlak model. *IEEE Nucl Sci Symp Med Imaging Conf.* (2013) 2013:1–9.
55. Karakatsanis NA, Lodge MA, Casey ME, Zaidi H, Rahmim A. Impact of acquisition time-window on clinical whole-body PET parametric imaging. *IEEE Nucl Sci Symp Med Imaging Conf.* (2014) 2014:1–8. doi: 10.1109/NSSMIC.2014.7430770
56. Messa C, Choi Y, Hoh CK, Jacobs EL, Glaspy JA, Rege Sheila, et al. Quantification of glucose utilization in liver metastases: parametric imaging of FDG uptake with PET. *J Comput Assist Tomogr.* (1992) 16:684–9. doi: 10.1097/00004728-199209000-00003
57. Karakatsanis NA, Casey ME, Lodge M, Rahmim A, Zaidi H. Whole-body direct 4D parametric PET imaging employing nested generalized Patlak expectation-maximization reconstruction. *Phys Med Biol.* (2016) 61:5456–85. doi: 10.1088/0031-9155/61/15/5456
58. Karakatsanis N, Lodge M, Fahrni G, Casey ME, Zhou Y, Subramaniam R, et al. Simultaneous SUV/Patlak-4D Whole-Body PET: a multiParametric 4D imaging framework for routine clinical application. *J Nucl Med.* (2016) 57(Supplement 2):367.
59. Merlin T, Visvikis D, Fernandez P, Lamare F. Dynamic PET image reconstruction integrating temporal regularization associated with respiratory motion correction for applications in oncology. *Phys Med Biol.* (2018) 63:04501. doi: 10.1088/1361-6560/aaa86a

Conflict of Interest: The authors declare that the research was conducted in the absence of any commercial or financial relationships that could be construed as a potential conflict of interest.

frontiers in Medicine

SYSTEMATIC REVIEW
published: 26 November 2021
doi: 10.3389/fmed.2021.771912

Prognostic Value of Volume-Based Parameters Measured by SSTR PET/CT in Neuroendocrine Tumors: A Systematic Review and Meta-Analysis

Jiale Hou[1], *Yi Yang*[1], *Na Chen*[1], *Dengming Chen*[1] *and Shuo Hu*[1,2,3]*

[1] Department of Nuclear Medicine, Xiangya Hospital, Central South University, Changsha, China, [2] Key Laboratory of Biological Nanotechnology, Changsha, China, [3] National Clinical Research Center for Geriatric Disorders (XIANGYA), Xiangya Hospital, Central South University, Changsha, China

Purpose: A meta-analysis was conducted to investigate the value of the volume parameters based on somatostatin receptor (SSTR)-positron emission tomography (PET) in predicting the prognosis in patients with neuroendocrine tumors (NETs).

Material: PUBMED, EMBASE, Cochrane library, and Web of Knowledge were searched from January 1990 to May 2021 for studies evaluating prognostic value of volume-based parameters of SSTR PET/CT in NETs. The terms used were "volume," "positron emission tomography," "neuroendocrine tumors," and "somatostatin receptor." Pooled hazard ratio (HR) values were calculated to assess the correlations between volumetric parameters, including total tumor volume (TTV) and total-lesion SSTR expression (TL-SSTR), with progression-free survival (PFS) and overall survival (OS). Heterogeneity and subgroup analysis were performed. Funnel plots, Begg's and Egger's test were used to assess possible underlying publication bias.

Results: Eight eligible studies involving 593 patients were included in the meta-analysis. In TTV, the pooled HRs of its prognostic value of PFS and OS were 2.24 (95% CI: 1.73–2.89; $P < 0.00001$) and 3.54 (95% CI, 1.77–7.09; $P = 0.0004$), respectively. In TL-SSTR, the pooled HR of the predictive value was 1.61 (95% CI, 0.48–5.44, $P = 0.44$) for PFS.

Conclusion: High TTV was associated with a worse prognosis for PFS and OS in with patients NETs. The TTV of SSTR PET is a potential objective prognosis predictor.

Keywords: positron emission tomography/CT, neuroendocrine tumors, somatostatin receptors, prognosis, tumor volume

OPEN ACCESS

Edited by:
Ronan ABGRAL, Centre Hospitalier Regional Universitaire (CHU) de Brest, France

Reviewed by:
Virginia Liberini, University of Turin, Italy
Giorgio Treglia, Ente Ospedaliero Cantonale (EOC), Switzerland

***Correspondence:**
Shuo Hu
hushuo2018@163.com

Specialty section:
This article was submitted to Nuclear Medicine, a section of the journal Frontiers in Medicine

Received: *07 September 2021*
Accepted: *19 October 2021*
Published: *26 November 2021*

Citation:
Hou J, Yang Y, Chen N, Chen D and Hu S (2021) Prognostic Value of Volume-Based Parameters Measured by SSTR PET/CT in Neuroendocrine Tumors: A Systematic Review and Meta-Analysis. Front. Med. 8:771912. doi: 10.3389/fmed.2021.771912

Advanced in Knowledge

The volume parameters based on SSTR PET can provide additional value for the prognosis of neuroendocrine tumors.

INTRODUCTION

Neuroendocrine tumors (NETs) are a group of highly heterogeneous neoplasm originating from neuroendocrine cells and it can occur in different organs. The emergence of diagnostic technologies

increases early-stage NETs and the detection rate of metastases, raising its incidence and prevalence (1). However, in patients with the same tumor stage and grade, the outcome of disease and survival of NET patients vary greatly (2, 3). Therefore, identifying the prognostic markers is crucial for the management of patients with NETs. Some studies showed that morphological imaging is of limited value in predicting the survival, disease progression, and treatment effects of NETs (4, 5). Several widely-studied diagnostic biomarkers, especially chromogranin A (CgA), has been widely studied. Its plasma level is affected by many factors including the use of proton pump inhibitors (6, 7), but its prognostic utility is still controversial (8, 9).

Somatostatin receptors (SSTRs) are expressed in most NET cells, particularly type 2, and is an ideal target for imaging and therapy method (10). SSTR-mediated imaging is considered to be more accurate than SSTR immunostaining in determining individual prognosis (11). SSTR PET imaging is considered a better imaging method than SSTR scintigraphy using ^{111}In-octreotide due to its higher spatial resolution, higher image quality, and higher lesion detection rate (12). ^{68}Ga-DOTA-peptides can be used to reflect the expression of SSTR, especially in well-differentiated NETs (WD-NETs). High maximum standardized uptake value (SUV_{max}) is associated with a lower grade, better progression-free survival (PFS), and higher responsiveness to peptide receptor radionuclide therapy (PRRT) (13, 14). A meta-analysis by Lee and Kim (15) showed that the SUV_{max} of ^{68}Ga-SSA is an important prognostic parameter for NETs patients. Low SUV_{max} is associated with the high risk of disease progression and mortality.

However, SUV_{max} reflects the value of a single voxel but does not represent the entire tumor. The volume parameters derived from PET in predicting the prognoses and monitoring the treatment can directly estimate systemic tumor burden, such as metabolic tumor volume (MTV) and total disease glycolysis (TLG), based on 2-deoxy-2-(^{18}F) fluoro-D-glucose (^{18}F-FDG) (16–19). However, well-differentiated NETs (WD-NETs) do not usually show high ^{18}F-FDG uptake (20). SSTR-based PET/CT may be suitable for predicting the prognosis of WD-NETs patients. However, there are conflicting results regarding the prognostic value of volumetric parameters based on SSTR-PET in NETs (21, 22).

Therefore, we performed this meta-analysis to analyze the predictive value of volumetric parameters based on SSTR-PET for survival outcome in patients with NETs.

MATERIALS AND METHODS

The preferred reporting items for systematic reviews and meta-analyses (PRISMA statement) guidelines were used to perform this meta-analysis (23).

Data Search and Study Selection

We performed a systematic search of PUBMED (to May 2021), EMBASE (to May 2021), Web of Science (to May 2021), and Cochrane (to May 2021) for English publications. The terms were as follows: ("neuroendocrine tumors" or "neuroendocrine tumor" or "tumor neuroendocrine" or "tumors neuroendocrine" or "neuroendocrine") and ("PET") or ("positron emission tomography") and ("somatostatin receptor" or "SSTR") and ("volume" or "volume-based parameters" or "tumor burden" or "tumor volume" or "volumetrical parameter") and ("prognos*" or "predict*" or "Survival" or "outcome" or "PFS" or "OS" or "progress free survival" or "overall survival"). All searches were limited to human studies.

The inclusion criteria were studies using SSTR-based PET as an imaging tool, including volumetric parameters [total tumor volume (TTV) or total-lesion SSTR expression (TL-SSTR)] for whole body lesions and reported survival data. Reviews, abstracts, case reports, and editorial materials were excluded. Two authors independently searched and screened the eligible articles. A consensus resolved any discrepancies.

Data Extraction and Quality Assessment

Data were extracted from the enrolled studies independently by two reviewers and the following information was recorded: first author, publication year, country, patient number, tumor grade, tumor site, radiotracer used, treatment after PET/CT scans, reported survival, PET volumetric parameters, and cut-off values of volumetric parameters.

Two reviewers independently used the quality in prognostic studies (QUIPS) tool to evaluate the quality of the included studies (24). The tool assesses the risk of bias in six domains including study participation, study attrition, measurement of prognostic factors, measurement of outcome, study confounding, and statistical analysis and reporting. Consensus was reached through discussion.

Statistical Analysis

The primary outcome was PFS, including disease-free survival, recurrence-free survival, and event-free survival as the main outcome, and also the time interval from the date of starting therapy to the date of recurrence or metastasis. The secondary endpoint was overall survival (OS), defined as the time interval from the start of therapy to death from any cause. The effect of TTV or TL-SSTR on PFS and OS was measured by the effect size of the hazard ratio (HR). PFS or OS data were extracted using methods suggested in previous research (25). Univariate HR and 95% confidence intervals (CI) were extracted for each study, if provided by the author. If not, we used the Engauge Digitizer (http://markummitchell.github.io/engauge-digitizer/) to determine the survival rate according to the Kaplan–Meier curve to reconstruct HR estimate and its variance, assuming that patients were censored at a constant rate during the follow-up. Heterogeneity between studies was assessed by χ^2 test and I^2 statistics described by Higgins et al. (26). When $I^2 \leq 50\%$ and Cochran Q was $P \geq 0.1$, a fixed effects model was used; when $I^2 > 50\%$ or Cochran Q is $P < 0.1$, the random effect model was used. Subgroup analyses were performed according to the tumor grade and type of radiotracer. Further, funnel plots Begg's and Egger's test were performed to assess for any publication bias (27). Meanwhile, we performed the sensitivity analysis for prognosis by omitting each study to assess the influence of an individual study on the whole meta-analysis. P-values < 0.05 were considered

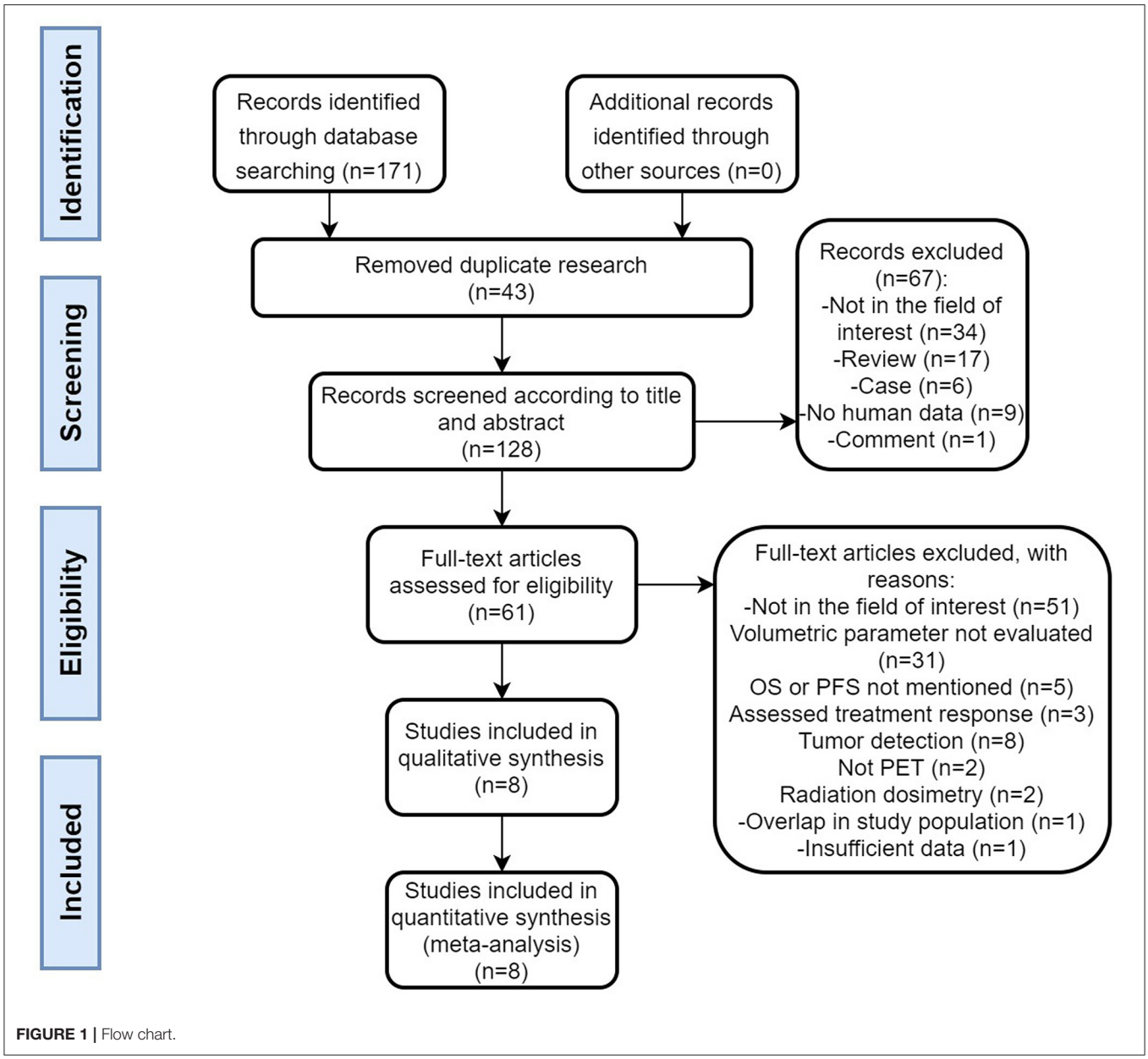

FIGURE 1 | Flow chart.

statistically significant. Data from each study were analyzed using Review Manager (RevMan, Version 5.3; The Nordic Cochrane Centre, Copenhagen, Denmark) and Stata Version 15.0 (College Station, TX).

RESULTS

Study Characteristics

A flow chart of the data search and selection is presented in **Figure 1**. A total of eight studies involving 593 patients were included in our meta-analysis. Five studies (21, 22, 28–30) were retrospective and three studies (31–33) were a prospective design. According to the WHO grade, three researches (22, 29, 30) included well-differentiated NETs (grade 1 and/or 2). Three studies had heterogeneous populations containing all grades (21, 31, 33) and the remaining two studies did not clearly state the grade of the enrolled patients (28, 32). All the eight studies included pancreas origin NETs and seven studies enrolled gastric intestinal (GI) tract origin NETs, including the stomach or/and midgut or/and rectum (21, 22, 28, 29, 31–33). Seven studies had other site origin NETs such as the lung, extrahepatic biliary tract, adrenal, and cancer of unknown primary origin (21, 22, 28, 29, 31–33).

The characteristics of the included study are shown in **Table 1**. From them, four studies used ^{68}Ga-DOTATATE (22, 29, 31, 32), three studies used ^{68}Ga-DOTATOC (21, 28, 30), and one study (33) used ^{64}Cu-DOTATATE for PET imaging. The parameters included TTV in eight studies and TL-SSTR

TABLE 1 | Characteristics of the included study.

No.	Study	Year	Country	Study design	Patient No.	Tumor Grade	Tumor site	Radio-tracer	Treatment After 68Ga-SSTR PET	End Point	Studied PET Parameters	Tumor delineation	Cut off value
1	Tirosh et al.	2018	USA	prospective	184	I–III	Pancreas GI tract CUP Lung	^{68}Ga-DOTATATE	medical, PRRT, LDT, Surgery	PFS and Disease-specific mortality	Total TV	Adaptive threshold by visual inspection	7.0 ml 35.8 ml
2	Toriihara et al.	2019	USA	retrospective	92	I–II	Pancreas GI tract CUP	^{68}Ga-DOTATATE	Surgery, somatostatin analog, LDT, Radiation, PRRT	PFS	Total TV and TL-SSTR	50% of SUV_{max}	11.29 ml
3	Ohlendorf et al.	2019	Germany	retrospective	33	I–II	Pancreas GI tract CUP	^{68}Ga-DOTATATE	PRRT	PFS	Total TV and TL-SSTR	40% of SUV_{max}	140.8 ml 4,852 ml
4	Ohnona et al.	2019	France	retrospective	50	I–II	Pancreas	^{68}Ga-DOTATOC	surgery, somatostatin analog, chemotherapy, targeted therapy, PRRT, local therapy of a single metastatic site.	PFS	Total TV	41% of SUV_{max}	13.8 ml
5	Kim et al.	2020	Republic of Korea	retrospective	64	I–III	Pancreas GI tract CUP	^{68}Ga-DOTATOC	somatostatin analog	PFS	Total TV and TL-SSTR	1.5*liver SUV_{mean} + 2*standard deviation	58.9 ml 778.5
6	Pauwels et al.	2020	Belgium	retrospective	57	(–)	GI tract Pancreas CUP Other	^{68}Ga-DOTATOC	PRRT	PFS and OS	Total TV and TL-SSTR	Adaptive threshold by visual inspection	578 ml
7	Carlsen et al.	2021	Denmark	prospective	116	I–III	GI tract Pancreas Extrahepatic biliary tract Lung CUP	^{64}Cu-DOTATATE	Surgery LDT, external radiation. Interferon, somatostatin analog, chemotherapy and/or PRRT.	PFS and OS	Total TV	1.5*liver SUV_{mean} + 2*standard deviation	54.9 ml
8	Ortega et al.	2021	Canada	prospective	96	(–)	GI Pancreas CUP Lung Adrenal	^{68}Ga-DOTATATE	PRRT	PFS	Total TV	SUV_{max} of liver/spleen	(-)

CUP indicates cancer of unknown primary; PRRT, peptide receptor- radionuclide therapy; LDT, liver-directed treatment; OS, overall survival; PFS, progress free survival; TTV, total tumor volume; TL-SSTR, total-lesion somatostatin receptors expression; SUV_{max}, maximum standardized uptake value.

in two studies (21, 29). Seven studies (21, 22, 29–33) analyzed the prognostic value of TTV regarding PFS, and three studies further evaluated the relationship between TTV and OS (or disease-specific mortality) (28, 31, 33). Four studies reported the relationship between PFS and TL-SSTR (21, 22, 28, 29). Six threshold methods were applied for the measurement of TTV and TL-SSTR of whole-body lesions (**Table 1**). Cutoff value of TTV ranged from 7 to 578 ml, and the cutoff value of TL-SSTR in PET in two studies were 778.5 and 4,852 ml, respectively.

Quality Assessment

According to the QUIPS tool quality assessment results, four studies (22, 30, 31, 33) had a moderate risk selection bias because they did not report whether the study population was consecutively selected, and two studies (21, 30) had high selection bias due to the relatively small number of cases enrolled in the group. All included studies showed a low risk of attrition bias. Regarding the measurement of prognostic factors, four studies (21, 29–31) showed a higher risk of bias due to the dependence on the cutoff value of the data, while two studies showed a moderate risk of bias because it was not mentioned whether blinded-manner was used in the measurement. For outcome measurement, seven studies (21, 22, 28–32) showed a moderate risk of bias because it was not clear whether the outcome measurement was performed without prognostic factors or the method used for the outcome measurement was unclear.

Regarding confounding bias, two studies (29, 31) showed high risk due to the lack of multivariate analysis. One study (28) showed moderate risk because grade was not considered. In terms of statistical analysis, two studies (22, 32) showed a higher risk of bias because the study included all variables that might be affected by multicollinearity into the multiple

regression. In general, the results of the QUIPS tool indicated that the overall quality of the included studies was moderate (**Supplementary Table 1**).

Prognostic Value of TTV and TL-SSTR on PFS and OS

The effect of TTV on PFS was analyzed using seven studies. However, in one study (32), the study was omitted because HR could not be combined using continuous variables, while the other six studies were combined because all HR used binary variables. The combined HRs of 2.24 (95% CI: 1.73–2.89) was given a I^2 of 0% using a fixed-model, showing a correlation between TTV and PFS ($P < 0.00001$) (**Table 2**; **Figure 2**). Also, we conducted sensitivity analysis (**Supplementary Figure 1**) to further estimate the impact on the combined HRs.

The effect of TTV on OS was analyzed using three studies. The combined HR was 3.54 with statistical significance (95% CI, 1.77–7.09; $P = 0.0004$). Heterogeneity was moderate ($\chi^2 = 4.12$, $P = 0.13$; $I^2 = 52\%$). The combined HRs were found to be stable, suggesting no individual study significantly affected the results (**Supplementary Figure 1**).

The effect of TL-SSTR on PFS was analyzed using three studies (21, 22, 29). A random-effects model was used and the pooled HR was 1.61 (95% CI, 0.48–5.44, $P = 0.05$; $I^2 = 66\%$, **Figure 2**; **Table 2**) with significant heterogeneity. The results showed no statistically significant correlations with PFS and TL-SSTR ($P = 0.44$).

TABLE 2 | Summary of the meta-analysis results.

Parameter	Study no.	End point	HR	95%CI	*P*	Model
TTV	6	PFS	2.24	1.73–2.89	<0.00001*	Fixed
TTV	3	OS	3.54	1.77–7.09	0.0004*	Random
TL-SSTR	3	PFS	1.61	0.48, 5.44	0.44	Random

TTV, total tumor volume; TL-SSTR, total-lesion somatostatin receptors expression; HR, hazard ratio; CI: confidence intervals.
**Statistically significant (P < 0.05).*

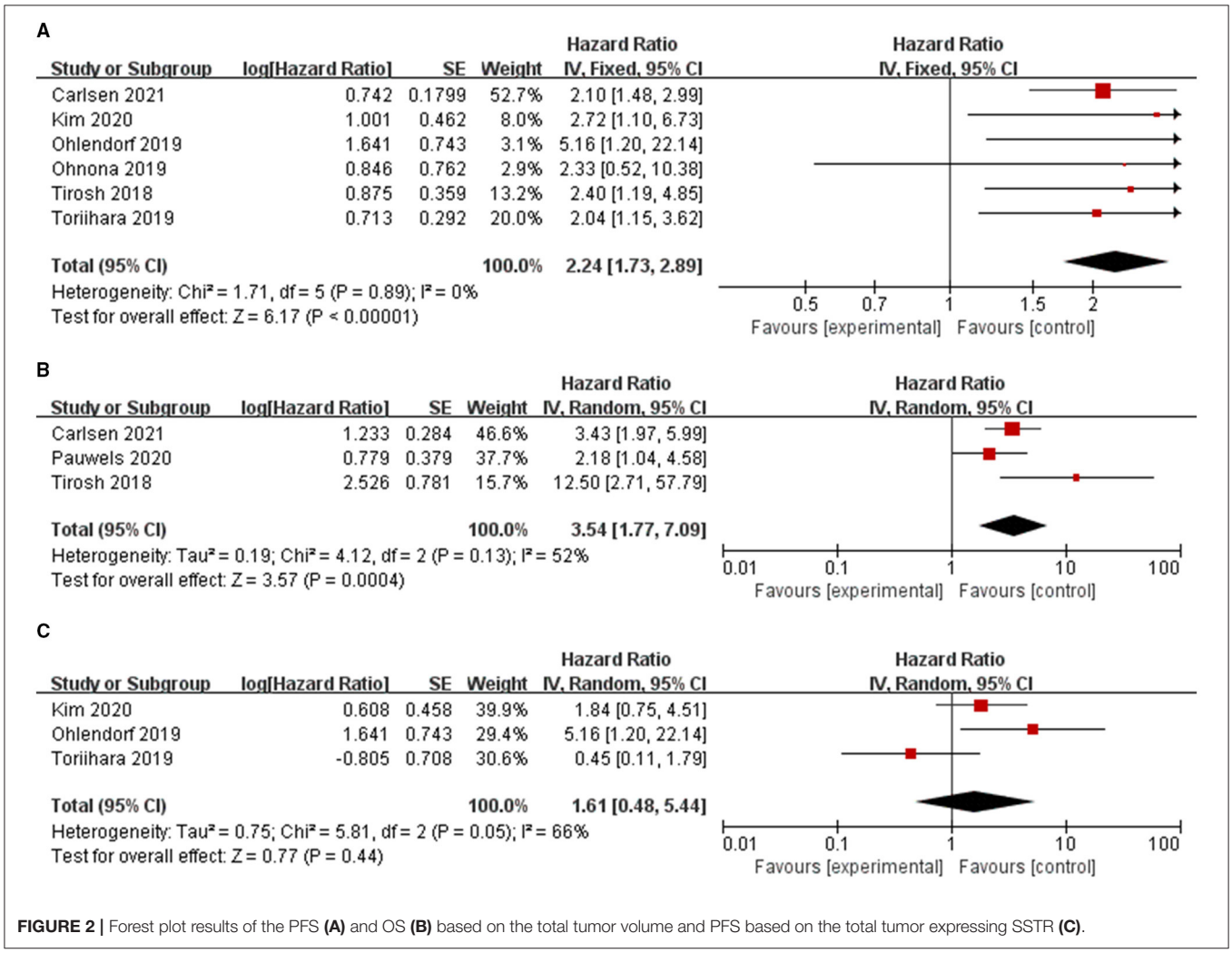

FIGURE 2 | Forest plot results of the PFS **(A)** and OS **(B)** based on the total tumor volume and PFS based on the total tumor expressing SSTR **(C)**.

TABLE 3 | Results of subgroup analysis in PFS based on TTV.

End point	Factor	Study no.	Heterogeneity test (I^2, P)	HR	95%CI of HR	P-value	Model
PFS	Well-differentiated NETs (G1, 2)	3	0%, 0.51	2.31	1.40-3.82	0.001*	Fixed
	All grades of NETs (G1–3)	3	0%, 0.85	2.21	1.64-2.98	<0.00001*	Fixed
PFS	^{68}Ga-DOTATATE	3	0%, 0.51	2.34	1.53-3.58	<0.0001*	Fixed
	^{68}Ga-DOTATOC	2	0%, 0.86	2.61	1.20-5.66	0.02*	Fixed
	^{64}Cu-DOTATATE	1	NA	NA	NA	NA	NA

NA, Not applicable.
PFS, progression-free survival; TTV, total tumor volume.
**Statistically significant ($P < 0.05$).*

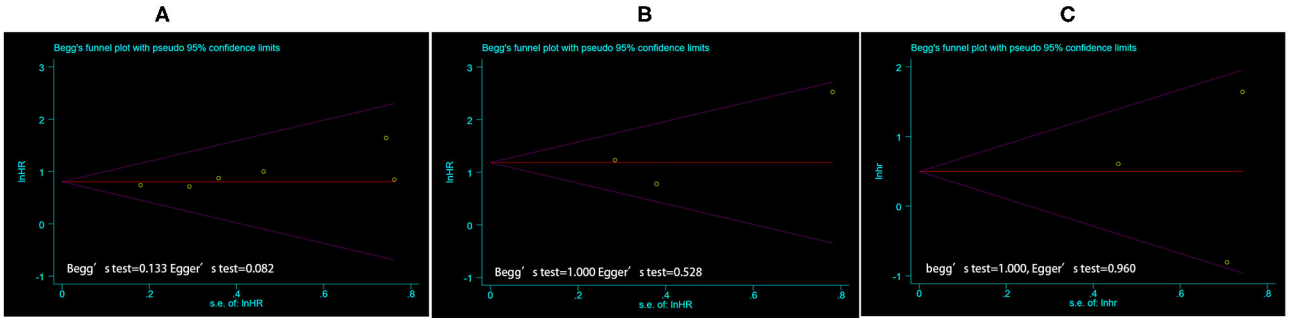

FIGURE 3 | The funnel plot of publication bias estimates the results of PFS **(A)** and OS **(B)** based on TTV, and PFS based on TL-SSTR **(C)** in the meta-analysis. Egger's test and Begg's test were used for statistical analysis, where the $P < 0.05$ was considered as significant. PFS, Progress free survival; OS, overall survival; TTV, total tumor volume; TL-SSTR, total-lesion somatostatin receptors expression.

Subgroup Analysis

Subgroup analysis was performed to the tumor grade and type of radiotracer. Since the research on PFS based on TL-SSTR and the research on OS by TTV are relatively small, we only performed subgroup analysis on PFS based on TTV (**Table 3**). Among studies of TTV on PFS, no obvious heterogeneity was found between the studies on well-differentiated NETs (G1/2) (HR: 2.31, 95%CI: 1.40–3.82; $P = 0.001$) and studies on all grades of NETs (HR: 2.21, 95%CI: 1.64–2.98; $P < 0.00001$) ($I^2 = 0\%$, $P = 0.88$). Also there is no statistical difference between different imaging agents for predicting PFS ($I^2 = 0\%$, $P = 0.88$).

Publication Bias

Begg's and Egger's tests were used to assess publication bias. The funnel plot and P-value estimation indicated no publication bias for TTV on PFS and OS, as well as for TL-SSTR on PFS (**Figure 3**).

DISCUSSION

To our knowledge, this is the first systematic review and meta-analysis to evaluate the prognostic value of volume-based parameters of SSTR PET/CT in NETs. The volumetric parameter based on SSTR PET is useful in predicting PFS. Subgroup analysis reveals that tumor grade and radiotracers may not affect the prognosis.

^{18}F-FDG is the most common PET imaging agent, which can non-invasively assess tumor glucose metabolism and proliferation (34, 35). ^{18}F-FDG PET can be used not only for diagnosis and staging, but also for assessing the proliferative activity and malignancy of tumors. Studies have shown that ^{18}F-FDG may also reflect the prognosis of many tumors, including NET (36–38). A meta-analysis based on ^{18}F-FDG PET/CT showed that MTV as a volumetric parameter of ^{18}F-FDG PET may be an independent prognostic factor for survival (39). However, none of the studies we included had ^{18}F-FDG PET volume parameters for predictive evaluation of prognosis. Although it is not clear whether volumetric parameters based on SSTR PET have better prognostic value than volumetric parameters based on FDG (MTV and TLG) in this study, tumor volume and total tumor expressing SSTR based on SSTR-PET as prognostic biomarkers of NETs have unique advantages compared with MTV or TLG. On the one hand, SSTR2 was an independent prognostic marker in NETs (11), and tumor volume based on SSTR was also correlated with PFS and OS (40). On the other hand, these SSTR-based volume parameters can better reflect the SSTR situation in entire tumors. In the future, we expect to directly compare the ability of ^{18}F-FDG and SSTR PET parameters to predict prognosis through prospective studies.

In this review, higher TTV based on SSTR-PET showed shorter PFS and OS. Although the study of Ortega et al. (32) did not include the meta-analysis, the study still suggests that higher TTV is associated with a worse prognosis. Of six studies (21, 22, 28, 30, 32, 33) in which multivariate analysis for PFS was performed, four out of (22, 30, 32, 33) six were prognostic markers for PFS. Two out of (30, 32) three studies showed

that the TTV were prognostic markers for OS. However, TL-SSTR was not significantly related to the prognosis in our study. Only Ohlendorf et al. (29) showed TL-SSTR was associated with PFS. The author believed that the difference may come from the different methods of tumor burden measurement and the samples of enrolled patients.

Heterogeneity was detected in this meta-analysis. In pooled data, significant heterogeneity was found for TTV based on SSTR-PET in predicting PFS. After excluding the study of Ortega et al. (32), the results of the overall estimated values aggregated by PFS reduced heterogeneity (I^2, from 87 to 0%) with a HR of 2.24 (95% CI: 1.73–2.89). This may be due to the different tumor volume threshold, which should be discussed in a prospective study. Further analysis found that tumor grade revealed that the TTV of SSTR-PET could predict PFS and OS of all grades of NETs. Since the NET grade depends on the biopsy site, and the heterogeneity of NETs is high, the volume parameter may be more conducive to predicting the prognosis, but it still needs further research to confirm. Additionally, we also performed subgroup analysis of radiotracer types. Subgroup analysis found that the use of single ^{68}Ga-DOTANOC and ^{68}Ga-DOTATATE showed prognostic value. As we all know, ^{68}Ga-DOTANOC, which binds specifically to sst_2, sst_3, and sst_5 (41), has ten-times lower sst_2 affinity than the sst_2-selective tracer ^{68}Ga-DOTATATE (42). A study has shown that ^{68}Ga-DOTANOC performed better in detecting liver metastasis and had a higher tumor-to-background ratio in liver lesions due to the broader SSTR-binding profile (43). However, another study showed that ^{68}Ga-DOTATATE detected more liver lesions, mainly due to a higher lesion uptake (44). Therefore, whether different radiotracers have a significant impact on the prognosis of tumor burden remains to be further studied.

To the best of our knowledge, this is the first meta-analysis to evaluate the prognostic value of volumetric parameters in the SSTR-PET in NETs. However, due to limited literature, it is difficult to directly compare the HRs between SUV_{max} and the volume parameter. In our study, volumetric parameters based on SSTR-PET were independent prognostic markers in three studies (29–31) of eight. SUV was found to be an independent prognostic marker in only one study (28) of eight.

This study has several limitations. Firstly, there were only three studies involving OS, and few studies involving TL-SSTR. Secondly, there were significant differences in study design, image analysis, cutoff value, sample sizes, and patient selection among the studies included in the current meta-analysis, leading to publication bias. Thirdly, due to the limited studies we enrolled, we cannot evaluate the best cut-off value of tumor burden parameters for prognostic prediction under the same primary site, treatment, and course of disease. We look forward to further research in future large-sample prospective studies.

CONCLUSION

The TTV of SSTR-PET is a significant prognostic parameter in NETs patients. The high TTV is associated with an increased risk of disease progression and mortality, whether it is a well-differentiated NET group or a NET group of all grades. In the future, the TTV of SSTR-PET could be used as a potential predictor of prognosis in patients with NETs.

DATA AVAILABILITY STATEMENT

The original contributions presented in the study are included in the article/**Supplementary Material**, further inquiries can be directed to the corresponding author/s.

AUTHOR CONTRIBUTIONS

JH was responsible for experimental design, experimental analysis and thesis writing. YY and NC were responsible for literature retrieval, data screening, and article revision. DC and SH were responsible for the guidance and review of the thesis. All authors contributed to the article and approved the submitted version.

FUNDING

This study was supported by the National Natural Science Foundation of China (Grant No. 91859207).

SUPPLEMENTARY MATERIAL

The Supplementary Material for this article can be found online at: https://www.frontiersin.org/articles/10.3389/fmed.2021.771912/full#supplementary-material

REFERENCES

1. Dasari A, Shen C, Halperin D, Zhao B, Zhou S, Xu Y, et al. Trends in the Incidence, Prevalence, and Survival Outcomes in Patients With Neuroendocrine Tumors in the United States. *JAMA Oncol.* (2017) 3:1335–42. doi: 10.1001/jamaoncol.2017.0589
2. Hallet J, Law CH, Cukier M, Saskin R, Liu N, Singh S. Exploring the rising incidence of neuroendocrine tumors: a population-based analysis of epidemiology, metastatic presentation, and outcomes. *Cancer.* (2015) 121:589–97. doi: 10.1002/cncr.29099
3. Zandee WT, Herder WWde. The evolution of neuroendocrine tumor treatment reflected by ENETS guidelines. *Neuroendocrinology.* (2018) 106:357–65. doi: 10.1159/000486096
4. Schmid-Tannwald C, Schmid-Tannwald CM, Morelli JN, Neumann R, Haug AR, Jansen N, et al. Comparison of abdominal MRI with diffusion-weighted imaging to 68Ga-DOTATATE PET/CT in detection of neuroendocrine tumors of the pancreas. *Eur J Nucl Med Mol Imaging.* (2013) 40:897–907. doi: 10.1007/s00259-013-2371-5
5. Janssen I, Chen CC, Millo CM, Ling A, Taieb D, Lin FI, et al. PET/CT comparing (68)Ga-DOTATATE and other radiopharmaceuticals and in comparison with CT/MRI for the localization of sporadic metastatic pheochromocytoma and paraganglioma. *Eur J Nucl Med Mol Imaging.* (2016) 43:1784–91. doi: 10.1007/s00259-016-3357-x
6. Fisher AV, Lopez-Aguiar AG, Rendell VR, Pokrzywa C, Rocha FG, Kanji ZS. et al. Predictive value of chromogranin A and a pre-operative risk score to predict recurrence after resection of pancreatic neuroendocrine

tumors. *J Gastrointest Surg.* (2019) 23:651–8. doi: 10.1007/s11605-018-04080-1
7. Lee L, Ito T, Jensen RT. Prognostic and predictive factors on overall survival and surgical outcomes in pancreatic neuroendocrine tumors: recent advances and controversies. *Expert Rev Anticancer Ther.* (2019) 19:1029–50. doi: 10.1080/14737140.2019.1693893
8. Jilesen AP, Busch OR, van Gulik TM, Gouma DJ, Nieveen van Dijkum EJ. Standard pre- and postoperative determination of chromogranin a in resectable non-functioning pancreatic neuroendocrine tumors—diagnostic accuracy: NF-pNET and low tumor burden. *Dig Surg.* (2014) 31:407–14. doi: 10.1159/000370007
9. Di Giacinto P, Rota F, Rizza L, Campana D, Isidori A, Lania A. et al. From Laboratory to Clinical Aspects of Patients with Neuroendocrine Tumors. *Int J Endocrinol.* (2018) 2018:8126087. doi: 10.1155/2018/8126087
10. Binderup T, Knigge U, Mellon Mogensen A, Palnaes Hansen C, Kjaer A. Quantitative gene expression of somatostatin receptors and noradrenaline transporter underlying scintigraphic results in patients with neuroendocrine tumors. *Neuroendocrinology.* (2008) 87:223–32. doi: 10.1159/000113128
11. Brunner P, Jörg AC, Glatz K, Bubendorf L, Radojewski P, Umlauft M, et al. The prognostic and predictive value of sstr(2)-immunohistochemistry and sstr(2)-targeted imaging in neuroendocrine tumors. *Eur J Nucl Med Mol Imaging.* (2017) 44:468–75. doi: 10.1007/s00259-016-3486-2
12. Deppen SA, Blume J, Bobbey AJ, Shah C, Graham MM, Lee P, et al. 68Ga-DOTATATE compared with 111In-DTPA-octreotide and conventional imaging for pulmonary and gastroenteropancreatic neuroendocrine tumors: a systematic review and meta-analysis. *J Nucl Med.* (2016) 57:872–8. doi: 10.2967/jnumed.115.165803
13. Campana D, Ambrosini V, Pezzilli R, Fanti S, Labate AM, Santini D, et al. Standardized uptake values of (68)Ga-DOTANOC PET: a promising prognostic tool in neuroendocrine tumors. *J Nucl Med.* (2010) 51:353–9. doi: 10.2967/jnumed.109.066662
14. Stefanova M, Kratochwil C, Mavriopoulou E, Afshar-Oromieh A, Mier W, Schwartz L, et al. SUV of [68Ga]DOTATOC-PET/CT predicts response probability of PRRT in neuroendocrine tumors. *Mol Imaging Biol.* (2015) 17:313–8. doi: 10.1007/s11307-014-0795-3
15. Lee DY, Kim YI. Prognostic value of maximum standardized uptake value in 68Ga-somatostatin receptor positron emission tomography for neuroendocrine tumors: a systematic review and meta-analysis. *Clin Nucl Med.* (2019) 44:777–83. doi: 10.1097/RLU.0000000000002694
16. Tatsumi M, Isohashi K, Matsunaga K, Watabe T, Kato H, Kanakura Y. et al. Volumetric and texture analysis on FDG PET in evaluating and predicting treatment response and recurrence after chemotherapy in follicular lymphoma. *Int J Clin Oncol.* (2019) 24:1292–300. doi: 10.1007/s10147-019-01482-2
17. Nakamoto R, Zaba LC, Rosenberg J, Reddy SA, Nobashi TW, Davidzon G. et al. Prognostic value of volumetric PET parameters at early response evaluation in melanoma patients treated with immunotherapy. *Eur J Nucl Med Mol Imaging.* (2020) 47:2787–95. doi: 10.1007/s00259-020-04792-0
18. Werner RA, Bundschuh RA, Higuchi T, Javadi MS, Rowe SP, Zsótér N, et al. Volumetric and texture analysis of pretherapeutic (18)F-FDG PET can predict overall survival in medullary thyroid cancer patients treated with Vandetanib. *Endocrine.* (2019) 63:293–300. doi: 10.1007/s12020-018-1749-3
19. Mohamed E, Needham A, Psarelli E, Carroll M, Vinjamuri S, Sanghera B, et al. Prognostic value of (18)FDG PET/CT volumetric parameters in the survival prediction of patients with pancreatic cancer. *Eur J Surg Oncol.* (2020) 46:1532–8. doi: 10.1016/j.ejso.2020.02.002
20. Panagiotidis E, Alshammari A, Michopoulou S, Skoura E, Naik K, Maragkoudakis E, et al. Comparison of the Impact of 68Ga-DOTATATE and 18F-FDG PET/CT on clinical management in patients with neuroendocrine tumors. *J Nucl Med.* (2017) 58:91–6. doi: 10.2967/jnumed.116.178095
21. Kim YI, Yoo C, Oh SJ, Lee SJ, Kang J, Hwang HS, et al. Tumour-to-liver ratio determined by [68Ga]Ga-DOTA-TOC PET/CT as a prognostic factor of lanreotide efficacy for patients with well-differentiated gastroenteropancreatic-neuroendocrine tumours. *EJNMMI Res.* (2020) 10:1–1. doi: 10.1186/s13550-020-00651-z
22. Toriihara A, Baratto L, Nobashi T, Park S, Hatami N, Davidzon G, et al. Prognostic value of somatostatin receptor expressing tumor volume calculated from (68)Ga-DOTATATE PET/CT in patients with well-differentiated neuroendocrine tumors. *Eur J Nucl Med Mol Imaging.* (2019) 46:2244–51. doi: 10.1007/s00259-019-04455-9
23. Page MJ, McKenzie JE, Bossuyt PM, Boutron I, Hoffmann TC, Mulrow CD, et al. The PRISMA 2020 statement: an updated guideline for reporting systematic reviews. *BMJ.* (2021) 372:n71. doi: 10.1136/bmj.n71
24. Hayden JA, van der Windt DA, Cartwright JL, Côté P, Bombardier C. Assessing bias in studies of prognostic factors. *Ann Intern Med.* (2013) 158:280–6. doi: 10.7326/0003-4819-158-4-201302190-00009
25. Parmar MK, Torri V, Stewart L. Extracting summary statistics to perform meta-analyses of the published literature for survival endpoints. *Stat Med.* (1998) 17:2815–34. doi: 10.1002/(sici)1097-0258(19981230)17:24<2815::aid-sim110>3.0.co;2-8
26. Higgins JP, Thompson SG, Deeks JJ, Altman DG. Measuring inconsistency in meta-analyses. *BMJ.* (2003) 327:557–60. doi: 10.1136/bmj.327.7414.557
27. Egger M, Davey Smith G, Schneider M, Minder C. Bias in meta-analysis detected by a simple, graphical test. *BMJ.* (1997) 315:629–34. doi: 10.1136/bmj.315.7109.629
28. Pauwels E, Van Binnebeek S, Vandecaveye V, Baete K, Vanbilloen H, Koole M, et al. Inflammation-based index and (68)Ga-DOTATOC PET-derived uptake and volumetric parameters predict outcome in neuroendocrine tumor patients treated with (90)Y-DOTATOC. *J Nucl Med.* (2020) 61:1014–20. doi: 10.2967/jnumed.119.236935
29. Ohlendorf F, Henkenberens C, Brunkhorst T, Ross TL, Christiansen H, Bengel FM, et al. Volumetric 68Ga-DOTA-TATE PET/CT for assessment of whole-body tumor burden as a quantitative imaging biomarker in patients with metastatic gastroenteropancreatic neuroendocrine tumors. *Q J Nucl Med Mol Imaging.* (2020) 17: 2815–34. doi: 10.1055/s-0039-1683655
30. Ohnona J, Nataf V, Gauthe M, Balogova S, Belissant Benesty O, Zhang-Yin J, et al. Prognostic value of functional tumor burden on 68Ga-DOTATOC PET/CT in patients with pancreatic neuro-endocrine tumors. *Neoplasma.* (2019) 66:140–8. doi: 10.4149/neo_2018_180328N209
31. Tirosh A, Papadakis GZ, Millo C, Hammoud D, Sadowski SM, Herscovitch P, et al. Prognostic utility of total (68)Ga-DOTATATE-avid tumor volume in patients with neuroendocrine tumors. *Gastroenterology.* (2018) 154:998–1008.e1. doi: 10.1053/j.gastro.2017.11.008
32. Ortega C, Wong RK, Schaefferkoetter J, Veit-Haibach P, Myrehaug S, Juergens R, et al. Quantitative 68Ga-DOTATATE PET/CT parameters for the prediction of therapy response in patients with progressive metastatic neuroendocrine tumors treated with 177Lu-DOTATATE. *J Nucl Med.* (2021). doi: 10.2967/jnumed.120.256727
33. Carlsen EA, Johnbeck CB, Loft M, Pfeifer A, Oturai P, Langer SW, et al. Semi-automatic tumor delineation for evaluation of 64Cu-DOTATATE PET/CT in patients with neuroendocrine neoplasms: prognostication based on lowest lesion uptake and total tumor volume. *J Nucl Med.* (2021) 62:1564–70. doi: 10.2967/jnumed.120.258392
34. Delbeke D, Martin WH. Positron emission tomography imaging in oncology. *Radiol Clin North Am.* (2001) 39:883–917. doi: 10.1016/S0033-8389(05)70319-5
35. Hustinx R, Bénard F, Alavi A. Whole-body FDG-PET imaging in the management of patients with cancer. *Semin Nucl Med.* (2002) 32:35–46. doi: 10.1053/snuc.2002.29272
36. Xuan D, Wen W, Tian S, Piao M, Xu D, Liu L. Prognostic value of maximum standard uptake value, metabolic tumor volume, and total lesion glycolysis of 18F-FDG PET/CT in patients with renal carcinoma: a protocol for systematic review and meta analysis. *Medicine.* (2020) 99:e19988. doi: 10.1097/MD.0000000000019988
37. Chan DL, Bernard EJ, Schembri G, Roach PJ, Johnson M, Pavlakis N, et al. High metabolic tumour volume on 18-fluorodeoxyglucose positron emission tomography predicts poor survival from neuroendocrine neoplasms. *Neuroendocrinology.* (2020) 110:950–8. doi: 10.1159/000504673
38. Ito K, Schöder H, Teng R, Humm JL, Ni A, Wolchok JD, et al. Prognostic value of baseline metabolic tumor volume measured on (18)F-fluorodeoxyglucose positron emission tomography/computed tomography in melanoma patients treated with ipilimumab therapy. *Eur J Nucl Med Mol Imaging.* (2019) 46:930–9. doi: 10.1007/s00259-018-4211-0
39. Kim HS, Choi JY, Choi DW, Lim HY, Lee JH, Hong SP, et al. Prognostic value of volume-based metabolic parameters measured by (18)F-FDG PET/CT of

pancreatic neuroendocrine tumors. *Nucl Med Mol Imaging*. (2014) 48:180–6. doi: 10.1007/s13139-013-0262-0

40. Lee L, Ito T, Jensen RT. Imaging of pancreatic neuroendocrine tumors: recent advances, current status, and controversies. *Expert Rev Anticancer Ther.* (2018) 18:837–60. doi: 10.1080/14737140.2018.1496822
41. Wild D, Mäcke HR, Waser B, Reubi JC, Ginj M, Rasch H, et al. 68Ga-DOTANOC: a first compound for PET imaging with high affinity for somatostatin receptor subtypes 2 and 5. *Eur J Nucl Med Mol Imaging.* (2005) 32:724. doi: 10.1007/s00259-004-1697-4
42. Antunes P, Ginj M, Zhang H, Waser B, Baum RP, Reubi JC. et al. Are radiogallium-labelled DOTA-conjugated somatostatin analogues superior to those labelled with other radiometals? *Eur J Nucl Med Mol Imaging.* (2007) 34:982–93. doi: 10.1007/s00259-006-0317-x
43. Wild D, Bomanji JB, Benkert P, Maecke H, Ell PJ, Reubi JC, et al. Comparison of 68Ga-DOTANOC and 68Ga-DOTATATE PET/CT within patients with gastroenteropancreatic neuroendocrine tumors. *J Nucl Med.* (2013) 54:364–72. doi: 10.2967/jnumed.112.111724
44. Kabasakal L, Demirci E, Ocak M, Decristoforo C, Araman A, Ozsoy Y. et al. Comparison of 68Ga-DOTATATE and 68Ga-DOTANOC PET/CT imaging in the same patient group with neuroendocrine tumours. *Eur J Nucl Med Mol Imaging.* (2012) 39:1271–7. doi: 10.1007/s00259-012-2123-y

Conflict of Interest: The authors declare that the research was conducted in the absence of any commercial or financial relationships that could be construed as a potential conflict of interest.

Publisher's Note: All claims expressed in this article are solely those of the authors and do not necessarily represent those of their affiliated organizations, or those of the publisher, the editors and the reviewers. Any product that may be evaluated in this article, or claim that may be made by its manufacturer, is not guaranteed or endorsed by the publisher.

frontiers in Medicine

ORIGINAL RESEARCH
published: 16 December 2021
doi: 10.3389/fmed.2021.791131

Monitoring and Predicting Treatment Response of Extraocular Muscles in Grave's Orbitopathy by ^{99m}Tc-DTPA SPECT/CT

Chengzhi Jiang[1,2], *Zilong Deng*[1], *Jin Huang*[1], *Haoyu Deng*[1], *Jia Tan*[3], *Xinhui Li*[1]* and *Min Zhao*[1,4]*

[1] Department of Nuclear Medicine, Xiangya Hospital, Central South University, Changsha, China, [2] Department of PET-CT Center, Hunan Cancer Hospital/The Affiliated Cancer Hospital of Xiangya School of Medicine, Central South University, Changsha, China, [3] Department of Ophthalmology, Xiangya Hospital, Central South University, Changsha, China, [4] National Clinical Research Center of Geriatric Disorders, Xiangya Hospital, Central South University, Changsha, China

Objective: To investigate single-photon emission computed tomography/computed tomography (SPECT/CT) for assessing inflammation in the extraocular muscles (EOMs) and predicting the therapeutic efficacy of periocular glucocorticoid therapy (PGT) for Grave's ophthalmopathy (GO).

Materials and Methods: A total of 412 eyes from 206 patients with GO referred for ^{99m}Tc-DTPA orbital SPECT/CT were enrolled. Fourteen age- and gender-matched healthy controls (28 eyes) were included. The thickness and uptake ratio (UR) of four EOMs were derived from SPECT/CT. Eighty-six eyes from patients with GO patients received PGT. Changes in SPECT/CT parameters were evaluated between the pre- and post-treatment.

Results: 195 eyes and 217 eyes were classified as active and inactive stages by clinical activity score (CAS). Values of the thickness and UR of each EOM, T_{max}, and U_{max} were all significantly higher in the active GO than in the inactive GO and controls ($p < 0.01$). Among the 86 eyes (48 GO patients) included in the efficacy analysis, 56 eyes and 30 eyes were classified as responders and non-responders. Values of thicknesses and UR of each EOM, the maximum thickness (T_{max}), and the maximum UR (U_{max}) all dropped following PGT in the responders ($p < 0.01$). Logistic regression analysis identified the U_{max} as an independent predictor for the responders ($p < 0.01$). Moreover, the U_{max} demonstrated incremental predictive value over clinical characters and CAS, as evidenced by the improved area under the curve (0.85 vs. 0.78) and global chi-square (34.12 vs. 18.1).

Conclusion: ^{99m}Tc-DTPA SPECT/CT has the potential to assess inflammatory activity by detecting the involvement of EOMs in GO. Pre-treatment UR provides independent and incremental values for the prediction of PGT treatment response.

Keywords: Grave's ophthalmopathy, extraocular muscles, single-photon emission computed tomography/computed tomography, glucocorticoid, treatment response

OPEN ACCESS

Edited by:
Désirée Deandreis, University of Turin, Italy

Reviewed by:
Alberto Miceli, Università di Genova, Italy
Maria Mathew D'Souza, Institute of Nuclear Medicine and Allied Sciences (DRDO), India

***Correspondence:**
Xinhui Li
dclxh@139.com
Min Zhao
mzhao1981@csu.edu.cn

Specialty section:
This article was submitted to Nuclear Medicine, a section of the journal Frontiers in Medicine

Received: *08 October 2021*
Accepted: *15 November 2021*
Published: *16 December 2021*

Citation:
Jiang C, Deng Z, Huang J, Deng H, Tan J, Li X and Zhao M (2021) Monitoring and Predicting Treatment Response of Extraocular Muscles in Grave's Orbitopathy by ^{99m}Tc-DTPA SPECT/CT. Front. Med. 8:791131. doi: 10.3389/fmed.2021.791131

INTRODUCTION

Grave's orbitopathy (GO) is the most common extrathyroidal manifestation of Grave's disease and one of the most prevalent orbital disorders in adults (1–3). Signs and symptoms include eyelid retraction, proptosis, motility restriction, exposure keratopathy, and even vision loss, associated with a significant decrease in the quality of life of patients. As an autoimmune disease, GO follows a two-stage process, with an active inflammatory stage followed by an inactive fibrotic stage (2, 3). Anti-inflammatory treatment is usually considered effective during the active stage, but it has little value during the inactive stage (1, 4). Therefore, an accurate and objective assessment of inflammatory activity is essential to determine the appropriate treatment for GO.

The clinical activity score (CAS), based on inflammatory signs and symptoms, has been widely used for GO evaluation and as a criterion and guideline for therapeutic management (1). However, the acute inflammatory involvement of EOM or orbital fat may fail to be adequately assessed, especially when diplopia or motility impairment is not present (5–8). Moreover, diplopia and strabismus can be induced by either inflammation in the active stage or fatty degeneration and fibrosis in the inactive stage. MRI is another useful modality for GO imaging by the nature of its superior soft tissue contrast and no ionizing radiation. Especially, T2-weighted images can assist in staging and deciding treatment. However, the overall accuracy is still limited (9). Thus, a more precise assessment of EOM inflammatory activity is needed.

Currently, ^{99m}technetium (^{99m}Tc)-labeled diethylene triamine pentaacetic acid (DTPA) orbital single-photon emission computed tomography/computed tomography (SPECT/CT) or SPECT has proven to be a valuable method for the detection of inflammation in GO (5, 10). Theoretically, DTPA is uniformly distributed throughout the extracellular space, binds to polypeptides in the extracellular fluid, and does not cross the blood-tissue barrier. The amount of ^{99m}Tc-DTPA accumulation in the soft tissue of orbital cavity (mainly in the EOMs) is directly proportionate to the activity of the inflammation with associated hyperpermeability and breakdown of blood-tissue barrier (5, 11). This may explain the high uptake of ^{99m}Tc-DTPA in GO due to inflammation. Moreover, it provides not only visual but also semi-quantitative information about the activity of the disease. Although DTPA SPECT/CT imaging in patients with GO has been validated in some cases (10, 11), a systematic evaluation of the DTPA uptake of EOMs has not been validated. The aim of our study was to examine the SPECT/CT parameters of EOMs for assessing the inflammatory activity of GO, and to evaluate the role in predicting the efficacy of treatment.

MATERIALS AND METHODS

Study Population and Clinical Assessment

This study was approved by the Ethics Committee of Xiangya Hospital (No. 202101021). All the patients provided written informed consent for the imaging procedures as well as for participation in anonymized analyses. Data from 302 patients with GO who underwent orbital ^{99m}Tc-DTPA SPECT/CT were retrospectively collected in a single center from November 2016 to May 2017. All the patients with GO were diagnosed based on Bartley's criteria (1). Ninety-six patients with orbital tumors, other orbital inflammatory lesions, sinusitis, and history of systemic GC or radiation therapy were excluded. Finally, the remaining 206 patients with GO (412 eyes) were enrolled in this study.

All the patients underwent a full ophthalmological examination. The inflammatory activity of the eyes was assessed using the seven-point modified formulation of the CAS (1). Fourteen healthy subjects (28 eyes) without ophthalmological disorders and systemic immune diseases served as the control group.

Among the patients with GO, we selected those who received periocular corticosteroid therapy (PGT) for efficacy analysis. Inclusion criteria included CAS $\geq$ 2 and elevated uptake of EOMs by SPECT/CT. Patients with corticosteroid contraindication and pregnant or lactating women were excluded in this study. A total of 86 eyes received a periocular injection of 20 mg triamcinolone acetonide (40 mg/ml) (Jida Corporation, Kunming, China) weekly for 7 consecutive weeks. The selection of injection was based mainly on the CAS score or lesion of high uptake on SPECT/CT images. If SPECT/CT had high DTPA uptake only in the superior rectus, the injection was applied at the superomedial quadrants; if high uptake was present only in the inferior rectus, the injection was applied at the inferolateral quadrants. When SPECT/CT uptake was high in several recti, the injection was applied alternately at the inferolateral and superomedial quadrants. All the patients were evaluated by the same experienced ophthalmologist and had a final examination 3 to 6 months after the treatment. Response was assessed and defined by at least one of the following criteria: (1) the CAS dropped by at least 2 points and CAS $<$ 3; (2) no residual uptake of EOMs was observed on the follow-up SPECT/CT images. Patients who did not fulfill the above criteria were classified as "non-responders."

Orbital ^{99m}Tc-DTPA SPECT/CT Acquisition

All the subjects were scanned with a hybriddouble head SPECT/CT scanner (Precedence 16, SPECT/CT; Philips, Netherlands) using a low-energy and high-resolution collimator. After 20 min of intravenous administration of 555 MBq ^{99m}Tc-DTPA (Chinese Atomic Energy Institute, Beijing, China), an orbital CT scan (140 kV, 100 mA, 1 slice thickness) for attenuation correction was obtained with the patient's head positioned parallel to the Frankfurt plane. Then, SPECT images were acquired with 64 projections in step-and-shoot mode over 360 degrees (5.6 degrees per step), and matrix size was 64 $\times$ 64. The energy window was open by $\pm$10% centered at 141 keV. Subsequently, the CT and SPECT images were loaded into an EBW workstation (Philips, Netherlands) for further analysis.

SPECT/CT Imaging Measurement

Manual rigid registration of SPECT and CT images was carried out on the EBW workstation. Two experienced nuclear medicine specialists (MZ and CZJ) who were blinded to the SPECT/CT results evaluated the orbital SPECT/CT images together. The

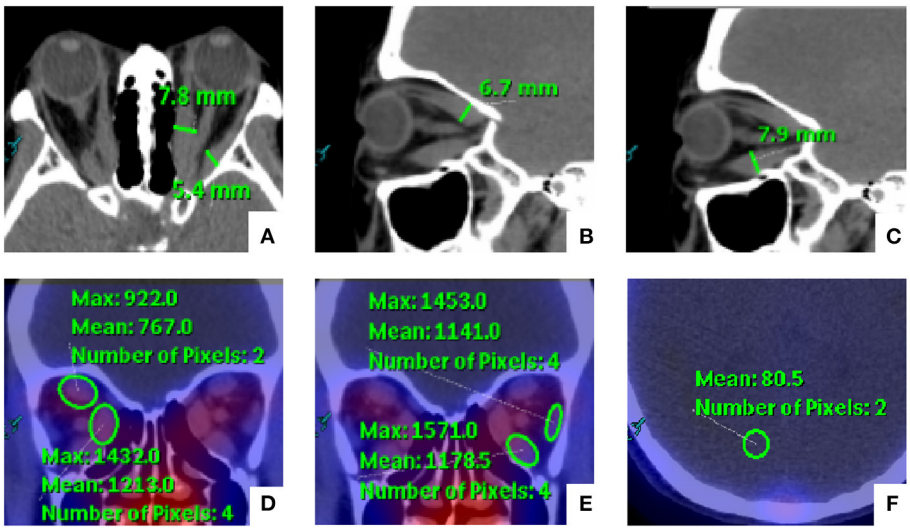

FIGURE 1 | Schematic diagram for the measurement of orbital single-photon emission computed tomography/computed tomography (SPECT/CT) semi-quantitative parameters of extraocular muscles (EOMs). **(A–C)** The medial rectus (MR) and lateral rectus (LR) were measured on the axial images, and the vertical diameters of the superior rectus (SR) and inferior rectus (IR) were measured on the sagittal images. In addition, **(D,E)** the EOM uptake values were determined by manually placing a round region of interest (ROI) within the consensus highest uptake portion of each EOM on the CT attenuation-corrected SPECT images. **(F)** The background uptake value was similarly determined through the analogous placement of an ROI on the occipital lobe.

thickness and DTPA uptake of EOMs were evaluated by the two readers. Horizontal diameters of the medial rectus (MR) and lateral rectus (LR), and the vertical diameters of the superior rectus (SR) and inferior rectus (IR) were measured on the series of images. In addition, the DTPA uptake was determined by manually placing a round region of interest (ROI) with the consensus highest uptake of each EOM on the CT attenuation-corrected SPECT images. The background uptake value was similarly determined through analogous placement of an ROI on the occipital lobe based on our previous studies (12). The methods for SPECT/CT parameter measurement are illustrated in **Figure 1**. For the same patient, the value of uptake ratio (UR) was calculated as the ratio of the maximum EOM uptake value to the maximum background uptake value. Furthermore, we chose the highest value of thickness and UR among the four EOMs as the maximum thickness (T_{max}) and the maximum UR (U_{max}).

Statistical Analysis

Continuous values were expressed as mean ± SD. The comparison among groups of continuous variables was performed by Student's *t*-test, Mann–Whitney U test, and one-way ANOVA depending on the nature of data. Categorical variables were presented as numbers and percentages and analyzed by Fisher's exact test. The univariate binary logistic regression analysis was applied to estimate potential predictors for the response of PGT. The multivariable binary logistic regression was performed to analyze the independent predictors, and variables with $p < 0.05$ in the univariate analysis were included. Moreover, the efficacy of treatment was evaluated by comparing the receiver operator characteristic (ROC) curve of binary logistic regression from different models. χ^2 Statistic by a likelihood ratio test was performed to calculate the incremental value of UR. Intra- and inter-observer agreements of parameters were assessed by the respective intraclass correlation coefficients (ICCs) from 20 randomly selected sets of images. Statistical analysis was performed using the IBM SPSS 25.0 software (IBM Corp., Armonk, NY, United States). $P < 0.05$ was considered statistically significant.

RESULTS

Comparison of EOM Parameters

According to the CAS, all the eyes were classified into the active GO (CAS ≥ 3/7, 104 patients, $n = 195$) and inactive GO (CAS < 3/7, 115 patients, $n = 217$) groups. The average age of active GO was 46 ± 12 years, which was higher than that of the inactive GO and control groups ($p < 0.01$ and $p < 0.05$ respectively). There was a significant difference in gender and smoking history between active GO and inactive GO ($p < 0.01$ and $p < 0.05$ respectively). Active GO patients showed significant increased thicknesses and UR of each EOM and U_{max} than those in both the inactive GO patients and the controls (all $p < 0.01$). The thickness values for the MR, SR, IR, T_{max}, UR of each EOM, and U_{max} in inactive GO were higher than those in the control group ($p < 0.05$). No significant difference in thickness value for the LR was found between the inactive and control subjects. The clinical characteristic and SPECT/CT parameters are summarized in **Table 1**.

Outcomes and Effectiveness of PGT

Of the 86 eyes treated with PGT, 56 eyes (65.1%) exhibited response. At baseline, the responders had greater thickness of the

TABLE 1 | Extraocular muscles (EOM) measurements among the three groups.

Characteristics	Active group (195 eyes)	Inactive group (217 eyes)	Control (28 eyes)	*p*-value
Female, *n* (%)	95 (48.7)$^{\#\#}$	153 (70.5)*	16 (57.1)	0.000
Age (years)	46 ± 12$^{*\#\#}$	39 ± 12	41 ± 12	0.112
Smokers, *n* (%)	68 (34.9)$^{\#}$	56 (25.8)	12 (42.9)	0.171
CAS, points	3.6 ± 0.9$^{\#\#}$	1.4 ± 0.7	/	0.000
Thickness, mm				
LR	4.2 ± 1.2$^{**\#\#}$	3.5 ± 1.0	2.8 ± 0.6	0.000
MR	5.6 ± 2.0$^{**\#\#}$	4.3 ± 1.5*	3.2 ± 0.5	0.000
SR	4.9 ± 2.0$^{**\#\#}$	3.7 ± 1.5*	2.7 ± 0.7	0.000
IR	6.1 ± 2.0$^{**\#\#}$	4.6 ± 1.7*	3.3 ± 0.6	0.000
T_{max}	6.9 ± 2.0$^{**\#\#}$	5.2 ± 1.7**	3.6 ± 0.5	0.000
UR, no unit				
LR	8.56 ± 1.99$^{**\#\#}$	7.32 ± 1.85*	6.82 ± 1.19	0.108
MR	11.63 ± 2.38$^{**\#\#}$	9.16 ± 1.96*	8.15 ± 1.34	0.001
SR	9.22 ± 3.18$^{**\#\#}$	7.29 ± 2.18*	6.08 ± 1.34	0.000
IR	11.06 ± 2.49$^{**\#\#}$	8.91 ± 2.05**	7.73 ± 1.24	0.001
U_{max}	12.31 ± 2.27$^{**\#\#}$	9.76 ± 2.03**	8.39 ± 1.20	0.002

CAS, clinical activity score; LR, lateral rectus; MR, medial rectus; SR, super rectus; IR, inferior rectus; T_{max}, maximum thickness among the four EOMs; U_{max}, maximum uptake ratio among the four EOMs.
Compare with the control group, $^{*}P$ <0.05, $^{**}P$ <0.01; compare with the inactive group, $^{\#}P$ <0.05, $^{\#\#}P$ <0.01.

TABLE 2 | Baseline EOM measurements.

Characteristics	Responders (56 eyes)	Non-responders (30 eyes)	*p*-value
Female, *n* (%)	32 (57.1)	15 (50.0)	0.526
Age (years)	41 ± 12	47 ± 11	0.026
Smokers, *n* (%)	17 (30.4)	8 (26.7)	0.719
TRAb (IU/L)	14.51 ± 13.63	15.02 ± 11.24	0.871
CAS, points	3.1 ± 0.9	2.8± 1.0	0.240
CAS≥3, *n* (%)	40 (71.4%)	15 (50.0%)	0.061
Thickness, mm			
LR	3.8 ± 1.0	4.3 ± 1.0	0.027
MR	5.6 ± 2.3	5.1 ± 1.8	0.306
SR	4.3 ± 1.5	5.2 ± 1.8	0.026
IR	6.1 ± 1.8	6.3 ± 2.8	0.742
T_{max}	6.7 ± 2.0	7.0 ± 2.5	0.539
Uptake ratio, no unit			
LR	8.31 ± 1.53	7.58 ± 1.42	0.035
MR	11.34 ± 2.08	9.65 ± 2.19	0.001
SR	9.02 ± 2.34	8.63 ± 2.30	0.465
IR	10.82 ± 1.88	8.92 ± 2.37	0.000
U_{max}	11.93 ± 1.74	10.46 ± 2.07	0.001

TRAb, thyroid-stimulating hormone (TSH) receptor antibodies; CAS, clinical activity score; LR, lateral rectus; MR, medial rectus; SR, super rectus; IR, inferior rectus; T_{max}, maximum thickness among the four EOMs; U_{max}, maximum uptake ratio among the four EOMs.

LR and SR and higher UR of the LR, MR, IR and U_{max} than the non-responders ($p < 0.05$); whereas, sex, smoking status, serum TRAb, CAS, CAS staging, thickness of the MR and IR, T_{max}, and UR of SR were similar between the two groups (all $p > 0.05$) (**Table 2**).

Subgroup analyses were performed between pre-treatment and post-treatment (**Figure 2**). The thickness and UR of each EOM, T_{max}, and U_{max} were reduced accordingly in the responders (all $p < 0.01$). In the non-responders, the thickness of the LR and SR decreased after PGT ($p < 0.01$, $p < 0.05$), but the UR of each EOM and U_{max} remained unchanged following PGT (all $p > 0.05$).

Variables for Predicting the Response to PGT

Univariate and multivariate logistic regression analyses were further performed to identify the predictive factors of response following PGT, such as age, gender, smoking habit, TRAb, CAS, T_{max}, and U_{max}. In the univariate analysis, age (OR 0.96, 95% CI 0.92–1.00, $p = 0.03$) and U_{max} (OR 1.57, 95% CI 1.71–2.11, $p = 0.002$) were significantly associated with the responders. In the multivariate analysis, age (OR 0.91; 95% CI 0.86–0.96; $p = 0.001$) and U_{max} (OR 2.08, 95% CI 1.41–3.06, $p < 0.001$) remained the independent predictors of the responders. The results are shown in **Table 3**.

In the ROC analysis of predictive models (**Figure 3**), model 1, incorporating clinical characters, alone showed the lowest area under the curve (AUC) (sensitivity 0.64, specificity 0.66, AUC 0.67). The AUC of model 2 combining clinical characters and CAS ≥ 3 (sensitivity 0.75, specificity 0.70, AUC 0.78), model 3 combining clinical characters and U_{max} (sensitivity 0.82, specificity 0.73, AUC 0.82), and model 4 combining clinical characters, CAS ≥ 3, and U_{max} (sensitivity 0.89, specificity 0.73, AUC 0.85) increased sequentially. Furthermore, likelihood ratio tests indicated that both CAS ≥ 3 and U_{max} provided a significant incremental predictive value for PGT response (**Figure 4**). The addition of CAS ≥ 3 and U_{max} increased the global chi-square as compared to the clinical characters (6.60 vs. 18.1, 6.60 vs. 29.34, $p < 0.001$, respectively). The model 4 further yield the greater global chi-square when compared to the model 1, 2, and 3 ($p < 0.001$, $p < 0.001$, and $p < 0.05$, respectively).

Reproducibility

The intra-observer reproducibility of measuring thickness and UR of EOMs were excellent, as reflected by high ICCs (0.985, 95% CI 0.981–0.989, $p < 0.001$;0.981, 95% CI 0.977–0.985, $p < 0.001$, respectively). Furthermore, the reproducibility of inter-observer was 0.971 (95% CI 0.965–0.981, $p < 0.001$) for thickness and 0.968 (95% CI 0.958–0.973, $p < 0.001$) for UR.

DISCUSSION

The notable results of this study were as follows: (1)we found significantly higher uptake and thickening of EOM evaluated by orbital SPECT/CT in patients with active GO than in patients with inactive GO. These parameters appeared useful for the differentiation disease activity between inactive and active GO; (2) the UR of EOMs as determined from SPECT/CT at

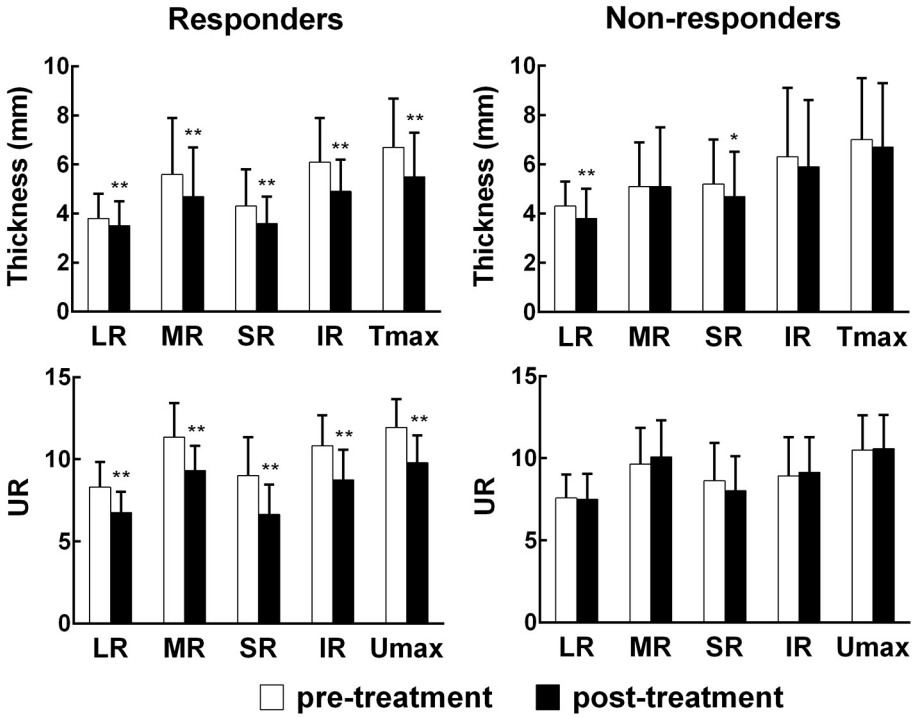

FIGURE 2 | Comparisons of orbital SPECT/CT parameters before and after treatment. EOM, extraocular muscle; LR, lateral rectus; MR, medial rectus; SR, super rectus; IR, inferior rectus; T_{max}, maximum thickness among the four EOMs; U_{max}, maximum uptake ratio among the four EOMs.*$p < 0.05$, **$p < 0.01$, compared with the pre-treatment group.

TABLE 3 | Univariate and multivariate logistic regression analyses in predicting response to therapy.

Variables	Univariate analysis			Multivariate analysis		
	OR	95%CI	*P*-valve	OR	95%CI	*P*-valve
Age (years)	0.96	0.92–1.00	0.030	0.91	0.86–0.96	0.001
Female (%)	1.33	0.55–3.25	0.526			
Smoking (%)	1.20	0.45–3.23	0.720			
TRAb (IU/L)	0.99	0.95–1.02	0.439			
CAS ≥ 3(%)	0.40	0.16–1.01	0.051			
T_{max}, mm	0.94	0.77–1.15	0.535			
U_{max}, no unit	1.57	1.17–2.11	0.002	2.08	1.41–3.06	<0.001

TRAb, thyroid-stimulating hormone (TSH) receptor antibodies; CAS, clinical activity score; T_{max}, maximum thickness among the four EOMs; U_{max}, maximum uptake ratio among the four EOMs.

baseline provided the independent and incremental values for the prediction of response following PGT.

To date, the CAS is the most commonly used clinical scale to determine the indication and duration of anti-inflammatory treatment. However, it presents some limitations that reflect ocular surface inflammation and has certain subjectivity. Orbital CT can provide information on exophthalmos and fat and muscle enlargement, which can be useful for diagnosis. The current study showed that the thickness of four EOMs in the active GO group were greater than those in the inactive GO group and control group, consistent with previous studies (13, 14). Additionally, we found that abdominal enlargement of the EOMs, especially the inferior and medial rectus muscles, was most common in GO. Although the thickness of the EOMs could reflect the stage of GO, the involvement of each EOM can occur in different phases, and it may be difficult to identify which EOM is in the inflammatory phase by clinical assessment alone. Therefore, it is challenging to evaluate the inflammatory activity from CT measurement.

Orbital ^{99m}Tc-DTPA SPECT has been used to evaluate autoimmune inflammation of the retro-bulbar area in patients with GO for many years (5, 11). However, only the retro-orbital area of a SPECT image could be analyzed for the assessment of inflammation, without allowing for a more precise indication of which EOM is involved. In addition, physiological uptake in adjacent nasal sinuses can sometimes lead to falsely positive accumulation in the retro-orbital cavity. Thus, our study aimed to evaluate the EOMs of GO using a hybrid SPECT/CT method. SPECT/CT depiction of EOM inflammation may help clinicians to accurately evaluate the inflammatory staging of GO (10, 13). Our findings showed that the UR of EOM, especially the medial and inferior rectus muscles, in the active GO group was higher than that in the inactive GO group and the control group, suggesting that the UR has a potential for the evaluation of inflammatory infiltration within EOMs.

The European Group of Grave's Orbitopathy (EUGOGO) recommended systemic GC treatment for patients with

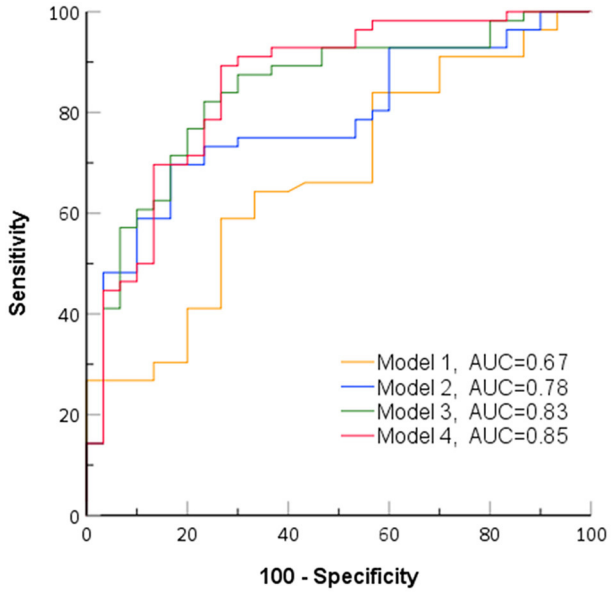

FIGURE 3 | Receiver operating characteristic curves of identified models for predicting response to periocular glucocorticoid therapy (PGT). AUC, area under the curve; model 1, clinical characteristics; model 2, clinical characteristics + clinical activity score (CAS) ≥ 3; model 3, clinical characteristics + U_{max}; model 4, clinical characteristics + CAS ≥ 3+ U_{max}.

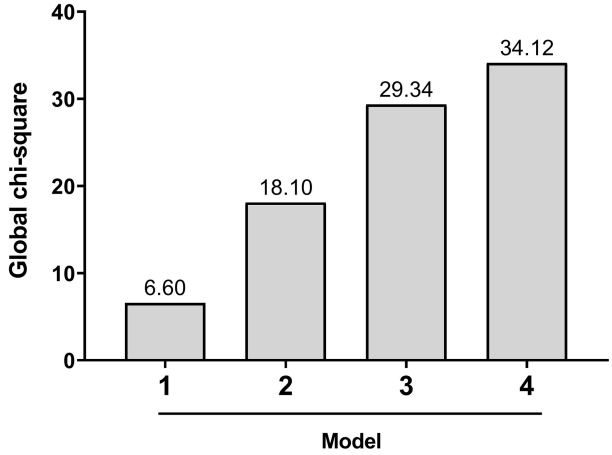

FIGURE 4 | Incremental value of U_{max} for the prediction of responder to PGT. Model 1, clinical characteristic; model 2, clinical characteristics + CAS ≥ 3; model 3, clinical characteristics + U_{max}; model 4, characteristics + CAS ≥ 3 + U_{max}.

moderate-to-severe GO as the first-line therapy (1, 15–18). However, medications can cause many side effects. Previous studies have found that periocular injections of GC were safe and effective in mild-to-moderate GO without causing serious complications (10). In clinical practice, the classification of clinical outcomes following GC therapy in GO has not been consistent: some patients with mild GO had significant improvements with local steroid therapy (5, 10), but a portion of patients with moderate-to-severe GO did not respond to systemic steroids (9, 19). This heterogeneity could be attributed to the presence of fibrosis and residual inflammation not detectable by current imaging modalities. Thus, it is essential to accurately evaluate the degree of inflammation and select the appropriate time for treatment.

In this study, we evaluated the predictive value of DTPA SPECT/CT for the efficacy of PGT in GO. Our results showed that the UR and thickness of EOMs all significantly dropped after treatment in the responders. However, in the non-responders, the UR of EOMs remained unchanged after treatment, even if the thickness of the superior and lateral rectus muscles decreased after the treatment. Additionally, it appeared that the UR of EOMs provided independent and incremental information for the prediction of response following PGT. These findings suggested that GO was likely to improve significantly with PGT in patients with high inflammatory burden at baseline.

What is also interesting is that this study suggests that initial CAS may not predict improvement following PGT. This can be explained by the fact that only patients with mild GO and elevated DTPA uptake, in spite of having low CAS (2–3 points), were included for analysis. This was because based on our previous study (10), patients with GO and CAS below 3 points might also benefit from PGT as long as the SPECT/CT showed DTPA activity in the eyes. Moreover, another reason is that CAS is judged on the basis of eye signs and symptoms in anterior segment, while SPECT/CT reflects activity in the posterior orbital segment, the major site of inflammation deposit. Thus, we speculated that patients with high uptake ratio of EOMs would, thus, be recommended to receive PGT, which would be superior to the conventional CAS score methods.

This study has several limitations. First, no uniform consensus regarding the definition of treatment response exists, and various factors (such as the CAS) complicate the objective evaluation of inflammatory activity. Second, partial volume effect remains one of the major degrading factors that hamper quantitative accuracy in SPECT imaging, particularly for small structures. Further studies using PET/CT will be needed to validate this finding, as PET/CT has a higher spatial resolution than SPECT/CT. Third, our study concerned only the predictability of DTPA SPECT/CT for the efficacy of periocular steroid treatment in patients with GO, and evaluation of the efficacy of systemic steroid treatment in patients with GO, thus, needs to be further investigated.

CONCLUSION

Orbital ^{99m}Tc-DTPA SPECT/CT provided a reliable and feasible technique for assessing the inflammatory activity of EOMs in patients with GO. The UR of EOMs could be used as an objective index for evaluating the therapeutic efficacy in patients with GO.

DATA AVAILABILITY STATEMENT

The original contributions presented in the study are included in the article/supplementary material, further inquiries can be directed to the corresponding authors.

ETHICS STATEMENT

The studies involving human participants were reviewed and approved by Xiangya Hospital (No. 202101021). The patients/participants provided their written informed consent to participate in this study.

AUTHOR CONTRIBUTIONS

CZJ participated in study design and data analysis and interpretation, performed the statistical analysis, and drafted the manuscript. ZLD and JH collected the imaging data. HYD and JT contributed to editing and review of the manuscript. MZ and XHL contributed to study design and editing and review of the manuscript. All the authors read and approved the submitted version.

FUNDING

This study was supported by the National Natural Science Foundation of China (No. 81901784 to MZ) and Hunan Provincial Clinical Technology Innovation Project (No. 2020SK53705 to MZ).

REFERENCES

1. Bartalena L, Baldeschi L, Boboridis K, Eckstein A, Kahaly GJ, Marcocci C, et al. The 2016 European thyroid association/European group on grave's orbitopathy guidelines for the management of grave's orbitopathy. *Eur Thyroid J.* (2016) 5:9–26. doi: 10.1159/000443828
2. Bartalena L, Baldeschi L, Dickinson A, Eckstein A, Kendall-Taylor P, Marcocci C, et al. Consensus statement of the European Group on grave's orbitopathy (EUGOGO) on management of GO. *Eur J Endocrinol.* (2008) 158:273–85. doi: 10.1530/EJE-07-0666
3. Bartalena L, Pinchera A, Marcocci C. Management of grave's ophthalmopathy: reality and perspectives. *Endocr Rev.* (2000) 21:168–99. doi: 10.1210/edrv.21.2.0393
4. Mourits MP, Koornneef L, Wiersinga WM, Prummel MF, Berghout A, van der Gaag R. Clinical criteria for the assessment of disease activity in Grave's ophthalmopathy: a novel approach. *Br J Ophthalmol.* (1989) 73:639–44. doi: 10.1136/bjo.73.8.639
5. Ujhelyi B, Erdei A, Galuska L, Varga J, Szabados L, Balazs E, et al. Retrobulbar 99mTc-diethylenetriamine-pentaacetic-acid uptake may predict the effectiveness of immunosuppressive therapy in Grave's ophthalmopathy. *Thyroid.* (2009) 19:375–80. doi: 10.1089/thy.2008.0298
6. Souza AD, Ruiz EE, Cruz AA. Extraocular muscle quantification using mathematical morphology: a semi-automatic method for analyzing muscle enlargement in orbital diseases. *Comput Med Imaging Graph.* (2007) 31:39–45. doi: 10.1016/j.compmedimag.2006.09.010
7. Barras CD, Tress BM, Christensen S, Collins M, Desmond PM, Skolnick BE, et al. Quantitative CT densitometry for predicting intracerebral hemorrhage growth. *AJNR Am J Neuroradiol.* (2013) 34:1139–44. doi: 10.3174/ajnr.A3375
8. Mombaerts I, Rose GE, Verity DH. Diagnosis of enlarged extraocular muscles: when and how to biopsy. *Curr Opin Ophthalmol.* (2017) 28:514–21. doi: 10.1097/ICU.0000000000000395
9. Ma Z, Ozaki H, Ishikawa Y, Jingu K. Improvement of the MRI and clinical features of Asian Grave's ophthalmopathy by radiation therapy with steroids. *Jpn J Radiol.* (2019) 37:612–8. doi: 10.1007/s11604-019-00846-y
10. Liu D, Xu X, Wang S, Jiang C, Li X, Tan J, et al. 99mTc-DTPA SPECT/CT provided guide on triamcinolone therapy in Grave's ophthalmopathy patients. *Int Ophthalmol.* (2020) 40:553–61. doi: 10.1007/s10792-019-01213-6
11. Galuska L, Leovey A, Szucs-Farkas Z, Garai I, Szabo J, Varga J, et al. SPECT using 99mTc-DTPA for the assessment of disease activity in Grave's ophthalmopathy: a comparison with the results from MRI. *Nucl Med Commun.* (2002) 23:1211–6. doi: 10.1097/00006231-200212000-00010
12. Jiang C, Li X, Deng H, Liu J, Huang J, Liu D, et al. Nontarget areaand threshold selection in 99m Tc-DTPA orbital SPECT/CT imagingin thyroid associated ophthalmopathy. *J Cent South Univ Med Sci.* (2018) 43:869–74. doi: 10.11817/j.issn.1672-7347.2018.08.008
13. Szumowski P, Abdelrazek S, Zukowski Ł, Mojsak M, Sykała M, Siewko K, et al. Efficacy of (99m)Tc-DTPA SPECT/CT in diagnosing Orbitopathy in grave's disease. *BMC Endocr Disord.* (2019) 19:10. doi: 10.1186/s12902-019-0340-0
14. Szabados L, Nagy EV, Ujhelyi B, Urbancsek H, Varga J, Nagy E, et al. The impact of 99mTc-DTPA orbital SPECT in patient selection for external radiation therapy in grave's ophthalmopathy. *Nucl Med Commun.* (2013) 34:108–12. doi: 10.1097/MNM.0b013e32835c19f0
15. Sahli E, Gündüz K. Thyroid-associated ophthalmopathy. *Turk J Ophthalmol.* (2017) 47:94–105. doi: 10.4274/tjo.80688
16. Wang Y, Zhang S, Zhang Y, Liu X, Gu H, Zhong S, et al. A single-center retrospective study of factors related to the effects of intravenous glucocorticoid therapy in moderate-to-severe and active thyroid-associated ophthalmopathy. *BMC Endocr Disord.* (2018) 18:13. doi: 10.1186/s12902-018-0240-8
17. Zhu W, Ye L, Shen L, Jiao Q, Huang F, Han R, et al. A prospective, randomized trial of intravenous glucocorticoids therapy with different protocols for patients with grave's ophthalmopathy. *J Clin Endocrinol Metab.* (2014) 99:1999–2007. doi: 10.1210/jc.2013-3919
18. Wiersinga WM. Advances in treatment of active, moderate-to-severe Grave's ophthalmopathy. *Lancet Diabetes Endocrinol.* (2017) 5:134–42. doi: 10.1016/S2213-8587(16)30046-8
19. Choi JH, Lee JK. Efficacy of orbital radiotherapy in moderate-to-severe active grave's orbitopathy including long-lasting disease: a retrospective analysis. *Radiat Oncol.* (2020) 15:220. doi: 10.1186/s13014-020-01663-8

Conflict of Interest: The authors declare that the research was conducted in the absence of any commercial or financial relationships that could be construed as a potential conflict of interest.

frontiers in Medicine

PERSPECTIVE
published: 12 January 2022
doi: 10.3389/fmed.2021.793975

Molecular Imaging of Lower Extremity Peripheral Arterial Disease: An Emerging Field in Nuclear Medicine

Mitchel R. Stacy [1,2]*

[1] Center for Regenerative Medicine, The Research Institute at Nationwide Children's Hospital, Columbus, OH, United States, [2] Division of Vascular Diseases and Surgery, Department of Surgery, The Ohio State University College of Medicine, Columbus, OH, United States

Peripheral arterial disease (PAD) is an atherosclerotic disorder of non-coronary arteries that is associated with vascular stenosis and/or occlusion. PAD affecting the lower extremities is characterized by a variety of health-related consequences, including lifestyle-limiting intermittent claudication, ulceration of the limbs and/or feet, increased risk for lower extremity amputation, and increased mortality. The diagnosis of lower extremity PAD is typically established by using non-invasive tests such as the ankle-brachial index, toe-brachial index, duplex ultrasound, and/or angiography imaging studies. While these common diagnostic tools provide hemodynamic and anatomical vascular assessments, the potential for non-invasive physiological assessment of the lower extremities has more recently emerged through the use of magnetic resonance- and nuclear medicine-based approaches, which can provide insight into the functional consequences of PAD-related limb ischemia. This perspectives article specifically highlights and discusses the emerging applications of clinical nuclear medicine techniques for molecular imaging investigations in the setting of lower extremity PAD.

Keywords: peripheral arterial disease (PAD), positron emission tomography (PET), single photon emission computed tomography (SPECT), computed tomography, molecular imaging

OPEN ACCESS

Edited by:
Désirée Deandreis, University of Turin, Italy

Reviewed by:
Luca Camoni, University of Brescia, Italy
Ivan Martinez Duncker, Universidad Autónoma del Estado de Morelos, Mexico

***Correspondence:**
Mitchel R. Stacy
mitchel.stacy@nationwidechildrens.org

Specialty section:
This article was submitted to Nuclear Medicine, a section of the journal Frontiers in Medicine

Received: *12 October 2021*
Accepted: *14 December 2021*
Published: *12 January 2022*

Citation:
Stacy MR (2022) Molecular Imaging of Lower Extremity Peripheral Arterial Disease: An Emerging Field in Nuclear Medicine. Front. Med. 8:793975. doi: 10.3389/fmed.2021.793975

INTRODUCTION

Peripheral arterial disease (PAD) is an atherosclerotic disease affecting non-coronary arteries that is associated with vascular stenosis and/or occlusion. Lower extremity PAD is defined as an atherosclerotic obstruction affecting arterial inflow at any vascular site from the aortoiliac segments to the pedal arteries. This atherosclerotic condition negatively impacts lower extremity functional capacity and quality of life by reducing blood flow, perfusion, and oxygen delivery to skeletal muscle of the calves and feet, as well as through resulting in reductions in calf muscle area and increases in fatty infiltration of muscle and muscle fibrosis (1). Furthermore, PAD of the lower extremities is associated with increased morbidity and mortality, with PAD now representing the third leading cause of atherosclerotic morbidity, ranking only behind coronary artery disease and stroke (2). More than 12 million Americans (3) and >230 million people worldwide (2) are estimated to have PAD; however, PAD continues to be largely underdiagnosed and undertreated (4) due to a lack of screening in the general population (5). Therefore, accurate, non-invasive tools are critical

for screening, diagnosing, and monitoring PAD patients to improve risk stratification, facilitate treatment options, and better quantify responses to treatment.

Standard non-invasive clinical tools such as the ankle-brachial index (ABI), toe-brachial index (TBI) are common for screening patients with suspected PAD and for evaluating patients during clinic visits; however, ABI and TBI are arterial hemodynamic measures that can be misleading in the setting of medial calcification and incompressible vessels, which often occurs in the setting of diabetes mellitus (DM). Duplex ultrasound can also be utilized to detect the presence of arterial obstruction, but it also is limited in its application by only offering assessment of arterial patency and flow. Computed tomography (CT) and magnetic resonance (MR) angiographic approaches exist for assessing patients with PAD, however, these methods also only evaluate arterial patency. Catheter-based angiography continues to be the gold standard for diagnosing PAD, but requires arterial catheterization, only evaluates arterial patency, and is only recommended for patients who are undergoing endovascular revascularization procedures (6).

Compared with other more established clinical PAD imaging tools that primarily measure vascular anatomy and hemodynamics, the nuclear imaging modalities of single photon emission computed tomography (SPECT) and positron emission tomography (PET) may offer unique insight into PAD pathophysiology and play an important role in the non-invasive evaluation of both lower extremity arteries and skeletal muscle in the setting of PAD. Historically, nuclear imaging of lower extremity skeletal muscle perfusion first emerged in the 1940s (7, 8), with very little incremental change or application of nuclear imaging in the setting of PAD until several decades later following the clinical integration of scintigraphy imaging (9, 10). However, the last decade has seen an emergence of new applications and methods for using nuclear imaging modalities to quantify lower extremity pathophysiology in PAD. While novel MR- (11–15) and ultrasound-based (16, 17) imaging approaches have also emerged in recent years that offer physiological evaluation of lower extremity skeletal muscle, these techniques are beyond the scope of this article. This perspectives article will discuss current advances and emerging applications of clinical nuclear imaging modalities in recent years in the setting of lower extremity PAD, with particular focus on perfusion imaging and molecular imaging of atherosclerosis and vascular inflammation.

IMAGING OF LOWER EXTREMITY SKELETAL MUSCLE PERFUSION

Impairment of lower extremity skeletal muscle perfusion is a hallmark of PAD and a primary contributor to functional decrements that are common for many patients with PAD. Severe perfusion abnormalities can lead to the onset of critical limb ischemia (CLI), the severe manifestation of PAD, which is characterized by a high risk for non-healing wounds, lower extremity amputation, and death (3). While perfusion deficits are a known contributor to symptom severity and morbidity and mortality in PAD, an ongoing clinical challenge is the lack of a validated vascular test for detecting and monitoring these common perfusion abnormalities. Indeed, this challenge was recently highlighted in a scientific statement by the American Heart Association (3). The establishment of an accurate non-invasive approach for quantifying regional lower extremity muscle perfusion in both the calves and the feet could greatly facilitate diagnosis of PAD and CLI, clinical decision making, and monitoring of responses to treatments directed at wound healing and limb salvage.

Recently published nuclear imaging studies in the last 3 years focused on evaluating lower extremity perfusion in PAD patients have demonstrated the utility of hybrid SPECT/CT imaging for non-invasively detecting abnormalities in microvascular perfusion within the feet of diabetic patients with CLI. Specifically, SPECT/CT imaging with technetium-99m (^{99m}Tc)-tetrofosmin, a standard myocardial perfusion radionuclide that is retained based on mitochondrial membrane potential and tissue viability (18), has been shown to allow for evaluation of relative perfusion defects within specific vascular territories, or angiosomes, of the feet (19). Additionally, this approach has revealed utility for detecting resting differences in regional foot perfusion between CLI patients and healthy control subjects (19), assessing tissue viability that corresponds with the subsequent level of amputation (20), and quantifying regional improvements in relative perfusion within the foot that occurs in response to endovascular revascularization (21, 22). Most recently and importantly, perfusion imaging of the feet using SPECT/CT imaging has also demonstrated prognostic value for predicting risk for lower extremity amputation in patients with CLI who underwent endovascular revascularization for limb salvage, where patients who were high perfusion responders to revascularization experienced greater limb salvage success compared to those who were categorized as low perfusion responders (**Figure 1**) (22). Along with three-dimensional SPECT perfusion imaging showing promising results for evaluating resting perfusion and the response to revascularization in patients with CLI, two-dimensional scintigraphy imaging studies have also been used in recent years to evaluate the response to angiogenesis-promoting cell therapies in the setting of CLI, where resting uptake of ^{99m}Tc-tetrofosmin significantly increased 4 weeks after transplantation of bone marrow mononuclear cells in the calves and feet (23).

Beyond the application of nuclear imaging of perfusion in the setting of CLI, other research teams have also demonstrated that SPECT-derived measures of resting calf muscle perfusion may possess prognostic value for predicting risk for major cardiovascular adverse events in the PAD patient population (24). Additionally, ^{99m}Tc-tetrofosmin SPECT/CT perfusion imaging of the calves has recently been shown to significantly correlate with both exercise capacity and cardiovascular fitness in non-PAD clinical populations, thus suggesting that nuclear imaging of calf muscle perfusion could serve as a non-invasive correlate for investigating lower extremity physiological adaptations to exercise training programs in the setting of PAD (25). The latter study may be of particular relevance for the PAD community considering the 2017 approval for national coverage

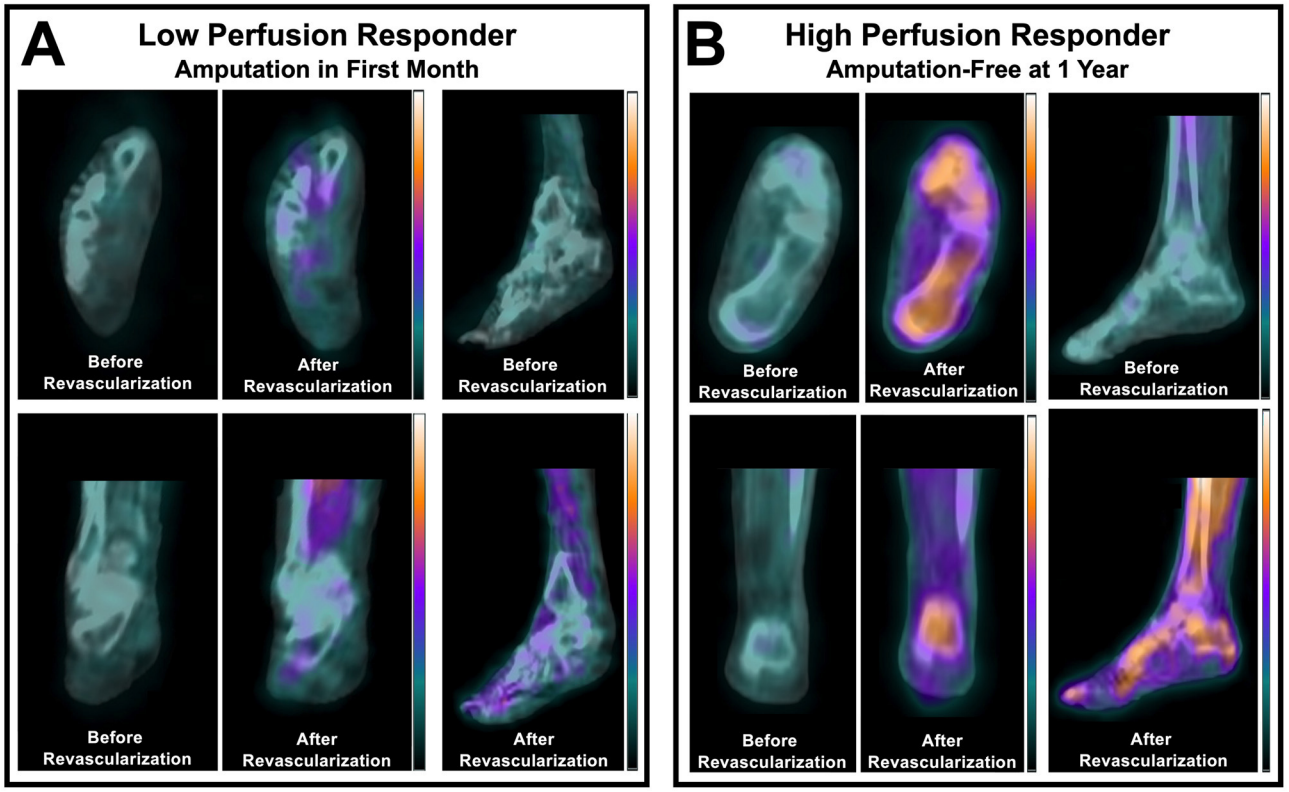

FIGURE 1 | SPECT/CT imaging of the perfusion response to lower extremity revascularization in patients with CLTI. Non-invasive imaging identified differential perfusion responses to peripheral balloon angioplasty in **(A)** a patient with a low perfusion response who underwent amputation within one month, and **(B)** a patient who had a high relative perfusion response and remained amputation-free for one year after intervention. Adapted from Chou et al. (22). For a complete description of perfusion imaging methodology, please refer to Chou et al. (22).

of supervised exercise therapy for symptomatic PAD by the Centers for Medicare and Medicaid Services (26). Furthermore, this study highlighted the feasibility and practicality of additional perfusion imaging of the lower extremities in patients already undergoing clinically-indicated myocardial perfusion imaging, where quantitative assessment of calf muscle perfusion reserve was achieved without the need for additional radionuclide injections, additional stress testing, or additional time in clinic (25). Thus, patients could undergo simultaneous screening of lower extremity perfusion at the time of cardiac imaging, which could potentially allow for early identification of perfusion abnormalities in asymptomatic/undiagnosed PAD patients.

While several noteworthy developments have been made in the past decade using SPECT- and scintigraphy-based perfusion imaging methods for the PAD patient population, interestingly, similar advancements have not been made with regard to PET perfusion imaging of lower extremity muscle perfusion in PAD aside from a small number of studies published in past decades that used oxygen-15 (^{15}O)-water to assess calf muscle perfusion (27–29). ^{15}O-water, which is a freely diffusible and metabolically inert radionuclide that represents the gold standard for quantitative perfusion (30), has specifically demonstrated its potential for providing absolute measures of lower extremity muscle perfusion (i.e., ml/min/g) (27), which has not been previously shown using other PET radioisotopes or SPECT imaging techniques. Thus, the opportunities for growth and application of PET-based perfusion methodologies is apparent and could ultimately enable enhanced quantitative evaluation of skeletal muscle perfusion in the setting of PAD.

MOLECULAR IMAGING OF PERIPHERAL ARTERY INFLAMMATION AND ATHEROSCLEROSIS

PET imaging of arterial inflammation and atherosclerosis has also garnered attention in the cardiology community in the past decade, with a large majority of published studies focusing on the application of fluorine-18 (^{18}F)-fluorodeoxyglucose (FDG) and ^{18}F-sodium fluoride (NaF) for molecular imaging of inflammation and atherosclerotic disease progression in the carotid arteries, coronary arteries, and aorta (31). ^{18}F-FDG in particular continues to be one of the most widely used PET-based approaches for assessing arterial inflammation due to it being a glucose analog that possesses an affinity for metabolically active macrophages that are present in inflamed atherosclerotic plaques (32–34). Despite the overwhelming existing body of literature focused on PET imaging of various arterial networks, to

date, PET imaging of inflammation and atherosclerosis remains relatively understudied in the setting of lower extremity PAD. In non-PAD patient populations, ^{18}F-FDG PET/CT imaging has been found to be useful for evaluating vascular inflammation in the lower extremities, and these PET-derived measures significantly correlate with measures of peripheral vascular stiffness (35). Additionally, serial ^{18}F-FDG PET/CT has shown utility for non-invasively detecting statin-induced reductions in inflammation within the femoral arteries of patients with dyslipidemia (36). However, only a limited number of recent studies have specifically evaluated the utility of ^{18}F-FDG PET as a tool for quantifying arterial inflammation in patients with PAD. One recent study by Jiang et al. (37) applied serial ^{18}F-FDG PET/CT imaging in PAD patients before and after sonodynamic therapy to the femoropopliteal artery, which demonstrated that PET/CT imaging could detect and quantify therapeutic reductions in arterial inflammation in the setting of PAD. Another recent study focused on evaluating the utility of a combined ^{18}F-FDG PET and MR imaging approach for simultaneous assessment of both plaque morphology and arterial inflammation in a small sample size of PAD patients, but did not find any significant correlations between ^{18}F-FDG arterial uptake and histological measures of arterial inflammation (38). Thus, ongoing work focused on targeted imaging of arterial inflammation in the setting of PAD is warranted to fully elucidate the potential role of PET imaging as a non-invasive biomarker of PAD-induced inflammation.

In addition to ^{18}F-FDG, ^{18}F-NaF has more recently emerged as a radionuclide of interest for studying the active process of atherosclerosis. Historically, ^{18}F-NaF was originally approved in the 1960s and used for targeted imaging of bone remodeling due to its high affinity for hydroxyapatite, the mineral form of calcium apatite (39). However, in the last 10–15 years, a large body of cardiovascular literature has emerged that has explored the utility of ^{18}F-NaF as a tool for quantifying the active process of vascular microcalcification (31). As with ^{18}F-FDG, ^{18}F-NaF has only recently been applied and investigated in the setting of lower extremity PAD. Initial studies using ^{18}F-NaF in PAD patients approximately 10 years ago demonstrated the feasibility of using this radionuclide for PET imaging of the lower extremities (40) and revealed that femoral artery uptake of ^{18}F-NaF was strongly associated with cardiovascular risk factors and high-risk profiles for cardiovascular events (41). Following an ∼7 year period of time passing without a single study published in this field, an increasing number of studies have emerged in the last 2 years using ^{18}F-NaF to evaluate peripheral atherosclerosis in patients with PAD. These studies have demonstrated that arterial uptake of ^{18}F-NaF is significantly higher in non-lower extremity arteries of PAD patients compared to non-PAD patients (42) and that femoral artery ^{18}F-NaF uptake is significantly associated with various modifiable cardiovascular risk factors (i.e., cholesterol, triglycerides, HbA1c) (43), thus suggesting that ^{18}F-NaF PET/CT imaging could be used in the future for non-invasively monitoring the response to treatments focused on cholesterol reduction and/or glucose management. Pictured in **Figure 2** is a representative example of ^{18}F-NaF PET/CT imaging in a patient with DM and CLI, which demonstrates the ability of ^{18}F-NaF to detect active disease progression in the lower extremities.

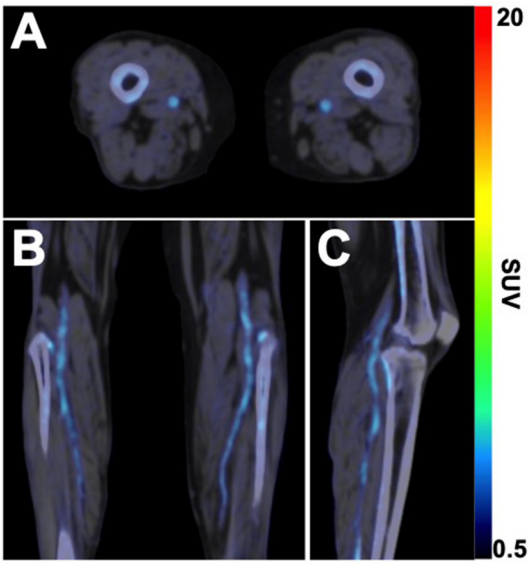

FIGURE 2 | ^{18}F-NaF PET/CT imaging of active microcalcification in PAD. **(A)** Axial, **(B)** coronal, and **(C)** sagittal fused ^{18}F-NaF PET/CT images acquired in a 63-year old female patient with CLTI and type 2 diabetes mellitus demonstrates the active process of microcalcification in above- and below-the-knee arteries. Non-contrast CT images were acquired for attenuation correction of PET data, followed by static PET imaging of the lower extremities 75 min after intravenous administration of ^{18}F-NaF (296 MBq). SUV, standardized uptake value.

Other additional applications of ^{18}F-NaF in the setting of PAD over the past 2 years have demonstrated the feasibility of using ^{18}F-NaF PET/CT imaging to evaluate active microcalcification of occlusive lower extremity aneurysms (44), quantify the inflammatory response to lower extremity balloon angioplasty and predict risk for vascular restenosis after peripheral interventions (45), and evaluate the role of arterial inflammation in promoting systemic vascular calcification (46). Thus, the applications for ^{18}F-NaF PET/CT are rapidly evolving, with numerous future research directions on the horizon for molecular imaging of atherosclerosis in patients with PAD.

DISCUSSION

Nuclear and molecular imaging of PAD is an emerging field that provides numerous opportunities for physiological investigation into this traditionally underdiagnosed and undertreated disease. Recent studies have demonstrated that SPECT/CT perfusion imaging may enable the screening, diagnosis, and monitoring of responses to treatment (21, 22, 25), while PET/CT imaging may provide novel opportunities for molecular imaging of atherosclerosis and vascular inflammation (47), which to date, have remained relatively understudied in the setting of lower extremity PAD. Additionally, these hybrid nuclear imaging approaches that utilize CT can offer simultaneous

evaluation of calcium burden in the lower extremities that is not possible with conventional vascular imaging techniques (20). While nuclear imaging approaches in the setting of PAD remain exploratory in nature, these imaging techniques could potentially assist with screening for and diagnosis of regional perfusion abnormalities related to PAD and severity of PAD, which could subsequently assist clinicians by guiding targeted revascularization procedures or evaluating the response to revascularization. Additionally, PET/CT imaging of arterial inflammation and active atherosclerosis may assist clinicians by detecting regions of active disease, thereby guiding endovascular therapy or monitoring of problematic lesions. Currently, hemodynamic tools such as ABI, TBI, and Doppler ultrasound are a mainstay of screening for PAD due to their relative efficiency and cost-effectiveness; however, perfusion imaging with nuclear techniques has proven to provide further physiological information beyond traditional hemodynamic assessment by detecting the specific anatomical region of underlying tissue ischemia, thus potentially setting the stage for their use during PAD diagnosis and treatment planning. Collectively, nuclear imaging techniques advance the non-invasive evaluation of PAD beyond traditional means by offering quantitative regional analysis of vascular and muscle physiology, whereas traditional non-invasive vascular diagnostic tools have primarily focused on hemodynamic (e.g., ABI, TBI, ultrasound) or structural (e.g., angiography) assessments of the lower extremities. It's important to note that while SPECT/CT and PET/CT imaging have demonstrated potential in PAD, the recent emergence of PET/MR imaging may also provide additional opportunities for partnering high-sensitivity molecular (PET) and high-resolution structural (MR) imaging in the setting of lower extremity PAD (38, 48).

Given the multifactorial nature of PAD-related complications, ongoing advancements in nuclear medicine and molecular imaging should facilitate development of novel imaging strategies that are capable of targeting the underlying pathophysiology associated with lower extremity PAD and enable serial monitoring of physiological responses to medical treatment. Specifically, advancements with cadmium zinc telluride (CZT) SPECT systems and whole-body PET cameras may offer new approaches for quantifying absolute perfusion of lower extremity skeletal muscle beyond what has been previously accomplished with conventional ^{15}O-water PET imaging. Expanded application of ^{18}F-FDG and ^{18}F-NaF to the lower extremities, along with other developing radionuclides meant for atherosclerosis and thrombosis targeted imaging, could also allow for novel opportunities to investigate mechanisms associated with PAD disease progression and non-invasively detect occlusive peripheral thrombi (49–53). Additionally, the use of multi-tracer imaging of different physiological processes in the lower extremities could theoretically be achieved with SPECT imaging of radionuclides that possess distinctly different gamma ray energy photopeaks, or with PET imaging by staggering injection times of short half-life radionuclides; however, the advantages and disadvantages associated with increased radiation exposure for patients receiving multiple radionuclide injections in a single imaging session would need to be carefully considered. Beyond the various clinical investigations focused on nuclear imaging of PAD, a large number of pre-clinical studies have been published in recent years that also highlight ongoing developments in the field of molecular imaging that could possess translational potential for PAD patients. These studies have utilized large and small animal models of atherosclerosis and hindlimb ischemia to validate novel SPECT- and PET-based approaches directed at perfusion (54) and angiogenesis targeted imaging (55–57), which continue to be the primary areas of pre-clinical PAD research. Overall, molecular imaging of lower extremity PAD remains a developing and exciting field of research that should provide novel insight into PAD pathophysiology and eventually expand the repertoire of non-invasive tests available to vascular medicine specialists.

DATA AVAILABILITY STATEMENT

The original contributions presented in the study are included in the article/supplementary material, further inquiries can be directed to the corresponding author/s.

ETHICS STATEMENT

The studies involving human participants were reviewed and approved by Nationwide Children's Hospital Institutional Review Board. The patients/participants provided their written informed consent to participate in this study.

AUTHOR CONTRIBUTIONS

The author confirms being the sole contributor of this work and has approved it for publication.

FUNDING

This work was supported by National Institutes of Health award R01 HL135103.

REFERENCES

1. McDermott MM, Ferrucci L, Gonzalez-Freire M, Kosmac K, Leeuwenburgh C, Peterson CA, et al. Skeletal muscle pathology in peripheral artery disease: a brief report. *Arter Thromb Vasc Biol.* (2020) 40:2577–85. doi: 10.1161/ATVBAHA.120.313831
2. Criqui MH, Matsushita K, Aboyans V, Hess CN, Hicks CW, Kwan TW, et al. Lower extremity peripheral artery disease: contemporary epidemiology, management gaps, and future directions: a scientific statement from the American Heart Association. *Circulation.* (2021) 144:e171–91. doi: 10.1161/CIR.0000000000001005
3. Misra S, Shishehbor MH, Takahashi EA, Aronow HD, Brewster LP, Bunte MC, et al. Perfusion assessment in critical limb ischemia: principles for understanding and the development of evidence and evaluation of devices: a scientific statement from the American Heart Association. *Circulation.* (2019) 140:e657–72. doi: 10.1161/CIR.0000000000000708

4. Shu J, Santulli G. Update on peripheral artery disease: Epidemiology and evidence-based facts. *Atherosclerosis.* (2018) 275:379–81. doi: 10.1016/j.atherosclerosis.2018.05.033
5. Andras A, Ferket B. Screening for peripheral arterial disease. *Cochrane Database Syst Rev.* (2014) 7:CD010835. doi: 10.1002/14651858.CD010835.pub2
6. Gerhard-Herman MD, Gornik HL, Barrett C, Barshes NR, Corriere MA, Drachman DE, et al. 2016 AHA/ACC guideline on the management of patients with lower extremity peripheral artery disease: a report of the American College of Cardiology/American Heart Association task force on clinical practice guidelines. *J Am Coll Cardiol.* (2017) 69:e71–e126. doi: 10.1016/j.jacc.2016.11.007
7. Smith BC, Quimby EH. The use of radioactive sodium as a tracer in the study of peripheral vascular disease. *Radiology.* (1945) 45:335–46. doi: 10.1148/45.4.335
8. Kety S. Measurement of regional circulation by the local clearance of radioactive sodium. *Am Hear J.* (1949) 38:321–8. doi: 10.1016/0002-8703(49)90845-5
9. Seder JS, Botvinick EH, Rahimtoola SH, Goldstone J, Price DC. Detecting and localizing peripheral arterial disease: assessment of 201Tl scintigraphy. *AJR Am J Roentgenol.* (1981) 137:373–80. doi: 10.2214/ajr.137.2.373
10. Hamanaka D, Odori T, Maeda H, Ishii Y, Hayakawa K, Torizuka K, et al. Quantitative assessment of scintigraphy of the legs using 201Tl. *Eur J Nucl Med.* (1984) 9:12–6. doi: 10.1007/BF00254343
11. Galanakis N, Maris TG, Kontopodis N, Ioannou CV, Tsetis K, Karantanas A, et al. The role of dynamic contrast-enhanced MRI in evaluation of percutaneous transluminal angioplasty outcome in patients with critical limb ischemia. *Eur J Radiol.* (2020) 129:109081. doi: 10.1016/j.ejrad.2020.109081
12. Zheng J, Sorensen C, Li R, An H, Hildebolt CF, Zayed MA, et al. Deteriorated regional calf microcirculation measured by contrast-free MRI in patients with diabetes mellitus and relation with physical activity. *Diab Vasc Dis Res.* (2021) 18:1–8. doi: 10.1177/14791641211029002
13. Stacy MR, Qiu M, Papademetris X, Caracciolo CM, Constable RT, Sinusas AJ. Application of BOLD MR imaging for evaluating regional volumetric foot tissue oxygenation: a feasibility study in healthy volunteers. *Eur J Vasc Endovasc Surg.* (2016) 51:743–9. doi: 10.1016/j.ejvs.2016.02.008
14. Stacy MR, Caracciolo CM, Qiu M, Pal P, Varga T, Constable RT, et al. Comparison of regional skeletal muscle tissue oxygenation in college athletes and sedentary control subjects using quantitative BOLD MR imaging. *Physiol Rep.* (2016) 4:e12903. doi: 10.14814/phy2.12903
15. Suo S, Zhang L, Tang H, Ni Q, Li S, Mao H, et al. Evaluation of skeletal muscle microvascular perfusion of lower extremities by cardiovascular magnetic resonance arterial spin labeling, blood oxygenation level-dependent, and intravoxel incoherent motion techniques. *J Cardiovasc Magn Reson.* (2018) 20:18. doi: 10.1186/s12968-018-0441-3
16. Davidson BP, Hodovan J, Mason OR, Moccetti F, Gupta A, Muller M, et al. Limb perfusion during exercise assessed by contrast ultrasound varies according to symptom severity in patients with peripheral artery disease. *J Am Soc Echocardiogr.* (2019) 32:1086–94. doi: 10.1016/j.echo.2019.05.001
17. Mason OR, Davidson BP, Sheeran P, Muller M, Hodovan JM, Sutton J, et al. Augmentation of tissue perfusion in patients with peripheral artery disease using microbubble cavitation. *JACC Cardiovasc Imaging.* (2020) 13:641–51. doi: 10.1016/j.jcmg.2019.06.012
18. Younes A, Songadele JA, Maublant J, Platts E, Pickett R, Veyre A. Mechanism of uptake of technetium-tetrofosmin. II: Uptake into isolated adult rat heart mitochondria. *J Nucl Cardiol.* (1995) 2:327–33. doi: 10.1016/S1071-3581(05)80077-7
19. Alvelo JL, Papademetris X, Mena-Hurtado C, Jeon S, Sumpio BE, Sinusas AJ, et al. Radiotracer imaging allows for noninvasive detection and quantification of abnormalities in angiosome foot perfusion in diabetic patients with critical limb ischemia and nonhealing wounds. *Circ Cardiovasc Imaging.* (2018) 11:e006932. doi: 10.1161/CIRCIMAGING.117.006932
20. Chou TH, Tram NK, Eisert SN, Bobbey AJ, Atway SA, Go MR, et al. Dual assessment of abnormal microvascular foot perfusion and lower extremity calcium burden in a patient with critical limb ischemia using hybrid SPECT/CT imaging. *Vasc Med.* (2021) 26:225–7. doi: 10.1177/1358863X20964563
21. Chou TH, Atway SA, Bobbey AJ, Sarac TP, Go MR, Stacy MR. SPECT/CT imaging: a non-invasive approach for evaluating serial changes in angiosome foot perfusion in critical limb ischemia. *Adv Wound Care.* (2020) 9:103–10. doi: 10.1089/wound.2018.0924
22. Chou TH, Alvelo JL, Janse S, Papademetris X, Sumpio BE, Mena-Hurtado C, et al. Prognostic value of radiotracer-based perfusion imaging in critical limb ischemia patients undergoing lower extremity revascularization. *JACC Cardiovasc Imaging.* (2021) 14:1614–24. doi: 10.1016/j.jcmg.2020.09.033
23. Takagi G, Miyamoto M, Fukushima Y, Yasutake M, Tara S, Takagi I, et al. Imaging angiogenesis using ^{99m}Tc-MAA scintigraphy in patients with peripheral artery disease. *J Nucl Med.* (2016) 57:192–7. doi: 10.2967/jnumed.115.160937
24. Hashimoto H, Fukushima Y, Kumita S-I, Miyamoto M, Takagi G, Yamazaki J, et al. Prognostic value of lower limb perfusion single-photon emission computed tomography-computed tomography in patients with lower limb atherosclerotic peripheral artery disease. *Jpn J Radiol.* (2017) 35:68–77. doi: 10.1007/s11604-016-0602-y
25. Chou TH, Janse S, Sinusas AJ, Stacy MR. SPECT/CT imaging of lower extremity perfusion reserve: a non-invasive correlate to exercise tolerance and cardiovascular fitness in patients undergoing clinically indicated myocardial perfusion imaging. *J Nucl Cardiol.* (2020) 27:1923–33. doi: 10.1007/s12350-019-02019-w
26. Treat-Jacobson D, McDermott MM, Bronas UG, Campia U, Collins TC, Criqui MH, et al. Optimal exercise programs for patients with peripheral artery disease: a scientific statement from the American Heart Association. *Circulation.* (2019) 139:e10–33. doi: 10.1161/CIR.0000000000000623
27. Burchert W, Schellong S, van den Hoff J, Meyer G-J, Alexander K, Hundeshagen H. Oxygen-15-water PET assessment of muscular blood flow in peripheral vascular disease. *J Nucl Med.* (1997) 38:93–8.
28. Schmidt MA, Chakrabarti A, Shamim-Uzzaman Q, Kaciroti N, Koeppe RA, Rajagopalan S. Calf flow reserve with H(2)(15)O PET as a quantifiable index of lower extremity flow. *J Nucl Med.* (2003) 44:915—9.
29. Scremin OU, Figoni SF, Norman K, Scremin AME, Kunkel CF, Opava-Rutter D, et al. Preamputation evaluation of lower-limb skeletal muscle perfusion with (15)O H2O positron emission tomography. *Am J Phys Med Rehabil.* (2010) 89:473–86. doi: 10.1097/PHM.0b013e3181d89b08
30. Iida H, Kanno I, Takahashi A, Miura S, Murakami M, Takahashi K, et al. Measurement of absolute myocardial blood flow with H215O and dynamic positron-emission tomography. Strategy for quantification in relation to the partial-volume effect. *Circulation.* (1988) 78:104–15. doi: 10.1161/01.CIR.78.1.104
31. Stacy MR. Radionuclide imaging of atherothrombotic diseases. *Curr Cardiovasc Imaging Rep.* (2019) 12:17. doi: 10.1007/s12410-019-9491-7
32. Cocker MS, Spence JD, Hammond R, deKemp RA, Lum C, Wells G, et al. [18F]-fluorodeoxyglucose PET/CT imaging as a marker of carotid plaque inflammation: comparison to immunohistology and relationship to acuity of events. *Int J Cardiol.* (2018) 271:378–86. doi: 10.1016/j.ijcard.2018.05.057
33. Tawakol A, Migrino RQ, Bashian GG, Bedri S, Vermylen D, Cury RC, et al. *In vivo* 18F-fluorodeoxyglucose positron emission tomography imaging provides a noninvasive measure of carotid plaque inflammation in patients. *J Am Coll Cardiol.* (2006) 48:1818–24. doi: 10.1016/j.jacc.2006.05.076
34. Zhang Z, Machac J, Helft G, Worthley SG, Tang C, Zaman AG, et al. Non-invasive imaging of atherosclerotic plaque macrophage in a rabbit model with F-18 FDG PET: a histological correlation. *BMC Nucl Med.* (2006) 6:3. doi: 10.1186/1471-2385-6-3
35. De Boer SA, Hovinga-De Boer MC, Heerspink HJL, Lefrandt JD, van Roon AM, Lutgers HL, et al. Arterial stiffness is positively associated with 18F-fluorodeoxyglucose positron emission tomography-assessed subclinical vascular inflammation in people with early type 2 diabetes. *Diabetes Care.* (2016) 39:1440–7. doi: 10.2337/dc16-0327
36. Ishii H, Nishio M, Takahashi H, Aoyama T, Tanaka M, Toriyama T, et al. Comparison of atorvastatin 5 and 20 mg/d for reducing F-18 fluorodeoxyglucose uptake in atherosclerotic plaques on positron emission tomography/computed tomography: a randomized, investigator-blinded, open-label, 6-month study in Japanese adults scheduled. *Clin Ther.* (2010) 32:2337–47. doi: 10.1016/j.clinthera.2010.12.001
37. Jiang Y, Fan J, Li Y, Wu G, Wang Y, Yang J, et al. Rapid reduction in plaque inflammation by sonodynamic therapy in patients with symptomatic

femoropopliteal peripheral artery disease: a randomized controlled trial. *Int J Cardiol.* (2021) 325:132–9. doi: 10.1016/j.ijcard.2020.09.035
38. Dregely I, Koppara T, Nekolla SG, Nahrig J, Kuhs K, Langwieser N, et al. Observations with simultaneous 18F-FDG PET and MR imaging in peripheral artery disease. *JACC Cardiovasc Imaging.* (2017) 10:709–11. doi: 10.1016/j.jcmg.2016.06.005
39. Czernin J, Satyamurthy N, Schiepers C. Molecular mechanisms of bone 18F-NaF deposition. *J Nucl Med.* (2010) 51:1826–9. doi: 10.2967/jnumed.110.077933
40. Derlin T, Richter U, Bannas P, Begemann P, Buchert R, Mester J, et al. Feasibility of (18)F-sodium fluoride PET/CT for imaging of atherosclerosis plaque. *J Nucl Med.* (2010) 51:862–5. doi: 10.2967/jnumed.110.076471
41. Janssen T, Bannas P, Herrmann J, Veldhoen S, Busch JD, Treszl A, et al. Association of linear (18)F-sodium fluoride accumulation in femoral arteries as a measure of diffuse calcification with cardiovascular risk factors: a PET/CT study. *J Nucl Cardiol.* (2013) 20:569–77. doi: 10.1007/s12350-013-9680-8
42. Asadollahi S, Rojulpote C, Bhattaru A, Patil S, Gonuguntla K, Karambelkar P, et al. Comparison of atherosclerotic burden in non-lower extremity arteries in patients with and without peripheral artery disease using 18F-NaF-PET/CT imaging. *Am J Nucl Med Mol Imaging.* (2020) 10:272–8.
43. Takx RAP, van Asperen R, Bartstra JW, Zwakenberg SR, Wolterink JM, Celeng C, et al. Determinants of 18F-NaF uptake in femoral arteries in patients with type 2 diabetes mellitus. *J Nucl Cardiol.* (2020) 28:2700–5. doi: 10.1007/s12350-020-02099-z
44. Eisert SN, Chou TH, Bobbey AJ, Go MR, Stacy MR. Noninvasive detection of active microcalcification in an occlusive peripheral vascular aneurysm using 18F-NaF PET/CT imaging. *Clin Nucl Med.* (2020) 45:1029–31. doi: 10.1097/RLU.0000000000003344
45. Chowdhury MM, Tarkin JM, Albaghdadi MS, Evans NR, Le EPV, Berrett TB, et al. Vascular positron emission tomography and restenosis in symptomatic peripheral arterial disease: a prospective clinical study. *JACC Cardiovasc Imaging.* (2020) 13:1008–17. doi: 10.1016/j.jcmg.2019.03.031
46. Reijrink M, de Boer SA, Te Velde-Keyzer CA, Sluiter JKE, Pol RA, Heerspink HJL, et al. [18F]FDG and [18F]NaF as PET markers of systemic atherosclerosis progression: a longitudinal descriptive imaging study in patients with type 2 diabetes mellitus. *J Nucl Cardiol.* (2021). doi: 10.1007/s12350-021-02781-w. [Epub ahead of print].
47. Chou TH, Stacy MR. Clinical applications for radiotracer imaging of lower extremity peripheral arterial disease and critical limb ischemia. *Mol Imaging Biol.* (2020) 22:245–55. doi: 10.1007/s11307-019-01425-3
48. Fernandez-Friera L, Fuster V, Lopez-Melgar B, Oliva B, Sanchez-Gonzalez J, Macias A, et al. Vascular inflammation in subclinical atherosclerosis detected by hybrid PET/MRI. *J Am Coll Cardiol.* (2019) 73:1371–82. doi: 10.1016/j.jacc.2018.12.075
49. Lohrke J, Siebeneicher H, Berger M, Reinhardt M, Berndt M, Mueller A, et al. 18F-GP1, a novel PET tracer designed for high-sensitivity, low-background detection of thrombi. *J Nucl Med.* (2017) 58:1094–9. doi: 10.2967/jnumed.116.188896
50. Chae SY, Kwon T-W, Jin S, Kwon SU, Sung C, Oh SJ, et al. A phase 1, first-in-human study of 18F-GP1 positron emission tomography for imaging acute arterial thrombosis. *EJNMMI Res.* (2019) 9:3. doi: 10.1186/s13550-018-0471-8
51. Lee N, Oh I, Chae SY, Jin S, Oh SJ, Lee SJ, et al. Radiation dosimetry of [18F]GP1 for imaging activated glycoprotein IIb/IIIa receptors with positron emission tomography in patients with acute thromboembolism. *Nucl Med Biol.* (2019) 72–73:45–48. doi: 10.1016/j.nucmedbio.2019.07.003
52. Andrews JPM, Portal C, Walton T, Macaskill MG, Hadoke PWF, Corral CA, et al. Non-invasive *in vivo* imaging of acute thrombosis: development of a novel factor XIIIa radiotracer. *Eur Hear J Cardiovasc Imaging.* (2020) 21:673–82. doi: 10.1093/ehjci/jez207
53. Hugenberg V, Zerna M, Berndt M, Zabel R, Preuss R, Rolfsmeier D, et al. GMP-compliant radiosynthesis of [18F]GP1, a novel PET tracer for the detection of thrombi. *Pharm.* (2021) 14:739. doi: 10.3390/ph14080739
54. Stacy MR, Yu DY, Maxfield MW, Jaba IM, Jozwik BP, Zhuang ZW, et al. Multimodality imaging approach for serial assessment of regional changes in lower extremity arteriogenesis and tissue perfusion in a porcine model of peripheral arterial disease. *Circ Cardiovasc Imaging.* (2014) 7:92–9. doi: 10.1161/CIRCIMAGING.113.000884
55. Stacy MR, Sinusas AJ. Novel applications of radionuclide imaging in peripheral vascular disease. *Cardiol Clin.* (2016) 34:167–77. doi: 10.1016/j.ccl.2015.06.005
56. Johnson LL, Johnson J, Ali Z, Tekabe Y, Ober R, Geist G, et al. VEFG receptor targeted imaging of angiogenic response to limb ischemia in diabetic vs. non-diabetic Yucatan minipigs. *EJNMMI Res.* (2020) 10:48. doi: 10.1186/s13550-020-00626-0
57. Goggi JL, Haslop A, Boominathan R, Chan K, Soh V, Cheng P, et al. Imaging the proangiogenic effects of cardiovascular drugs in a diabetic model of limb ischemia. *Contrast Media Mol Imaging.* (2019) 2019:2538909. doi: 10.1155/2019/2538909

Conflict of Interest: The author declares that the research was conducted in the absence of any commercial or financial relationships that could be construed as a potential conflict of interest.

Publisher's Note: All claims expressed in this article are solely those of the authors and do not necessarily represent those of their affiliated organizations, or those of the publisher, the editors and the reviewers. Any product that may be evaluated in this article, or claim that may be made by its manufacturer, is not guaranteed or endorsed by the publisher.

frontiers in Medicine

BRIEF RESEARCH REPORT
published: 18 February 2022
doi: 10.3389/fmed.2022.795925

Novel Application of ^{18}F-NaF PET/CT Imaging for Evaluation of Active Bone Remodeling in Diabetic Patients With Charcot Neuropathy: A Proof-of-Concept Report

Nguyen K. Tram[1†], *Ting-Heng Chou*[1†], *Surina Patel*[1], *Laila N. Ettefagh*[1], *Michael R. Go*[2], *Said A. Atway*[3] *and Mitchel R. Stacy*[1,2*]

[1] Center for Regenerative Medicine, The Research Institute at Nationwide Children's Hospital, Columbus, OH, United States, [2] Division of Vascular Diseases and Surgery, Department of Surgery, The Ohio State University College of Medicine, Columbus, OH, United States, [3] Department of Orthopaedics, The Ohio State University College of Medicine, Columbus, OH, United States

OPEN ACCESS

Edited by:
Martin Huellner,
University Hospital Zürich, Switzerland

Reviewed by:
Debanjali Sinha,
Institute of Neurosciences, Kolkata (I-NK), India
Kun Zheng,
Peking Union Medical College Hospital (CAMS), China

***Correspondence:**
Mitchel R. Stacy
Mitchel.Stacy@NationwideChildrens.org

[†]These authors have contributed equally to this work

Specialty section:
This article was submitted to Nuclear Medicine, a section of the journal Frontiers in Medicine

Received: 15 October 2021
Accepted: 26 January 2022
Published: 18 February 2022

Citation:
Tram NK, Chou T-H, Patel S, Ettefagh LN, Go MR, Atway SA and Stacy MR (2022) Novel Application of ^{18}F-NaF PET/CT Imaging for Evaluation of Active Bone Remodeling in Diabetic Patients With Charcot Neuropathy: A Proof-of-Concept Report. Front. Med. 9:795925. doi: 10.3389/fmed.2022.795925

Charcot neuropathic osteoarthropathy (CN) is a serious and potentially limb-threatening complication for patients with diabetes mellitus and peripheral arterial disease. In recent decades, nuclear medicine-based approaches have been used for non-invasive detection of CN; however, to date, a positron emission tomography (PET) radionuclide specifically focused on targeted imaging of active bone remodeling has not been explored or validated for patients with CN. The radionuclide ^{18}F-sodium fluoride (NaF) has historically been used as a bone imaging probe due to its high sensitivity for targeting hydroxyapatite and bone turnover, but has not been applied in the context of CN. Therefore, the present study focused on novel application of ^{18}F-NaF PET/computed tomography (CT) imaging to three clinical cases of CN to evaluate active bone remodeling at various time courses of CN. PET/CT imaging in all 3 cases demonstrated focal uptake of ^{18}F-NaF in the bones of the feet afflicted with CN, with bone retention of ^{18}F-NaF persisting for up to 5 years following surgical reconstruction of the foot in two cases. On a group level, ^{18}F-NaF bone uptake in the CN foot was significantly higher compared to the healthy, non-CN foot ($p = 0.039$). ^{18}F-NaF PET/CT imaging may provide a non-invasive tool for monitoring active bone remodeling in the setting of CN, thereby offering novel opportunities for tracking disease progression and improving treatment and surgical intervention.

Keywords: sodium fluoride, positron emission tomography, charcot, computed tomography, bone remodeling

INTRODUCTION

Charcot neuropathic osteoarthropathy (CN) is a condition that can impair quality of life and increase risk of limb loss in patients with diabetes mellitus (DM) and peripheral arterial disease (PAD) (1, 2). CN is characterized by local inflammation in the early phase of the condition, followed by degeneration of the bone architecture and ulceration of soft tissues in the foot and ankle in the

later phases (3). If left untreated, CN can result in major disruption of normal skeletal structure that can cause significant loss of function and increased morbidity (4). Current treatment for early phases of CN consists of offloading the affected foot using a total contact cast (5), while common surgical interventions for later stages of CN include exostectomy, application of fixators, and minor or major amputations. The overall rate of amputation in patients with CN and diabetes is 3.3–11 per 1,000 patients, with 70–84% of these patients having a preceding ulceration (6). Patients with CN and diabetes undergoing amputation also have a high mortality rate that is ∼70% in the first 5 years after amputation (7).

Imaging techniques such as radiography and magnetic resonance imaging (MRI) are often used to evaluate CN. However, x-ray imaging possesses low sensitivity and specificity for diagnosing the early stages of CN (8) while MRI can poorly differentiate between CN and osteomyelitis, which often exist concurrently (9). The nuclear imaging-based approaches of scintigraphy and single photon emission computed tomography (SPECT) are commonly used to detect the early stages of inflammation that precede bone morphology changes related to CN and ultimately assist with early diagnosis of CN. One traditional scintigraphy/SPECT radionuclide used for diagnosing CN is technetium-99m (^{99m}Tc)-methylene diphosphonate (MDP), a bone targeted radionuclide which possesses excellent sensitivity for diagnosing CN and can assist with differentiating between osteomyelitis and CN (10). Another scintigraphy- and SPECT-based approach that has been used for imaging of CN includes the use of ^{99m}Tc-MDP bone imaging with indium-111 (^{111}In)-labeled white blood cells (WBC) or ^{99m}Tc-WBC (11–13), which has been shown to be useful for distinguishing between soft tissue vs. bone infection in patients with CN. While these imaging methods have proven useful, the current gold standard for differentiating between foot infection vs. CN remains dual-isotope scintigraphy/SPECT imaging with ^{99m}Tc-sulfur colloid and ^{111}In-WBC, which possesses the best accuracy for detecting CN (14–16).

Along with scintigraphy and SPECT imaging methods, PET imaging with fluorine-18 (^{18}F)-fluorodeoxyglucose (FDG) has emerged in recent years for evaluating the inflammatory origins of CN (17). Multimodality imaging studies have demonstrated superior accuracy of ^{18}F-FDG PET vs. MRI in the diagnosis of CN lesions (17, 18) and higher specificity of PET/CT than MRI for diagnosing osteomyelitis in patients with chronic CN (19). Additionally, ^{18}F-FDG PET/CT imaging has shown potential for monitoring of serial changes in inflammation in patients with CN (20).

While SPECT- and PET-based imaging approaches have shown promise for evaluating CN, a PET imaging method that specifically targets active bone remodeling in the setting of CN has not been investigated, which would offer considerable advantages over current SPECT methods by providing improved image spatial resolution and quantification. ^{18}F-sodium fluoride (NaF) has historically been used since the 1960s as a radionuclide for targeting bone remodeling due to its high affinity for hydroxyapatite, the mineral form of calcium apatite (21). ^{18}F-NaF has also been used for other indications, such as low back pain (22), brown tumors in hyperparathyroidism (23), and bone metastases (24). However, to date, ^{18}F-NaF has not been studied in the context of CN. Additionally, while several imaging approaches have been used to identify early onset CN (stage 0) (25), targeted bone imaging in patients with CN following surgical intervention remains understudied. Therefore, the purpose of this study was to evaluate the utility of ^{18}F-NaF PET/CT imaging as a tool for non-invasively characterizing active bone remodeling in a series of patients with CN who were at various time points following surgical reconstruction of the foot.

METHODS

Three patients with CN, type 2 diabetes mellitus (DM), and peripheral arterial disease (PAD) were prospectively enrolled into an ongoing study evaluating the prognostic value of nuclear imaging techniques in patients with PAD (https://clinicaltrials.gov, NCT03622359) (26). As an additional component of this study, PET/CT imaging was performed 75 min after intravenous injection of ^{18}F-NaF (375.6 ± 10.9 MBq) to evaluate active remodeling of the bones in the feet. All patients underwent PET imaging using a commercially available scanner (Discovery PET/CT 690, GE Healthcare). A low-dose CT scan of the feet was also acquired to guide manual image segmentation of the bones in the feet and ankles, and for PET image attenuation correction. All PET data was converted to standardized uptake values (SUVs) following correction for injected dose, patient body weight, attenuation, and radionuclide decay.

Semiautomated segmentation of the bones of the ankle and foot from CT images for each limb was performed using commercially available image analysis software (PMOD Technologies LLC, Zürich, Switzerland). First, a volume of interest (VOI) was drawn around the foot. Second, within the foot VOI, any tissues with Hounsfield units (HUs) equal to or >100 HU were classified as bone, based on our own experience evaluating common HU values for bones of the feet in our clinical sample. Following segmentation of bones using this approach, the segmentation was further evaluated for accuracy and manually corrected on a slice-by-slice basis, as needed.

For PET image analysis, the average target-to-background ratio (TBR_{avg}) of each foot was calculated using the SUVs acquired for each leg, with the average SUV across all bones of the feet representing the target value while a small (5 mm^3) piece of the cortical bone of the tibia represented the background value. A paired *t*-test was used to compare the TBR between the diseased foot and the healthy foot. A $p < 0.05$ was considered statistically significant. All statistical analysis was performed using Prism v9 for macOS (GraphPad Software, San Diego, CA, USA).

RESULTS

Patient 1 initially presented with a chronic left foot wound deep to the level of bone. MRI was consistent with osteomyelitis of the navicular bone as well as the medial and middle cuneiform bones. The patient also had a history of CN due to type 2

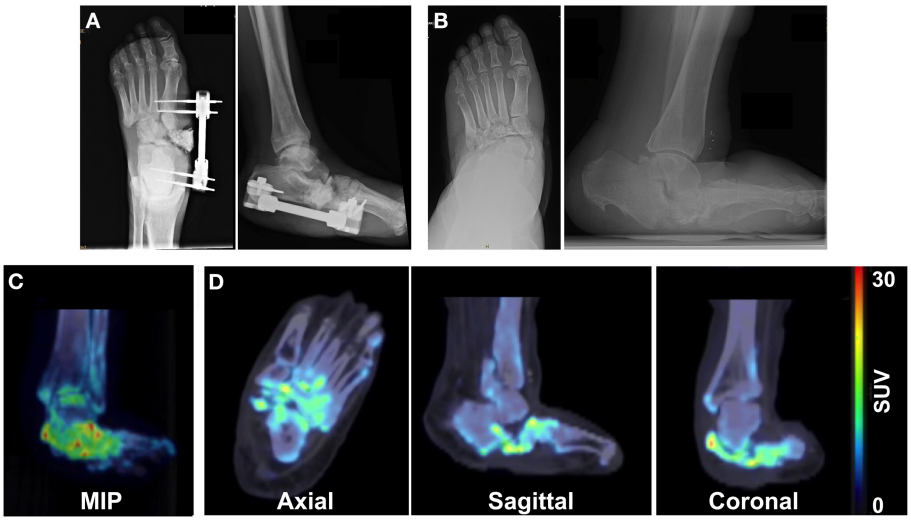

FIGURE 1 | Multimodality imaging evaluation of a 65-year old male patient with a history of Charcot foot, type 2 DM, and PAD. X-rays acquired at **(A)** the time of external fixation and **(B)** 5 years after surgery reveal the architecture of the foot. **(C)** Maximum intensity projection (MIP) images and **(D)** axial, sagittal, and coronal ^{18}F-NaF PET/CT images of the foot 5 years after surgery demonstrate focal increased uptake of ^{18}F-NaF in the bones of the foot, indicating ongoing physiological remodeling of the afflicted foot 5 years after surgical reconstruction.

DM. Conservative treatment options were exhausted, and the patient underwent surgical intervention. External fixation was applied to the medial foot, which consisted of a Biomet Mini-Rail and four half pins across the mid-tarsal joint (**Figure 1A**) that were then removed 2 months later. Five years after surgery, radiography demonstrated stable bone structures (**Figure 1B**). PET/CT images were also acquired 5 years after surgery and revealed focal uptake of ^{18}F-NaF within the bones of the foot with CN, which suggested ongoing bone remodeling 5 years post-surgical reconstruction (**Figures 1C,D**).

Patient 2 originally presented with a Charcot deformity of the right foot with chronic ulceration to the medial aspect of the foot. Following successful wound healing, the patient elected to have surgical intervention to reconstruct the foot and excise the prominent navicular bone (**Figure 2A**). After complete removal of the navicular bone, a medial column BioMet Advanced Locking Plate System plate was fixated across the talo-medial cuneiform joint and across the first tarsometatarsal joints using a total of three non-locking and four locking screws. Five years after surgery, x-rays demonstrated stable bone architecture with partial fusion at the midfoot architecture (**Figure 2B**). However, PET/CT images also acquired 5 years post-surgery revealed increased focal uptake of ^{18}F-NaF in the bones of the right foot, thus indicating an ongoing process of bone remodeling (**Figures 2C,D**).

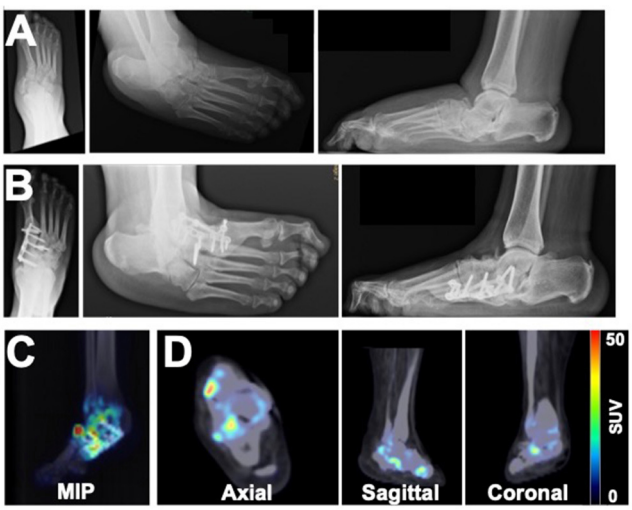

FIGURE 2 | Imaging assessment of a 49-year old female patient with a history of right foot Charcot deformity. X-rays were acquired at **(A)** the time of navicular bone removal and **(B)** 5 years after surgical reconstruction of the foot. **(C)** MIP and **(D)** PET/CT images acquired 5 years after surgery revealed heterogeneous boney uptake of ^{18}F-NaF and suggested potential for ongoing remodeling of the foot.

Patient 3 presented with a chronic wound on the plantar aspect of the right third digit as well as semi-rigid hammertoe contractures of digits 2 and 3 of the right foot, with the third digit ultimately undergoing amputation. The patient also had a history of Charcot joint of the right ankle and had intramedullary fixation applied to stabilize the ankle. X-rays acquired 9 months after surgical fixation showed stable bone structures without progression of the CN deformity (**Figure 3A**). PET/CT imaging at 9 months after surgical intervention revealed increased focal uptake of ^{18}F-NaF at the level of the right ankle (**Figures 3B,C**), suggesting ongoing bone remodeling at the level of prior surgery.

Segmentation of the bones of the ankle and feet was achieved using our semiautomated CT image analysis approach

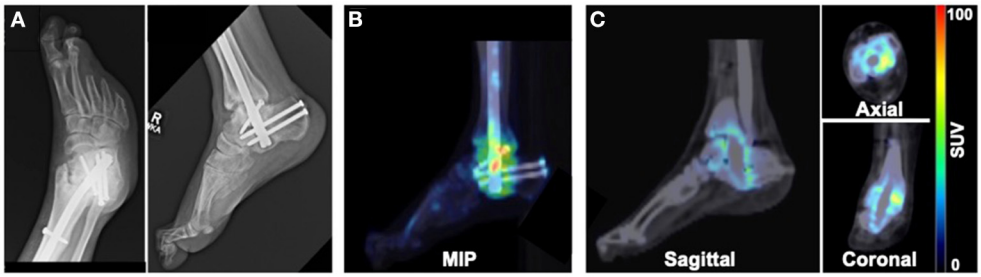

FIGURE 3 | Imaging evaluation of 40-year old male patient with history of Charcot joint of the right ankle. **(A)** X-rays acquired 9 months after surgical reconstruction revealed stable bone architecture. **(B)** MIP and **(C)** PET/CT images acquired 9 months after surgery demonstrated focal uptake of ^{18}F-NaF in the region of the surgically reconstructed ankle impacted by CN, suggesting ongoing remodeling of the bones of the ankle.

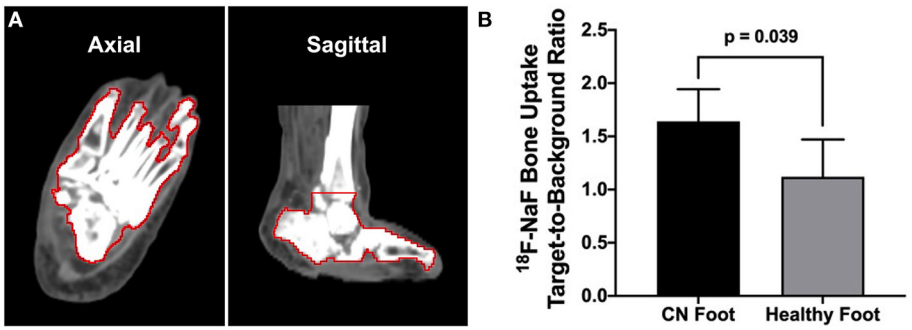

FIGURE 4 | CT image-guided segmentation of the bones of the foot and quantitative ^{18}F-NaF PET/CT image analysis. **(A)** Semiautomated segmentation of the bones of the foot and ankle (bone VOI outlined in red). **(B)** Quantitative analysis of PET/CT imaging demonstrated significantly higher bone uptake of ^{18}F-NaF in the CN foot compared to the healthy non-CN foot. N = three patients. Values represent means ± SD.

(**Figure 4A**). Quantitative PET/CT image analysis demonstrated significantly higher ^{18}F-NaF uptake (i.e., TBR) in the foot afflicted by CN compared to the healthy foot (CN foot: 1.64 ± 0.30 vs. healthy foot: 1.12 ± 0.35; $p = 0.039$) (**Figure 4B**).

DISCUSSION

The series of cases in the present study represent the first clinical application of ^{18}F-NaF PET/CT imaging for assessing active bone remodeling in patients with CN. PET/CT imaging demonstrated increased retention of ^{18}F-NaF in the lower extremity bones impacted by CN as early as 9 months and as late as 5 years following surgical reconstruction of the foot/ankle, thus suggesting that CN is a persistent condition characterized by active bone turnover that may not be fully suppressed for years after surgical intervention. Additionally, these initial cases reveal the potential of ^{18}F-NaF PET/CT imaging for non-invasively detecting the active process of CN. By comparison, standard of care x-rays of the feet/ankles could not identify the continued neuroarthropathic process following surgical reconstruction.

Prior studies using nuclear medicine imaging approaches have primarily focused on assessing the inflammatory origins of CN or differentiating between soft tissue infection vs. osteomyelitis in the feet of patients with CN (25). In recent years, PET/CT imaging with ^{18}F-FDG has emerged as a quantitative imaging approach for non-invasively evaluating the inflammatory origins of CN; however, ^{18}F-FDG does not provide insight into the active process of bone remodeling. While ^{99m}Tc-MDP does provide insight into active remodeling of bone, ^{18}F-NaF has significantly more bone absorption than MDP. Additionally, PET imaging is more quantitative in nature and possesses higher spatial resolution than scintigraphy or SPECT, thereby offering potential advantages over conventional approaches for the evaluation of bone remodeling in patients with CN. Furthermore, due to its well-established use as a bone perfusion imaging radionuclide (21), future studies performing dynamic PET imaging at the time of ^{18}F-NaF administration may provide additional functional assessment of the feet in patients with CN. The present investigation is the first imaging study to evaluate active bone remodeling in patients with CN using a quantitative PET/CT imaging method. This proof-of-concept report reveals that ^{18}F-NaF PET/CT imaging may serve as a non-invasive biomarker for monitoring ongoing bone remodeling for months or years following surgical reconstruction of the foot in patients with CN. Additional work

is needed to understand the potential role of ^{18}F-NaF PET/CT imaging in the diagnosis and treatment planning for patients with CN.

DATA AVAILABILITY STATEMENT

The raw data supporting the conclusions of this article will be made available by the authors, without undue reservation.

ETHICS STATEMENT

The studies involving human participants were reviewed and approved by the Institutional Review Board at Nationwide Children's Hospital. The patients/participants provided their written informed consent to participate in this study.

AUTHOR CONTRIBUTIONS

NT, T-HC, and MS were involved in the conception and design of the study. T-HC collected and organized the data. SP and LE assisted with patient enrollment and chart review. NT analyzed the imaging data and wrote the initial draft of the manuscript. MG, SA, and MS critically reviewed and assisted in the preparation of the manuscript. All authors made critical contributions to the manuscript, approved the final version of the manuscript, and took responsibility for the findings of the study.

FUNDING

This work was supported by National Institutes of Health award R01 HL135103.

REFERENCES

1. Cates NK, Elmarsafi T, Akbari CM, Tefera E, Evans KK, Steinberg JS, et al. Complications of Charcot reconstruction in patients with peripheral arterial disease. *J Foot Ankle Surg.* (2021) 60:941–5. doi: 10.1053/j.jfas.2019.08.039
2. Bandeira MA, Dos Santos ALG, Woo K, Gamba MA, de Gouveia Santos VLC. Incidence and predictive factors for amputations derived from Charcot's neuroarthropathy in persons with diabetes. *Int J Low Extrem Wounds*. (2021). doi: 10.1177/15347346211025893. [Epub ahead of print].
3. Dodd A, Daniels TR. Charcot neuroarthropathy of the foot and ankle. *J Bone Joint Surg Am.* (2018) 100:696–711. doi: 10.2106/JBJS.17.00785
4. Ha J, Hester T, Foley R, Reichert ILH, Vas PRJ, Ahluwalia R, et al. Charcot foot reconstruction outcomes: a systematic review. *J Clin Orthop Trauma.* (2020) 11:357–68. doi: 10.1016/j.jcot.2020.03.025
5. Rosskopf AB, Loupatatzis C, Pfirrmann CWA, Boni T, Berli MC. The Charcot foot: a pictorial review. *Insights Imaging.* (2019) 10:77. doi: 10.1186/s13244-019-0768-9
6. Evans KK, Attinger CE, Al-Attar A, Salgado C, Chu CK, Mardini S, et al. The importance of limb preservation in the diabetic population. *J Diabetes Complications.* (2011) 25:227–31. doi: 10.1016/j.jdiacomp.2011.02.001
7. McCabe CJ, Stevenson RC, Dolan AM. Evaluation of a diabetic foot screening and protection programme. *Diabet Med.* (1998) 15:80–4. doi: 10.1002/(SICI)1096-9136(199801)15:1<80::AID-DIA517>3.0.CO;2-K
8. Ergen FB, Sanverdi SE, Oznur A. Charcot foot in diabetes and an update on imaging. *Diabet Foot Ankle.* (2013) 4:21884. doi: 10.3402/dfa.v4i0.21884
9. Ledermann HP, Morrison WB. Differential diagnosis of pedal osteomyelitis and diabetic neuroarthropathy: MR imaging. *Semin Musculoskelet Radiol.* (2005) 9:272–83. doi: 10.1055/s-2005-921945
10. Peterson N, Widnall J, Evans P, Jackson G, Platt S. Diagnostic imaging of diabetic foot disorders. *Foot Ankle Int.* (2017) 38:86–95. doi: 10.1177/1071100716672660
11. Crerand S, Dolan M, Laing P, Bird M, Smith ML, Klenerman L. Diagnosis of osteomyelitis in neuropathic foot ulcers. *J Bone Joint Surg Br.* (1996) 78:51–5. doi: 10.1302/0301-620X.78B1.0780051
12. Schauwecker DS, Park HM, Burt RW, Mock BH, Wellman HN. Combined bone scintigraphy and indium-111 leukocyte scans in neuropathic foot disease. *J Nucl Med.* (1988) 29:1651–5.
13. Poirier JY, Garin E, Derrien C, Devillers A, Moisan A, Bourguet P, et al. Diagnosis of osteomyelitis in the diabetic foot with a 99mTc-HMPAO leucocyte scintigraphy combined with a 99mTc-MDP bone scintigraphy. *Diabetes Metab.* (2002) 28:485–90.
14. Palestro CJ, Love C, Tronco GG, Tomas MB, Rini JN. Combined labeled leukocyte and technetium 99m sulfur colloid bone marrow imaging for diagnosing musculoskeletal infection. *Radiographics.* (2006) 26:859–U228. doi: 10.1148/rg.263055139
15. Palestro CJ, Mehta HH, Patel M, Freeman SJ, Harrington WN, Tomas MB, et al. Marrow versus infection in the Charcot joint: indium-111 leukocyte and technetium-99m sulfur colloid scintigraphy. *J Nucl Med.* (1998) 39:346–50.
16. Palestro CJ, Roumanas P, Swyer AJ, Kim CK, Goldsmith SJ. Diagnosis of musculoskeletal infection using combined in-111 labeled leukocyte and Tc-99m Sc marrow imaging. *Clin Nucl Med.* (1992) 17:269–73. doi: 10.1097/00003072-199204000-00001
17. Basu S, Chryssikos T, Houseni M, Malay DS, Shah J, Zhuang HM, et al. Potential role of FDG PET in the setting of diabetic neuro-osteoarthropathy: can it differentiate uncomplicated Charcot's neuroarthropathy from osteomyelitis and soft-tissue infection? *Nucl Med Commun.* (2007) 28:465–72. doi: 10.1097/MNM.0b013e328174447f
18. Hopfner S, Krolak C, Kessler S, Tiling R, Brinkbaumer K, Hahn K, et al. Preoperative imaging of Charcot neuroarthropathy in diabetic patients: comparison of ring PET, hybrid PET, and magnetic resonance imaging. *Foot Ankle Int.* (2004) 25:890–5. doi: 10.1177/107110070402501208
19. Rastogi A, Bhattacharya A, Prakash M, Sharma S, Mittal BR, Khandelwal N, et al. Utility of PET/CT with fluorine-18-fluorodeoxyglucose-labeled autologous leukocytes for diagnosing diabetic foot osteomyelitis in patients with Charcot's neuroarthropathy. *Nucl Med Commun.* (2016) 37:1253–9. doi: 10.1097/MNM.0000000000000603
20. Ruotolo V, Di Pietro B, Giurato L, Masala S, Meloni M, Schillaci O, et al. A new natural history of charcot foot clinical evolution and final outcome of stage 0 charcot neuroarthropathy in a tertiary referral diabetic foot clinic. *Clin Nucl Med.* (2013) 38:506–9. doi: 10.1097/RLU.0b013e318292eecb
21. Czernin J, Satyamurthy N, Schiepers C. Molecular mechanisms of bone 18F-NaF deposition. *J Nucl Med.* (2010) 51:1826–9. doi: 10.2967/jnumed.110.077933
22. Mabray MC, Brus-Ramer M, Behr SC, Pampaloni MH, Majumdar S, Dillon WP, et al. (18)F-Sodium fluoride PET-CT hybrid imaging of the lumbar facet joints: tracer uptake and degree of correlation to CT-graded arthropathy. *World J Nucl Med.* (2016) 15:85–90. doi: 10.4103/1450-1147.174698
23. Graf C, Huellner M, Tschopp O, Bode-Lesniewska B, Schmid C. (18)F-NaF-PET/CT in patients with primary hyperparathyroidism and brown tumors. *J Bone Miner Metab.* (2020) 38:299–309. doi: 10.1007/s00774-019-01059-z
24. Araz M, Aras G, Kucuk ON. The role of 18F-NaF PET/CT in metastatic bone disease. *J Bone Oncol.* (2015) 4:92–7. doi: 10.1016/j.jbo.2015.08.002
25. Chou TH, Stacy MR. Clinical applications for radiotracer imaging of lower extremity peripheral arterial disease and critical limb ischemia. *Mol Imaging Biol.* (2020) 22:245–55. doi: 10.1007/s11307-019-01425-3
26. U.S. National Institutes of Health, U.S. National Library of Medicine Website, *ClinicalTrials.gov. Radiotracer-Based Perfusion Imaging of Patients With Peripheral Arterial Disease*. (2021). Available online at: https://clinicaltrials.gov/ct2/show/NCT03622359 (accessed December 22, 2021).

Conflict of Interest: The authors declare that the research was conducted in the absence of any commercial or financial relationships that could be construed as a potential conflict of interest.

Publisher's Note: All claims expressed in this article are solely those of the authors and do not necessarily represent those of their affiliated organizations, or those of the publisher, the editors and the reviewers. Any product that may be evaluated in this article, or claim that may be made by its manufacturer, is not guaranteed or endorsed by the publisher.

frontiers in Medicine

ORIGINAL RESEARCH
published: 28 February 2022
doi: 10.3389/fmed.2022.840261

Exploring the Utility of Radiomic Feature Extraction to Improve the Diagnostic Accuracy of Cardiac Sarcoidosis Using FDG PET

Nouf A. Mushari[1], Georgios Soultanidis[2], Lisa Duff[1,3], Maria G. Trivieri[2,4], Zahi A. Fayad[2], Philip Robson[2] and Charalampos Tsoumpas[1,2,5]*

[1] Leeds Institute of Cardiovascular and Metabolic Medicine, University of Leeds, Leeds, United Kingdom, [2] BioMedical Engineering and Imaging Institute, Icahn School of Medicine at Mount Sinai, New York, NY, United States, [3] Institute of Medical and Biological Engineering, University of Leeds, Leeds, United Kingdom, [4] Cardiovascular Institute, Icahn School of Medicine at Mount Sinai, New York, NY, United States, [5] Department of Nuclear Medicine and Molecular Imaging, University Medical Centre Groningen, University of Groningen, Groningen, Netherlands

OPEN ACCESS

Edited by:
Ronan Abgral, Centre Hospitalier Regional Universitaire (CHU) de Brest, France

Reviewed by:
Francesco Dondi, Università degli Studi di Brescia, Italy
Francois Rouzet, Assistance Publique Hopitaux De Paris, France

***Correspondence:**
Nouf A. Mushari
ml16nam@leeds.ac.uk

Specialty section:
This article was submitted to Nuclear Medicine, a section of the journal Frontiers in Medicine

Received: *20 December 2021*
Accepted: *01 February 2022*
Published: *28 February 2022*

Citation:
Mushari NA, Soultanidis G, Duff L, Trivieri MG, Fayad ZA, Robson P and Tsoumpas C (2022) Exploring the Utility of Radiomic Feature Extraction to Improve the Diagnostic Accuracy of Cardiac Sarcoidosis Using FDG PET. Front. Med. 9:840261. doi: 10.3389/fmed.2022.840261

Background: This study aimed to explore the radiomic features from PET images to detect active cardiac sarcoidosis (CS).

Methods: Forty sarcoid patients and twenty-nine controls were scanned using FDG PET-CMR. Five feature classes were compared between the groups. From the PET images alone, two different segmentations were drawn. For segmentation A, a region of interest (ROI) was manually delineated for the patients' myocardium hot regions with standardized uptake value (SUV) higher than 2.5 and the controls' normal myocardium region. A second ROI was drawn in the entire left ventricular myocardium for both study groups, segmentation B. The conventional metrics and radiomic features were then extracted for each ROI. Mann-Whitney *U*-test and a logistic regression classifier were used to compare the individual features of the study groups.

Results: For segmentation A, the SUV_{min} had the highest area under the curve (AUC) and greatest accuracy among the conventional metrics. However, for both segmentations, the AUC and accuracy of the TBR_{max} were relatively high, >0.85. Twenty-two (from segmentation A) and thirty-five (from segmentation B) of 75 radiomic features fulfilled the criteria: *P*-value < 0.00061 (after Bonferroni correction), AUC >0.5, and accuracy >0.7. Principal Component Analysis (PCA) was conducted, with five components leading to cumulative variance higher than 90%. Ten machine learning classifiers were then tested and trained. Most of them had AUCs and accuracies ≥0.8. For segmentation A, the AUCs and accuracies of all classifiers are >0.9, but k-neighbors and neural network classifiers were the highest (=1). For segmentation B, there are four classifiers with AUCs and accuracies ≥0.8. However, the gaussian process classifier indicated the highest AUC and accuracy (0.9 and 0.8, respectively).

Conclusions: Radiomic analysis of the specific PET data was not proven to be necessary for the detection of CS. However, building an automated procedure will help to

accelerate the analysis and potentially lead to more reproducible findings across different scanners and imaging centers and consequently improve standardization procedures that are important for clinical trials and development of more robust diagnostic protocols.

Keywords: cardiac sarcoidosis, PET-MRI, imaging, radiomics, machine learning

INTRODUCTION

Sarcoidosis is a multisystem, granulomatous inflammatory disease of unknown etiology, characterized by the presence of non-caseating granulomas in the involved organs (1, 2). Sarcoidosis primarily affects the lungs. The development of this disease in the pulmonary system has been identified in more than 90% of reported cases (3, 4). However, it can affect the extrapulmonary organs as well, including the heart (5). Clinically, cardiac involvement is uncommon, manifesting in only ∼5% of sarcoid patients, but it can occur without apparent symptoms, i.e., a "clinically silent" disease, which is reflected in the high rate of cardiac involvement in autopsy studies. At least 25% of patients with sarcoidosis are diagnosed with cardiac involvement (6–8).

The challenging in diagnosing cardiac sarcoidosis (CS) is due to the probability of involving any organ, leads to variability in clinical presentation (9). In addition, a lack of reliable biomarkers or diagnostic tests poses a challenge to diagnosing cardiac sarcoidosis. Furthermore, the role of advanced imaging modalities such as Cardiovascular Magnetic Resonance Imaging (CMR) with Late Gadolinium Enhancement (LGE) and [^{18}F] Fluorodeoxyglucose Positron Emission Tomography [[^{18}F] FDG PET] have been demonstrated in the literature to improve the identification and treatment of patients with CS. Currently, these imaging tools are critical for early diagnosis, disease prediction and progression, and therapeutic response monitoring.

To increase the diagnostic performance of [^{18}F] FDG PET, it is important to suppress the use of glucose by normal cardiomyocytes as this improves its specificity. Several approaches have been proposed, including following a ketogenic diet (high fats and low carbohydrates), prolonged fasting, intravenous heparin, and usually, a combination of these methods (10). However, strategies to improve diagnostic performance do not help in up to 25% of patients, which can result in false-positive findings (11) due to failure to suppress the physiological uptake of the myocardium. A semi-quantitative analysis can be used to diagnose CS. A common tool, a maximum standardized uptake value (SUV_{max}), can identify the highest uptake value within the region of interest (ROI). This can differentiate positive (CS^+) and negative (CS^-) results; however, in the presence of high physiological uptake, this metric fails to detect sarcoidosis within this region (12). In addition, the maximum target-to-background ratio (TBR_{max}) is more robust than SUV_{max} due to the effective normalization for blood uptake (12, 13), which makes it more reliable for comparing data across patients and institutions. Radiomic features, which rely on the spatial correlations of image values or derived image-based metrics, have the potential to elucidate features robust to background physiological uptake. The purpose of this study is to explore radiomic features from PET images to identify potential candidate radiomic metrics. Specifically, this study will characterize radiomic features that separate active CS from controls.

Abbreviations: CS, cardiac sarcoidosis; SUV, standardized uptake value; [^{18}F]FDG PET, [^{18}F]-fluorodeoxyglucose positron emission tomography; CMR, cardiovascular magnetic resonance imaging; AUC, area under the curve; PCA, principal component analysis.

MATERIALS AND METHODS

Ethical Approval

This study was conducted with the approval of the Institutional Review Board at Mount Sinai (GCO # 01-1032), and all subjects gave written informed consent.

Subject Selection

Subjects with clinical suspicion of CS based on demonstrated clinical manifestations of extracardiac lesions and/or disease were recruited at Mount Sinai Hospital in New York, to undertake a PET-CMR examination. All subjects were treatment-naïve and had to avoid carbohydrate diet for 24 h before the scan and fast during the last 12 h. The preparation for imaging followed the recent recommendations by Ishida et al. (14). After the acquisition, the results were assessed by an expert cardiologist for indications of CS and had no indications of failed suppression of FDG uptake. Subjects were divided into patients and controls based on their results. Subjects with patchy FDG uptake were designated as CS+ and were assigned to the patient group for this study (15), and those without either FDG or CMR findings were designated as control subjects for this study. Control population had normal cardiac appearance and regular echocardiography. Forty patients and twenty-nine controls met these criteria for this study. Exclusion criteria include insulin-dependent diabetes mellitus, pretest blood glucose >200 mmol/dl, menopausal phobia, pregnancy/lactation, the presence of a cardiac pacemaker or automatic implantable cardioverter-defibrillator, and renal dysfunction.

Imaging Protocol

The simultaneous CMR with LGE and [^{18}F] FDG PET on an integrated PET-CMR system (Biograph^{TM} mMR, Siemens Healthcare, Erlangen, Germany) was used in this study. Five MBq/kg of [^{18}F] FDG was injected into the patients intravenously, who then waited for 10 min. Thoracic PET acquisition (one-bed position centered on the heart) took about 90 min but for this study only a late time window (last 60 min) was selected. PET images were reconstructed using the iterative ordinary Poisson ordered subset expectation maximization (OP-OSEM) with three iterations and 21 subsets on a 344 × 344 ×

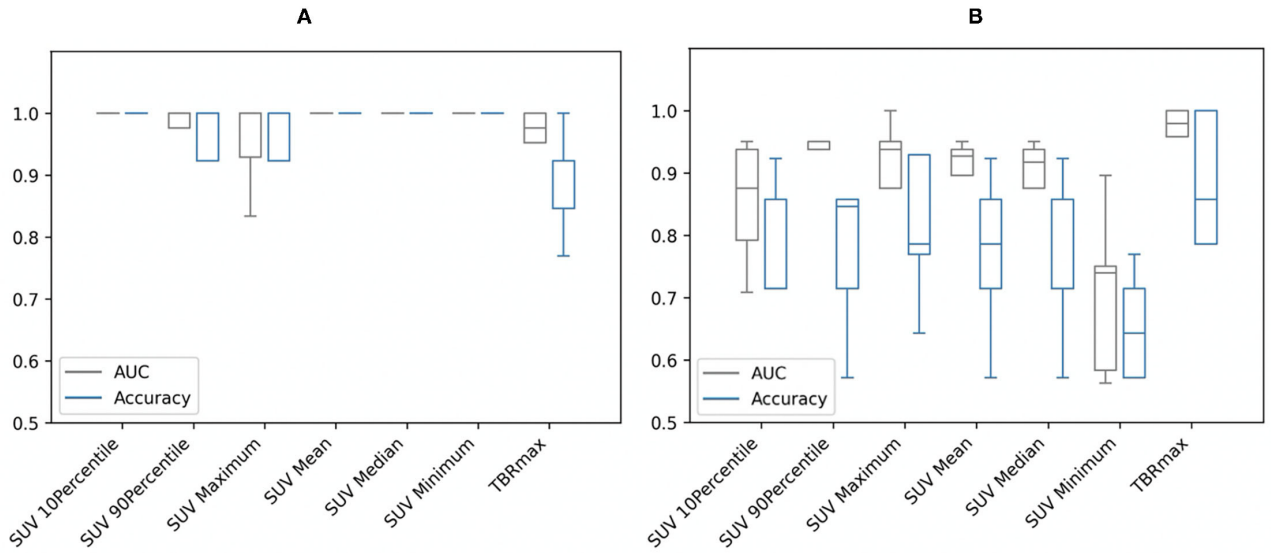

FIGURE 1 | Area under the curve (AUC) and accuracy with stratified 5-fold cross-validation of the conventional metrics of **(A)** segmentation A and **(B)** segmentation B. SUV, standardized uptake value; TBRmax, maximum target-to-background ratio.

129 image matrix and an isotropic voxel size of 2 mm, followed by an isotropic 4 mm Gaussian post-filtering. The data obtained with PET were not respiratory-gated or ECG-gated and were not corrected for any potential motion artifacts. A 3D breath-hold Dixon-based MR image was used for attenuation correction. Simultaneously with PET imaging, CMR was performed with electrocardiograph triggered; the scan included short-axis T2 mapping and cine images. Approximately 15 min after 0.2 mmol/kg gadolinium injection, inversion-recovery fast gradient-echo LGE sequences were acquired.

Segmentations

3D slicer software (Version 4.11.2; https://www.slicer.org) was used for the segmentation (16, 17). Segmentations were performed by study personnel according to methods used in a previous study (12).

Segmentation A

From the PET images (with use of CMR for anatomical localization, and aiding in focal lesion identification when possible) of the patient group, an ROI was manually drawn in the hot region of the myocardium with an SUV higher than 2.5, which is a cut-off value previously used to differentiate between benign (normal in cases of CS) and malignant (abnormal in cases of CS) lesions (18, 19). For patients with more than one focal lesion, the largest and most active was selected. Due to the focal nature of the disease, applying a threshold helped ensure that the extracted features are only from voxels with abnormal uptakes. For the control group, an ROI was drawn manually in the normal myocardium. Once the SUV_{max} and SUV_{mean} (in the blood pool of the right atrium) were extracted, the TBR_{max} was calculated using the following equation:

$$\mathbf{TBR_{max}} = \frac{\mathbf{SUV_{max}\ (target)}}{\mathbf{SUV_{mean}\ (background)}}$$

Thirty-five subjects out of forty who had a TBR_{max} within the range of 1 to 3 and patchy uptake were labeled as patients. The remaining five subjects who had $TBR_{max} > 3$ were excluded as failed suppression could not be completely discounted in these cases (12) even though the FDG was patchy and initially included in the study cohort and subsequently in the study cohort for segmentation B.

Segmentation B

As the approach A took into account both intensity and pattern, it was useful to investigate a different approach that was independent of these. From the PET images, an ROI was drawn in the entire left ventricular myocardium for forty patients and twenty-nine controls regardless of the TBR_{max} findings and SUV thresholds to compare the reliability of features among segmentation approaches. Radiomic features and conventional metrics were then extracted.

Feature Extraction

PyRadiomics (Version 3.0.1) was used to extract five feature classes (75 features in total) from the PET image ROIs of the patients and controls (20) in addition to the conventional metrics (7 metrics). PyRadiomics adheres to the image biomarker standardization initiative (IBSI's feature definitions). A bin width of 0.05 was applied. All other parameters were left as default. Harmonization was not required for these datasets as they originated from a single scanner. A list of all radiomic features and conventional metrics is shown in **Supplementary Material 1**.

TABLE 1 | Conventional metrics and five best performing radiomic features for the different segmentations based on *P*-values.

	Segmentation A			Segmentation B		
	Feature	***P*-value**	**AUC**	**Feature**	***P*-value**	**AUC**
Conventional	SUV 10 percentile	1×10^{-11}	0.99	SUV 10 percentile	6×10^{-7}	0.85
	SUV 90 percentile	1×10^{-10}	0.96	SUV 90 percentile	3×10^{-8}	0.90
	SUV maximum	3×10^{-10}	0.95	SUV maximum	8×10^{-9}	0.90
	SUV mean	1×10^{-10}	0.97	SUV mean	6×10^{-8}	0.88
	SUV median	1×10^{-10}	0.97	SUV median	2×10^{-7}	0.88
	SUV minimum	6×10^{-13}	1.00	SUV minimum	9×10^{-3}	0.71
	TBR_{max}	1×10^{-10}	0.96	TBR_{max}	3×10^{-11}	0.96
Radiomics	GLDM_small dependence low gray level emphasis	3×10^{-13}	1.00	GLSZM_low gray level zone emphasis	5×10^{-8}	0.85
	GLCM_inverse difference normalized	1×10^{-11}	1.00	GLDM_dependence non-uniformity	1×10^{-7}	0.87
	GLSZM_small area low gray level emphasis	1×10^{-11}	0.99	NGTDM_complexity	1×10^{-7}	0.85
	GLSZM_large area high gray level emphasis	3×10^{-11}	1.00	GLSZM_high gray level zone emphasis	1×10^{-7}	0.85
	GLCM_maximal correlation coefficient	5×10^{-11}	0.98	GLSZM_small area high gray level emphasis	1×10^{-7}	0.85

SUV, Standardized Uptake Value; TBR_{max}, maximum Target-to-Background Ratio; GLDM, Gray Level Dependence Matrix; GLCM, Gray Level Co-occurrence Matrix; GLSZM, Gray Level Size Zone Matrix; NGTDM, Neighboring Gray Tone Difference Matrix.

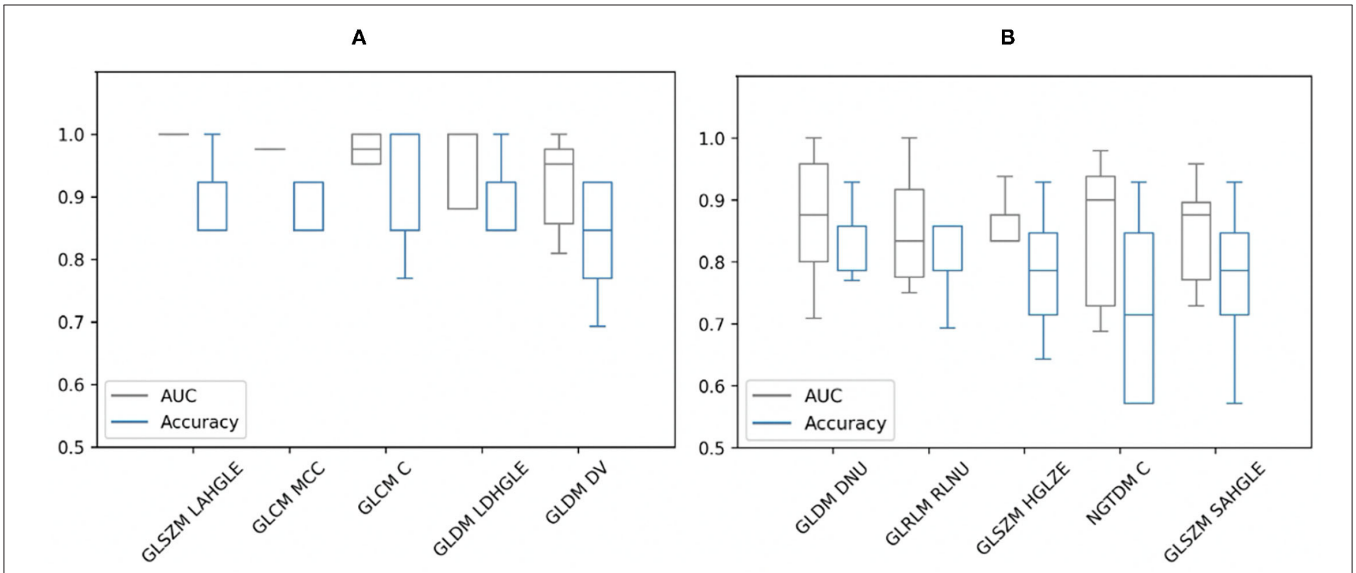

FIGURE 2 | Area under the curve (AUC) and accuracy with stratified 5-fold cross-validation of the five best-performing radiomic features of **(A)** segmentation A and **(B)** segmentation B based on AUC values. GLSZM, Gray Level Size Zone Matrix; LAHGLE, Large Area High Gray Level Emphasis; GLCM, Gray Level Co-occurrence Matrix; MCC, Maximal Correlation Coefficient; GLCM C, Correlation; GLDM, Gray Level Dependence Matrix; LDHGLE, Large Dependence High Gray Level Emphasis; DV, Dependence Variance; DNU, Dependence Non-Uniformity; GLRLM, Gray Level Run Length Matrix; RLNU, Run Length Non-Uniformity; HGLZE, High Gray Level Zone Emphasis; NGTDM, Neighboring Gray Tone Difference Matrix; NGTDM C, Complexity; SAHGLE, Small Area High Gray Level Emphasis.

Statistical Analysis

Statistical analyses were undertaken using Scikit-learn software (Version 0.23.2) (21). Mann–Whitney *U*-test was used to compare the radiomic features of the study groups. The *P*-value was adjusted using a Bonferroni correction approach for multiple tests [*P*-value (0.05) divided by the number of features (82)] and the corrected *P*-value of < 0.00061 was considered to be statistically significant. Logistic regression classifiers were then trained with individual features. Stratified 5-fold cross-validation was used to determine the mean area

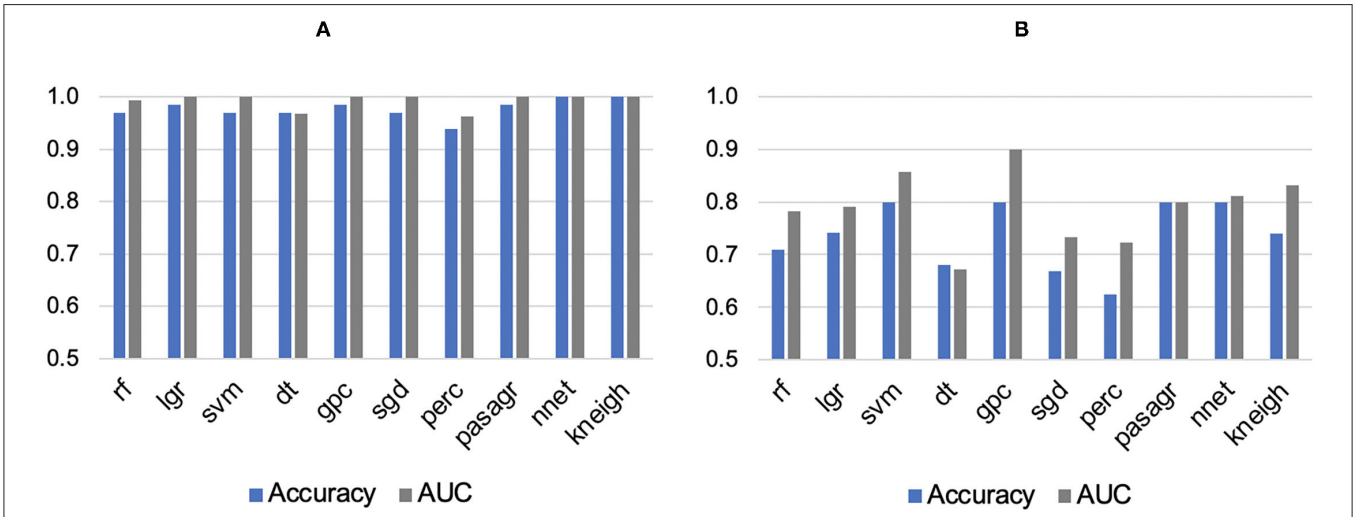

FIGURE 3 | Areas under the curve (AUC) and accuracies of machine learning classifiers for **(A)** Segmentation A and **(B)** Segmentation B. rf, Random Forest; lgr, Logistic Regression; svm, Support Vector Machine; dt, Decision Tree; gpc, Gaussian Process Classifier; sgd, Stochastic Gradient Descent; perc, Perceptron Classifier; pasagr, Passive Aggressive Classifier; nnet, Neural Network Classifier; kneigh, K-neighbors Classifier.

under the curve (AUC), mean accuracy, and 95% confidence intervals (CIs). Features with a *P*-value < 0.00061, AUC >0.5, and accuracy >0.7 were retained. In addition, principal component analysis (PCA) was used to identify highly correlated features and reduce feature redundancy. PCA reduces a large number of features into a small number of principal components (PCs). Components that explained 90% of the cumulative variance were retained. Lastly, to find the best machine learning (ML) algorithm, PCs were used as an input to test and train the following ten classifiers: Random Forest, Logistic Regression, Support Vector Machine, Decision Tree, Gaussian Process Classifier, Stochastic Gradient Descent, Perceptron Classifier, Passive Aggressive Classifier, Neural Network Classifier and K-neighbors Classifier with stratified 5-fold cross-validation.

RESULTS

Conventional Metrics Diagnostic Utility

The results are relatively different by applying the Mann–Whitney *U*-tests on the conventional metrics of the different study groups for each segmentation separately. Predictably, for segmentation A, the SUV_{min} had the highest AUC and greatest accuracy due to specifying SUV >2.5 as the minimum value for the patient group, while for segmentation B, the highest performance was for TBR_{max} (see **Figure 1**). However, for both segmentations, the AUC and accuracy of the TBR_{max} were relatively high and had similar results regardless of the segmentation approach (AUC 0.96; accuracy 0.88–0.89 for segmentation A & B, respectively). This slight difference in TBR_{max} results between both segmentations came from the difference in the number of participants in the patient group who met the criteria for each segmentation.

Individual Radiomic Features Diagnostic Utility

From the Mann–Whitney *U*-tests, for segmentation A: 40 of the 75 radiomic features and for segmentation B: 61 of the 75 showed statistically significant differences between patients and controls, with a *P*-value < 0.00061. The five best radiomic features based on *P*-values for both segmentations are shown in **Table 1**. After applying a logistic regression classifier, only 22 radiomic features for segmentation A and 35 radiomic features for segmentation B fulfilled the following criteria: *P*-value < 0.00061, AUC >0.5, and accuracy >0.7. The AUC and accuracy (95% CI for each criterion) with stratified 5-fold cross-validation of the five best-performing radiomic features based on the AUC value are shown in **Figure 2**. All values of radiomic features and conventional metrics for both segmentations are provided in **Supplementary Material 2**.

Principal Component Analysis and Machine Learning

As the SUV-related metrics tend to overperform, and to study the performance of non-first order features, the SUV-related metrics were excluded from the PCA. By applying PCA, five PCs were retained to explain 90% of the information. These PCs were used to test and train the ML classifiers. Most of them had AUCs and accuracies ≥ 0.8. For segmentation A, all classifiers showed high performance in terms of AUC (95% CI 0.88–1.00) and accuracy (95% CI 0.87–1.00), with values >0.9. A k-neighbors and neural network classifiers showed the highest AUC and greatest accuracy, with values equal to 1.00, as shown in **Figure 3**. For segmentation B, there are four classifiers with AUCs and accuracies ≥ 0.8, **Figure 3**. However, the gaussian process

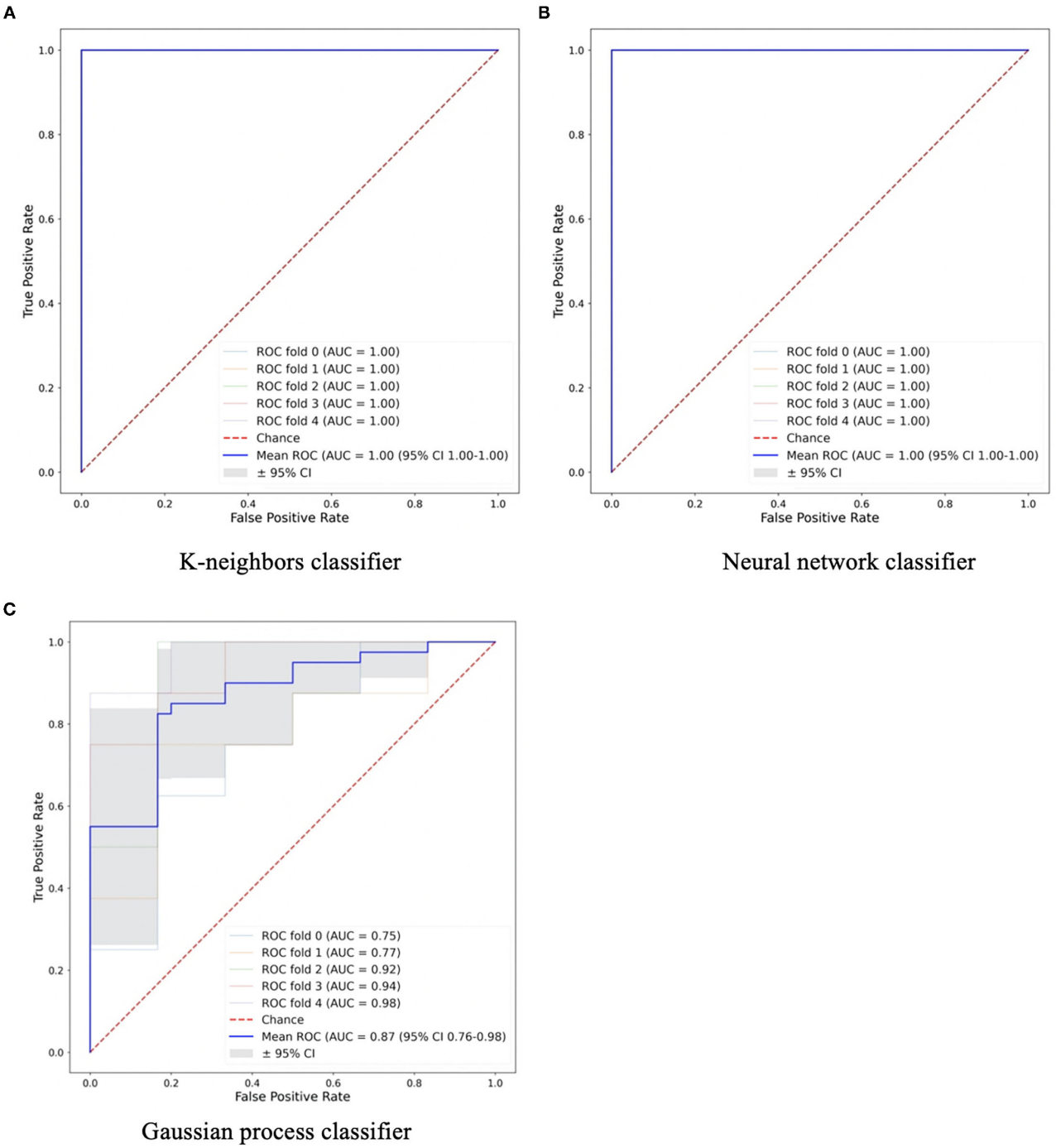

FIGURE 4 | The machine learning classifiers with high performance in **(A,B)** Segmentation A and **(C)** Segmentation B.

classifier indicated the highest AUC and accuracy (0.9 and 0.8, respectively). The ROC curves of the k-neighbors, neural network, and gaussian process classifiers are shown in **Figure 4**. The actual values of **Figures 2**, **3** are provided in **Supplementary Material 3**.

DISCUSSION

This study aimed to explore the diagnostic utility of radiomic features compared to conventional metrics to distinguish between study groups and find the best performance ML classifier

to create an automated model. From segmentation A, some conventional metrics like SUV_{min} showed high performance individually. These results were predictable as they are affected by the distribution of voxel intensities within the ROI, one of the criteria for including the patients at the first place. In addition, these features cannot be relied upon because they are greatly affected by the success of glucose suppression in normal cardiomyocytes. TBR_{max} was the most reliable metric over other conventional metrics among both segmentations. Although the TBR_{max} is sensitive to noise and it is not necessarily easy to harmonize across different scanners and imaging centers, types of data, and parameters, this is not the case in this study as datasets originated from a single scanner and institution. Therefore, when comparing TBR_{max} with those of the five-best performance radiomic features, the superiority of TBR_{max} over the rest of the features can be clearly seen. This outcome supports any previous studies that utilized TBR_{max}.

From segmentation A, by comparing the diagnostic utility of individual radiomic features, GLSZM-Large Area High Gray Level Emphasis radiomic feature showed the best performance in terms of AUC and accuracy. This feature measures the proportion in the image of the joint distribution of larger size zones with higher gray level values. This means there is a difference in gray level zones between patients and controls. However, it cannot be reliable due to the criteria of this segmentation approach that is based on SUV threshold and TBR_{max}. On the other hand, from segmentation B, the best performing radiomic feature was GLDM_Dependence Non-Uniformity with AUC (0.87) and accuracy (0.83). This feature measures the heterogeneity in the ROIs. The values of this feature are higher in sarcoid patients than controls which illustrates more heterogeneous regions in the group of patients. In addition, many other features measure heterogeneity with high AUCs and accuracies. These features look at the spatial relationships rather than voxels values themselves. However, these features had large error bars, unlike the TBR_{max} which had very small bars regardless of the segmentation approach.

Several studies of different diseases advocated the importance of radiomic analysis to predict outcomes (22, 23). However, the findings across these studies are not replicated; instead, they are conflicted. Technical issues may illustrate this difference in results among studies, such as ROI size, scanner resolution, reconstruction, and segmentation algorithms, or any other unrevealed factors. High scanner resolution and large number of voxels can affect some radiomic features by increasing their values (24). In terms of segmentation algorithms, numerous studies indicated that using different segmentation methods gave close results in survival analyses (23, 25). In addition, Cheng et al. (23) argued that no significant difference exists between radiomic features when using different segmentation methods, unlike SUV_{max} and SUV_{mean}. They reported, in addition, that the effect of utilizing different attenuation correction methods on radiomic features was not significant. At the same time Yip et al. (26) had contrasting results, as some of the features were affected by the attenuation correction method. However, in this study, there was a clear difference between radiomic features when using different segmentation approaches. This may be due to the different sizes of ROIs and the voxel intensities included in each segmentation. Applying the approach of segmentation A, it can provide a good differentiation between study groups based on the conventional metrics such as SUV_{min} and TBR_{max}. However, this approach can be influenced by observer experience, especially for cases with very small hotspots. Conversely, segmentation B approach is more robust and efficient.

This study is subject to some limitations. First, the sample size is relatively small, and more extensive studies are needed to confirm these results. This is of great significance to prevent overfitting and type I errors. Applying a Bonferroni correction and dimensionality reduction techniques resulted in reducing the effect of this issue. In addition, the lack of an automated segmentation, a segmentation reference to compare with, unavailability of an independent clinical gold standard to validate the performance of the model that was trained on initial input data are other limitations for this study. In addition, the selection of only one focal lesion per patient in segmentation A was considered a limitation of this approach. Furthermore, the models proposed in this study should be validated in normal controls showing non-specific physiological uptake. This study showed uncertainty results of radiomic features and expanding the study to test the reproducibility of the results is required. New knowledge gained from this study is that using radiomic analysis does not provide any additional information related to disease activity in these patients. However, building an automated model regardless of the strategies used for glucose suppression and/or observer experience may prove helpful in further studies. Furthermore, in this study, the MRI acquisitions were not utilized, except for providing anatomical information. In this study the main goal was the radiomic features on PET; the designated tool for CS.

CONCLUSION

Radiomic analysis of PET data may not be a useful approach to detect CS. Several radiomic features that were not related to first-order tracer uptake showed high AUC and accuracy with P-value < 0.00061. However, by measuring AUCs and accuracies, large error bars can weaken the results. TBR_{max} showed its superiority over all other conventional and radiomic features in both segmentation approaches. This methodology needs to be validated further in normal control subjects showing non-specific physiological uptake.

DATA AVAILABILITY STATEMENT

The original contributions presented in the study are included in the article/**Supplementary Material**, further inquiries can be directed to the corresponding author/s.

ETHICS STATEMENT

This study was conducted with the approval of the Institutional Review Board at Mount Sinai. The patients/participants provided their written informed consent to participate in this study.

AUTHOR CONTRIBUTIONS

NM segmented all the datasets using 3D slicer software, analyzed the data using PyRadiomics, performed the statistical analysis, analyzed the results, and wrote the manuscript. GS shared datasets, reviewed segmentations, and helped in modifying code as well as in the guidance of the project. LD wrote python code and helped to modify it and provide essential guidance on how to perform the optimization of the radiomic analysis, and machine learning approaches. MT facilitated the availability of data. MT, ZF, and PR contributed to reviewing the manuscript and the overall guidance of the project and data. ZF is the PI of the NIH grant. CT supervised the specific study and helped in restructuring and reviewing the manuscript. All authors contributed to the article and approved the submitted version.

FUNDING

NM is fully funded by Taif University, Saudi Arabia. GS and PR are supported by NIH grant R01HL071021. LD is fully funded by the EPSRC Centre for Doctoral Training in Tissue Engineering and Regenerative Medicine: Innovation in Medical and Biological Engineering – grant number EP/L014823/1.

ACKNOWLEDGMENTS

We wish to thank our colleagues at the University of Leeds, Drs. Eylem Levelt and Karen Porter and Professors David Buckley, Alejandro Frangi, and Andrew Scarsbrook for fruitful discussions and overall support during this project.

SUPPLEMENTARY MATERIAL

The Supplementary Material for this article can be found online at: https://www.frontiersin.org/articles/10.3389/fmed.2022.840261/full#supplementary-material

REFERENCES

1. Birnie DH, Nery PB, Ha AC, Beanlands RS. Cardiac sarcoidosis. *J Am Coll Cardiol.* (2016) 68:411–21. doi: 10.1016/j.jacc.2016.03.605
2. Hulten E, Aslam S, Osborne M, Abbasi S, Bittencourt MS, Blankstein R. Cardiac sarcoidosis—state of the art review. *Cardiovasc Diag Therapy.* (2016) 6:50. doi: 10.3978/j.issn.2223-3652.2015.12.13
3. Ginelliová A, Farkaš D, Iannaccone SF, Vyhnálková V. Sudden unexpected death due to severe pulmonary and cardiac sarcoidosis. *Forensic Sci Med Pathol.* (2016) 12:319–23. doi: 10.1007/s12024-016-9792-y
4. Petek BJ, Rosenthal DG, Patton KK, Behnia S, Keller JM, Collins BF, et al. Cardiac sarcoidosis: diagnosis confirmation by bronchoalveolar lavage and lung biopsy. *Res Med.* (2018) 144:S13–S9. doi: 10.1016/j.rmed.2018.09.008
5. Deng JC, Baughman RP, Lynch Iii JP, editors. *Cardiac Involvement in Sarcoidosis. Seminars in Respiratory and Critical Care Medicine*. Copyright© 2002 by Thieme Medical Publishers, Inc., 333 Seventh Avenue, New (2002).
6. Iwai K, Tachibana T, Takemura T, Matsui Y, Kitalchi M, Kawabata Y. Pathological studies on sarcoidosis autopsy. I. Epidemiological features of 320 cases in Japan. *Pathol Int.* (1993) 43:372–6. doi: 10.1111/j.1440-1827.1993.tb01148.x
7. Perry A, Vuitch F. Causes of death in patients with sarcoidosis. A morphologic study of 38 autopsies with clinicopathologic correlations. *Arch Pathol Lab Med.* (1995) 119:167.
8. Kim JS, Judson MA, Donnino R, Gold M, Cooper Jr LT, Prystowsky EN, et al. Cardiac sarcoidosis. *Am Heart J.* (2009) 157:9–21. doi: 10.1016/j.ahj.2008.09.009
9. Trivieri MG, Spagnolo P, Birnie D, Liu P, Drake W, Kovacic JC, et al. Challenges in cardiac and pulmonary sarcoidosis: JACC state-of-the-art review. *J Am Coll Cardiol.* (2020) 76:1878–901. doi: 10.1016/j.jacc.2020.08.042
10. Chareonthaitawee P, Beanlands RS, Chen W, Dorbala S, Miller EJ, Murthy VL, et al. Joint SNMMI–ASNC expert consensus document on the role of 18F-FDG PET/CT in cardiac sarcoid detection and therapy monitoring. *J Nucl Med.* (2017) 58:1341–53. doi: 10.2967/jnumed.117.196287
11. Osborne MT, Hulten EA, Murthy VL, Skali H, Taqueti VR, Dorbala S, et al. Patient preparation for cardiac fluorine-18 fluorodeoxyglucose positron emission tomography imaging of inflammation. *J Nucl Cardiol.* (2017) 24:86–99. doi: 10.1007/s12350-016-0502-7
12. Dweck MR, Abgral R, Trivieri MG, Robson PM, Karakatsanis N, Mani V, et al. Hybrid magnetic resonance imaging and positron emission tomography with fluorodeoxyglucose to diagnose active cardiac sarcoidosis. *JACC.* (2018) 11:94–107. doi: 10.1016/j.jcmg.2017.02.021
13. Chen W, Dilsizian V. PET assessment of vascular inflammation and atherosclerotic plaques: SUV or TBR? *J Nucl Med.* (2015) 56:503–4. doi: 10.2967/jnumed.115.154385
14. Ishida Y, Yoshinaga K, Miyagawa M, Moroi M, Kondoh C, Kiso K, et al. Recommendations for 18 F-fluorodeoxyglucose positron emission tomography imaging for cardiac sarcoidosis: Japanese society of nuclear cardiology recommendations. *Ann Nucl Med.* (2014) 28:393–403. doi: 10.1007/s12149-014-0806-0
15. Birnie DH, Sauer WH, Bogun F, Cooper JM, Culver DA, Duvernoy CS, et al. HRS expert consensus statement on the diagnosis and management of arrhythmias associated with cardiac sarcoidosis. *Heart Rhythm.* (2014) 11:1304–23. doi: 10.1016/j.hrthm.2014.03.043
16. Fedorov A, Beichel R, Kalpathy-Cramer J, Finet J, Fillion-Robin J-C, Pujol S, et al. 3D Slicer as an image computing platform for the Quantitative Imaging Network. *Magn Res Imag.* (2012) 30:1323–41. doi: 10.1016/j.mri.2012.05.001
17. Kikinis R, Pieper SD, Vosburgh KG. *3D Slicer: A Platform for Subject-Specific Image Analysis, Visualization, and Clinical Support. Intraoperative Imaging and Image-Guided Therapy*. New York, NY: Springer (2014). p. 277–89.
18. Kadaria D, Freire AX, SultanAli I, Zaman MK, Archie DS, Weiman DS. Dual time point positron emission tomography/computed tomography scan in evaluation of intrathoracic lesions in an area endemic for histoplasmosis and with high prevalence of sarcoidosis. *Am J Med Sci.* (2013) 346:358–62. doi: 10.1097/MAJ.0b013e31827b9b6d
19. Wang T, Sun H, Guo Y, Zou L. 18F-FDG PET/CT quantitative parameters and texture analysis effectively differentiate endometrial precancerous lesion and early-stage carcinoma. *Mol Imag.* (2019) 18:1536012119856965. doi: 10.1177/1536012119856965
20. Van Griethuysen JJ, Fedorov A, Parmar C, Hosny A, Aucoin N, Narayan V, et al. Computational radiomics system to decode the radiographic phenotype. *Can Res.* (2017) 77:e104–7. doi: 10.1158/0008-5472.CAN-17-0339
21. Pedregosa F, Varoquaux G, Gramfort A, Michel V, Thirion B, Grisel O, et al. Scikit-learn: machine learning in python. *J Mach Learn Res.* (2011) 12:2825–30.
22. Apostolova I, Ego K, Steffen IG, Buchert R, Wertzel H, Achenbach HJ, et al. The asphericity of the metabolic tumour volume in NSCLC: correlation with histopathology and molecular markers. *Eur J Nucl Med Mol Imag.* (2016) 43:2360–73. doi: 10.1007/s00259-016-3452-z

23. Cheng N-M, Fang Y-HD, Tsan D-L, Hsu C-H, Yen T-C. Respiration-averaged CT for attenuation correction of PET images–impact on PET texture features in non-small cell lung cancer patients. *PLoS ONE.* (2016) 11:e0150509. doi: 10.1371/journal.pone.0150509
24. Han S, Woo S, Suh CH, Kim YJ, Oh JS, Lee JJ. A systematic review of the prognostic value of texture analysis in 18 F-FDG PET in lung cancer. *Ann Nucl Med.* (2018) 32:602–10. doi: 10.1007/s12149-018-1281-9
25. Bashir U, Azad G, Siddique MM, Dhillon S, Patel N, Bassett P, et al. The effects of segmentation algorithms on the measurement of 18 F-FDG PET texture parameters in non-small cell lung cancer. *Ejnmmi Res.* (2017) 7:60. doi: 10.1186/s13550-017-0310-3
26. Yip S, McCall K, Aristophanous M, Chen AB, Aerts HJ, Berbeco R. Comparison of texture features derived from static and respiratory-gated PET images in non-small cell lung cancer. *PLoS ONE.* (2014) 9:e115510. doi: 10.1371/journal.pone.0115510

Conflict of Interest: The authors declare that the research was conducted in the absence of any commercial or financial relationships that could be construed as a potential conflict of interest.

frontiers in Medicine

ORIGINAL RESEARCH
published: 02 March 2022
doi: 10.3389/fmed.2022.796085

Reproducibility of Standardized Uptake Values Including Volume Metrics Between TOF-PET-MR and TOF-PET-CT

Aruki Tanaka[1], *Tetsuro Sekine*[1,2,3,4]*, *Edwin E. G. W. ter Voert*[3,4], *Konstantinos G. Zeimpekis*[3,4,5], *Gaspar Delso*[6], *Felipe de Galiza Barbosa*[3,4], *Geoffrey Warnock*[3,4,7], *Shin-ichiro Kumita*[1], *Patrick Veit Haibach*[3,4,8,9] and *Martin Huellner*[3,4]

[1] Department of Radiology, Nippon Medical School Hospital, Tokyo, Japan, [2] Department of Radiology, Nippon Medical School Musashi Kosugi Hospital, Kanagawa, Japan, [3] Departments of Nuclear Medicine, University Hospital Zurich, Zurich, Switzerland, [4] University of Zurich, Zurich, Switzerland, [5] Department of Nuclear Medicine, Inselspital, Bern University Hospital, University of Bern, Bern, Switzerland, [6] GE Healthcare, Waukesha, WI, United States, [7] PMOD Technologies Ltd., Zurich, Switzerland, [8] Toronto Joint Department Medical Imaging, University Health Network, Sinai Health System, Women's College Hospital, Toronto, ON, Canada, [9] Department of Medical Imaging, University of Toronto, Toronto, ON, Canada

OPEN ACCESS

Edited by:
Giorgio Treglia, Ente Ospedaliero Cantonale (EOC), Switzerland

Reviewed by:
Maria Mathew D'Souza, Institute of Nuclear Medicine & Allied Sciences (DRDO), India
Luca Camoni, University of Brescia, Italy

***Correspondence:**
Tetsuro Sekine
tetsuro.sekine@gmail.com

Specialty section:
This article was submitted to Nuclear Medicine, a section of the journal Frontiers in Medicine

Received: *15 October 2021*
Accepted: *07 February 2022*
Published: *02 March 2022*

Citation:
Tanaka A, Sekine T, ter Voert EEGW, Zeimpekis KG, Delso G, de Galiza Barbosa F, Warnock G, Kumita S-i, Veit Haibach P and Huellner M (2022) Reproducibility of Standardized Uptake Values Including Volume Metrics Between TOF-PET-MR and TOF-PET-CT. Front. Med. 9:796085. doi: 10.3389/fmed.2022.796085

Purpose: To investigate the reproducibility of tracer uptake measurements, including volume metrics, such as metabolic tumor volume (MTV) and tumor lesion glycolysis (TLG) obtained by TOF-PET-CT and TOF-PET-MR.

Materials and Methods: Eighty consecutive patients with different oncologic diagnoses underwent TOF-PET-CT (Discovery 690; GE Healthcare) and TOF-PET-MR (SIGNA PET-MR; GE Healthcare) on the same day with single dose−18F-FDG injection. The scan order, PET-CT following or followed by PET-MR, was randomly assigned. A spherical volume of interest (VOI) of 30 mm was placed on the liver in accordance with the PERCIST criteria. For liver, the maximum and mean standard uptake value for body weight (SUV) and lean body mass (SUL) were obtained. For tumor delineation, VOI with a threshold of 40 and 50% of SUVmax was used (VOI40 and VOI50). The SUVmax, SUVmean, SUVpeak, MTV and TLG were calculated. The measurements were compared between the two scanners.

Results: In total, 80 tumor lesions from 35 patients were evaluated. There was no statistical difference observed in liver regions, whereas in tumor lesions, SUVmax, SUV mean, and SUVpeak of PET-MR were significantly underestimated ($p < 0.001$) in both VOI40 and VOI50. Among volume metrics, there was no statistical difference observed except TLG on VOI50 ($p = 0.03$). Correlation between PET-CT and PET-MR of each metrics were calculated. There was a moderate correlation of the liver SUV and SUL metrics ($r = 0.63$–0.78). In tumor lesions, SUVmax and SUVmean had a stronger correlation with underestimation in PET-MR on VOI 40 (SUVmax and SUVmean; $r = 0.92$ and 0.91 with slope = 0.71 and 0.72, respectively). In the evaluation of MTV and TLG, the stronger correlations were observed both on VOI40 (MTV and TLG; $r = 0.75$ and 0.92) and VOI50 (MTV and TLG; $r = 0.88$ and 0.95) between PET-CT and PET-MR.

Conclusion: PET metrics on TOF-PET-MR showed a good correlation with that of TOF-PET-CT. SUVmax and SUVpeak of tumor lesions were underestimated by 16% on PET-MRI. MTV with % threshold can be regarded as identical volumetric markers for both TOF-PET-CT and TOF-PET-MR.

Keywords: PET/MR, PET/CT, reproducibility, metabolic tumor volume, FDG-F production 18, TOF (time-of-flight), SUV

INTRODUCTION

18F-fluorodeoxyglucose (FDG) positron emission tomography (PET) is used routinely in the diagnosis, staging, restaging, and treatment monitoring of various cancers (1). The maximum standardized uptake value (SUVmax) remains the main uptake measurement parameters of tumors, owing to its simplicity and high reproducibility. In order to achieve a more detailed assessment of tumor characteristics, recent studies have focused on demonstrating the prognostic value of positron emission tomography (PET)-based volumetric parameters, such as metabolic tumor volume (MTV) and total lesion glycolysis (TLG) (2–6). MTV is defined as the sum of the volume of voxels, and TLG is the product of the MTV and SUVmean. These indicators can be used for prognostication as they reflect the activity of glucose metabolism in the entire tumor compared to SUVmax which only reflects a single voxel value.

Following the success of the positron emission tomography and computed tomography (PET-CT) system, integrated PET and magnetic resonance (PET-MR) systems have been clinically introduced and the number of these scanners is gradually increasing worldwide (7–10). In clinical or research settings, several PET machines were used for identical clinical and research purposes. In such a situation, reproducibility among scanners remains an issue to be solved (11, 12). Especially on PET-MR, the error derived from the attenuation correction based on MRI (MRAC) impairs its reproducibility (13–23). Several studies have been conducted to assess the impact of this impairment. In these studies, the metrics of max, mean, or peak SUVs were mainly evaluated (24–26); however, the studies on the correlations of MTV and TLG between PET-CT and PET-MR are still very limited (27–31). Specifically, in the case of time-of-flight (TOF)-PET-MR instruments, no study has evaluated the volumetric parameters. In these machines, the effect of the MRAC error is reduced by TOF-reconstruction (32–34).

In this study, we aimed to determine the TOF-PET-CT and TOF-PET-MR reproducibility of FDG PET-SUV measurements, including volumetric metrics obtained by PET-CT and PET-MR examinations performed on the same day in oncologic patients.

MATERIALS AND METHODS

Ethical Statement

Patients were enrolled in this retrospective study as part of a larger prospective study (NCT02316431). All patients provided written informed consent prior to their inclusion in the study.

Study Subjects

Eighty consecutive patients with different oncologic disease underwent 18F-FDG PET-CT and 18F-FDG PET-MR. All examinations were performed on the same day with a single injection of FDG. The inclusion criteria called for patients with visible tumors both on PET-CT and PET-MR. The scan interval between both examinations was <70 min. A sufficient tracer activity was maintained to generate PET images on PET-MR equivalent to a 70% dose of PET-CT (35).

Image Acquisition

PET-CT acquisition followed a standard protocol for clinical oncologic imaging on a TOF-PET-CT scanner (Discovery 690; GE Healthcare, Waukesha, Wisconsin, USA) (12). The whole-body PET data were acquired in 3D TOF mode with a scan duration of 2 min per bed position, an axial FOV of 153 mm, and 23% overlap of bed positions—resulting in a total PET acquisition time of 16–20 min. Standard CT was acquired for diagnostic purposes and CT attenuation correction (CTAC).

For the PET-MR imaging examination, we used a simultaneous TOF-PET-MR system, which comprised a 3.0-T whole-body MR imaging system and SiPM PET detectors (SIGNA PET-MR; GE Healthcare, Waukesha, Wisconsin, USA). Whole-body list-mode PET data were acquired in 3D TOF mode with a scan duration of 2–4 min per bed position. The scan time per bed position depended on the imaging protocol selected according to clinical indication. An axial FOV of 250 mm and a 24% overlap of bed positions were used, resulting in a total PET acquisition time of 12–24 min. During PET-MR imaging, a 3D liver acquisition with volume acquisition (LAVA Flex) T1-weighted pulse sequence (repetition time—∼4 ms; echo time—2.23 ms; flip angle—5°; section thickness—5.2 mm with 2.6 mm overlap; 120 sections; pixel size—1.95 × 1.95 mm^2, partial Fourier—70.3%; and acquisition time—18 s per bed position) was acquired for MRAC (33, 36). Additionally, different anatomic MR pulse sequences were also used for diagnostic imaging.

Imaging Reconstruction

The reconstruction parameters of PET images on PET-CT and PET-MR were selected to be as similar as possible. The detailed parameters were described elsewhere (35). In PET-CT, a fully 3D OSEM iterative reconstruction, including PSF compensation with three iterations and 18 subsets and a 256 × 256 image grid (2.73 × 2.73 × 3.27-mm voxels), was used. In PET-MR imaging, OSEM, including PSF compensation with three iterations and 16 subsets, and a 256 × 256 image grid (2.34 × 2.34 × 2.78-mm voxels), was used for reconstruction of the PET images. In both systems, transaxial post-reconstruction Gaussian filter

4 mm, axial filter 1:4:1, normalization, random, scatter, dead-time and decay correction were applied. The parameters of PET-CT had been fixed as clinical scan. The minor difference of parameters between both scanners were due to the restriction by the vendor. We could not choose the parameter freely but one out of several options. Both PET image datasets were generated by TOF calculation. CTAC was used to generate PET on PET-CT and MRAC for PET on PET-MR. To compensate for the difference in sensitivity between the two scanners derived from SiPM detectors on PET-MR, we retrospectively un-listed the list mode PET data on PET-MR and generated 70% simulated-dose PET-MR images comparable to PET-CT (35).

Imaging Analysis

We extracted normal liver regions and oncologic lesions for further evaluation. As normal liver regions, the liver mean SUV (SUVmean) normalized to lean body mass (SULmean) was measured. These values have been proposed as a quality control measure for FDG PET-CT in solid tumors (PERCIST) 2.0 (12). A VOI with a diameter of 3 cm was manually drawn on the right lobe of the liver to analyze the concordance between PET-CT and PET-MR.

As target lesions, a maximum of three tumors were extracted per each of the four body parts (head and neck, chest, upper abdomen, and pelvis) by two independent board-certified radiologists (T.S and B.F). Tumors larger than 25 mL were excluded to maintain stability in the statistical analysis. We also excluded target lesions that could not reliably be delineated from physiological uptake (such as the heart, kidney, and bladder).

The volume-of-interest (VOI) was defined by manually drawing polygonal VOIs to enclose the entire tumor with sufficient margins on every slice where the target tumor was seen. Physiological uptake was carefully avoided. In this study, we used the fixed 40 and 50% to SUVmax threshold method (VOI40 and VOI50, respectively), which is a procedure for defining the area of the tumor as a region with a higher SUV than a certain percentage of the SUVmax within the tumor (12).

We used PMOD (version 4.0; PMOD Inc., Zurich, Switzerland) for VOI segmentation and calculation of SUVmax, SUVpeak, SUVmean, MTV, and TLG. VOIs below 1 mL were excluded for the static of peak (37).

Statistical Analysis

We performed the Kolmogorov–Smirnov test for the continuous variables. The values of liver SUV and SUL were normally distributed and listed as mean ± standard deviation. The values of tumor SUV were not normally distributed and listed as median and interquartile range (IQR). To clarify the difference in PET metrics between the two scanners, we performed a paired *t*-test for normally distributed variables and Wilcoxon signed-rank test for not normally distributed variables, respectively. In order to prove the correlation between the two scanners, Pearson's test was performed for these metrics as well. To visualize the deviation of the difference, Bland–Altman plots with limits of agreement were generated (38). Statistical significance was set at $p < 0.05$. Statistical analyses were performed using SPSS Statistics, version 19.0.0 (IBM, Armonk, NY, USA).

TABLE 1 | Demographic and clinical data.

Age in years, mean ± SD (range)	63.1 ± 10.7 (40–84)
Body height in meters, mean ± SD (range)	1.7 ± 0.1 (1.49–1.9)
Body weight in kilograms, mean ± SD (range)	71.7 ± 15.2 (44–110)
BMI, mean ± SD (range)	24.5 ± 4.1 (17.4–32.7)
Injected dose in MBq/kg, mean ± SD (range)	3.20 ± 0.30 (2.84–4.07)
Gender (*n*)	
Male	22
Female	13
Clinical indication (*n*)	
Head and neck cancer	9
Lung cancer	8
Pancreatic cancer	3
Breast cancer	2
Esophageal cancer	2
Rectal cancer	2
Cancer of unknown primary	2
Malignant lymphoma	2
Colon cancer	2
Intrahepatic cholangiocarcinoma	1
Multiple myeloma	1
Malignant melanoma	1
PET-MR images acquired after injection in minutes, mean ± SD (range)	75 ± 12 (46–104)
PET-CT images acquired after injection in minutes, mean ± SD (range)	63 ± 26 (37–144)
Scan interval (PET-MR minus PET-CT) (min), mean ± SD (range)	−12 ± 32 (−54–68)

RESULTS

A total of 35 patients with 80 tumor lesions were included. The detailed information is given in **Table 1**. The mean and standard deviation of each metric on both PET-CT and PET-MR is given in **Table 2**. There was no statistical difference observed in the liver regions, whereas the tumor SUVmax, and SUVpeak of PET-MR were significantly underestimated ($p < 0.001$). Among volume metrics consisting of MTV and TLG, there was no statistical difference observed except for the TLG of VOI50 ($p = 0.03$). The correlation analysis between PET-CT and PET-MR is given in **Table 3**. The correlation of the liver SUVs and SULs was moderate ($r = 0.63$–0.78) (**Figures 1A–D**). In tumor lesions, SUVmax, SUVmean, and SUVpeak were strongly correlated with an underestimation on PET-MR ($r = 0.92$, 0.91, and 0.95, respectively; slope = 0.71, 0.72, and 0.79, respectively) (**Figures 2A–D**). For MTV and TLG, high correlations were observed with slightly better results on VOI50 compared to VOI40 (0.88 and 0.95 vs. 0.75 and 0.92, respectively) (**Figures 3A–D**). The results of the Bland-Altman analysis are presented in **Table 4**. Mean differences of all measurements were negative except MTV in VOI40 and

TABLE 2 | Details of SUV measurements in liver and tumor lesions.

			PET-CT mean ± SD	PET-MR mean ± SD	*P* (paired *t*-test)
Liver		SUVmax	3.63 ± 0.70	3.48 ± 0.84	0.17
		SUVmean	2.21 ± 0.35	2.13 ± 0.47	0.14
		SULmax	2.74 ± 0.44	2.64 ± 0.61	0.22
		SULmean	1.67 ± 0.20	1.61 ± 0.30	0.16
			PET-CT median ± IQR	**PET-MR median ± IQR**	**(Wilcoxon signed-rank test)**
Tumor lesion	VOI40	SUVmax	9.54 (6.32–14.09)	8.23 (5.62–12.18)	<0.001
		SUVpeak	6.11 (3.80–9.24)	4.98 (3.44–7.92)	<0.001
		SUVmean	5.92 (4.09–8.57)	5.07 (3.52–7.31)	<0.001
		MTV	2.30 (0.78–6.15)	2.34 (0.92–5.97)	0.850
		TLG	15.35 (4.07–31.38)	12.42 (4.07–38.60)	0.002
		SUVmean	6.57 (4.94–9.38)	5.60 (4.04–8.13)	<0.001
	VOI50	MTV	1.42 (0.45–2.87)	1.50 (0.59–3.43)	0.694
		TLG	9.54 (2.80–21.75)	8.10 (2.67–23.02)	0.002

TABLE 3 | The result of linear regression analysis where x-axis is PET/MR measurements and y-axis is PET/CT measurements.

			Slope	Intercept	*r*
Liver		SUVmax	0.83	0.45	0.69
		SUVmean	1.05	−0.19	0.78
		SULmax	0.89	0.21	0.63
		SULmean	0.99	−0.04	0.64
Tumor lesion	VOI40	SUV max	0.71	1.48	0.92
		SUVpeak	0.80	0.35	0.94
		SUVmean	0.72	0.87	0.91
		MTV	0.92	0.68	0.75
		TLG	0.85	1.24	0.92
	VOI50	SUVmean	0.71	0.95	0.93
		MTV	0.90	0.35	0.88
		TLG	0.84	0.98	0.95

VOI50 (**Figures 1E–H**, **2E–H**, **3E–H**). The representative cases are shown in **Figures 4**, **5**.

DISCUSSION

This study demonstrated that SUV measurements correlate well between PET-MR and PET-CT. SUVmax and SUVmean of the reference area, liver regions, were not under- or overestimated on PET-MR. However, the SUVmax, SUVpeak, and SUVmean of tumor lesions were underestimated by ∼16%. Fortunately, MTV was maintained between both scanners.

There are notable strengths to the current study. First, we evaluated the reproducibility of volume metrics between PET-CT and PET-MR, which was evaluated only by the sole previous study where non-TOF-PET-MR machines were used (27). TOF-reconstruction clearly compensates for the error from the MRAC (32, 33). For this reason, their results cannot be transferred to a TOF-PET-MR machine, but separate analysis is required. Second, the scan order, PET-MR following or followed by PET-CT, was randomly in our study. Delayed uptake is a critical issue when comparing the reproducibility (39). Third, we generated PET images on PET-MR equivalent to a 70% dose of PET-CT. The higher sensitivity of SiPM detectors or novel reconstruction techniques can influence PET metrics (40, 41). For a fair comparison regardless of detector sensitivity, we developed the current study design.

Although the extent of the difference was within the limit of repeatability (i.e., 25%) (42), a significant underestimation of several parameters was observed on PET-MR. The underestimation of SUVmax, mean, and peak is expected to be derived from two factors. One is that incomplete

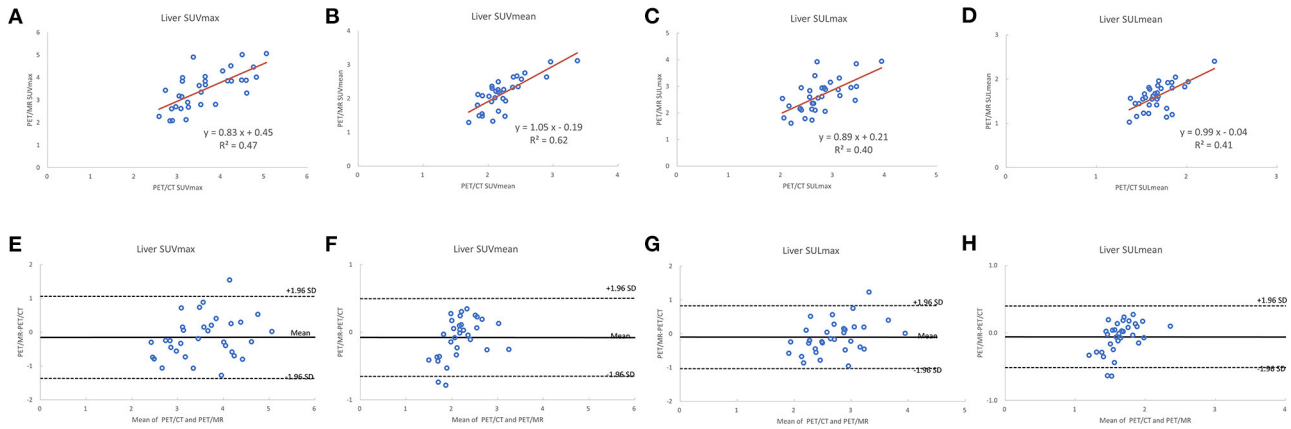

FIGURE 1 | Scatter diagram with regression line and Bland-Altman plots of PET-CT and PET-MR for SUVmax and SUVmean corrected to body weight **(A,B,E,F)** and lean body mass **(C,D,G,H)**.

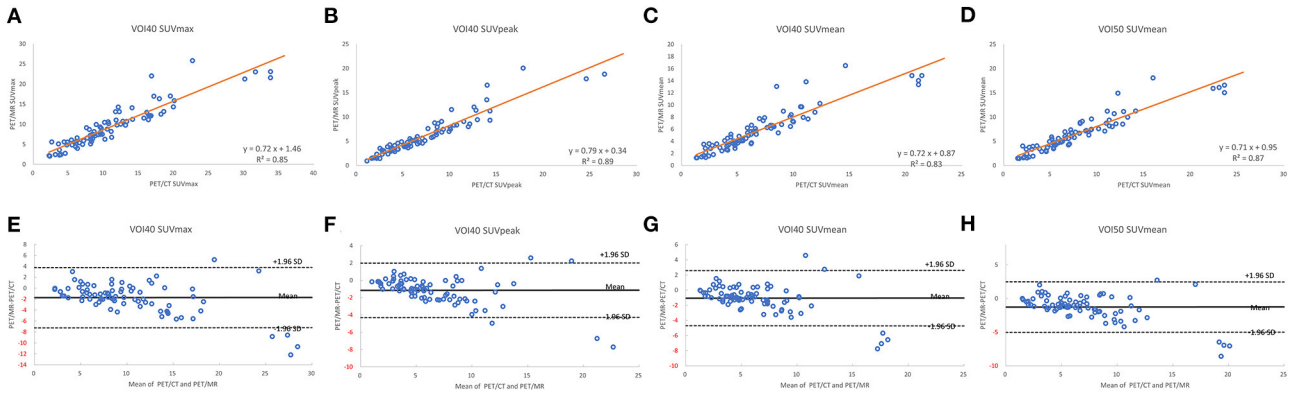

FIGURE 2 | Scatter diagram with regression line and Bland-Altman plots of PET-CT and PET-MR for SUVmax **(A,E)**, SUVpeak **(B,F)**, and SUVmean **(C,G)** of VOI40 and SUVmean of VOI50 **(D,H)**.

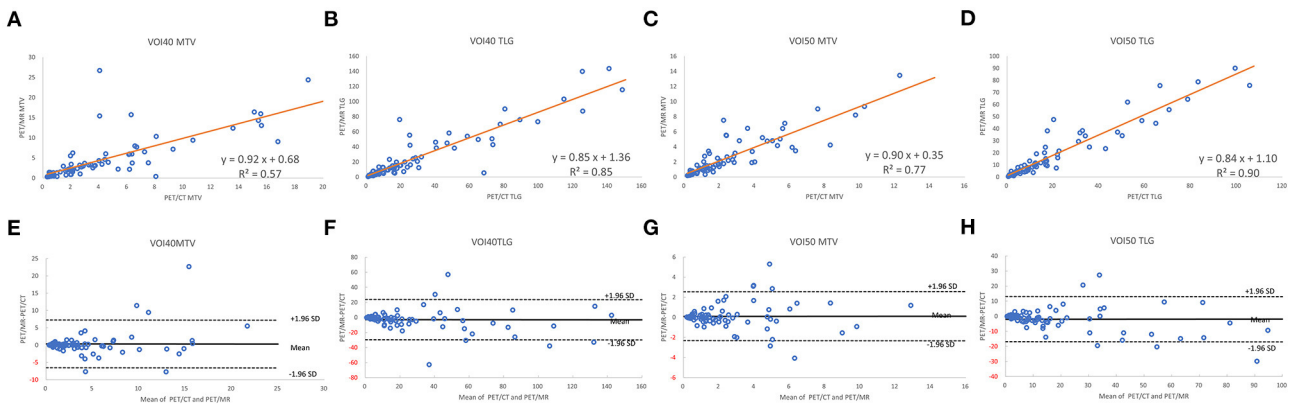

FIGURE 3 | Scatter diagram with regression line and Bland-Altman plots of PET-CT and PET-MR for MTV and TLG of VOI40 **(A,B,E,F)** and VOI50 **(C,D,G,H)**.

MRAC based on 4-compartment models which consist of air, lung, fat, and soft tissue. Neglecting bone tissues causes an underestimation of SUV uptake more than 10% (13, 43). The incorrect estimation of bone tissue AC correction factors affect mostly PET signal quantification or other regions proximity to bone and this effect becomes negligible for regions at a

TABLE 4 | The result of Bland-Altman analysis of SUV measurements between PET/CT and PET/MR.

			Mean difference (PET-MR – PET-CT)	Limits of agreement	
				Lower	Upper
Liver		SUVmax	−0.15 ± 0.62	−1.37	1.06
		SUVmean	−0.08 ± 029	−0.65	0.50
		SULmax	−0.10 ± 048	−1.03	0.83
		SULmean	−0.06 ± 023	−0.51	0.40
Tumor lesion	VOI40	SUVmax	−1.71 ± 2.83	−7.22	3.80
		SUVpeak	−1.25 ± 1.76	−4.69	2.19
		SUVmean	−1.06 ± 1.87	−4.71	2.59
		MTV	0.35 ± 3.55	−6.57	7.27
		TLG	−2.94 ± 13.75	−29.76	23.88
	VOI50	SUVmean	−1.26 ± 1.92	−5.00	2.48
		MTV	0.11 ± 1.25	−2.33	2.55
		TLG	−1.86 ± 7.70	−16.88	13.15

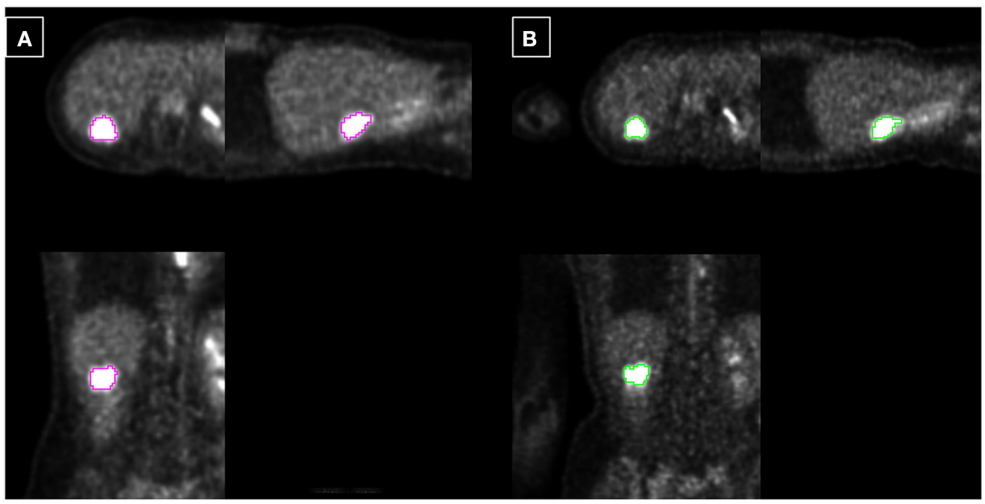

FIGURE 4 | Example 1: 40-year-old female with liver metastasis of breast cancer. Each PET-CT **(A)** and PET-MR **(B)** was acquired 72 and 115 min after injection. The tumor is delineated based on fixed 40% threshold to SUVmax.

larger distance from bone tissues. This might explain why the SUV metrics of the liver were not statistically different between the two scanners. Around the liver, there is no solid bone except for the thin rib bone, which results in maintaining the accuracy of attenuation correction. It may cause secondary critical problems in the calculation of the tumor/liver ratio or tumor delineation from the uptake of the liver. To improve upon the insufficiency of MRAC, model-based bone imposition (44), bone estimation using ZTE/UTE MRI (45, 46), and deep-learning methods (45) have been proposed. In addition, dual-tracer approach where one of the tracers is that of interest and the other may be 18F Sodium Fluoride, NaF, from which the bone can be segmented (20). However, other than the model-based methods, an implementation into clinical scans has yet to occur. Another factor is that the reconstruction parameters were set to be as similar as possible, but were not identical for both scanners. The reason is that scanner software restricted users tune parameters freely (e.g., voxel resolution).

Compared to the previous MTV-reproducibility research by Groshar et al. (27), the bias of MTV in the current study was smaller (3.0 vs. 27.3%); this may be because we had a smaller scan interval (−12 ± 32 min in the current study vs. 53 ± 17 min in the previous study). In contrast, the 95% limits of agreement had a larger range (−96.5 and 102.5 vs. −41.7 to 96.2%). This might be owing to our inclusion criteria. Whereas the previous study included extremely large tumors (> 150 mL), we chose to exclude tumors larger than 25 mL to maintain statistical stability. Four previous studies evaluated the reproducibility between TOF-PET-CT and TOF-PET-MR using the same commercial scanner, GE SIGNA-PET-MR; however, none of these studies performed a truly "fair"

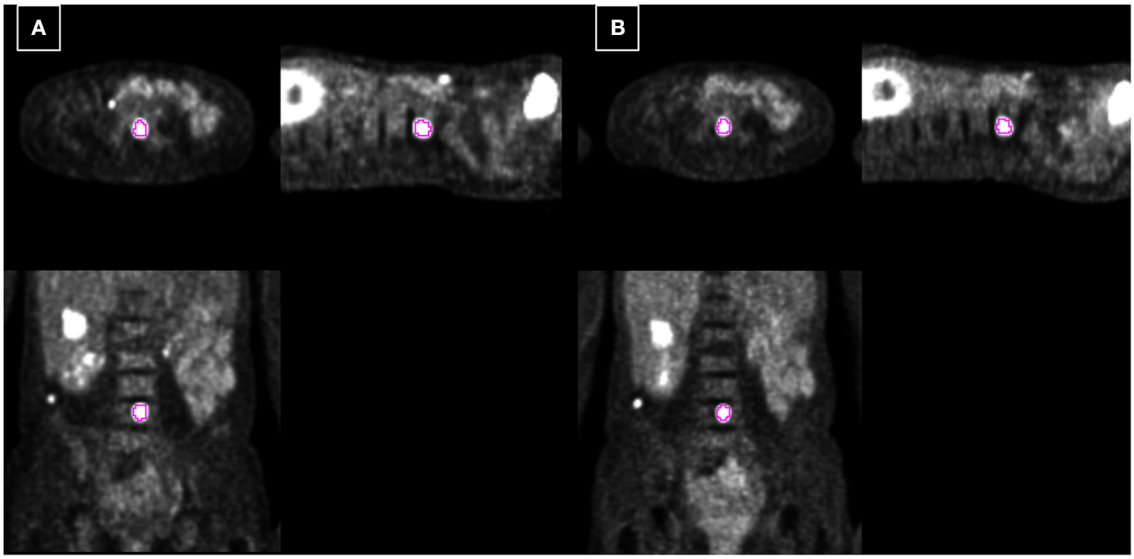

FIGURE 5 | Example 2: 54-year-old female with spine metastasis of melanoma. Each PET-CT **(A)** and PET-MR **(B)** was acquired 73 and 48 min after injection. The tumor is delineated based on fixed 40% threshold to SUVmax.

comparison between the two scanners in terms of a fixed scan order (i.e., PET-CT following or followed by PET-MR) with a long scan interval (e.g., more than 80 min) (25, 47–49). Our study represents the first report using a random sequence of PET-CT and PET-MR acquisition, with a comparably short scan interval.

Based on our results, the SUVmax or SUVpeak metrics should be carefully considered when both PET-CT and PET-MR machines are used in follow-up or multi-center studies (50). Unlike SUVmax, SUVmean, or SUVpeak, there was no statistical difference in MTV between the two scanners. One can speculate that the tumor volume was determined by the ratio of maximum uptake and the SUV on the edge of the delineation. Therefore, if the tumor is uniformly underestimated by MRAC, the MTV does not change.

Our study has a few limitations. First, we used the 70%dose un-list PET-MR, hence evaluated data may differ from clinical data. However, the purpose of this study was to perform a fair comparison of PET-CT and PET-MR, regardless of detector sensitivity or advanced reconstruction techniques. Second, both the scan time and scan interval of PET-CT and PET-MR were not uniform. For example, some PET-CT scanned after 144 min, which was quite over from recommended protocol for PET-CT (50–70 min according to PERCIST) (51). In the delayed acquisition, the SUV-increase in tumor and SUV-decrease in benign lesion were expected, as FDG accumulation of tumor has unique characteristic, Warburg Effect, which is different from the characteristic of physiological uptake (52–56). One must consider this limitation when interpreting the current result of each liver and tumor, respectively. This limitation represents an inherent problem for a reproducibility study because repeated injection of tracer is ethically hard to justify. The same-day repeatability ruled out additional sources of quantitative error deriving from patient habitus or the progression/regression of tumors between the two scans. Third, there might be some room to adjust the parameter of PET-MR to PET-CT, although we chose both parameters as same as possible. For further implementation of the current result into clinical research such as multi-center study, the phantom-validation applying multiple reconstruction parameters would be required. In such a case, to achieve harmonization, an automatic and secondary reconstruction of the PET-MR images which match PET-CT images would be practical (50).

CONCLUSION

PET metrics from TOF-PET-MR had good correlation to those from TOF-PET-CT. SUVmax and SUVpeak of tumor lesions were underestimated by 16% on PET-MR. Careful consideration should be paid to the difference of the extent of underestimation between reference tissue (liver) and target tissue (tumor) when semi-quantitative parameters are measured. MTV with a % threshold can be utilized as the identical volumetric markers both on TOF-PET-CT and TOF-PET-MR.

DATA AVAILABILITY STATEMENT

The raw data supporting the conclusions of this article will be made available by the authors, without undue reservation.

ETHICS STATEMENT

The studies involving human participants were reviewed and approved by the Ethics Committee of University Hospital Zurich.

The patients/participants provided their written informed consent to participate in this study.

AUTHOR CONTRIBUTIONS

TS and AT conceived the presented idea, developed the theory, performed the computations, and verified the analytical methods. MH and PV encouraged TS to investigate using this data and supervised the findings of this work. All authors discussed the results and contributed to the final manuscript.

ACKNOWLEDGMENTS

We gratefully acknowledge Kenji Hirata, Department of Diagnostic Imaging, Graduate School of Medicine, Hokkaido University, for his advice based on the comprehensive acknowledgment of volume segmentation.

REFERENCES

1. Ben-Haim S, Ell P. 18F-FDG PET and PET/CT in the evaluation of cancer treatment response. *J Nucl Med.* (2009) 50:88–99. doi: 10.2967/jnumed.108.054205
2. Moon SH, Choi JY, Lee HJ, Son Y-I, Baek C-H, Ahn YC, et al. Prognostic value of 18F-FDG PET/CT in patients with squamous cell carcinoma of the tonsil: comparisons of volume-based metabolic parameters. *Head Neck.* (2013) 35:15–22. doi: 10.1002/hed.22904
3. Choi E-S, Ha S-G, Kim H-S, Ha JH, Paeng JC, Han I. Total lesion glycolysis by 18F-FDG PET/CT is a reliable predictor of prognosis in soft-tissue sarcoma. *Eur J Nucl Med Mol Imaging.* (2013) 40:1836–42. doi: 10.1007/s00259-013-2511-y
4. Hyun SH, Ahn HK, Kim H, Ahn M-J, Park K, Ahn YC, et al. Volume-based assessment by 18F-FDG PET/CT predicts survival in patients with stage III non-small-cell lung cancer. *Eur J Nucl Med Mol Imaging.* (2014) 41:50–8. doi: 10.1007/s00259-013-2530-8
5. Lee JW, Cho A, Lee J-H, Yun M, Lee JD, Kim YT, et al. The role of metabolic tumor volume and total lesion glycolysis on 18F-FDG PET/CT in the prognosis of epithelial ovarian cancer. *Eur J Nucl Med Mol Imaging.* (2014) 41:1898–906. doi: 10.1007/s00259-014-2803-x
6. Ogawa S, Itabashi M, Kondo C, Momose M, Sakai S, Kameoka S. Prognostic Value of total lesion glycolysis measured by 18F-FDG-PET/CT in patients with colorectal cancer. *Anticancer Res.* (2015) 35:3495–500. Available online at: https://ar.iiarjournals.org/content/35/6/3495
7. Shao Y, Cherry SR, Farahani K, Meadors K, Siegel S, Silverman RW, et al. Simultaneous PET and MR imaging. *Phys Med Biol.* (1997) 42:1965–70. doi: 10.1088/0031-9155/42/10/010
8. Fendler WP, Czernin J, Herrmann K, Beyer T. Variations in PET/MRI operations: results from an international survey among 39 active sites. *J Nucl Med.* (2016) 57:2016–21. doi: 10.2967/jnumed.116.174169
9. Mayerhoefer ME, Prosch H, Beer L, Tamandl D, Beyer T, Hoeller C, et al. PET/MRI versus PET/CT in oncology: a prospective single-center study of 330 examinations focusing on implications for patient management and cost considerations. *Eur J Nucl Med Mol Imaging.* (2020) 47:51–60. doi: 10.1007/s00259-019-04452-y
10. Delso G, Fürst S, Jakoby B, Ladebeck R, Ganter C, Nekolla SG, et al. Performance measurements of the Siemens mMR integrated whole-body PET/MR scanner. *J Nucl Med.* (2011) 52:1914–22. doi: 10.2967/jnumed.111.092726
11. Quak E, Le Roux P-Y, Hofman MS, Robin P, Bourhis D, Callahan J, et al. Harmonizing FDG PET quantification while maintaining optimal lesion detection: prospective multicentre validation in 517 oncology patients. *Eur J Nucl Med Mol Imaging.* (2015) 42:2072–82. doi: 10.1007/s00259-015-3128-0
12. Boellaard R, Delgado-Bolton R, Oyen WJG, Giammarile F, Tatsch K, Eschner W. et al. FDG PET/CT: EANM procedure guidelines for tumour imaging: version 20. *Eur J Nucl Med Mol Imaging.* (2015) 42:328–54. doi: 10.1007/s00259-014-2961-x
13. Samarin A, Burger C, Wollenweber SD, Crook DW, Burger IA, Schmid DT, et al. PET/MR imaging of bone lesions–implications for PET quantification from imperfect attenuation correction. *Eur J Nucl Med Mol Imaging.* (2012) 39:1154–60. doi: 10.1007/s00259-012-2113-0
14. Robson PM, Kaufman A, Pruzan A, Dweck MR, Trivieri M-G, Abgral R, et al. Scan-rescan measurement repeatability of 18F-FDG PET/MR imaging of vascular inflammation. *J Nucl Cardiol.* (2021) doi: 10.1007/s12350-021-02627-5. [Epub ahead of print].
15. Robson PM, Vergani V, Benkert T, Trivieri MG, Karakatsanis NA, Abgral R, et al. Assessing the qualitative and quantitative impacts of simple two-class vs multiple tissue-class MR-based attenuation correction for cardiac PET/MR. *J Nucl Cardiol.* (2021) 28:2194–204. doi: 10.1007/s12350-019-02002-5
16. Akbarzadeh A, Ay MR, Ahmadian A, Alam NR, Zaidi H. MRI-guided attenuation correction in whole-body PET/MR: assessment of the effect of bone attenuation. *Ann Nucl Med.* (2013) 27:152–62. doi: 10.1007/s12149-012-0667-3
17. Dong X, Lei Y, Wang T, Higgins K, Liu T, Curran WJ, et al. Deep learning-based attenuation correction in the absence of structural information for whole-body positron emission tomography imaging. *Phys Med Biol.* (2020) 65:055011. doi: 10.1088/1361-6560/ab652c
18. Torrado-Carvajal A, Vera-Olmos J, Izquierdo-Garcia D, Catalano OA, Morales MA, Margolin J, et al. Dixon-VIBE Deep Learning (DIVIDE) pseudo-CT synthesis for pelvis PET/MR attenuation correction. *J Nucl Med.* (2019) 60:429–35. doi: 10.2967/jnumed.118.209288
19. Liu F, Jang H, Kijowski R, Bradshaw T, McMillan AB. Deep learning MR imaging-based attenuation correction for PET/MR imaging. *Radiology.* (2018) 286:676–84. doi: 10.1148/radiol.2017170700
20. Karakatsanis NA, Abgral R, Trivieri MG, Dweck MR, Robson PM, Calcagno C, et al. Hybrid PET- and MR-driven attenuation correction for enhanced 18F-NaF and 18F-FDG quantification in cardiovascular PET/MR imaging. *J Nucl Cardiol.* (2020) 27:1126–41. doi: 10.1007/s12350-019-01928-0
21. Paulus DH, Quick HH, Geppert C, Fenchel M, Zhan Y, Hermosillo G, et al. Whole-body PET/MR imaging: quantitative evaluation of a novel model-based MR attenuation correction method including bone. *J Nucl Med.* (2015) 56:1061–6. doi: 10.2967/jnumed.115.156000
22. Burgos N, Jorge Cardoso M, Thielemans K, Modat M, Pedemonte S, Dickson J, et al. Attenuation correction synthesis for hybrid PET-MR scanners: application to brain studies. *IEEE Trans Med Imaging.* (2014) 33:2332–41. doi: 10.1109/TMI.2014.2340135
23. Martinez-Möller A, Souvatzoglou M, Delso G, Bundschuh RA. Chefd'hotel C, Ziegler SI, et al. Tissue classification as a potential approach for attenuation correction in whole-body PET/MRI: evaluation with PET/CT data *J Nucl Med.* (2009) 50:520–6. doi: 10.2967/jnumed.108.054726
24. Afaq A, Fraioli F, Sidhu H, Wan S, Punwani S, Chen S-H, et al. Comparison of PET/MRI With PET/CT in the evaluation of disease status in lymphoma. *Clin Nucl Med.* (2017) 42:e1–7. doi: 10.1097/RLU.0000000000001344
25. Iagaru A, Mittra E, Minamimoto R, Jamali M, Levin C, Quon A, et al. Simultaneous whole-body time-of-flight 18F-FDG PET/MRI: a pilot study comparing SUVmax with PET/CT and assessment of MR image quality. *Clin Nucl Med.* (2015) 40:1–8. doi: 10.1097/RLU.0000000000000611
26. Drzezga A, Souvatzoglou M, Eiber M, Beer AJ, Fürst S, Martinez-Möller A, et al. First clinical experience with integrated whole-body PET/MR: comparison to PET/CT in patients with oncologic diagnoses. *J Nucl Med.* (2012) 53:845–55. doi: 10.2967/jnumed.111.098608
27. Groshar D, Bernstine H, Goldberg N, Nidam M, Stein D, Abadi-Korek I, et al. Reproducibility and repeatability of same-day two sequential FDG PET/MR and PET/CT. *Cancer Imaging.* (2017) 17:11. doi: 10.1186/s40644-017-0113-9
28. Tuli A, Ayache JB, Parekh S, Thamnirat K, Chari A. Comparison of sequential PET/CT and PET/MR in previously treated multiple myeloma patients. *J Nucl Med.* (2017) 58:187. Available online at: https://jnm.snmjournals.org/content/58/supplement_1/187.short

29. Virarkar M, Ganeshan D, Gulati AT, Palmquist S, Iyer R, Bhosale P. Diagnostic performance of PET/CT and PET/MR in the management of ovarian carcinoma—a literature review. *Abdom Radiol.* (2021) 46:2323–49. doi: 10.1007/s00261-020-02847-2
30. Gao J, Huang X, Meng H, Zhang M, Zhang X, Lin X, et al. Performance of multiparametric functional imaging and texture analysis in predicting synchronous metastatic disease in pancreatic ductal adenocarcinoma patients by hybrid PET/MR: initial experience. *Front Oncol.* (2020) 10:198. doi: 10.3389/fonc.2020.00198
31. Rasmussen JH, Fischer BM, Aznar MC, Hansen AE, Vogelius IR, Löfgren J, et al. Reproducibility of (18)F-FDG PET uptake measurements in head and neck squamous cell carcinoma on both PET/CT and PET/MR. *Br J Radiol.* (2015) 88:20140655. doi: 10.1259/bjr.20140655
32. Sekine T, Burgos N, Warnock G, Huellner M, Buck A, Ter Voert EEGW, et al. Multi-atlas-based attenuation correction for brain 18F-FDG PET imaging using a time-of-flight PET/mr scanner: comparison with clinical single-atlas- and CT-based attenuation correction. *J Nucl Med.* (2016) 57:1258–64. doi: 10.2967/jnumed.115.169045
33. Davison H. ter Voert EEGW, de Galiza Barbosa F, Veit-Haibach P, Delso G. Incorporation of time-of-flight information reduces metal artifacts in simultaneous positron emission tomography/magnetic resonance imaging: a simulation study. *Invest Radiol.* (2015) 50:423–9. doi: 10.1097/RLI.0000000000000146
34. Mehranian A, Zaidi H. Impact of time-of-flight PET on quantification errors in MR imaging-based attenuation correction. *J Nucl Med.* (2015) 56:635–41. doi: 10.2967/jnumed.114.148817
35. Sekine T, Delso G, Zeimpekis KG, de Galiza Barbosa F, Ter Voert EEGW, Huellner M. eet al. Reduction of 18F-FDG dose in clinical PET/MR imaging by using silicon photomultiplier detectors. *Radiology.* (2018) 286:249–59. doi: 10.1148/radiol.2017162305
36. Wollenweber SD, Ambwani S, Lonn AHR, Shanbhag DD, Thiruvenkadam S, Kaushik S, et al. "Comparison of 4-class and continuous fat/water methods for whole-body, MR-based PET attenuation correction," in *2012 IEEE Nuclear Science Symposium and Medical Imaging Conference Record (NSS/MIC)* (Anaheim, CA), 3019–25. doi: 10.1109/NSSMIC.2012.6551690
37. Boktor RR, Walker G, Stacey R, Gledhill S, Pitman AG. Reference range for intrapatient variability in blood-pool and liver SUV for 18F-FDG PET. *J Nucl Med.* (2013) 54:677–82. doi: 10.2967/jnumed.112.108530
38. Giavarina D. Understanding bland altman analysis. *Biochem Med.* (2015) 25:141–51. doi: 10.11613/BM.2015.015
39. Kitao T, Hirata K, Shima K, Hayashi T, Sekizawa M, Takei T, et al. Reproducibility and uptake time dependency of volume-based parameters on FDG-PET for lung cancer. *BMC Cancer.* (2016) 16:576. doi: 10.1186/s12885-016-2624-3
40. Orlhac F, Boughdad S, Philippe C, Stalla-Bourdillon H, Nioche C, Champion L, et al. A Postreconstruction harmonization method for multicenter radiomic studies in PET. *J Nucl Med.* (2018) 59:1321–8. doi: 10.2967/jnumed.117.199935
41. Sah B-R, Stolzmann P, Delso G, Wollenweber SD, Hüllner M, Hakami YA, et al. Clinical evaluation of a block sequential regularized expectation maximization reconstruction algorithm in 18F-FDG PET/CT studies. *Nucl Med Commun.* (2017) 38:57–66. doi: 10.1097/MNM.0000000000000604
42. de Langen AJ, Vincent A, Velasquez LM, van Tinteren H, Boellaard R, Shankar LK, et al. Repeatability of 18F-FDG uptake measurements in tumors: a metaanalysis. *J Nucl Med.* (2012) 53:701–8. doi: 10.2967/jnumed.111.095299
43. Andersen FL, Ladefoged CN, Beyer T, Keller SH, Hansen AE, Højgaard L, et al. Combined PET/MR imaging in neurology: MR-based attenuation correction implies a strong spatial bias when ignoring bone. *Neuroimage.* (2014) 84:206–16. doi: 10.1016/j.neuroimage.2013.08.042
44. Oehmigen M, Lindemann ME, Gratz M, Kirchner J, Ruhlmann V, Umutlu L, et al. Impact of improved attenuation correction featuring a bone atlas and truncation correction on PET quantification in whole-body PET/MR. *Eur J Nucl Med Mol Imaging.* (2018) 45:642–53. doi: 10.1007/s00259-017-3864-4
45. Leynes AP, Yang J, Wiesinger F, Kaushik SS, Shanbhag DD, Seo Y, et al. Zero-Echo-Time and Dixon Deep Pseudo-CT (ZeDD CT): direct generation of pseudo-CT images for Pelvic PET/MRI attenuation correction using deep convolutional neural networks with multiparametric MRI. *J Nucl Med.* (2018) 59:852–8. doi: 10.2967/jnumed.117.198051
46. Sekine T, Ter Voert EEGW, Warnock G, Buck A, Huellner M, Veit-Haibach P, et al. Clinical evaluation of zero-echo-time attenuation correction for brain 18F-FDG PET/MRI: comparison with atlas attenuation correction. *J Nucl Med.* (2016) 57:1927–32. doi: 10.2967/jnumed.116.175398
47. Minamimoto R, Iagaru A, Jamali M, Holley D, Barkhodari A, Vasanawala S, et al. Conspicuity of malignant lesions on PET/CT and simultaneous time-of-flight PET/MRI. *PLoS One.* (2017) 12:e0167262. doi: 10.1371/journal.pone.0167262
48. Queiroz MA, Delso G, Wollenweber S, Deller T, Zeimpekis K, Huellner M, et al. Dose optimization in TOF-PET/MR compared to TOF-PET/CT. *PLoS One.* (2015) 10:e0128842. doi: 10.1371/journal.pone.0128842
49. Vontobel J, Liga R, Possner M, Clerc OF, Mikulicic F, Veit-Haibach P, et al. MR-based attenuation correction for cardiac FDG PET on a hybrid PET/MRI scanner: comparison with standard CT attenuation correction. *Eur J Nucl Med Mol Imaging.* (2015) 42:1574–80. doi: 10.1007/s00259-015-3089-3
50. Aide N, Lasnon C, Veit-Haibach P, Sera T, Sattler B, Boellaard R. EANM/EARL harmonization strategies in PET quantification: from daily practice to multicentre oncological studies. *Eur J Nucl Med Mol Imaging.* (2017) 44:17–31. doi: 10.1007/s00259-017-3740-2
51. Wahl RL, Jacene H, Kasamon Y, Lodge MA. From RECIST to PERCIST: evolving considerations for PET response criteria in solid tumors. *J Nucl Med.* (2009) 50(Suppl 1):122S—50S. doi: 10.2967/jnumed.108.057307
52. Sanz-Viedma S, Torigian DA, Parsons M, Basu S, Alavi A. Potential clinical utility of dual time point FDG-PET for distinguishing benign from malignant lesions: implications for oncological imaging. *Rev Esp Med Nucl.* (2009) 28:159–66. doi: 10.1016/S0212-6982(09)71360-6
53. Pietrzak AK, Kazmierska J, Marszalek A, Cholewinski W. Evaluation of physiologic and abnormal glucose uptake in palatine tonsils: differential diagnostics with sequential dual-time-point 2-deoxy-2-[18F]FDG PET/CT. *Q J Nucl Med Mol Imaging.* (2020) 64:299–306. doi: 10.23736/S1824-4785.18.03065-0
54. Koppenol WH, Bounds PL, Dang CV. Otto Warburg's contributions to current concepts of cancer metabolism. *Nat Rev Cancer.* (2011) 11:325–37. doi: 10.1038/nrc3038
55. Houshmand S, Salavati A, Segtnan EA, Grupe P, Høilund-Carlsen PF, Alavi A. Dual-time-point imaging and delayed-time-point fluorodeoxyglucose-PET/computed tomography imaging in various clinical settings. *PET Clin.* (2016) 11:65–84. doi: 10.1016/j.cpet.2015.07.003
56. Shimizu K, Okita R, Saisho S, Yukawa T, Maeda A, Nojima Y, et al. Clinical significance of dual-time-point 18F-FDG PET imaging in resectable non-small cell lung cancer. *Ann Nucl Med.* (2015) 29:854–60. doi: 10.1007/s12149-015-1013-3

Conflict of Interest: GD is an employee of GE Healthcare. GW is an employee of Pmod Inc.

The remaining authors declare that the research was conducted in the absence of any commercial or financial relationships that could be construed as a potential conflict of interest.

Publisher's Note: All claims expressed in this article are solely those of the authors and do not necessarily represent those of their affiliated organizations, or those of the publisher, the editors and the reviewers. Any product that may be evaluated in this article, or claim that may be made by its manufacturer, is not guaranteed or endorsed by the publisher.

frontiers in Medicine

ORIGINAL RESEARCH
published: 02 March 2022
doi: 10.3389/fmed.2022.823292

Impact of TOF on Brain PET With Short-Lived ^{11}C-Labeled Tracers Among Suspected Patients With AD/PD: Using Hybrid PET/MRI

D.D.N Wimalarathne[1,2,3†], Weiwei Ruan[1,2†], Xun Sun[1,2], Fang Liu[1,2], Yongkang Gai[1,2], Qingyao Liu[1,2], Fan Hu[1,2] and Xiaoli Lan[1,2]*

[1] Department of Nuclear Medicine, Union Hospital, Tongji Medical College, Huazhong University of Science and Technology, Wuhan, China, [2] Hubei Province Key Laboratory of Molecular Imaging, Union Hospital, Tongji Medical College, Huazhong University of Science and Technology, Wuhan, China, [3] Department of Radiography and Radiotherapy, Faculty of Allied Health Sciences, General Sir John Kotelawala Defence University, Rathmalana, Sri Lanka

OPEN ACCESS

Edited by:
Désirée Deandreis, University of Turin, Italy

Reviewed by:
Maria Mathew D'Souza, Institute of Nuclear Medicine & Allied Sciences (DRDO), India
Kun Zheng, Peking Union Medical College Hospital (CAMS), China

***Correspondence:**
Xiaoli Lan
xiaoli_lan@hust.edu.cn

†These authors have contributed equally to this work

Specialty section:
This article was submitted to Nuclear Medicine, a section of the journal Frontiers in Medicine

Received: *27 November 2021*
Accepted: *12 January 2022*
Published: *02 March 2022*

Citation:
Wimalarathne DDN, Ruan W, Sun X, Liu F, Gai Y, Liu Q, Hu F and Lan X (2022) Impact of TOF on Brain PET With Short-Lived ^{11}C-Labeled Tracers Among Suspected Patients With AD/PD: Using Hybrid PET/MRI. Front. Med. 9:823292. doi: 10.3389/fmed.2022.823292

Objective: To explore the impact of the time-of-flight (TOF) reconstruction on brain PET with short-lived ^{11}C-labeled tracers in PET magnetic resonance (PET/MR) brain images among suspected patients with Alzheimer's and Parkinson's disease (AD/PD).

Methods: Patients who underwent ^{11}C-2-ß-carbomethoxy-3-b-(4-fluorophenyl) tropane (^{11}C-CFT) and 2-(4-N-[^{11}C] methylaminophenyl)-6-hydroxybenzothiazole (^{11}C-PiB) PET/MRI were retrospectively included in the study. Each PET LIST mode data were reconstructed with and without the TOF reconstruction algorithm. Standard uptake values (SUVs) of Caudate Nucleus (CN), Putamen (PU), and Whole-brain (WB) were measured. TOF and non-TOF SUVs were assessed by using paired *t*-test. Standard formulas were applied to measure contrast, signal-to-noise ratio (SNR), and percentage relative average difference of SUVs (%RAD-SUVs).

Results: Total 75 patients were included with the median age (years) and body mass index (BMI-kg/m^2) of 60.2 ± 10.9 years and 23.9 ± 3.7 kg/m^2 in ^{11}C-CFT ($n = 41$) and 62.2 ± 6.8 years and 24.7 ± 2.9 kg/m^2 in ^{11}C-PiB ($n = 34$), respectively. Higher average SUVs and positive %RAD-SUVs were observed in CN and PU in TOF compared with non-TOF reconstructions for the two ^{11}C-labeled radiotracers. Differences of SUV_{mean} were significant ($p < 0.05$) in CN and PU for both ^{11}C-labeled radiotracers. SUV_{max} was enhanced significantly in CN and PU for ^{11}C-CFT and CN for ^{11}C-PiB, but not in PU. Significant contrast enhancement was observed in PU for both ^{11}C-labeled radiotracers, whereas SNR gain was significant in PU, only for ^{11}C-PiB in TOF reconstruction.

Conclusion: Time-of-flight leads to a better signal vs. noise trade-off than non-TOF in ^{11}C-labeled tracers between CN and PU, improving the SUVs, contrast, and SNR, which were valuable for reducing injected radiation dose. Improved timing resolution

aided the rapid decay rate of short-lived ^{11}C-labeled tracers, and it shortened the scan time, increasing the patient comfort, and reducing the motion artifact among patients with AD/PD. However, one should adopt the combined TOF algorithm with caution for the quantitative analysis because it has different effects on the SUV_{max}, contrast, and SNR of different brain regions.

Keywords: time-of-flight, PET/MRI, quantification, SUV, reconstruction, ^{11}C-labeled tracers

INTRODUCTION

Alzheimer's disease (AD) and Parkinson's disease (PD) are the most common neurodegenerative diseases in the elderly. AD is caused due to abnormal build-up of amyloid and tau proteins in and around the neurons which disrupt the function of the neurons by triggering the neuronal damage or eventually dead cells, particularly in the cortex and hippocampus, whereas PD affects predominantly dopaminergic neurons in a specific area in the brain called substantia nigra (1, 2). In the diagnosis of AD/PD or differentiation of mild cognitive impairment (MCI) and AD from normal aging, it is essential to investigate the variations of metabolic activity and characteristic patterns of radiotracers with PET in key brain regions (3–7).

In recent years, the hybrid PET/MRI was developed successfully and has entered clinical practice. The hybrid PET/MRI, like two high-end technologies, can simultaneously obtain images of PET and MRI, which provide excellent anatomic information and functional MRI parameters with the metabolic and molecular information as a one-stop-shop. Therefore, the hybrid PET/MRI has always been used for neurodegenerative diseases, especially showing great potential for differential diagnosis of early AD/PD with some specific PET tracer (8–10). Among a tracer targeted dopamine transporters (DATs) level for early diagnosis of PD is ^{11}C labeled cocaine derivative, i.e., ^{11}C-2-ß-carbomethoxy-3-b-(4-fluorophenyl) tropane (^{11}C-CFT) (8). In the patients with PD, the DATs level will change, and the PET images with ^{11}C-CFT will show the asymmetrical reduction in the caudate nucleus (CN) or putamen (PU). The Pittsburgh compound B, i.e., 2-(4-N-[^{11}C] methylaminophenyl)-6-hydroxybenzothiazole (^{11}C-PiB) is a benzothiazole derivative of thioflavin T that is used to image beta-amyloid deposits in AD (9), and the corresponding PET images with ^{11}C-PiB will show the diffuse uptake in the brain. However, the synthesis and quality control of ^{11}C-CFT and ^{11}C-PiB are complicated processes which are followed by high-performance liquid chromatography (HPLC) purification (9, 10). As well, ^{11}C radioisotope tends to decay fast within a half-life ($\mathbf{T_{1/2}}$) of 20.38 min. In theory $\mathbf{T_{1/2} = 0.693/\lambda}$ where $\boldsymbol{\lambda}$ is the decaying constant and radioactivity (**A**) at a "**t**" time measured by $\mathbf{A = A_0 e^{\lambda t}}$ where $\mathbf{A_0}$is the radioactivity at time zero ($\mathbf{t = 0}$). Accordingly, shorten $T_{1/2}$ tends to decrease the **A** at a given time elapsed. Hence, improvising the PET image acquisition and reconstruction became more important for brain PET with short-lived radiotracers. Uptake time of said ^{11}C-labeled tracers is ∼40–60 min as mentioned in **Table 1,** where after consecutive $2T_{1/2}$ to $3T_{1/2}$ it remains $A_0/4$ to $A_0/8$ of original radioactivity within the body. Thus, it is found challenging to image under a low count field with existing conventional PET scanners (11).

Clinical PET image quality has drastically improved by utilizing several advanced reconstruction techniques, i.e., time-of-flight (TOF) reconstruction technology (12). The TOF system measures and records the time difference of two coincident photons and improves the activity localization by more accurately identifying an annihilation event along a line of response (LOR) (13). Thus, TOF effects on the gain in signal-to-noise ratio (SNR) (14) further, TOF results in a faster and more uniform convergence with three-dimensional (3D) iterative reconstruction (15).

In the past decade, it was proved that larger patients (BMI ≥ 25.0 kg/m^2) are benefitted from the TOF technique (16). Since, TOF reconstruction acts as a weight equalizer, gaining consistent image quality among patients, regardless of weight and size (17). Improved small lesion detection is reported among several TOF PET/MRI studies (18–22). Further improved TOF contributes in the reduction of injected radiation dose to the patient, so as lowering the radiation dose to the medical and general public (23). Budinger et al. elaborated that the TOF sensitivity gain equal to $\mathbf{D/\Delta x}$ (**D** is the object diameter and $\mathbf{\Delta x = (C^*\Delta t/2)}$ where **C** is the speed of the light and $\boldsymbol{\Delta t}$ is the full-width at half-maximum (FWHM) of the timing resolution of the scanner (24). Accordingly, it is proven that TOF gain is inversely proportionate with the time resolution of the PET detector system. The time resolution was significantly improved by the invention of newer embedded semiconductor detectors (e.g., SiPM) for PET by featuring TOF in PET/MR systems (15, 25, 26). Since scan time is reduced while keeping the same image quality (11). Subsequently, TOF vs. brain PET clinical studies were conducted in recent years (27, 28). Yet, to our knowledge, few studies have been conducted to assess the TOF reconstruction techniques for brain PET with short-lived ^{11}C-labeled tracers (29).

This study explored the effects of the TOF reconstruction technique on brain PET quantification with short-lived ^{11}C-CFT and ^{11}C-PiB in hybrid PET/MR brain imaging among suspected patients with AD/PD. Since ^{11}C-PiB showed a diffuse uptake throughout the whole-brain, the quantification evaluation for PET with TOF reconstruction was carried for the whole brain. The ^{11}C-CFT uptake was mainly focused on CN and PU regions. Hence, we evaluated the effect of TOF reconstruction on CN and PU volume of interests (VOIs) for ^{11}C-CFT brain PET, and the effects on CN and PU VOIs for ^{11}C-PiB brain PET were also further evaluated for comparing with the results from ^{11}C-CFT to investigate whether the effects of TOF technique were related with different tracer. The key purpose of this study was

TABLE 1 | Basic information of the patient.

Patient Information	^{11}C-CFT	^{11}C-PiB
Patients included (n)	41	34
Age (y)	60.2 ± 10.9	62.2 ± 6.8
BMI (kg/m^2)	23.9 ± 3.7	24.7 ± 2.9
Injected Dose/Weight (MBq/kg)	3.9 ± 1.4	4.3 ± 1.1
Mean uptake time (min)	54.4 ± 15.9	43.8 ± 19.5

to determine if quantification differences are present in TOF compared with the non-TOF technique among short-lived ^{11}C-labeled radiopharmaceuticals in PET/MRI brain imaging.

METHODS

Ethical Statement

This retrospective experimental study of exploring the effects of the TOF reconstruction technique on brain PET quantification with ^{11}C-CFT and ^{11}C-PiB in hybrid PET/MR brain imaging among suspected patients with AD/PD performed at our institute, which has been approved by the Institutional Review Board of Union Hospital, Tongji Medical College, Huazhong University of Science and Technology. The need for written informed consent was waived.

Subjects

Patients' studies of suspected AD/PD referred for ^{11}C-CFT and ^{11}C-PiB PET/MRI ($n = 75$) were retrieved by an independent data analyst prior to automated standard uptake value (SUV) analysis by using the PNEURO module of PMOD 3.906 software. The corresponding detailed information for the subjects is shown in **Table 1**.

PET/MRI

All acquisitions of patients were performed on a SIGNA TOF-PET/MRI (GE Healthcare, Waukesha, WI, USA) with subsequent specifications: 130 cm × 60 cm × 60 cm bore dimension, 3.0 Tesla superconductive magnet, gradient coils: 44 mT/m peak amplitude, and 200 T/m/s peak slew rate, Detector type: SiPM, TOF (timing resolution for fast TOF performance < 400 ps), Cryogen Type: Liquid Helium. The mean injected radiation dose (MBq/kg) and uptake time (minutes) for the two radiotracers are mentioned in **Table 1**. All patients were asked to void before scanning began. Prior to PET/MRI, patients were given an instruction sheet and an informed consent form to fill and to be submitted. Claustrophobic patients, patients with metal implants, and uncooperative patients were excluded from the investigations. The PET/MR 8-channel brain coil with a mirror was placed on the table on top of the adaptor. Patients were instructed verbally to keep the body aligned 90 degrees to the midsagittal plane in the supine position, hands alongside the trunk, and stay still 10 and 20 min for ^{11}C-CFT and ^{11}C-PiB, respectively. MRI was performed with T1-weighted imaging (3D gradient-echo sequence, flip angle = 12 degrees, time of echo [TE]/time of repetition [TR] = 2.6/6.9 ms, bandwidth = 50 KHz, field of view (FOV) = 24 cm × 24 cm, matrix = 384 ×384) during the ^{11}C-CFT and ^{11}C-PiB PET scanning.

PET Reconstruction

The PET images were reconstructed by using the ordered subsets expectation maximum (OSEM) algorithm with the TOF technique and non-TOF technique, respectively. The other parameters were same as followed: FOV = 30 cm × 30 cm, matrix = 192 × 192, filter cutoff = 3.0 mm, subsets = 28, iterations = 3. Gaussian post-reconstruction filtering with a 3.0 mm full width of half maximum (FWHM) was used to improve the image SNR. In all cases, the PET attenuation correction was atlas-based MRI attenuation correction, combined with Dixon water-fat separation methods (30). The additional corrections to scatter, random events, and dead-time were applied accordingly.

Image Analysis Semi-Quantitative Analysis

Reconstructed images were transferred from the scanner workstation to a data analysis PMOD workstation (PMOD version 3.906 Software, Zurich, Switzerland) for biomedical image quantification in different VOIs in the brain. PMOD-PNEURO Brain VOIs based on the maximum probability atlas (Hammers-N30R83) (31) was used in segmenting brain regions. **Figure 1** gives an analysis example. T1 weighted images were employed for outlining anatomical structures. The selected VOIs of the brain for this study are the CN and PU. Statistics associated with standard uptake value, such as maximum SUV (SUV_{max}), mean SUV (SUV_{mean}), and SD SUV (SUV_{SD}), of each above VOIs with Cerebellar cortex (CC) were calculated in all the ^{11}C-CFT and ^{11}C-PiB brain images.

For the evaluation of image quality among segmented VOIs between reconstruction methods, two metrics were used on each VOI, that is, SNR and contrast. SNR of the segmented VOI was calculated as the difference between the VOI and background compared with the background noise shown in Equation 1.

$$SNR_{VOI} = \frac{Signal - Background}{\sigma_B} \quad (1)$$

Where the signal is defined as the SUV_{mean} value in the segmented VOI, the background is defined as the SUV_{mean} value of the cerebellum cortex VOI and the σ_B (noise) in this formula is defined as the SUV_{SD} value of the background VOI. The use of cerebellum cortex VOI as the background is due to its homogeneous uptake patterns relative to other VOIs in the brain (17, 32–34).

In this work, contrast is defined as a ratio of signal to background.

$$Contrast_{VOI} = \frac{Signal}{Background} \quad (2)$$

Further, to calculate the percentage difference, the TOF values were expressed as a percentage difference from non-TOF values (Equation 3), according to the previous literature (35).

$$\%RAD(SUV_x) = \frac{(SUV_x\ TOF - SUV_x\ nonTOF)^*\ 100\%}{SUV_x\ nonTOF} \quad (3)$$

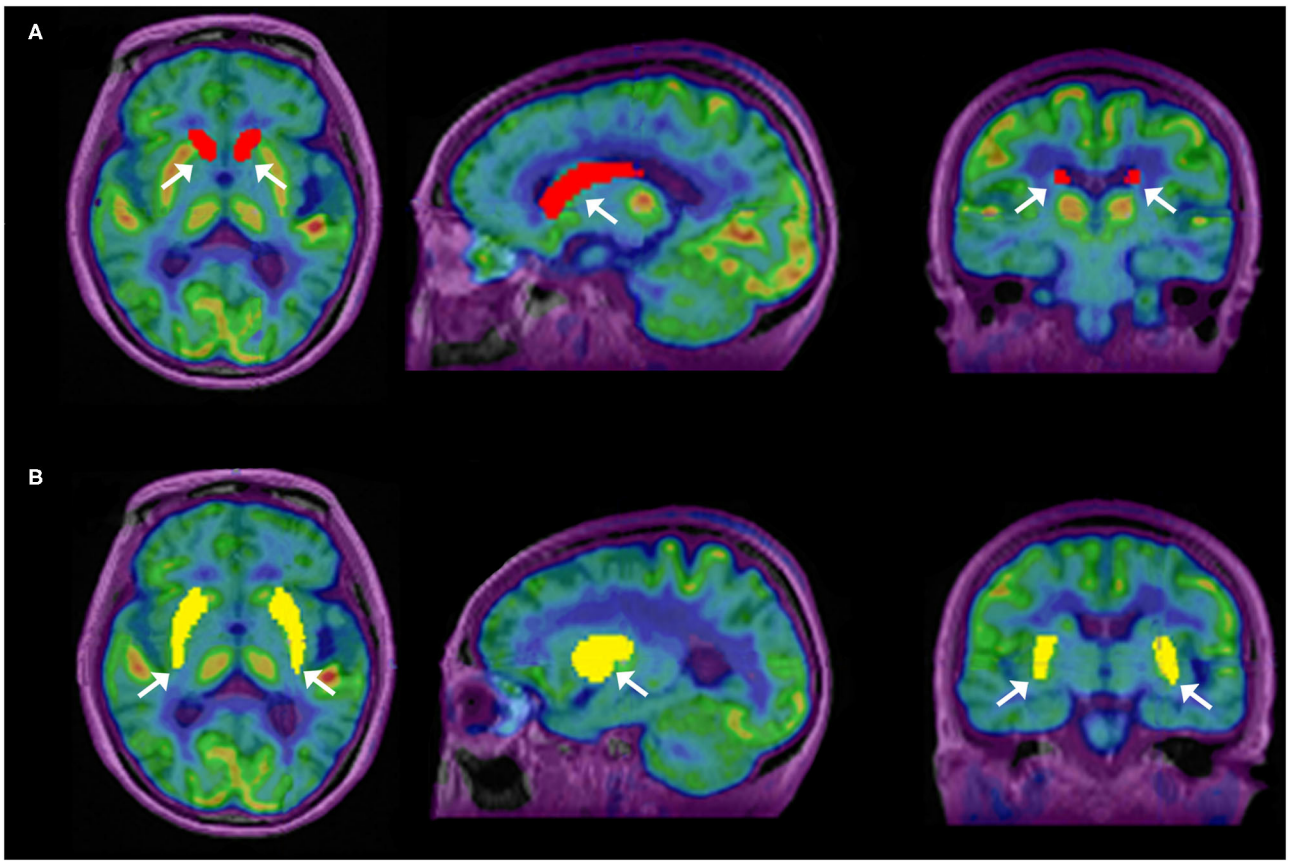

FIGURE 1 | Segmentation of caudate nuclei (CN) and putamen (PU) by using N30R83 atlas in PMOD; **(A)** shows the outlining of CN in sagittal, axial, and coronal planes; **(B)** shows the outlining of PU in sagittal, axial, and coronal planes.

Statistical Analysis

The IBM SPSS version 23.0 software was used to compare the TOF *vs.* non-TOF measurements. The comparisons among the SUVs of different brain regions of TOF *vs.* non-TOF reconstruction methods, TOF-contrast *vs.* non-TOF-contrast, and TOF-SNR *vs.* non-TOF-SNR were analyzed using the paired *t*-test. Before the *t*-test, the data had been tested and the distribution was normality and variance was homogeneous. The value of $p < 0.05$ was considered statistically significant. Box-plots were generated to display the distribution of data.

RESULTS

SUV_{max} and SUV_{mean}

Overall higher average SUV_{max} and SUV_{mean} values were observed among CN, PU regions, and whole brain in TOF compared with non-TOF reconstructions in ^{11}C-CFT, and ^{11}C-PiB brain images (**Figures 2A,B**, **3A,B**). A statistically significant difference ($p \approx 0.000$) was seen only in the CN region for SUV_{max} in TOF (1.293 ± 0.39) compared with non-TOF (1.192 ± 0.34) reconstruction in ^{11}C-PiB, the similar impact was observed for whole-brain $p \approx 0.003$ (1.966 ± 0.47, 1.869 ± 0.51). Statistically significant differences ($p < 0.05$) among both CN: $p \approx 0.000$ (8.339 ± 2.31, 7.533 ± 2.16) and PU: $p \approx 0.004$ (8.341 ± 2.28, 7.742 ± 2.13) regions for SUV_{max} in ^{11}C-CFT were observed. Statistically significant differences ($p < 0.05$) were seen for all the VOIs segmented for SUV_{mean} in TOF compared with non-TOF reconstruction for both ^{11}C-PiB and ^{11}C-CFT (**Table 2).** Though few potential outliers were found for TOF and non-TOF reconstruction in both CN and PU regions for ^{11}C-PiB (**Figure 2B**).

SNR and Contrast

The SNR gain was measured in TOF and non-TOF by Equation 1. Overall all the VOIs with whole-brain showed higher SNR gain in TOF compared with non-TOF reconstruction in ^{11}C-PiB (**Figure 2D**), significant SNR enhancement was observed in PU ($p \approx 0.034$; 1.782 ± 1.08, 1.630 ± 0.99) and whole-brain ($p \approx 0.018$; 1.129 ± 0.73, 1.028 ± 0.71); however, a significant difference in the result for the CN region is found. Similarly, for ^{11}C-CFT, CN and PU, both regions showed higher SNR gain in TOF compared with non-TOF reconstruction (**Figure 3D**), yet significant improvement was not found in results as shown in **Table 3**.

Image contrast of all brain VOIs was measured in TOF and non-TOF by Equation 2. CN and PU regions and whole-brain showed average higher contrast in TOF compared

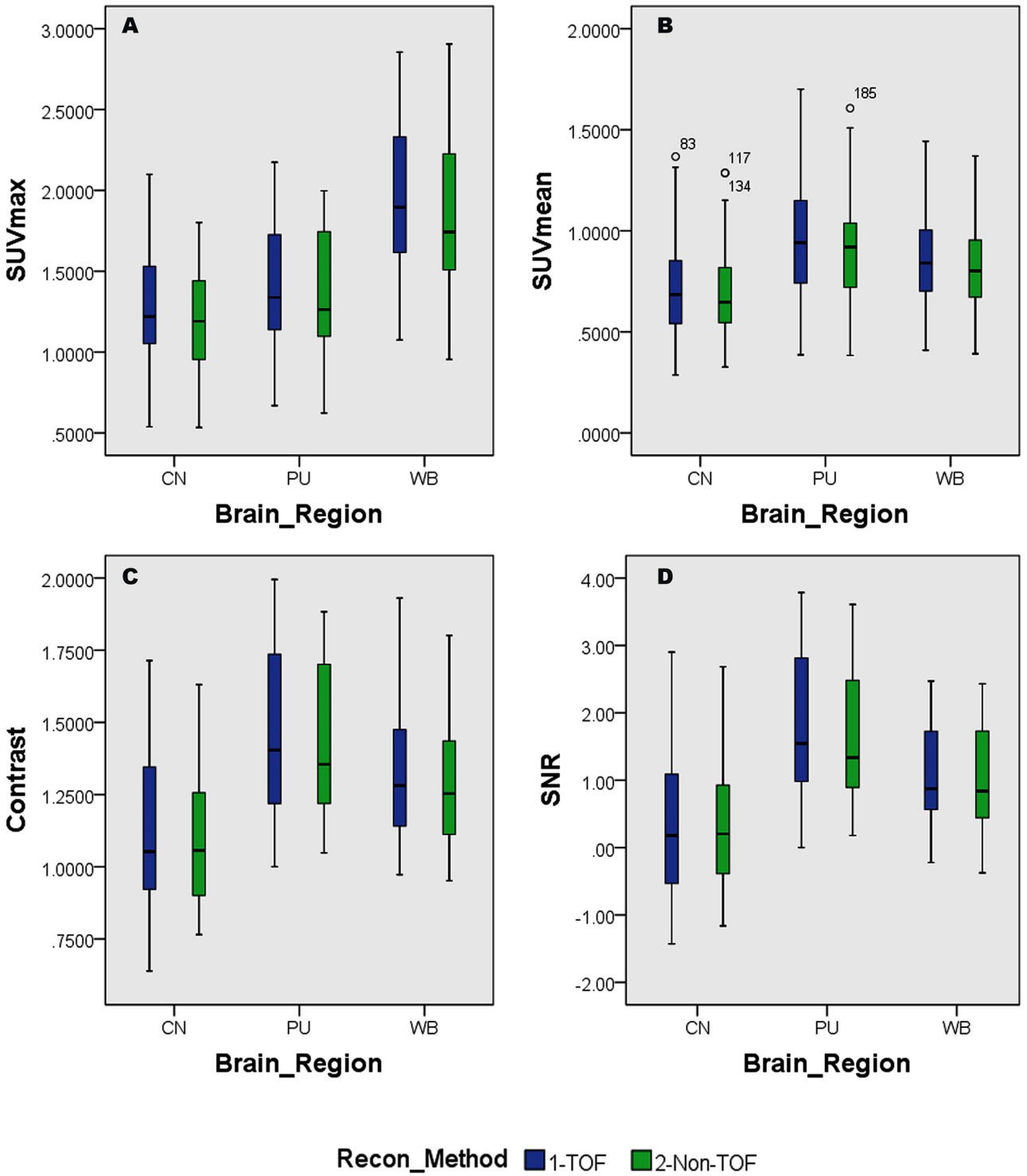

FIGURE 2 | Distribution of the standard uptake values (SUVs) and quantitative parameters with reconstruction methods per each brain regions of ^{11}C-PiB brain PET; **(A)** shows the distribution of individual subject's SUVmax values per segmented brain VOIs; **(B)** shows the distribution of individual subject's SUVmean values per segmented brain VOIs; **(C)** shows the distribution of individual subject's SNR values per segmented brain VOIs; **(D)** shows the distribution of individual subject's Contrast values per segmented brain VOIs; WB, Whole brain; CN, Caudate Nuclei; PU, Putamen.

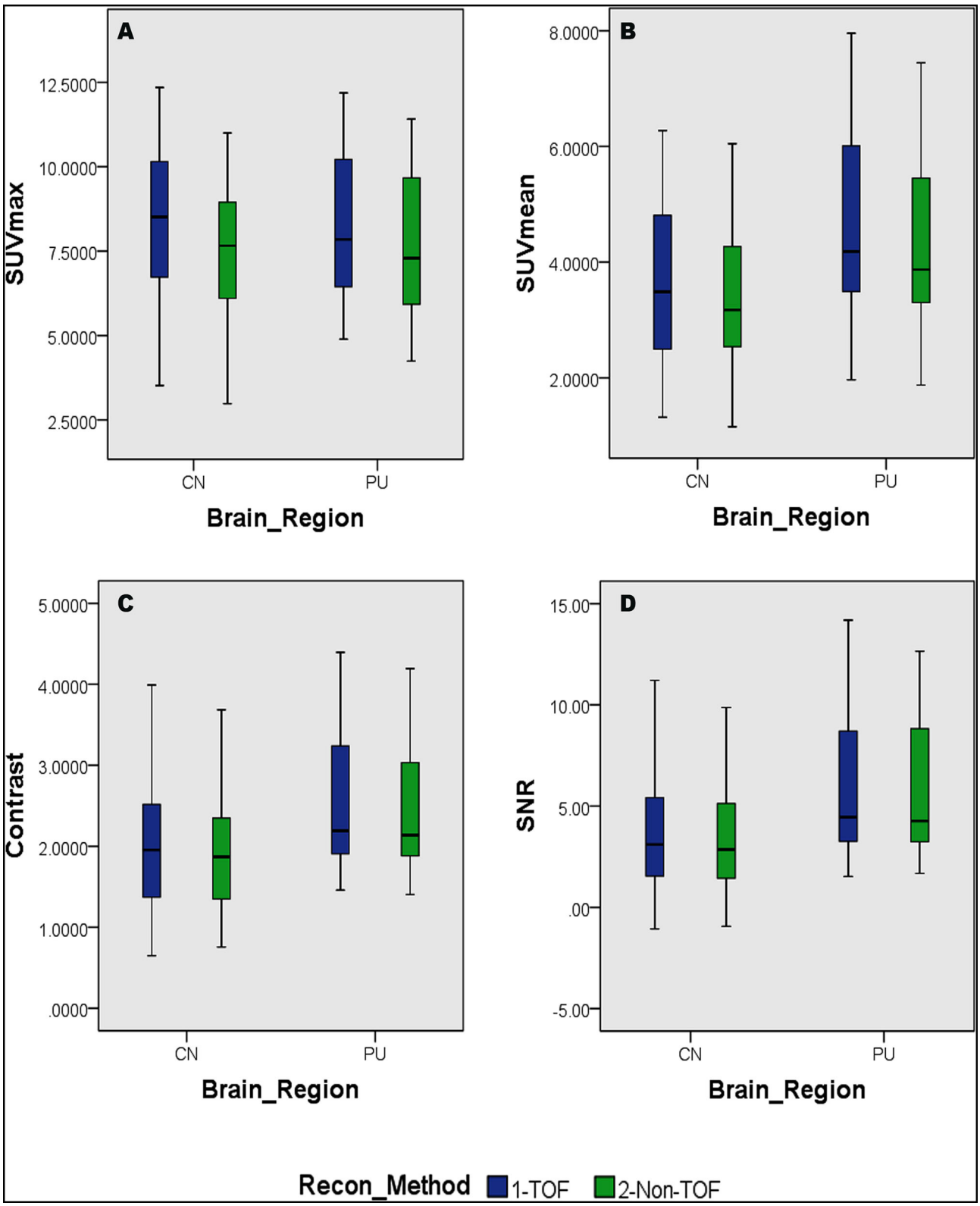

FIGURE 3 | Distribution of the SUVs and quantitative parameters with reconstruction methods per each brain regions of ^{11}C-PFT brain PET; **(A)** shows the distribution of individual subject's SUVmax values per segmented brain volume of interests (VOIs); **(B)** shows the distribution of individual subject's SUVmean values per segmented brain VOIs; **(C)** shows the distribution of individual subject's signal-to-noise ratio (SNR) values per segmented brain VOIs; **(D)** shows the distribution of individual subject's contrast values per segmented brain VOIs; WB, whole brain; CN, caudate Nuclei; PU, putamen.

TABLE 2 | The lists of maximum standard uptake value (SUVmax) and mean standard uptake value (SUVmean) for ^{11}C-PiB and ^{11}C-CFT with the time-of-flight (TOF) and non-TOF reconstruction, respectively.

Type of radiotracer	Brain regions	Mean ± SD							
		SUVmax				SUVmean			
		TOF	Non-TOF	%RAD	*p*-value	TOF	Non-TOF	%RAD	*p*-value
^{11}C-PiB	WB	1.966 ± 0.47	1.869 ± 0.51	5.165	**0.003**	0.862 ± 0.24	0.822 ± 0.23	4.797	**5E-06**
	CN	1.293 ± 0.39	1.192 ± 0.34	8.513	**0.000**	0.730 ± 0.26	0.707 ± 0.23	3.334	**3E-02**
	PU	1.409 ± 0.39	1.366 ± 0.40	3.135	0.110	0.975 ± 0.32	0.925 ± 0.29	5.328	**2E-04**
^{11}C-CFT	CN	8.339 ± 2.31	7.533 ± 2.16	10.702	**0.000**	3.613 ± 1.47	3.346 ± 1.29	7.981	**2E-04**
	PU	8.341 ± 2.28	7.742 ± 2.13	7.733	**0.004**	4.686 ± 1.60	4.301 ± 1.43	8.968	**2E-05**

The mean ± SD represented the mean value and SD. WB, whole-brain; CN, caudate nuclei; PU, putamen; %RAD, percentage relative average difference. p < 0.05: difference is significant at the level of 0.05. The bold values are the significant ones.

TABLE 3 | The quantitative parameters, such as the contrast and SNR were listed for the evaluation of image quality with TOF and non-TOF reconstruction, respectively.

Type of radiotracer	Brain regions	Mean ± SD							
		Contrast				SNR			
		TOF	non-TOF	%RAD	*p*-value	TOF	non-TOF	%RAD	*p*-value
^{11}C-PiB	WB	1.311 ± 0.22	1.281 ± 0.20	2.347	**0.002**	1.129 ± 0.73	1.028 ± 0.71	9.901	**0.018**
	CN	1.103 ± 0.27	1.097 ± 0.23	0.507	0.690	0.382 ± 1.09	0.344 ± 0.95	10.936	0.525
	PU	1.469±0.30	1.430±0.27	2.693	**0.007**	1.782±1.08	1.630±0.99	9.326	**0.034**
^{11}C-CFT	CN	1.964 ± 0.81	1.907 ± 0.73	2.997	0.138	3.496 ± 2.83	3.327 ± 2.57	5.069	0.174
	PU	2.527 ± 0.82	2.440 ± 0.75	3.571	**0.018**	5.767 ± 3.29	5.541 ± 3.08	4.068	0.076

The mean ± SD represented the mean value and SD. WB: whole-brain; CN: caudate nuclei; PU: putamen; %RAD: percentage relative average difference. p < 0.05: Difference is significant at the level of 0.05. The bold values are the significant ones.

with non-TOF for ^{11}C-PiB (**Figure 2C**). Nevertheless, significant contrast ($p < 0.05$) improvement was observed only in PU ($p \approx 0.007$; 1.469 ± 0.30, 1.430 ± 0.27) region. However, the whole-brain showed a similar impact ($p \approx 0.002$; 1.311 ± 0.22, 1.281 ± 0.20) with significantly improved contrast in TOF reconstruction. In ^{11}C-CFT, CN and PU showed higher contrast in TOF compared with non-TOF (**Figure 3C**), still significant contrast ($p < 0.05$) enhancement was observed only for PU region ($p \approx 0.018$; 2.527 ± 0.82, 2.440 ± 0.75) in TOF compared with non-TOF reconstruction.

Percentage of Relative Average Difference of SUV_{max}, SUV_{mean}, and Quantitative Parameters—(% RAD)

The percentage of relative average difference (%RAD) of SUV_{max} and SUV_{mean} among segmented brain VOIs for both ^{11}C-PiB and ^{11}C-CFT was measured in TOF compared with non-TOF by Equation 3. The %RAD-SUV_{max} and SUV_{mean} difference for all segmented brain VOIs were positive, and %TOF SUV gain of ^{11}C-CFT and ^{11}C-PiB are illustrated in **Table 2.** The %RAD of SNR and contrast was positive for CN and PU regions for both ^{11}C-CFT and ^{11}C-PiB (**Table 3).**

DISCUSSION

In the study, we evaluated the magnitude of quantitative difference produced by TOF reconstructions on CN and PU VOIs for short-lived ^{11}C-CFT brain PET and further compared with the same VOIs with ^{11}C-PiB for any correlation of TOF effect with a different short-lived tracer. Apparently, varying uptake properties of different VOIs caused a considerable impact on the TOF effect; however, the TOF effect has a consistent association with SUV_{mean} rather than SUV_{max} values in both VOIs between ^{11}C-CFT and ^{11}C-PiB. Significantly enhanced SUV_{mean} among segmented VOIs of both radiotracers confirmed that TOF facilitates short-lived radiotracers over non-TOF reconstruction. Moreover, the whole-brain, which is investigated due to its diffuse ^{11}C-PiB uptake qualities, spotted significantly enhanced SUV_{max}, SUV_{mean}, contrast, and SNR. It is observed that quantitative differences of image quality parameters vary among CN and PU with their uptake characteristics relative to the selected reference region. To the best of our knowledge, it is the first time that different tracers of short-lived ^{11}C for brain quantitation imaging were performed with TOF and non-TOF PET/MRI. Overall, the experiment revealed that TOF reconstructions significantly affect SUVs compared with non-TOF and further improved the image contrast and SNR for a considerable extent, which proposed the TOF technique with

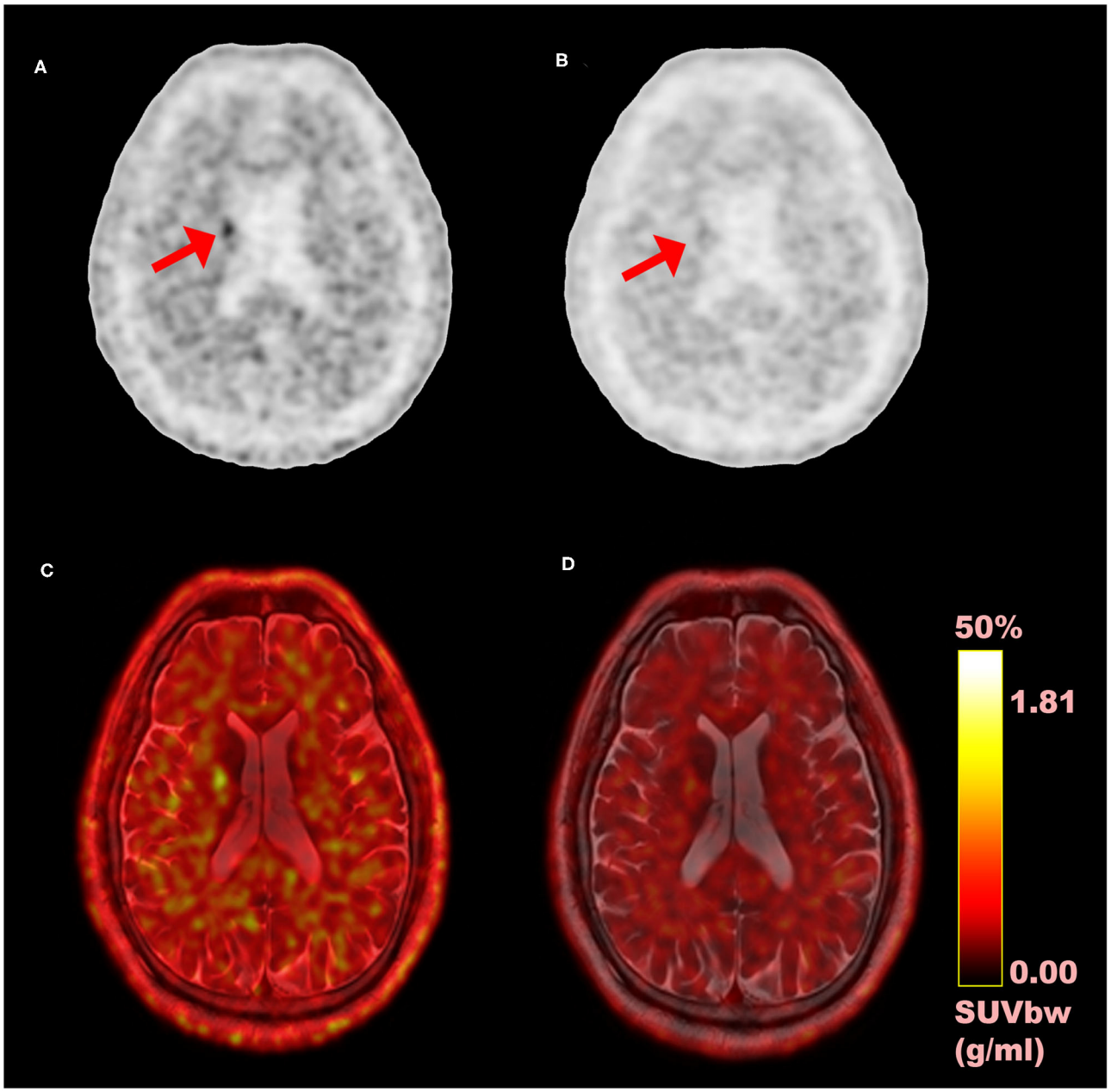

FIGURE 4 | Comparison of time-of-flight (TOF) vs. non-TOF ^{11}C-PiB PET images; **(A)** TOF reconstructed PET image (axial plane); **(B)** non-TOF reconstructed PET image (axial plane); **(C)** fusion image of TOF PET and MRI; **(D)** fusion image of non-TOF PET and MRI; red arrows: shows the signal enhancement difference in TOF and non-TOF PET images in ^{11}C-PiB PET images.

higher time resolution (lesser than 400 ps) that contributes in achieving the optimal performance reconstruction of brain PET images with short-lived ^{11}C-labeled tracers (**Figure 4**). Thus, it is recommended to consider the quantitative difference caused by TOF PET/MR modalities while diagnosing AD/PD.

The quantitative effect (SUVs) has benefitted in modern TOF PET for diagnosing neurodegenerative diseases by improving the spatial resolution and SNR (14). Further, Surti S et al. proved that the TOF reconstruction improves small lesion uptake measurement accuracy and precision by reducing normalized uptake values' (NUV) variability (22, 36). So as, the precision and accuracy of SUV are improved by TOF reconstruction. Oldan, J.D. et al. stated that SUV measurements of ^{18}F-NaF PET/CT fluctuate within the brain like soft tissue regions between TOF and non-TOF reconstructions due to their lower uptake characteristics (35). Experimenting, the point spread function (PSF) and TOF algorithms on brain regions, Shao, X. et al., evidenced different effects on the SUVs among different

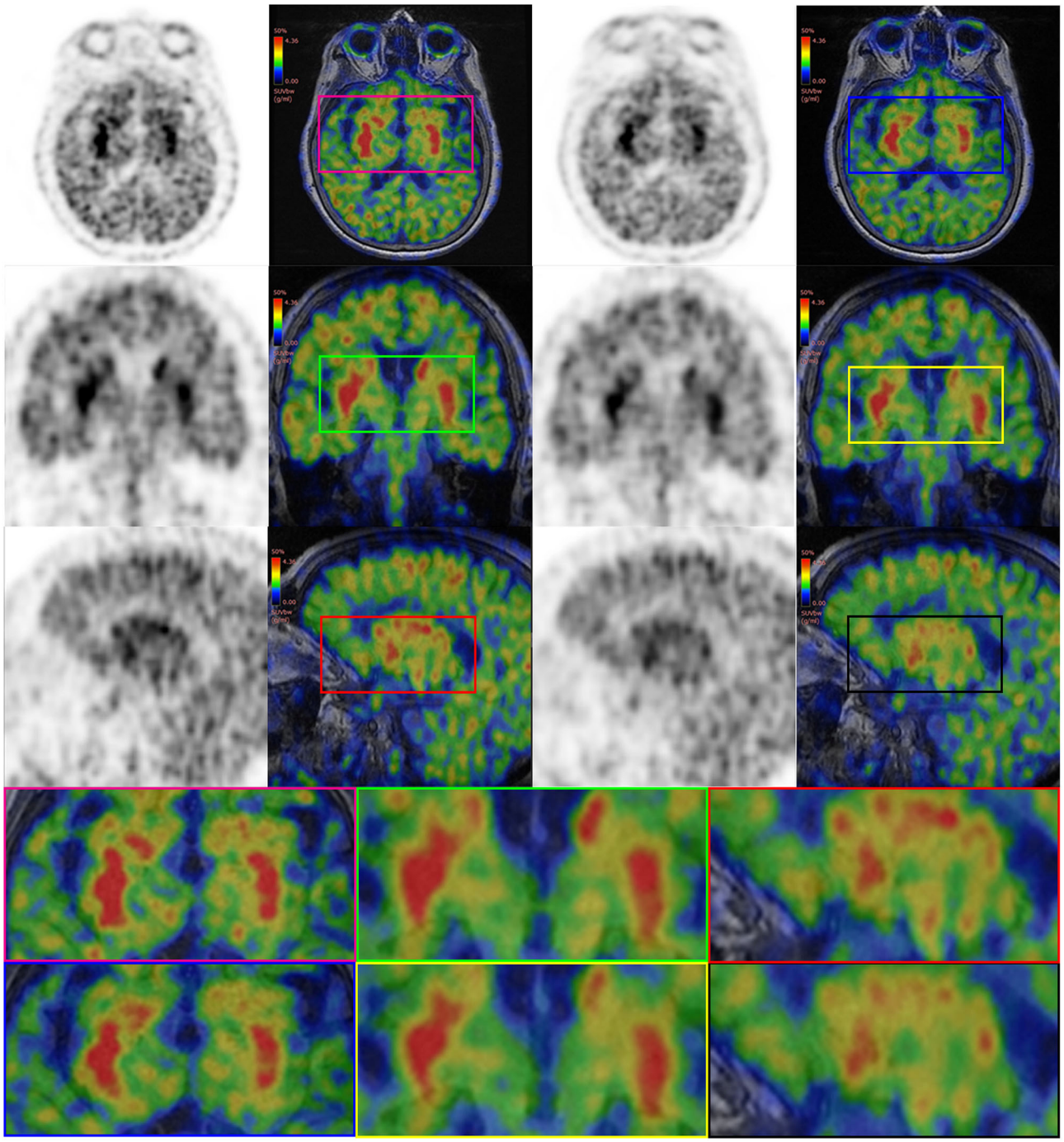

FIGURE 5 | The ^{11}C-CFT PET images demonstrating enhanced CN and PU with TOF and non-TOF reconstruction. First column demonstrating the enhanced CN and PU in TOF reconstruction; second column demonstrating the fused ^{11}C-CFT with T1W MRI in TOF reconstruction; third column demonstrating the enhanced CN and PU in non-TOF reconstruction; fourth column demonstrating the fused ^{11}C-CFT with T1W MRI in non-TOF reconstruction (axial, sagittal, and coronal planes are provided for comparisons).

brain regions for ^{18}F-FDG (27). Since consistent significant enhancement of SUV_{mean} among segmented brain VOIs in TOF reconstruction for short-lived ^{11}C-labeled tracers were seen, it is evidenced that TOF PET systems can be used as sensitivity amplifiers for short half-life radiopharmaceuticals, such as ^{11}C-labeled tracers with low count rate after an adequate uptake

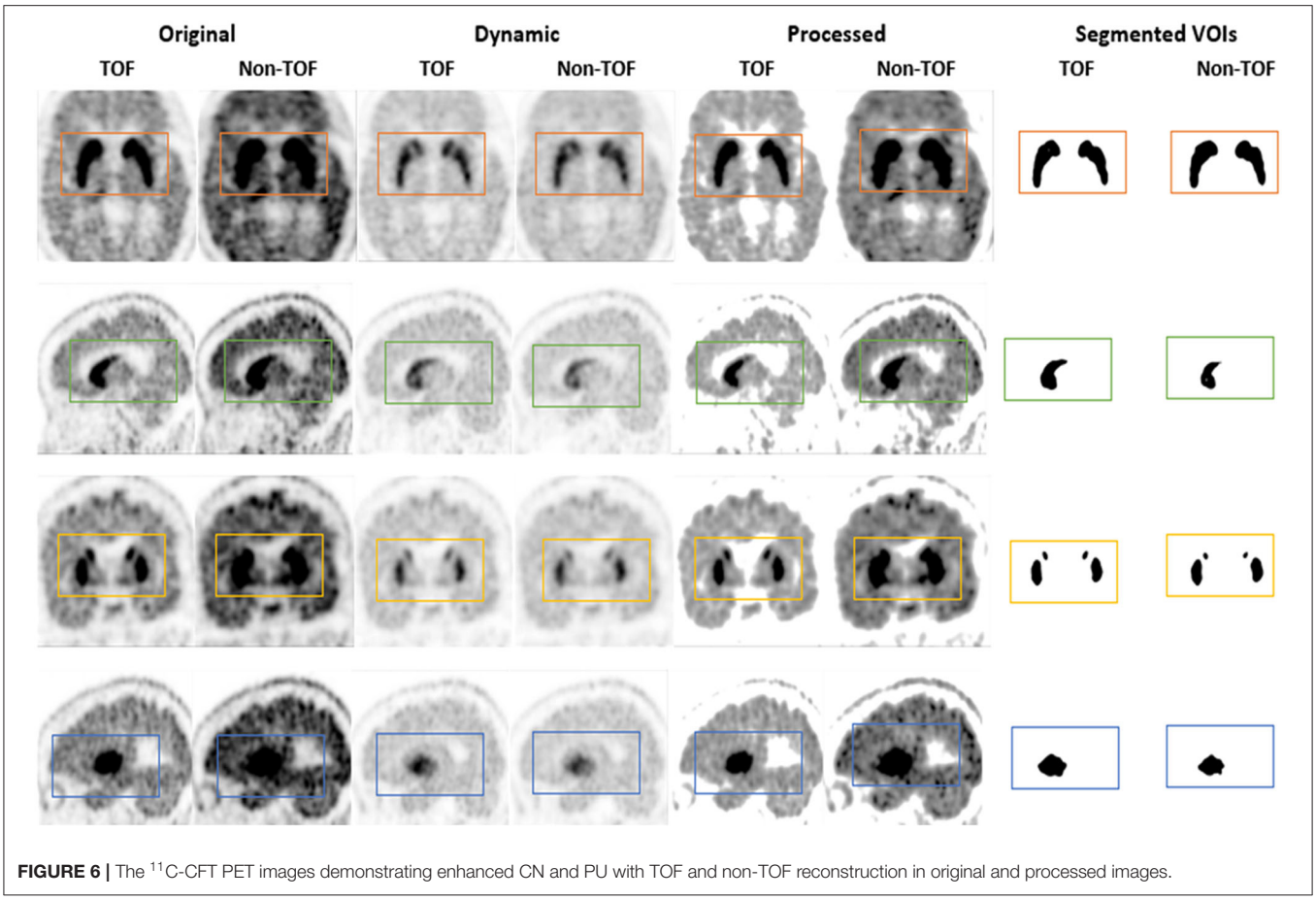

FIGURE 6 | The ^{11}C-CFT PET images demonstrating enhanced CN and PU with TOF and non-TOF reconstruction in original and processed images.

time. Injected radiation dose can be optimized by considering enhanced SUVs while maintaining the same image quality. So the patient radiation dose, as well as occupational and general public exposure to ionizing radiation, can be minimized (23). Motion artifacts are often complained while scanning patients with AD/PD for longer time, however, improved timing resolution considerably reduce the scan time which comfort patients with less time inside the PET/MR gantry.

Caudate nuclei showed significant enhancement in SUV_{max} and SUV_{mean} for TOF reconstruction in ^{11}C-CFT though a significant difference was not found in the results of the SNR and contrast. Similarly, ^{11}C-PiB showed identical results for both the VOIs. These results were caused due to a relatively improved signal in the reference region, which is the cerebellum cortex, compared with the CN region in TOF reconstruction. PU region with ^{11}C-PiB showed significant enhancement in contrast, SNR and SUV_{mean} for TOF compared with non-TOF reconstruction, which is consistent with previous literature using ^{18}F tracers for small lesion enhancement (16, 18, 19). However, PU did not show significant improvement in SUV_{max} in TOF reconstructed images compared with non-TOF, which probably was due to diffuse low uptake properties of ^{11}C-PiB tracer within the PU. A similar effect was observed in SUV_{max}, SUV_{mean}, and contrast for ^{11}C-CFT due to its higher uptake characteristics within the PU, (**Figures 5**, **6**) still SNR did not find significant development. The cause would be the incomparable noise produced in the background region, which is the cerebellum cortex (15), was relatively higher in TOF compared with non-TOF images due to ^{11}C-CFT uptake properties. In **Figure 2,** the box-plot illustrated overall whole-brain enhanced SUV_{mean}, SUV_{max}, and quantitative parameters with TOF reconstruction in ^{11}C-PiB.

Our study has several limitations. The number of cases are still limited due to the time limitation for data collection of ^{11}C-CFT and ^{11}C-PiB scans of suspected patients with AD/PD, which were archived in the Picture Archive and Communication System (PACS). A larger sample would possibly be needed to generalize these findings to a considerable population (e.g., a wider range of patient BMI and a wider range of age). Then, for outlining most of the cortical structures in the brain VOIs, PET-based Maximum Probability Atlas (MPA) was used to avoid slowness or interruption of the segmentation process of the PNEURO module in PMOD 3.9 software. Though T1 MR based parcellation is preferred over VOI outlining in deep nuclei region by the PMOD team, thus the quality of the VOI definition in the areas mentioned above is reduced. For the effective use of PNEURO with high-resolution data, a high-end workstation (e.g., 8 core, 16GB, or more RAM) is required.

CONCLUSION

Time-of-flight reconstruction improves SUVs and image quality parameters, which is an advantage of the TOF PET/MRI system with short-lived ^{11}C-labeled tracers for offering higher sensitivity. The improved temporal resolution supports the rapid decay rate of short-lived ^{11}C-labeled tracers and shortens scan time while increasing the patient comfort and reducing the motion artifacts in patients with AD/PD. However, the combined TOF algorithm should be used with caution for quantitative analysis because it has different effects on SUV_{max}, contrast, and SNR of different brain regions.

DATA AVAILABILITY STATEMENT

The original contributions presented in the study are included in the article/supplementary material, further inquiries can be directed to the corresponding author.

ETHICS STATEMENT

The studies involving human participants were reviewed and approved by Institutional Review Board of Union Hospital, Tongji Medical College, Huazhong University of Science and Technology. Written informed consent for participation was not required for this study in accordance with the national legislation and the institutional requirements.

AUTHOR CONTRIBUTIONS

XL and WR substantially contributed to the conception and design, analyzed and interpreted the data, and revised the manuscript critically for important intellectual content. DW analyzed and interpreted the data and drafted the article. DW, WR, and FH acquired the PET images. YG and QL prepared the compounds of ^{11}C-CFT and ^{11}C-PiB. XS and FL analyzed and interpreted the images. All authors read and approved the final manuscript, contributed to the article, and approved the submitted version.

FUNDING

This work was supported by the National Natural Science Foundation of China (Nos. 81701759 and 81901735), the Key Project of Hubei Province Technical Innovation (2017ACA182), and the Clinical Research Physician Program of Tongji Medical College, Huazhong University of Science and Technology (No. 5001530008).

ACKNOWLEDGMENTS

We would like to thank all the members in the PET Center, Union Hospital, Tongji Medical College, Huazhong University of Science and Technology.

REFERENCES

1. Nussbaum RL, Ellis CE. Alzheimer's disease and Parkinson's disease. *N Engl J Med.* (2003) 348:1356–64. doi: 10.1056/NEJM2003ra020003
2. McKhann G, Drachman D, Folstein M, Katzman R, Price D, Stadlan EM. Clinical diagnosis of Alzheimer's disease: Report of the NINCDS-ADRDA Work Group* under the auspices of Department of Health and Human Services Task Force on Alzheimer's Disease. *Neurology.* (1984) 34:939. doi: 10.1212/WNL.34.7.939
3. Silverman DH, Small GW, Chang CY, Lu CS, de Aburto MAK, Chen W, et al. Positron emission tomography in evaluation of dementia: regional brain metabolism and long-term outcome. *JAMA.* (2001) 286:2120–7. doi: 10.1001/jama.286.17.2120
4. Okello A, Koivunen J, Edison P, Archer H, Turkheimer F. Någren Ku, et al. Conversion of amyloid positive and negative MCI to AD over 3 years: an 11C-PIB PET study. *Neurology.* (2009) 73:754–60. doi: 10.1212/WNL.0b013e3181b23564
5. Faria DdP, Duran FL, Squarzoni P, Coutinho AM, Garcez AT, Santos PP, et al. Topography of 11C-Pittsburgh compound B uptake in Alzheimer's disease: a voxel-based investigation of cortical and white matter regions. Braz J Psychiatry. (2018) 41:101–11. doi: 10.1590/1516-4446-2017-0002
6. Nagasawa H, Tanji H, Nomura H, Saito H, Itoyama Y, Kimura I, et al. PET study of cerebral glucose metabolism and fluorodopa uptake in patients with corticobasal degeneration. *J Neurol Sci.* (1996) 139:210–7. doi: 10.1016/0022-510X(96)00057-3
7. Drzezga A. Diagnosis of Alzheimer's disease with [18F] PET in mild and asymptomatic stages. *Behav Neurol.* (2009) 21:101–15. doi: 10.1155/2009/276026
8. Poewe W, Wenning G. The differential diagnosis of Parkinson's disease. *Eur J Neurol.* (2002) 9 Suppl 3:23–30. doi: 10.1046/j.1468-1331.9.s3.3.x
9. Clemente G, Alves V, Abrunhosa A, editors. Synthesis optimization of pittsburgh compound B by the captive solvent method. In: *2012 IEEE 2nd Portuguese Meeting in Bioengineering (ENBENG); 2012: IEEE*. Coimbra.
10. Huang T, Wang H, Tang G, Liang X, Shi X, Zhang X. The influence of residual nor-β-CFT in 11C CFT injection on the Parkinson disease diagnosis: a 11C CFT PET study. *Clin Nucl Med.* (2012) 37:743–7. doi: 10.1097/RLU.0b013e31824c5fae
11. Conti M, Bendriem B. The new opportunities for high time resolution clinical TOF PET. *Clin Transl Imaging.* (2019) 7:139–47. doi: 10.1007/s40336-019-00316-5
12. Surti S, Karp JS. Advances in time-of-flight PET. *Phys Medica.* (2016) 32:12–22. doi: 10.1016/j.ejmp.2015.12.007
13. Lewellen T. Time-of-flight PET. *Semin Nucl Med.* (1998) 28:268–75. doi: 10.1016/S0001-2998(98)80031-7
14. Lindstrom E, Danfors T, Lindsjo L, Lubberink M. Brain-PET image reconstruction methods affect software-aided diagnosis in patients with neurodegenerative diseases. *J Nucl Med.* (2018) 59(suppl 1):1780. doi: 10.1016/j.nicl.2020.102386
15. Karp JS, Surti S, Daube-Witherspoon ME, Muehllehner G. Benefit of time-of-flight in PET: experimental and clinical results. *J Nucl Med.* (2008) 49:462–70. doi: 10.2967/jnumed.107.044834
16. Surti S, Scheuermann J, El Fakhri G, Daube-Witherspoon ME, Lim R, Abi-Hatem N, et al. Impact of time-of-flight PET on whole-body oncologic studies: a human observer lesion detection and localization study. *J Nucl Med.* (2011) 52:712–9. doi: 10.2967/jnumed.110.086678
17. Lois C, Jakoby BW, Long MJ, Hubner KF, Barker DW, Casey ME, et al. An assessment of the impact of incorporating time-of-flight information into clinical PET/CT imaging. *J Nucl Med.* (2010) 51:237–45. doi: 10.2967/jnumed.109.068098
18. Muehlematter UJ, Nagel HW, Becker A, Mueller J, Vokinger KN, de Galiza Barbosa F, et al. Impact of time-of-flight PET on quantification accuracy and

lesion detection in simultaneous 18F-choline PET/MRI for prostate cancer. *EJNMMI Res.* (2018) 8:41. doi: 10.1186/s13550-018-0390-8
19. van der Vos CS, Koopman D, Rijnsdorp S, Arends AJ, Boellaard R, van Dalen JA, et al. Quantification, improvement, and harmonization of small lesion detection with state-of-the-art PET. *Eur J Nucl Med Mol Imaging.* (2017) 44:4–16. doi: 10.1007/s00259-017-3727-z
20. Shang K, Cui B, Ma J, Shuai D, Liang Z, Jansen F, et al. Clinical evaluation of whole-body oncologic PET with time-of-flight and point-spread function for the hybrid PET/MR system. *Eur J Radiol.* (2017) 93:70–5. doi: 10.1016/j.ejrad.2017.05.029
21. Surti S. Update on time-of-flight PET imaging. *J Nucl Med.* (2015) 56:98–105. doi: 10.2967/jnumed.114.145029
22. Daube-Witherspoon ME, Surti S, Perkins AE, Karp JS. Determination of accuracy and precision of lesion uptake measurements in human subjects with time-of-flight PET. *J Nucl Med.* (2014) 55:602–7. doi: 10.2967/jnumed.113.127035
23. Murray I, Kalemis A, Glennon J, Hasan S, Quraishi S, Beyer T, et al. Time-of-flight PET/CT using low-activity protocols: potential implications for cancer therapy monitoring. *Eur J Nucl Med Mol Imaging.* (2010) 37:1643–53. doi: 10.1007/s00259-010-1466-5
24. Budinger TF. Time-of-flight positron emission tomography: status relative to conventional PET. *J Nucl Med.* (1983) 24:73.
25. Surti S, Karp S, Popescu LM, Daube-Witherspoon E, Werner M. Investigation of time-of-flight benefit for fully 3-DPET. *IEEE Trans Med Imaging.* (2006) 25:529–38. doi: 10.1109/TMI.2006.871419
26. Surti S, Karp J, Muehllehner G, Raby P, editors. Investigation of lanthanum scintillators for 3D PET. In: *2002 IEEE Nuclear Science Symposium Conference Record; 2002: IEEE*. Norfolk, VA.
27. Shao X, Shao X, Wang X, Wang Y. Applications of both time of flight and point spread function in brain PET image reconstruction. *Nucl Med Commun.* (2016) 37:422–7. doi: 10.1097/MNM.0000000000000459
28. Nagaki A, Onoguchi M, Matsutomo N. Clinical validation of high-resolution image reconstruction algorithms in brain 18F-FDG-PET: effect of incorporating Gaussian filter, point spread function, and time-of-flight. *Nucl Med Commun.* (2014) 35:1224–32. doi: 10.1097/MNM.0000000000000187
29. Prieto E, Martí-Climent JM, Morán V, Sancho L, Barbés B, Arbizu J, et al. Brain PET imaging optimization with time of flight and point spread function modelling. *Phys Med.* (2015) 31:948–55. doi: 10.1016/j.ejmp.2015.07.001
30. Leynes AP, Yang J, Shanbhag DD, Kaushik SS, Seo Y, Hope TA, et al. Hybrid ZTE/Dixon MR-based attenuation correction for quantitative uptake estimation of pelvic lesions in PET/MRI. *Med Phys.* (2017) 44:902–13. doi: 10.1002/mp.12122
31. Hammers A, Allom R, Koepp MJ, Free SL, Myers R, Lemieux L, et al. Three-dimensional maximum probability atlas of the human brain, with particular reference to the temporal lobe. *Hum Brain Mapp.* (2003) 19:224–47. doi: 10.1002/hbm.10123
32. Le Meunier L, Slomka PJ, Dey D, Ramesh A, Thomson LE, Hayes SW, et al. Enhanced definition PET for cardiac imaging. *J Nucl Cardiol.* (2010) 17:414–26. doi: 10.1007/s12350-010-9193-7
33. Tada T, Hasegawa C, Odagawa T, Abe S, Kato K. Comparative examination of the cerebellum and pons as reference regions for quantitative evaluation in PET imaging for Alzheimer's disease using ^{11}C-Pittsburgh Compound-B. In: *2019 Society of Nuclear Medicine and Molecular Imaging.* Anaheim, CA (2019).
34. Marcus C, Mena E, Subramaniam RM. Brain PET in the diagnosis of Alzheimer's disease. *Clin Nucl Med.* (2014) 39:e413. doi: 10.1097/RLU.0000000000000547
35. Oldan JD, Turkington TG, Choudhury K, Chin BB. Quantitative differences in [18F] NaF PET/CT: TOF versus non-TOF measurements. *Am J Nucl Med Mol Imaging.* (2015) 5:504.
36. Surti S, Perkins A, Clementel E, Daube-Witherspoon M, Karp J, editors. In: *Impact of TOF PET on variability of lesion uptake estimation. World Molecular Imaging Conf, Kyoto; 2010*. Kyoto.

Conflict of Interest: The authors declare that the research was conducted in the absence of any commercial or financial relationships that could be construed as a potential conflict of interest.

Publisher's Note: All claims expressed in this article are solely those of the authors and do not necessarily represent those of their affiliated organizations, or those of the publisher, the editors and the reviewers. Any product that may be evaluated in this article, or claim that may be made by its manufacturer, is not guaranteed or endorsed by the publisher.

frontiers in Medicine

ORIGINAL RESEARCH
published: 21 March 2022
doi: 10.3389/fmed.2022.809323

Value of FDG-PET/MR in Oral Focus Assessment in Head and Neck Cancer Patients—A Feasibility Study

Silvio Valdec[1,2*†], *Fabienne A. Bosshard*[1†], *Martin Hüllner*[3], *Dominic R. Schwaninger*[1], *Larissa Stocker*[4], *Barbara Giacomelli-Hiestand*[1] *and Bernd Stadlinger*[1]

[1] Clinic of Cranio-Maxillofacial and Oral Surgery, Center of Dental Medicine, University of Zurich, Zurich, Switzerland, [2] Division of Periodontology, Department of Stomatology, Dental School, University of São Paulo, São Paulo, Brazil, [3] Department of Nuclear Medicine, University Hospital Zürich, University of Zurich, Zurich, Switzerland, [4] Clinic of Orthodontics and Pediatric Dentistry, Center of Dental Medicine, University of Zurich, Zurich, Switzerland

FDG-PET/MR is a hybrid imaging modality used for the staging and restaging of advanced head & neck cancer (HNC) patients. Their treatment typically involves radiation therapy, which requires previous dental focus assessment. The aim of this study was to analyze if staging FDG-PET/MR is a valuable tool for oral focus assessment. For this purpose, FDG-PET/MR findings, such as metabolic activity of periapical radiolucencies and marginal periodontitis, were retrospectively compared with conventional standardized dental focus assessment, including dental radiographs and clinical assessment of 124 teeth in seven patients. Increased FDG uptake of periapical lesions was found in one out of 23 lesions. Increased FDG uptake of the marginal periodontium was recorded in one out of 34 lesions. In summary, standardized dental focus assessment by panoramic radiography and periapical radiographs may be enriched by information from FDG-PET/MR, showing active inflammation in dental foci. However, many dental foci have no correlate in FDG-PET/MR. The treatment decision for oral foci may benefit from the visualized presence or absence of metabolic activity on FDG-PET/MR.

Keywords: head and neck cancer, radiation therapy, dental focus, positron emission tomography–magnetic resonance imaging, periapical radiography, panoramic radiography

OPEN ACCESS

Edited by:
Domenico Albano,
University of Brescia, Italy

Reviewed by:
Natale Quartuccio,
ARNAS Ospedali Civico Di Cristina Benfratelli, Italy
Francesco Dondi,
Università degli Studi di Brescia, Italy

***Correspondence:**
Silvio Valdec
silvio.valdec@zzm.uzh.ch

†These authors have contributed equally to this work

Specialty section:
This article was submitted to Nuclear Medicine, a section of the journal Frontiers in Medicine

Received: *04 November 2021*
Accepted: *15 February 2022*
Published: *21 March 2022*

Citation:
Valdec S, Bosshard FA, Hüllner M, Schwaninger DR, Stocker L, Giacomelli-Hiestand B and Stadlinger B (2022) Value of FDG-PET/MR in Oral Focus Assessment in Head and Neck Cancer Patients—A Feasibility Study. Front. Med. 9:809323. doi: 10.3389/fmed.2022.809323

INTRODUCTION

Positron emission tomography/magnetic resonance (PET/MR) imaging using the radiotracer 18F-fluorodeoxyglucose (FDG-PET/MR) is a hybrid imaging modality, which is mainly used in oncological patients for staging and restaging purposes (1). However, it may also be used for imaging inflammation and infection (2).

Head & neck cancer (HNC) is the seventh most common cancer worldwide, with half a million new diagnoses per year (3, 4). In Switzerland, more than 1,000 new HNC cases are diagnosed each year, reverting to a lifetime HNC risk of 0.7% in women and 1.6% in men (5).

In advanced HNC, treatment typically involves radiation therapy with or without surgery and chemotherapy (4, 6, 7). This treatment harbors several short-term and long-term complications owing to tissue damage from ionizing radiation. Oral infection or inflammation is a known risk factor for such radiation-induced oral damages (8). Hence, it is highly recommended that patients undergo oral health screening, including clinical and radiological examination, to detect potential foci requiring treatment before the commencement of radiation therapy (4, 9, 10).

Panoramic radiography (OPT) serves as a standard radiological assessment for hard tissue pathologies. Its advantages are comparably low radiation exposure, widespread availability, and good image quality. OPT is mostly supplemented by periapical radiographs in selected cases, such as root canal treated teeth. After incidental findings, three-dimensional imaging such as cone beam computed tomography (CBCT) or MR can also be performed during the initial examination (11). Further, a thorough oral examination is performed. After dental focus assessment, any acute or potential inflammatory condition diagnosed, such as marginal and apical periodontitis, will be treated (12). The patient remains in dental care during and after radiotherapy or chemotherapy (10, 13). While dental focus assessment is not a reimbursed indication for FDG-PET imaging in Switzerland, dental foci are sometimes discovered incidentally on staging / restaging examinations of head and neck cancer patients.

At our institution, every HNC patient requiring radiation therapy undergoes either whole-body positron emission tomography/computed tomography (PET/CT) or PET/MR using the radiotracer 18F-fluorodeoxyglucose (FDG).

The aim of our study was to find out whether FDG-PET/MR offers added value in dental focus assessment. To the best of our knowledge, this is the first study analyzing the added value of FDG-PET/MR in dental focus assessment.

MATERIALS AND METHODS

Patient Selection

HNC patients who underwent FDG-PET/MR for staging and standardized dental focus assessment prior to radiation therapy at the University Hospital of Zurich between December 2016 and December 2018 were included into this study. FDG-PET/MR was conducted at the Department of Nuclear Medicine at the University Hospital Zürich, Switzerland. Dental focus assessment was performed at the Clinic of Cranio-Maxillofacial and Oral Surgery at the Center of Dental Medicine, University of Zurich. This study was approved by the local ethics committee of Zürich (Nr. 2017-01378).

Only patients with signed consent for the use of their medical data for research were included. Other inclusion criteria were scheduled radiotherapy with or without surgery and/or chemotherapy, and the availability of a FDG-PET/MR exam including a diagnostic head and neck MR protocol, as well as availability of panoramic radiography (OPT) and periapical X-rays. Only patients with a maximum time interval of 3 months between these exams, without any surgical or therapeutic intervention in between, were included. Patients with blurred radiographic images were excluded. Image angulations were ignored.

Image Acquisition

PET/MR image acquisition was carried out as described previously in detail (14).

A BMI-adapted body weight-dependent FDG dosage protocol was used (15). A Dixon-type MR pulse sequence was used for attenuation correction (16, 17). In brief, the MR protocol consisted of the following MR pulse sequences: Axial 2-point Dixon-type sequence and coronal T2-weighted sequence with fat suppression for the whole-body; axial respiration-triggered T2-weighted sequence for the lung and upper abdomen; regionalized head and neck axial and coronal T2-weighted sequence with fat suppression, axial T1-weighted sequence without gadolinium-based contrast and without fat suppression, axial, coronal and sagittal T1-weighted sequences with gadolinium-based contrast and with fat suppression.

Every dental focus assessment included a recording of radiographic findings. Panoramic radiography (OPT), periapical radiographs of every root canal-treated tooth and bite wings for caries evaluation were taken and archived in the PACS (Synedra, Apollon Innsbruck, Austria). OPTs were generated in a standardized position, using Cranex 3D (Soredex, KaVo, Biberach, Germany). Periapical radiographs were generated using Heliodent DS (Dentsply-Sirona, Bensheim, Germany). The intraoral X-ray was operated at 60 kV and 7 mA. Parallel technique was used, with a focus-patient distance of approximately 21 cm.

Image Analysis

The analysis of the X-rays, generated during the standardized dental focus assessment, was conducted by board-certified dentists (LS, DS) under the supervision of an oral surgeon (BGH). In case of disagreement, a consensus decision was reached by discussing the case in detail (LS DS, BGH and BS). All dental X-rays were analyzed in DICOM format using Synedra Viewer (Synedra, Apollon Innsbruck, Austria) under standardized conditions on a diagnostic monitor (NEC, MDview 243). FDG-PET/MR images were analyzed using a dedicated review workstation (AW 4.6, GE Healthcare) (MH). All imaging modalities (FDG-PET/MR, OPT, dental X-rays) were analyzed separately.

Analyzed Radiological Parameters

For radiological evaluation, the focus was set on two main parameters: periapical lesions and marginal bone level. These predefined parameters were assessed on the X-rays acquired during the standardized dental focus assessment (OPT, periapical radiographs and bite wings) and on FDG–PET/MR (except marginal bone level). On FDG-PET/MR, increased metabolic activity related to dental lesions was recorded as presence (expressed as SUV_{max}) or absence. Finally, all teeth were examined for root canal fillings.

Periapical Lesions

For the classification of the periapical lesions, the periapical index (PAI) described by Orstavik et al. (18) was used. This index ranges from 1 (healthy) to 5 (severe, exacerbating apical periodontitis). In addition, the size of periapical lesions was recorded (smaller or larger than 5 mm in diameter).

Marginal Periodontium

For the classification of the marginal bone level, the marginal periodontitis index (MPI) described by Kito et al. was applied (19). This index distinguishes 4 sections (1–4) and estimates the

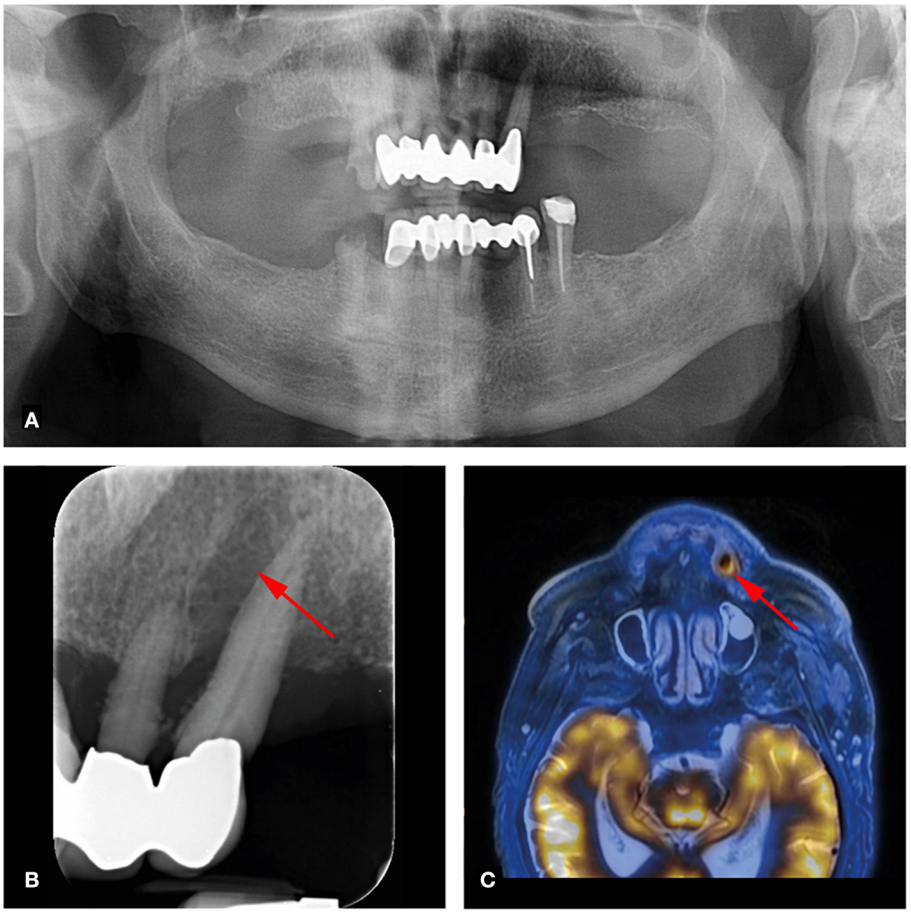

FIGURE 1 | 73-year-old man with right-sided hypopharynx carcinoma cT3 cN2b cM0. Panoramic **(A)** and dental radiography **(B)** shows a periapical lesion with marginal bone loss in region 23 (arrow; PAI score 4, MPI score: 4). **(C)** FDG-PET/MR shows a metabolically active osteolysis at tooth 23 with a SUVmax of 6.8 (arrow).

TABLE 1 | Periapical lesions (PL) in dental X-rays and FDG-PET/MR.

PAI Score	PL in dental radiographs ($n = 23$)	PL in PET/MR ($n = 19$)	PL with increased SUV_{max} ($n = 1$)	PL in dental radiographs >5mm ($n = 2$)	PL in dental radiographs <5mm ($n = 18$)	Percussion sensitivity
1	0	0	0	0	0	2
2	1	0	0	0	0	0
3	6	3	0	0	4	1
4	16	16	1	2	14	0

physiological bone level compared to the actual bone level. Bone loss of less than one-third was classified as "1", one-third up to half as "2", half up to two-thirds as "3", and more than two thirds as "4". A marginal bone lesion was defined as MPI score $\geq$2.

Clinical Outcome Parameter

Percussion Sensitivity

In addition to radiological data, the clinical parameter percussion sensitivity was extracted from the standardized patients' charts used at our institution. All teeth with periapical lesions were analyzed for their percussion sensitivity. Findings were noted as either 1 (sensitivity present) or 0 (sensitivity absent).

Statistics

Total number of patients, demographic data and the outcome measurements were recorded using Microsoft Excel. A descriptive analysis was performed for all analyzed parameters (PAI Score, PL, percussion sensitivity, MPI Score, MP, SUV_{max}). Tables were produced for data representation.

RESULTS

During the study period of 24 months, a total of 13 patients with diagnosed HNC underwent FDG-PET/MR for staging and dental

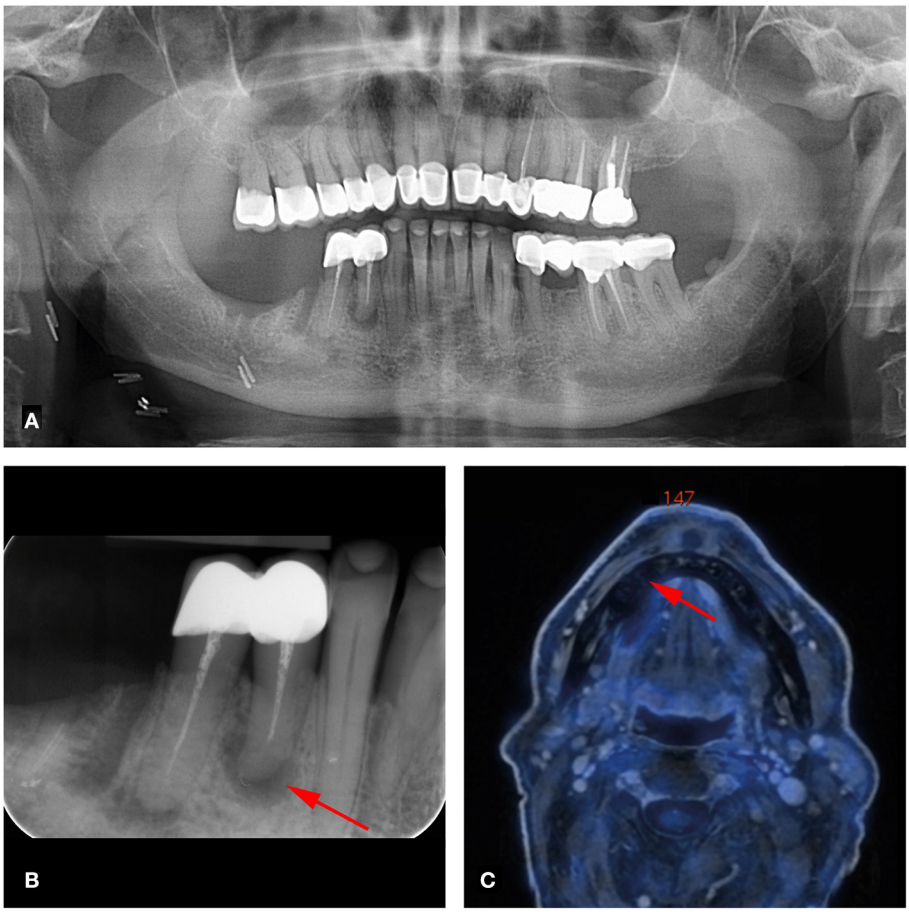

FIGURE 2 | 66-year-old man with right-sided oral cavity squamous cell carcinoma cT1 cN2b cMx. Panoramic **(A)** and dental radiography **(B)** shows a periapical lesion of tooth 44 of less than 5mm (arrow; PAI score 4, MPI score 1). **(C)** FDG-PET/MR shows no increased metabolic activity of this lesion (arrow).

TABLE 2 | Marginal periodontium (MP) in dental X-rays and FDG-PET/MR.

MPI score	MP ($n = 124$)	MP in dental radiographs ($n = 54$)	MP with increased SUV_{max} ($n = 1$)
1	90	20	0
2	16	16	0
3	12	12	0
4	6	6	1

focus assessment. Six of these patients were excluded because the required time interval of 3 months or less between FDG-PET/MR and dental focus assessment was not met. Thus, the final study population consisted of a total of seven patients (one woman and six men). The median age was 72 (23–82 years). The median time difference between the FDG-PET/MR scan and the dental focus assessment was 3 weeks (2–11 weeks). A total of 124 teeth were analyzed for dento-alveolar parameters.

Periapical Lesions

Of the 124 analyzed teeth, 23 (18.5%) showed periapical lesions (PAI $\geq$ 2) on dental radiographs (OPT/periapical X-rays). The PAI score ranged from 1 to 4, with a mean of 1.49 $\pm$ 1.06. Two periapical lesions were larger than 5 mm. On FDG-PET/MR, 19 of the 23 (82.6%) periapical lesions were detected. PET/MR did not detect any additional periapical lesions. Clinical data revealed a total of three percussion sensitive teeth. Increased FDG uptake of periapical lesions was recorded in one out of 19 lesions with an SUV_{max} of 6.8. This lesion showed a large marginal and apical bone resorption with a PAI score of 4 (**Figure 1**). This tooth showed no percussion sensitivity (**Table 1**). The other 18 teeth with apical lesions did not show increased FDG uptake, as illustrated in **Figure 2** and **Table 1**.

Marginal Periodontium

90 out of 124 Teeth (72.6%) showed an MPI score of 1 (marginal bone loss of less than one third compared to the physiological bone level) in dental radiographs. All marginal lesions (definition: MPI score $\geq$ 2) were visualized on dental radiographs. For these 34 marginal lesions, increased FDG uptake on FDG-PET/MR was seen in only one tooth (SUV_{max} 6.8) (**Table 2**). Images of this patient with increased FDG uptake of a periapical lesion and its marginal periodontium are shown in **Figure 1**.

DISCUSSION

The aim of our study was to investigate the added value of FDG-PET/MR in oral focus assessment of HNC patients. Dental radiographs, showing periapical and/or marginal periodontal lesions were compared to FDG-PET/MR. We analyzed whether metabolic activity on FDG-PET/MR correlates with findings on radiographs and clinical percussion data.

A total of 124 teeth in seven patients were examined for dento-alveolar parameters. Only one apical/marginal periodontal lesion showed increased FDG uptake with an SUV_{max} of 6.8. In contrast, another patient with a huge periapical lesion at tooth 44 (>5mm, PAI = 4) who further had no marginal bone loss (MPI = 1) showed no FDG uptake on FDG-PET/MR (**Figure 2**). While 23 apical lesions were detected on dental radiographs, FDG-PET/MR detected only 19 of these (82.6%).

Numerous studies have investigated the detection of apical lesions. Imaging modalities used include dental radiographs, ultrasound, and dental MR (20–22). A recent systematic review showed that ultrasound can distinguish periapical lesions better compared with dental radiographs, although dental radiographs still represent the gold standard (20). There is also a deep learning algorithm that surpasses experienced oral surgeons in the detection of periapical lesions in dental radiographs (22). However, the interpretation of the degree of inflammation of periapical lesions remains unclear. In dental radiographs, it could not be distinguished between apical granulomas and radicular cysts after evaluation of correlating histopathologic examinations (23). However, a recent study proofed that this differentiation is possible with MR (21). Nevertheless, interpretation of apical lesion clinical activity remains a challenge (24). In our study, most of the apical lesions as well as the marginal periodontal lesions did not show signal uptake.

Metabolic activity of potential oral foci cannot be determined on dental radiographs. Presence of metabolic activity, however, will contribute to a treatment decision. Active, presumably acute foci should be treated immediately, while inactive, presumably chronic foci may be treated in the later course under specific circumstances (12, 25). Another point in decision making, certainly is dynamic over time. For instance, radiotherapy or immunosuppression may transform a chronic, inactive lesion into an acute lesion.

In our study, no association between signs of inflammation on dental radiographs, clinical percussion data and increased FDG uptake on FDG PET/MR was found. Today, few studies have investigated the correlation of FDG PET/CT and oral foci. A retrospective study by Dijkstra et al. investigated endocarditis patients who underwent FDG-PET/CT. In their study, also no correlation between oral cavity PET findings and inflammation/infection was found (26). Nevertheless, the authors recommend further investigation to determine whether FDG-PET/CT imaging may proof useful for diagnosing inflammation and infection in the oral cavity (26). In our study, positive percussion sensitivity was not associated with increased metabolic activity on FDG-PET/MR.

Another study by Kito et al. demonstrated a correlation between FDG uptake and inflammatory extent of apical and periodontal lesions in 44 patients (19). Yamahiro et al. detected FDG uptake in different acute periodontal foci, whereas in chronic infection no increased FDG uptake was found. The authors concluded that FDG-PET/CT may serve as a valid tool to detect acute oral infections in high-risk patients (27).

In HNC imaging, FDG-PET/MR is a promising modality as it simultaneously provides morphological, functional, and molecular information (2, 7, 28, 29). In this respect, it may be expected that further studies will investigate the added value of FDG-PET/MR also in oral focus examinations in the future.

The main limitation of our study is its comparably small sample size, limiting the generalization of the results. Another limitation is the time interval between FDG-PET/MR and standardized focus assessment, which was up to 3 months, possibly resulting in changes of lesions during this time. Further prospective studies including follow-up data are desired to gain more information on the added value of FDG-PET/MR in dental diagnostics.

CONCLUSION

While FDG-PET/MR detected a certain percentage of periapical lesions, no association was found between FDG uptake and the degree of inflammation of apical lesions and marginal bone loss. Future studies with larger cohorts should determine if FDG-PET/MR results shall be considered by dentists carrying out oral focus assessment of HNC patients.

DATA AVAILABILITY STATEMENT

The raw data supporting the conclusions of this article will be made available by the authors, without undue reservation.

ETHICS STATEMENT

The studies involving human participants were reviewed and approved by Ethics committee of Zürich (No. 2017-01378). The patients/participants provided their written informed consent to participate in this study.

AUTHOR CONTRIBUTIONS

BS and MH conceived the idea. MH took responsibility of the FDG-PET MR part. LS, DS, and BG-H were involved in the planning and did the data collection. BG-H and BS supervised the data collection. Data analysis was performed by FB and SV. BS supervised the findings of this work. FB and SV created the manuscript. BS and MH edited the manuscript. All authors approved the final manuscript.

REFERENCES

1. Huellner MW, Appenzeller P, Kuhn FP, Husmann L, Pietsch CM, Burger IA, et al. Whole-body nonenhanced PET/MR versus PET/CT in the staging and restaging of cancers: preliminary observations. *Radiology.* (2014) 273:859–69. doi: 10.1148/radiol.14140090
2. Spick C, Herrmann K, Czernin J. 18F-FDG PET/CT and PET/MRI Perform Equally Well in Cancer: Evidence from Studies on More Than 2,300 Patients. *J Nucl Med.* (2016) 57:420–30. doi: 10.2967/jnumed.115.158808
3. Rettig EM, D'Souza G. Epidemiology of head and neck cancer. *Surg Oncol Clin N Am.* (2015) 24:379–96. doi: 10.1016/j.soc.2015.03.001
4. Devi S, Singh N. Dental care during and after radiotherapy in head and neck cancer. *Natl J Maxillofac Surg.* (2014) 5:117–25. doi: 10.4103/0975-5950.154812
5. Schweizerischer Krebsbericht 2021—Stand und Entwicklungen. *Bundesamt für Statistik (BFS))*. (2021). Contract No:19305696.
6. Cao C, Gan X, He Y, Su Y, Liu Z, Hu X, et al. Diagnostic efficacy of PET-CT, CT, and MRI in preoperative assessment of mandibular invasion caused by head and neck cancer: A systematic review and meta-analysis. *Oral Oncol.* (2021) 116:105264. doi: 10.1016/j.oraloncology.2021.105264
7. Hayashi K, Kikuchi M, Imai Y, Yamashita D, Hino M, Ito K, et al. Clinical Value of Fused PET/MRI for Surgical Planning in Patients With Oral/Oropharyngeal Carcinoma. *Laryngoscope.* (2020) 130:367–74. doi: 10.1002/lary.27911
8. Joshi VK. Dental treatment planning and management for the mouth cancer patient. *Oral Oncol.* (2010) 46:475–9. doi: 10.1016/j.oraloncology.2010.03.010
9. Shaw MJ, Kumar ND, Duggal M, Fiske J, Lewis DA, Kinsella T, et al. Oral management of patients following oncology treatment: literature review. *Br J Oral Maxillofac Surg.* (2000) 38:519–24. doi: 10.1054/bjom.2000.0468
10. Bichsel D, Lanfranchi M, Attin T, Gratz KW, Stadlinger B. Evaluation of oral prophylaxis during and after intensity-modulated radiotherapy due to head and neck cancer–a retrospective study. *Clin Oral Investig.* (2016) 20:721–6. doi: 10.1007/s00784-015-1546-9
11. Al-Haj Husain A, Solomons M, Stadlinger B, Pejicic R, Winklhofer S, Piccirelli M, et al. Visualization of the inferior alveolar nerve and lingual nerve using mri in oral and maxillofacial surgery: a systematic review. *Diagnostics (Basel).* (2021) 11:1657. doi: 10.3390/diagnostics11091657
12. Spijkervet FKL, Schuurhuis JM, Stokman MA, Witjes MJH, Vissink A. Should oral foci of infection be removed before the onset of radiotherapy or chemotherapy? *Oral Dis.* (2021) 27:7–13. doi: 10.1111/odi.13329
13. Alberga JM, Vosselman N, Korfage A, Delli K, Witjes MJH, Raghoebar GM, et al. What is the optimal timing for implant placement in oral cancer patients? A scoping literature review. *Oral Dis.* (2021) 27:94–110. doi: 10.1111/odi.13312
14. Maurer A, Meerwein CM, Soyka MB, Grunig H, Skawran S, Muhlematter UJ, et al. Whole-body hybrid positron emission tomography imaging yields clinically relevant information in the staging and restaging of sinonasal tumors. *Head Neck.* (2021) 43:3572–85. doi: 10.1002/hed.26856
15. Sekine T, Delso G, Zeimpekis KG, de Galiza Barbosa F, Ter Voert E, Huellner M, et al. Reduction of (18)F-FDG Dose in Clinical PET/MR Imaging by Using Silicon Photomultiplier Detectors. *Radiology.* (2018) 286:249–59. doi: 10.1148/radiol.2017162305
16. Huellner MW. PET/MR in Head and Neck Cancer - An Update. *Semin Nucl Med.* (2021) 51:26–38. doi: 10.1053/j.semnuclmed.2020.07.006
17. Queiroz MA, Huellner MW. PET/MR in cancers of the head and neck. *Semin Nucl Med.* (2015) 45:248–65. doi: 10.1053/j.semnuclmed.2014.12.005
18. Orstavik D, Kerekes K, Eriksen HM. The periapical index: a scoring system for radiographic assessment of apical periodontitis. *Endod Dent Traumatol.* (1986) 2:20–34. doi: 10.1111/j.1600-9657.1986.tb00119.x
19. Kito S, Koga H, Kodama M, Yamamoto N, Kokuryo S, Habu M, et al. Reflection of (1)(8)F-FDG accumulation in the evaluation of the extent of periapical or periodontal inflammation. *Oral Surg Oral Med Oral Pathol Oral Radiol.* (2012) 114:e62–9. doi: 10.1016/j.oooo.2012.05.027
20. Patil S, Alkahtani A, Bhandi S, Mashyakhy M, Alvarez M, Alroomy R, et al. Ultrasound imaging versus radiographs in differentiating periapical lesions: a systematic review. *Diagnostics (Basel).* (2021) 11:1208. doi: 10.3390/diagnostics11071208
21. Juerchott A, Pfefferle T, Flechtenmacher C, Mente J, Bendszus M, Heiland S, et al. Differentiation of periapical granulomas and cysts by using dental MRI: a pilot study. *Int J Oral Sci.* (2018) 10:17. doi: 10.1038/s41368-018-0017-y
22. Endres MG, Hillen F, Salloumis M, Sedaghat AR, Niehues SM, Quatela O, et al. Development of a deep learning algorithm for periapical disease detection in dental radiographs. *Diagnostics (Basel).* (2020) 10:430. doi: 10.3390/diagnostics10060430
23. Bornstein MM, Bingisser AC, Reichart PA, Sendi P, Bosshardt DD, von Arx T. Comparison between radiographic (2-dimensional and 3-dimensional) and histologic findings of periapical lesions treated with apical surgery. *J Endod.* (2015) 41:804–11. doi: 10.1016/j.joen.2015.01.015
24. Galler KM, Weber M, Korkmaz Y, Widbiller M, Feuerer M. Inflammatory response mechanisms of the dentine-pulp complex and the periapical tissues. *Int J Mol Sci.* (2021) 22:1480. doi: 10.3390/ijms22031480
25. Schuurhuis JM, Stokman MA, Witjes MJH, Reintsema H, Langendijk JA, Vissink A, et al. Patients with advanced periodontal disease before intensity-modulated radiation therapy are prone to develop bone healing problems: a 2-year prospective follow-up study. *Support Care Cancer.* (2018) 26:1133–42. doi: 10.1007/s00520-017-3934-y
26. Dijkstra GW, Glaudemans A, Erba PA, Wouthuyzen-Bakker M, Sinha B, Vallez Garcia D, et al. Relationship between (18)F-FDG Uptake in the Oral Cavity, Recent Dental Treatments, and Oral Inflammation or Infection: A Retrospective Study of Patients with Suspected Endocarditis. Diagnostics (Basel). (2020) 10. doi: 10.3390/diagnostics10090625
27. Yamashiro K, Nakano M, Sawaki K, Okazaki F, Hirata Y, Takashiba S. The potential of positron emission tomography/computerized tomography (PET/CT) scanning as a detector of high-risk patients with oral infection during preoperative staging. *Oral Surg Oral Med Oral Pathol Oral Radiol.* (2016) 122:242–9. doi: 10.1016/j.oooo.2016.04.006
28. Schlumpf MF, Haerle S. The current role of imaging in head and neck cancer: a clinician's perspective. *Swiss Med Wkly.* (2014) 144:w14015. doi: 10.4414/smw.2014.14015
29. Kim SY, Beer M, Tshering Vogel DW. Imaging in head and neck cancers: Update for non-radiologist. *Oral Oncol.* (2021) 120:105434. doi: 10.1016/j.oraloncology.2021.105434

Conflict of Interest: MH received research grants from GE Healthcare, grants from the CRPP Artificial Intelligence in oncological Imaging Network by the University of Zurich, and a fund by the Alfred and Annemarie von Sick legacy for translational and clinical cardiac and oncological research.

The remaining authors declare that the research was conducted in the absence of any commercial or financial relationships that could be construed as a potential conflict of interest.

Advantages of publishing in Frontiers

OPEN ACCESS
Articles are free to read for greatest visibility and readership

FAST PUBLICATION
Around 90 days from submission to decision

HIGH QUALITY PEER-REVIEW
Rigorous, collaborative, and constructive peer-review

TRANSPARENT PEER-REVIEW
Editors and reviewers acknowledged by name on published articles

Frontiers
Avenue du Tribunal-Fédéral 34
1005 Lausanne | Switzerland

Visit us: www.frontiersin.org
Contact us: frontiersin.org/about/contact

REPRODUCIBILITY OF RESEARCH
Support open data and methods to enhance research reproducibility

DIGITAL PUBLISHING
Articles designed for optimal readership across devices

FOLLOW US
@frontiersin

IMPACT METRICS
Advanced article metrics track visibility across digital media

EXTENSIVE PROMOTION
Marketing and promotion of impactful research

LOOP RESEARCH NETWORK
Our network increases your article's readership